OPTICAL AND MAGNETIC RESONANCE STUDIES OF ORGANIC MATERIALS USED IN PHOTOVOLTAIC APPLICATIONS

by

Golda Hukic-Markosian

A dissertation submitted to the faculty of
The University of Utah
in partial fulfillment of the requirements for the degree of

Doctor of Philosophy

in

Physics

Department of Physics and Astronomy

The University of Utah

December 2011

The University of Utah Graduate School

STATEMENT OF DISSERTATION APPROVAL

The dissertation of **Golda Hukic-Markosian**

has been approved by the following supervisory committee members:

Zeev Valy Vardeny	, Chair	**06/28/2011** Date Approved
Mikhail Raikh	, Member	**06/28/2011** Date Approved
Christoph Boehme	, Member	**06/28/2011** Date Approved
Calrton DeTar	, Member	**07/21/2011** Date Approved
Michael Morse	, Member	**06/28/2011** Date Approved

and by **David Kieda** , Chair of

the Department of **Physics and Astronomy**

and by Charles A. Wight, Dean of The Graduate School.

ABSTRACT

In this work we focused on the electronic processes in active materials used in organic photovoltaics. Films of several electron donors, acceptors, and their blends were investigated by means of steady state optical and magnetic resonance probes.

The efficiency of organic photovoltaics depends on film morphology, charge mobility and light absorption. Therefore we studied common donor materials with very different morphology: RR P3HT (regioregular poly(3-hexylthiophene)) and RRa P3HT (regio-random poly(3-hexylthiophene)). The charge transport is affected by regioregularity and molecular weight. Consequently, we examined RR P3HT polymers with various molecular weights. We learned that a polaron band at low photon energy only appears in the photoinduced absorption spectrum of low molecular weight RR P3HT.

We studied two main approaches for improving the efficiency of organic photovoltaics: modifying the lowest (highest) unoccupied (occupied) molecular orbital, LUMO (HOMO) of the donor (acceptor) materials; as well as synthesizing polymer donors with low optical gap.

TAES-V is a low-band gap polymer composed of three co-polymers having the structure of ‘donor-acceptor-donor’. Its record power conversion efficiency (~7%) when blended with $PC_{70}BM$ is partially due to the significantly red-shifted absorption. Our

results show that an intrachain charge transfer exciton (CTE) is long-lived in this polymer and that it persists in the blend with $PC_{70}BM$.

In addition we studied three fullerene derivatives. The LUMO of a fullerene derivative can be changed by the addition of functional side groups to the fullerene cage that improves the organic solar cells performance. The addition can also lead to hindering of aggregation in the films, which consequently decreases the charge transport in solar cells.

In the study of polymer/fullerene blends we mixed RR P3HT with three different fullerene derivatives. We conclude that higher power conversion efficiency of a blend is mainly due to the higher LUMO level and improved open circuit voltage.

We also compared DOO-PPV (H-polymer) with DOO-PPV enriched with deuterium (D-polymer). We show that hyperfine interaction is weaker in the D-polymer and that the spin relaxation rate is four times smaller than in H-polymer. Consequently, the longer spin diffusion length makes the D-polymer better suited for higher performing organic spin-valves.

To my husband Richard, my family and my dear friends who supported me in this amazing journey.

CONTENTS

ACKNOWLEDGMENTS

I would like to express my deepest gratitude to my advisor Prof. Valy Vardeny. This work wouldn't be possible without his constant guidance, encouragement, and care. I was so fortunate to experience and learn from his passion for understanding physics and finding scientific truth even when it differs from the mainstream beliefs. I would also like to thank my supervisory committee: Dr. Mikhail Raikh - who always believed in me and encouraged me to continue with my Ph.D., Dr. Christoph Boehme for his advice and lab resources, Dr. Carlton DeTar, and Dr. Michael Morse. The help and instructions provided by Dr. Randy Polson, Dr. Matt DeLong, Mr. Leonard Vojcik, and Wayne Wingert were invaluable. I would like to acknowledge Dr.Vladimir Burtman, Dr. Tromer Drori and Dr. Alexander Ndobe who introduced me to the field and the experimental techniques. I would like to thank Drs. Darin Laird and Sergey Li from Plextronics for their collaboration, support and invaluable new materials synthesized at Plextronics, Inc.

I would also like to thank my research group members: Dr. Tho Nguyen, Bhoj Gautam, Bill Pandit, Tek Basel, and Ella Olejnik for the collaboration, useful ideas, and fruitful discussions. My dear friends Maria Navas Moreno and Su Liu deserve special thanks for the emotional support during these long five years.

It is impossible to sufficiently express my gratitude to my husband Richard Paul Markosian and my family for their continuous support, patience, and love during my studies.

Finally, I would like to thank the funding agencies DOE (grant No DE-FG02-04ER46109) and NSF (grant No DMR 08-03325).

CHAPTER 1

INTRODUCTION

For a long time all polymers have been regarded as insulators. Moreover, any electrical conductance in polymers, which was mostly caused by loosely bound ions, was considered an undesirable effect.[1] However, in the 1970s significant work was done on conduction in π-conjugated polymers. Consequently, in 1977, Alan J. Heeger, Alan MacDiarmid and Hideki Shirakawa reported high conductivity in oxidized iodine-doped polyacetylene. Later, they received the 2000 Nobel Prize in Chemistry *"For the discovery and development of conductive polymers."*

Subsequently conducting polymers and their applications have become the focus of worldwide research. The flexibility, lightweight, and relatively inexpensive fabrication made polymers very attractive for a number of applications. In the past 30 years significant progress was made in the field of organic photovoltaics [2-6], organic light emitting diodes [7], organic field effect transistors [8], organic spin-valves [9], biological sensors, etc.

In this chapter we will briefly introduce π-conjugated polymers and their electronic processes; then we will introduce some of the applications such as organic

solar cells, organic light emitting diodes and organic spin-valves. In addition, we will mention some of the discoveries in organic spintronics and introduce magnetic field effect.

The focus of this work is mainly to study organic materials that can be used in organic photovoltaics as donor and acceptor materials. Using steady state optical and magnetic resonance probes we examine electronic processes in these materials. We also compare several donor and acceptor materials to understand how the morphology and the chemical structure can affect their optical and magnetic resonance properties. All of this can bring us closer to the understanding of why some materials are better suited for use in organic solar cells.

1.1. Π-conjugated polymers

The term polymer refers to a large molecule consisting of a number of repeat units connected by covalent chemical bonds. Most commonly, the continuously linked backbone of the polymers studied here consists of carbon atoms. The carbon atoms in the polymer backbone can be connected by single (sp^3 hybridization), double (sp^2 hybridization), or triple bonds (sp hybridization) as shown in Figure 1. If all carbon atoms are connected by single bonds, the result is a *saturated* polymer that behaves as an insulator.

In π-conjugated polymers, the sp^2p_z hybridization causes one electron to be bound in π bond (p_z) perpendicular to the polymer backbone (sp^2), while the other three electrons form planar σ-bonds with the two neighboring intrachain carbon atoms and one side group. The π-electrons are delocalized over a number of intrachain C-atoms [10].

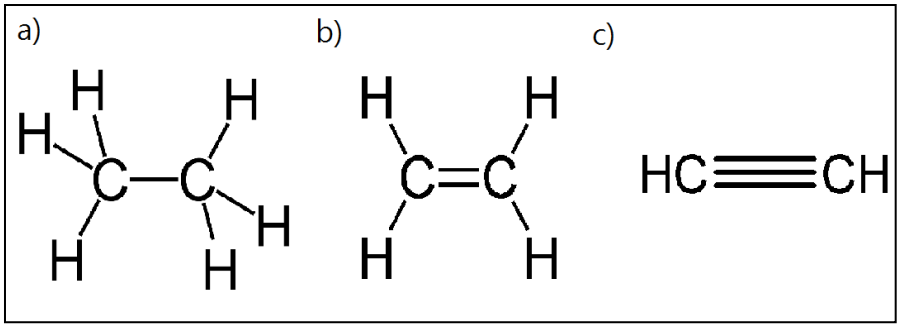

Figure 1 Hybridization types of carbon atoms and bonds in conjugated polymer subunits. a) ethane with single bonds and sp^3 hybridization, b) ethylene with a double bond and sp^2 hybridization, and c) acetylene with a triple bond and sp hybridization

Since there is one π-electron per C-atom in the chain, these types of polymers can be viewed as one-dimensional metals with half-filled electronic band.

One-dimensional metals distort and dimerize due to electron-phonon coupling [11]. For t-(CH)x in the dimerized configuration, the polymer backbone is made of a series of short double bonds and long single bonds. This causes formation of an energy gap at the metal Fermi energy that was named the optical gap. For other polymers benzene rings or five-member rings are also involved in the dimerization; these ministructures enhance the energy gap due to electron-phonon interaction, by adding a structural component to the gap equation.

1.1.1. Model for stable excitations in π-conjugated polymers

Su, Shriefer, and Heeger proposed a model, named SSH model, for t-$(CH)_x$ based on the tight binding approximation, taking into account only electron-phonon interaction, but ignoring electron-electron interaction [12]. In this model they applied a semiclassical Huckel Hamiltonian that consists of two components: the classically treated lattice kinetic energy and quantum mechanically treated electron-phonon interaction as seen in equation (1.1):

$$H_{SS} = \frac{K}{2}\sum_n (u_n - u_{n-1})^2 + \frac{M}{2}\sum_n \left(\frac{du}{dt}\right)^2 - \sum_{n,s}\left(t_0 + \alpha(u_{n+1} - u_n)\right)\left(C^+_{n+1,s}C_{n,s} + Cn,s+Cn+1,s,\right. \quad (1.1)$$

where t_0 is the hopping integral between the nearest carbon neighbors on the undistorted chain, α is the electron-lattice coupling constant, $C^+_{n,s}$ and $C_{n,s}$ are creation and annihilation operators of an electron on a site n with a spin s, K is spring constant due to π-electrons, and u_n is deviation of the n-th side from the equilibrium position in an undistorted chain with equal distances between the sites.

According to this model the dimerization lowers the system energy and opens the energy gap, $E_g = 2\Delta$, where $\Delta=4\alpha u$, and u is the dimerization amplitude in equilibrium. Consequently, the occupied electronic states in the equilibrium are lowered resulting in a more stable configuration. Therefore, the system has properties of a semiconductor instead of a one-dimensional metal, since the density of states at the Fermi level is null.

Models that take into account the electron-electron interaction and tri-dimensional chain coupling are based on the Hubbard Hamiltonian.

$$H_{Hubb} = U\sum_i n_{i,\uparrow}\, n_{i,\downarrow}, \quad (1.2)$$

where U is the Coulombic repulsion between two electrons on the same site, $n_{i,\uparrow}$ and $n_{i,\downarrow}$ describes the density operators for electrons with spin up and spin down.

However, the Hubbard model does not take into the account electron-phonon interaction. Therefore, more realistic model would be a combination between the SSH and Hubbard model. This is the Pariser – Parr - Pople (PPP) model, for example [13]

1.2. Major photoexcitations

Two types of photo-excitations are dominant in the π-conjugated polymers: neutral (excitons) and charged (polarons) photo-excitations. After photon absorption neutral, spinless excitons are photogenerated that later may either dissociate into charged excitations or undergo intersystem crossing to other type of neutral excitation with non-zero spin (Figure 2). These photoexcitations will be discussed in the following sections.

1.2.1. Excitons

Excitons are electron hole pairs bound through their mutual Coulombic interaction. They can have kinetic energy. In the dipole approximation excitons are formed via absorption of a single photon when electron is promoted to a higher energy level. The excitation causes structural and polarization relaxation of the surrounding geometry that leads to the exciton binding energy, E_b. In most π-conjugated polymers the value of the intrachain E_b is between 0.3 – 0.5 eV.

Based on the spin alignment, the electron and hole in an exciton can form singlet or triplet state with total spin 0 or 1, respectively, both excitations still remaining neutral. The wavefunction that describes the exction (two particle system) is antisymmetric in the spin and the electron coordinates and can be obtained from the Slater determinant:

$$\Psi = \begin{vmatrix} \psi_i(r)\chi_i(\sigma) & \psi_i(r')\chi_i(\sigma') \\ \psi_j(r)\chi_j(\sigma) & \psi_j(r')\chi_j(\sigma') \end{vmatrix}, \tag{1.3}$$

where $\psi_i(r)$ represent the electron part and $\chi_i(\sigma)$ represents the spin part of the wavefunction. The wavefunction with total spin quantum number S=0 corresponding to the singlet state and three wavefunctions with S=1 or triplet states are given by equations

(1.4) through (1.7) where the arrows ↑ and ↓ represent spin up and spin down projection of χ:

$$\Psi^{S=0} = \frac{1}{2}[\psi_1(1)\psi_2(2) + \psi_2(1)\psi_1(2)][\uparrow(1)\downarrow(2) - \uparrow(2)\downarrow(1)], \quad (1.4)$$

$$\Psi^{S=1} = \frac{1}{2}[\psi_1(1)\psi_2(2) - \psi_2(1)\psi_1(2)][\uparrow(1)\downarrow(2) + \uparrow(2)\downarrow(1)], \quad (1.5)$$

$$\Psi^{S=1} = \frac{1}{2}[\psi_1(1)\psi_2(2) + \psi_2(1)\psi_1(2)][\uparrow(1)\uparrow(2)], \quad (1.6)$$

$$\Psi^{S=1} = \frac{1}{2}[\psi_1(1)\psi_2(2) + \psi_2(1)\psi_1(2)][\downarrow(1)\downarrow(2)], \quad (1.7)$$

The exciton bands can be seen in Figure 2. The radiative recombination or photoluminescence (PL) from a singlet state is a fast process of the order of 100 picoseconds (ps). However, it is possible for an exciton to cross from singlet into triplet manifold via intersystem crossing (ISC) within ~10 nanoseconds (ns). The ISC process is permitted due to the spin flip of one of the exciton's electron due to spin-orbit coupling, hyperfine interaction, or existence of radical impurities in the polymer chains.

The optical transition from the triplet excited state to the singlet ground state is ordinarily forbidden. However, in π-conjugated polymers a weak radiative transition from the excited triplet lowest state, or phosphorescence (PH), is sometimes observed. This transition is allowed due to spin flip of one of the electrons caused by a spin-orbit interaction. This transition is relatively long-lived on the order of several milliseconds (ms) [14].

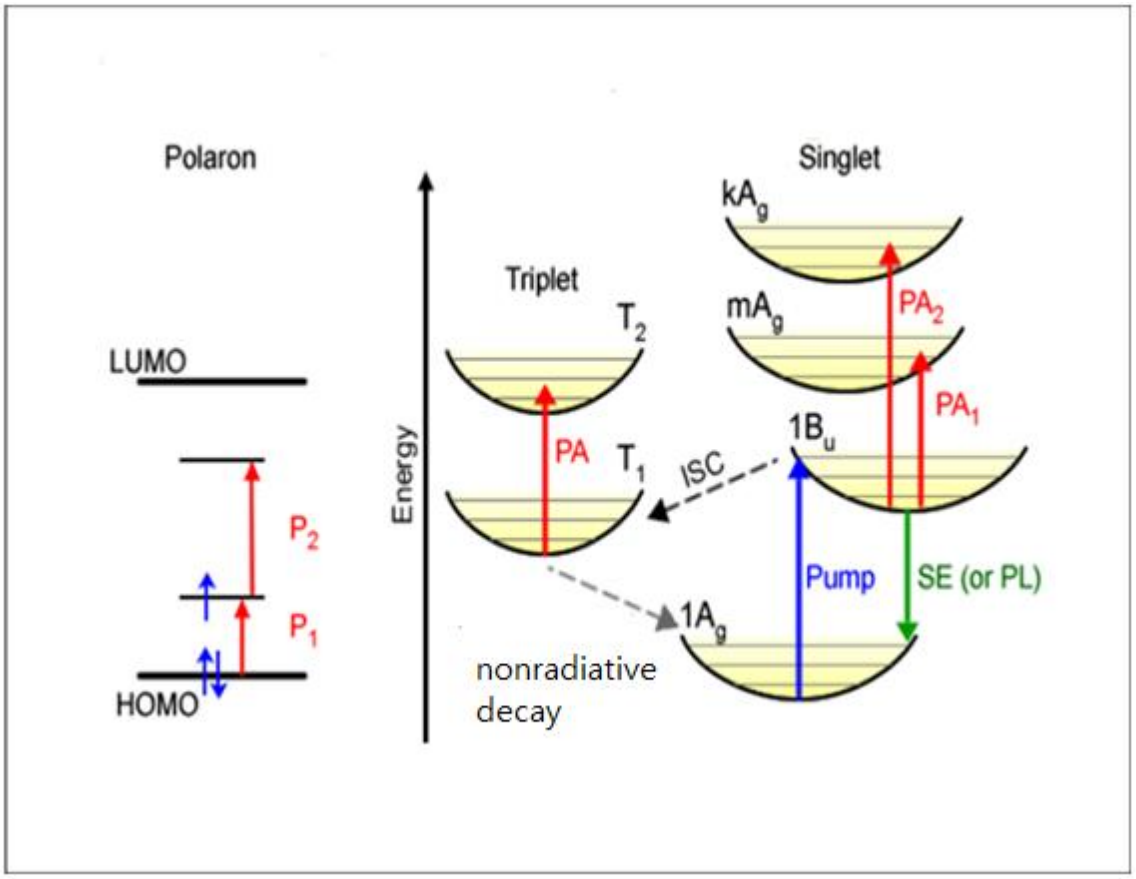

Figure 2 Photoexcitations in conjugated polymers: polaron excitation with P1 and P2 transitions on the left and exciton bands on the right. The triplet state has a lower energy than the singlet state. In CW photoinduced absorption we only can see long lived photoexcitations with the lifetime of the order of one millisecond such as absorption due to triplet exciton and polaron: P1 and P2 transitions. However, we cannot detect PA1 and PA2 transitions in the singlet manifold because of their short lifetimes.

1.5.1. Polaron excitations

The intermolecular forces in organic materials are relatively weak resulting in a less rigid structure compared to inorganic materials such as silicon. Consequently, a moving charge carrier can cause local distortion and form a charged quasiparticle with nonzero spin dubbed polaron. A polaron can be charged positively (P^+) or negatively (P^-) and has spin ½.

Polarons have two localized states in the gap and usually two allowed optical transitions P_1 and P_2 as shown in Figure 3. The third transition from u to u, or from g to g, is forbidden, but can become somewhat allowed due to symmetry breaking on the chain, for example by strong interchain interaction, or the existence of a sulfur atom with strong bonding.

Polarons move from chain to chain through hopping, and they are the major charge/current carriers in organic device applications such as organic photovoltaic devices, as will be discussed later in this chapter.

1.5.1. Polaron pairs

A polaron pair shown in Figure 4 is formed by two oppositely charged polarons on adjacent polymer chains [15]. A polaron pair that is generated by relaxation of a higher energy singlet exciton is called a geminate pair and it has spin 0. If a polaron pair is generated via an unrelated electron and a hole, then it is called a nongeminate polaron pair, and it can have spin 0 or 1 with a higher probability of having triplet than singlet configuration (3:1).

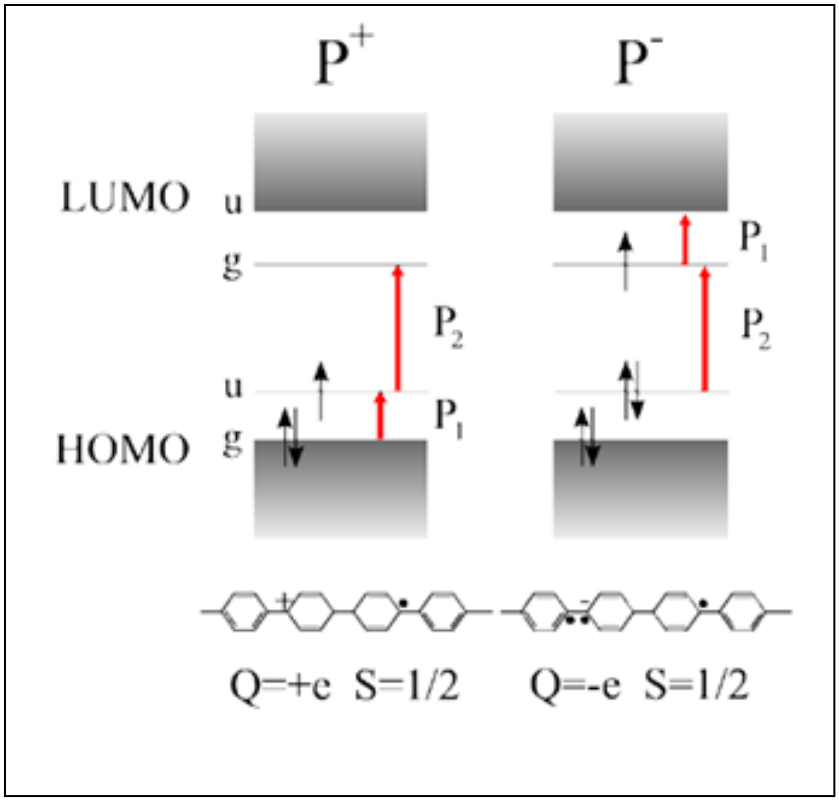

Figure 3 Energy levels and optical transition of positively and negatively charged polarons in the symmetric approximation.

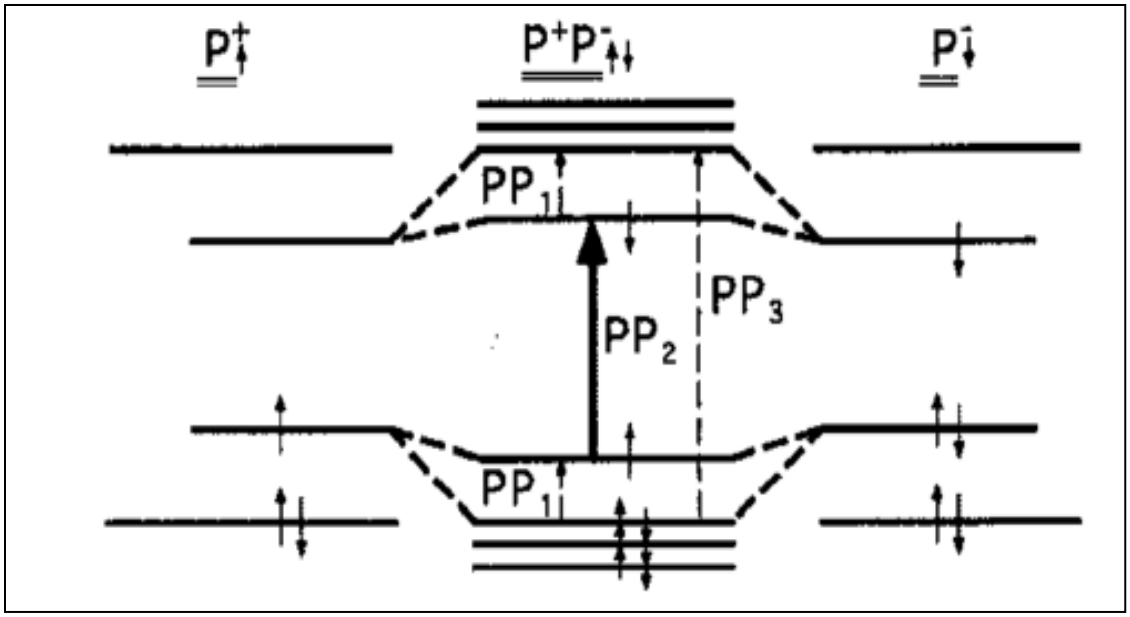

Figure 4 Polaron pair energy levels and optical transitions.

1.5.2. Bipolaron excitations

Bipolarons are formed by two equally charged polarons on the same site. They can be formed by either two positive polarons (BP^+) or by two negative polarons (BP^-). Bipolarons have two electronic levels in the gap, but only one allowed optical transition below the gap, as shown in Figure 5 [16]. BP excitations are formed in cases that there are polarons with high density; this is needed to overcome the Coulomb repulsion of two like charges on the same lattice distortion.

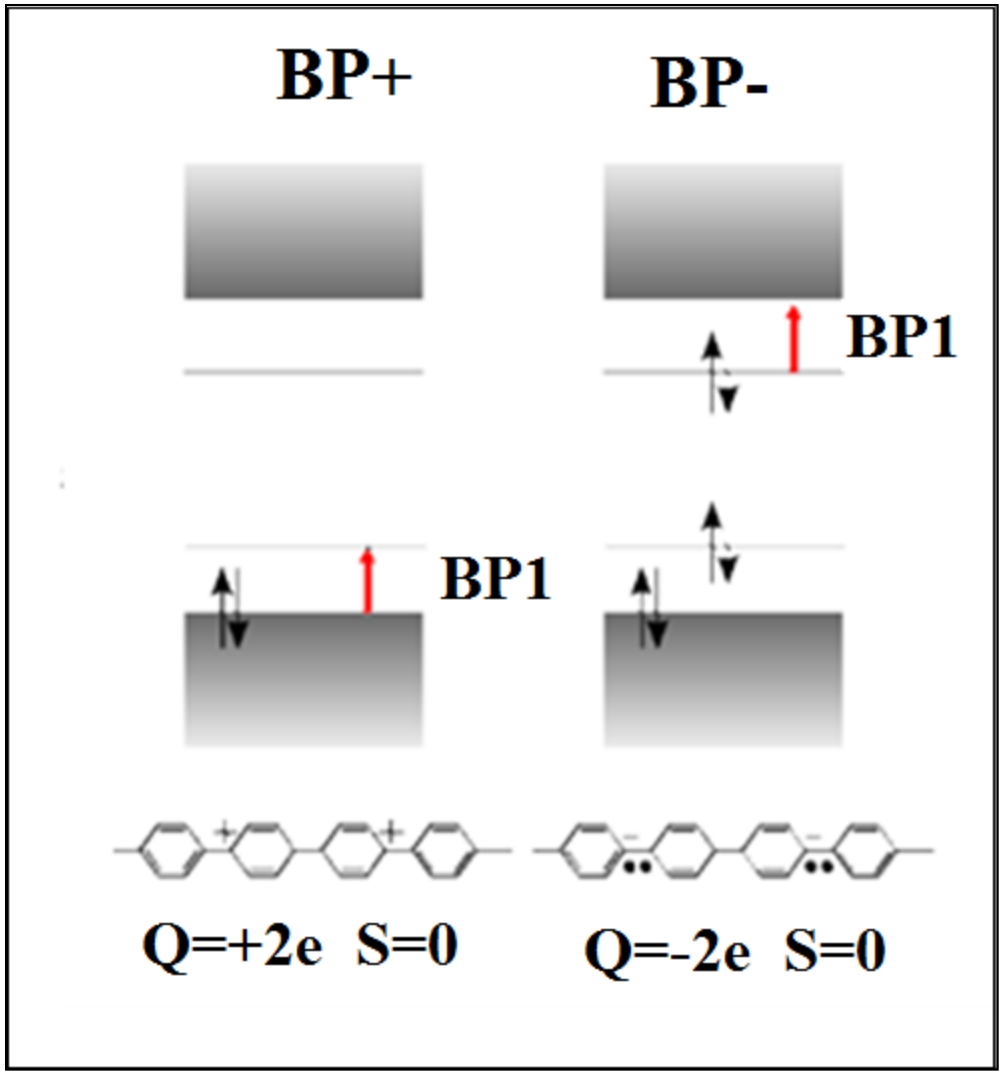

Figure 5 Bipolaron energy levels and allowed optical transitions.

1.3. Organic solar cells

Conventional solar cells, or silicon p-n junction cells were invented in the 1950s [17]. Since then there were considerable advances in efficiency, reliability and cost reduction of these photovoltaic solar cells. However, the cost of solar power still remains too high. Therefore considerable effort has been made in developing solar technology based on less expensive organic semiconductors [18].

The fundamental difference between organic and inorganic photovoltaic solar cells is that light absorption in the former results in the formation of excitons (coulombically bound electron-hole pair) rather than free electron-hole pairs as in the latter semiconductors.

The lifetime of an exciton in organic photovoltaic (OPV) device is ~1ns after which the exciton recombines emitting light. Therefore the achievement of a successful dissociation of excitons into free charge carriers-- namely electrons and holes that can be collected at the electrodes-- has greatly influenced the architecture of organic solar cells.

1.3.1. Single layer OPV device

A single layer architecture is the simplest. It consists of an organic semiconductor sandwiched between two electrodes with asymmetric work function (Figure 6). However, since most of the photogenerated excitons do not dissociate, this kind of OPV device has very low power conversion efficiency.

1.3.1. Bilayer OPV device

The bilayer OPV device consists of one layer of an electron donor (for example polymer) and the other layer of electron acceptor (for example fullerene molecule) sandwiched between two electrodes as shown in Figure 6.

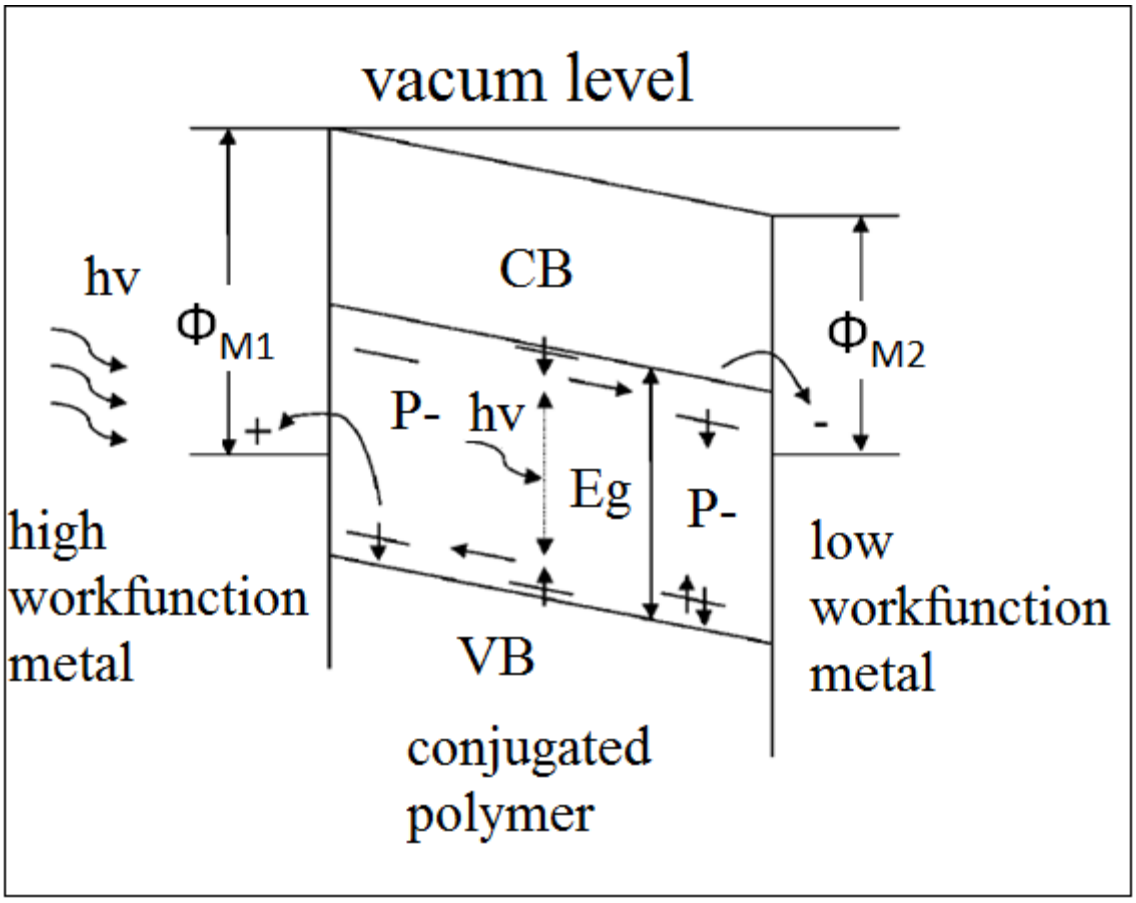

Figure 6 Processes in a single layered photovoltaic device in the rigid band approximation.

One of the electrodes (ITO on the glass) must be transparent so that light can penetrate and photoexcite the polymer. Following light absorption the photogenerated exciton diffuses through the polymer and relaxes into the loosely bound polaron pair if it reaches the donor/acceptor interface. Due to the electric field at the interface the polaron pair may further separate into a free hole and electron, because the electron tends to transfer to the acceptor layer that has a lower LUMO than the polymer, whereas the hole stays on the polymer.

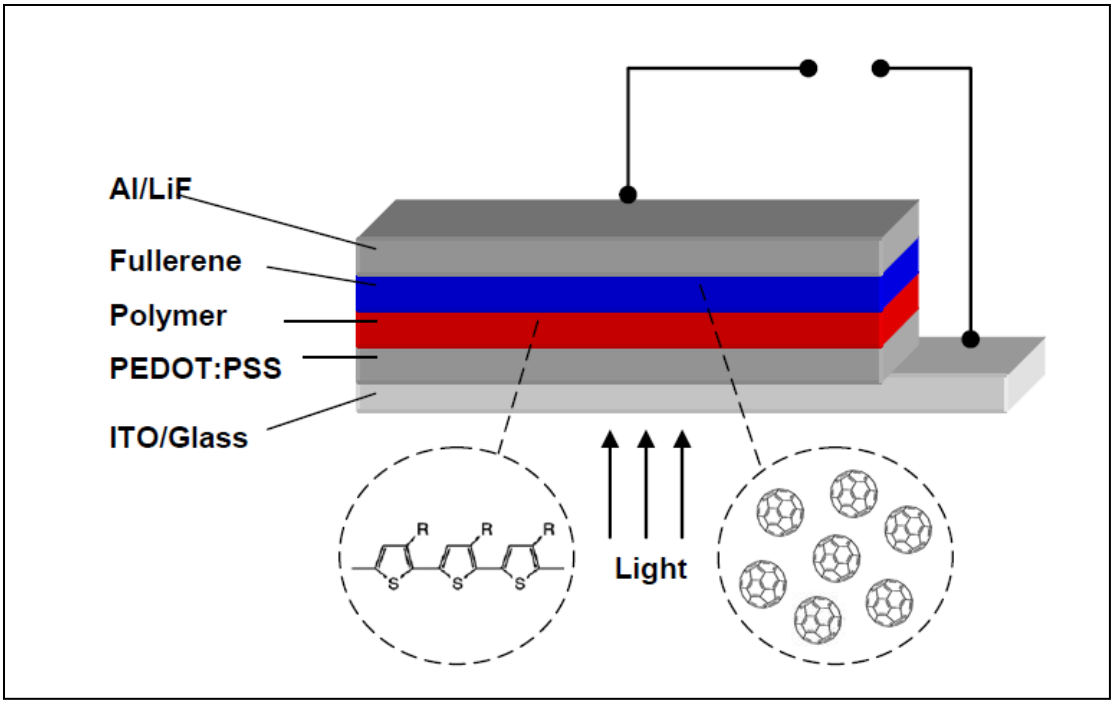

Figure 7 The schematic representation of a bilayer OPV device.

The dissociation efficiency of the polaron pair at the interface is nearly 100% because it is a very fast process on the order of femtoseconds (fs), much faster than the competing processes such as photoluminescence (~ns) and recombination due to charge back transfer (~μs).

Once separated, the electrons and holes may be transported to their electrodes to generated current and photovoltage.

The major flaw of this architecture lies in the difficulty in finding the optimal thickness of organic materials. The diffusion length of an exciton is ~10 nm, and thus if the polymer layer is too thick, then the photogenerated exciton recombines before reaching the donor/acceptor boundary. This results in a loss of photocurrent. However, if the polymer layer is too thin for collecting all the photogenerated excitons, then the

absorption will be low because most of the photons will pass through the material without photogenerating excitons.

1.3.2. Bulk heterojunction OPV device

The above mentioned thickness problem of the polymer layer is solved by changing the architecture. In bulk heterojunction the active layer consists of a mixture of the donors and acceptors as shown in Figure 8. Consequently, the donor and acceptor domains are spontaneously formed in the film cast from this mixture [19, 20]. The size of these domains is comparable to the exciton diffusion length, so that an exciton can reach the interface before it recombines. This results in a reduction of the exciton loss observed in bilayer devices. However, for successful transport of free charges to the electrodes, continuous pathways of acceptor (fullerene) and polymer (donor) to the electrodes are needed. Unfortunately, this is not always the case, since in a polymer/fullerene mixture the fullerene domains can be completely surrounded by a polymer (and vice versa), which results in loss due to charge back-transfer recombination.

1.3.3. Power conversion efficiency

Power conversion efficiency of an OPV cell presents the percentage of the solar energy shining on the device that is converted into electricity. It can be calculated from the I-V characteristics of a solar cell, as shown in Figure 9 and equation (1.8).

$$\eta = FF\,\frac{Jsc Voc}{Ps}. \tag{1.8}$$

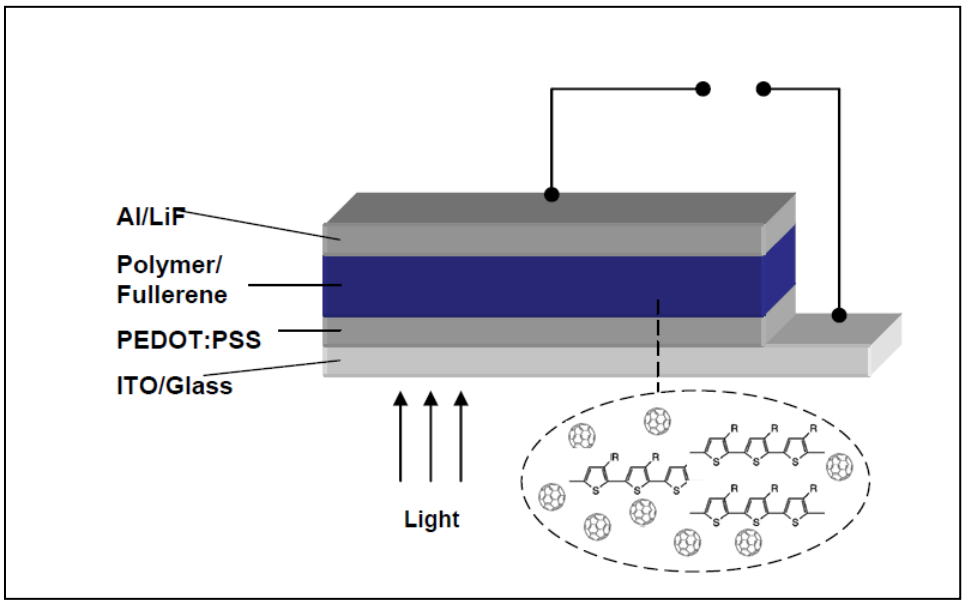

Figure 8 Bulk heterojunction architecture of an OPVC

Jsc is the short circuit current density. Voc is the open circuit voltage. FF or fill factor is the ratio of the maximum power delivered by solar cell (illustrated by light gray rectangular area in Figure 9 and product of Jsc and Voc). Ps is the optical irradiance of the incident light from the sun, 100mW/cm^2.

From equation (1.8) we can see that by increasing the fill factor, Jsc, or Voc we may raise the power conversion efficiency of a solar cell.

Depending on donor and acceptor materials used in organic photovoltaic cell, the power conversion efficiency may vary. In this work we present our studies of pure polymers, fullerene derivatives, as well as their mixture using optical and magnetic resonance experiments.

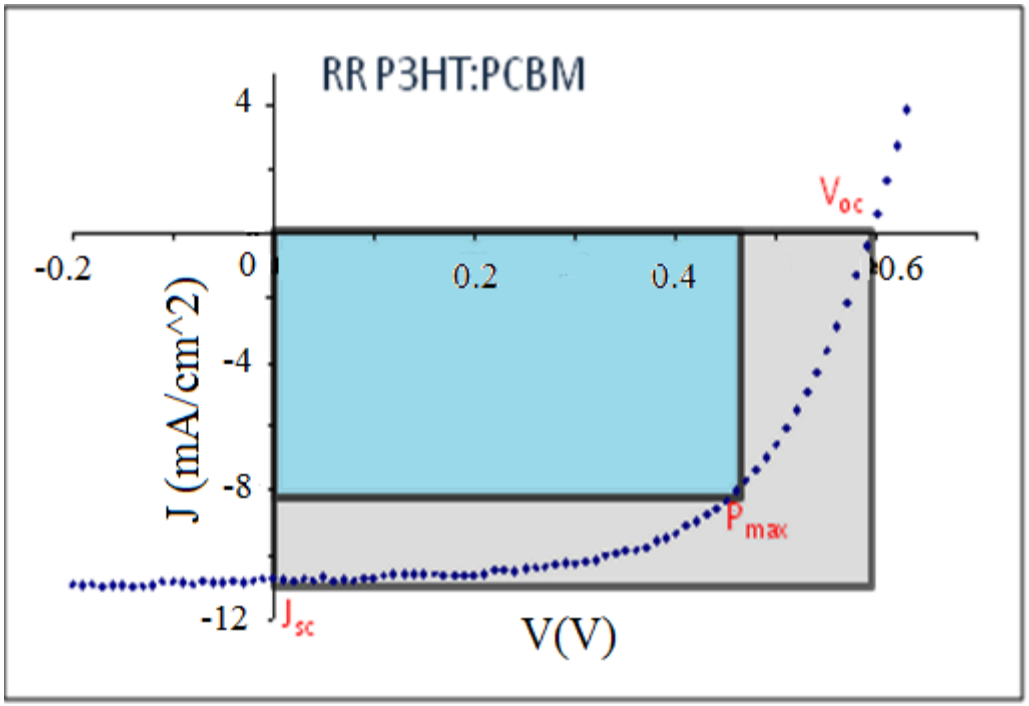

Figure 9 I-V characteristic of an organic solar cell with RR P3HT/PCBM as the active material. This measurement was done by Dr. Ye Zhang.

1.4. Organic light emitting diodes

A light emitting diode (LED) is a semiconductor light emitting source. LED was introduced as a practical electronic component in 1962.[21] An organic light emitting diode (OLED) is an LED in which the emissive electroluminescent layer is an organic semiconductor film which emits light when electric current is applied to the electrodes. The organic semiconductor is sandwiched between two electrodes (Figure 10). In a more sophisticated OLED the organic material consists of an electron and hole transport layers, named ETL and HTL, respectively. The electrons and holes are injected from the opposite electrodes when a biasing voltage is applied to them. They migrate through the ETL and HTL via hopping in the form of charge polarons. The oppositely charged

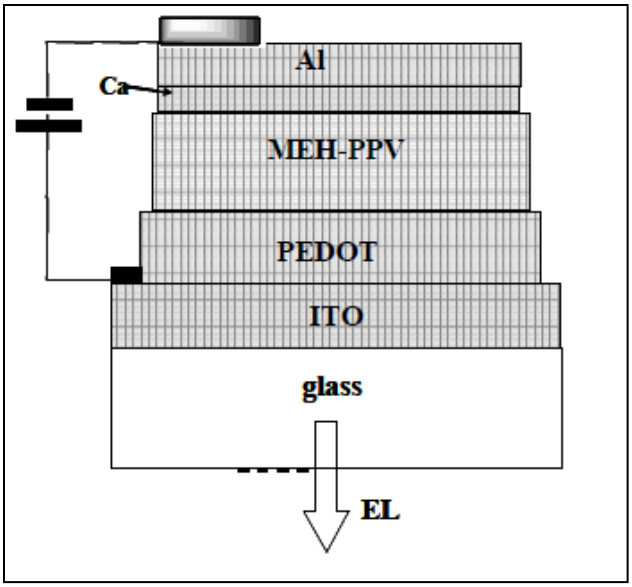

Figure 10 The configuration of a typical OLED. ITO coated glass acts as a transparent anode and calcium as a low work function cathode. Aluminum is evaporated on the top of calcium as a protection layer. PEDOT presents hole transport layer and MEH-PPV active organic material.

polarons sometimes meet in the active material, and if they are within capture distance (equation(1.9)), then they form bound polaron pairs, which are precursors to excitons. Subsequently, the exciton may recombine radiatively and emit light. The emitted light or electroluminescence (EL) is collected through the transparent electrode.

$$r_C = \frac{q^2}{4\pi\varepsilon_r\varepsilon_0 KT}, \tag{1.9}$$

The recombination rate in the OLED depends on charge density and mobility. The recombination zone within the active layer can be adjusted by changing the work-functions of electrodes, adjusting the HOMO-LUMO levels of transport media, and changing the thickness of electron and hole transport layers.

The electron-hole pairs can be either in singlet or triplet configuration. However, in polymers only the singlet configuration results in emission of light. In small molecules with large SOC it may be that PH emission prevails. Because of the triplet/singlet spin statistics (3:1) these types of OLEDs are more effective.

Consequently OLEDs have been categorized according to emissive materials as two different types: small molecule and polymer OLEDs. One of the advantages of polymer OLEDs that are studied in our group is that the active layer does not have to be evaporated like small molecules, but in contrast it can be spin-coated from the polymer solution. This type of processing is also suitable for large area OLED such as in TV screens.

White organic light emitting diode or WOLED refers to an organic light emitting diode emitting white light. The first WOLED was reported in 1994 by Kido et al.[22]

One of the challenges to be overcome is the emission spectrum. The perfect WOLED should emit continuous spectrum covering the entire visible range (400 nm to 800 nm) and should have similar spectral distribution to the sun light. The most common approach to solution of this problem is to combine electroluminescence from several lumophores (2 or 3). The lumophores can be blended into a single layer, separated into different layers in the same device, or contained in the several independent devices where each device emits light in a different color. [23]

The overall efficiency of an OLED (or WOLED) depends on a number of factors such as charge recombination efficiency; the ratio of generated singlet and triplet excited states; the internal electroluminescence quantum efficiency; and the fraction of photons extracted from the structure. The charge recombination efficiency in most cases

approaches 1. In contrast the other factors especially singlet to triplet ratio present significant loss in the overall efficiency.

According to spin statistics, 25% of all generated excitons are in singlet configuration and 75% are in the triplet configuration. Since only singlet excitons recombine radiatively in polymers, this puts an upper limit of 25% on the overall efficiency of an OLED based on these organic materials. However, this limitation can be overcome by using a heavy metal ion in a phosphorescent material[24]. A heavy metal ion relaxes the spin conservation law and promotes intersystem crossing between the triplet and singlet states. In this way it is possible to harvest emission from triplet state and increase the efficiency of an OLED.

However, the successful fabrication of WOLED based on phosphorescent materials is complicated because of fast degradation and instability of blue phosphorescent emitters. Therefore, the focus shifted to fabricating WOLEDs with luminescent blue emitters and phosphorescent emitters at longer wavelengths. Consequently, it is possible to recycle triplet states from blue luminescent emitters by transferring them to phosphorescent emitters at longer wavelengths where they can decay radiatively.[23]

1.4.1. Magnetic field effect

As mentioned earlier in an OLED device the generated polaron pairs can be either in singlet or triplet state. In the absence of an external magnetic field, triplet states are degenerate, and the singlet PP mixes with an entire PP triplet manifold due to the hyperfine interaction. However, when a strong magnetic field is applied to the device the degeneracy of the triplet states is lifted due to the Zeeman interaction, and then singlet PP

mixes only with the triplet PP spin sublevel that has magnetic quantum number 0. Consequently a magnetic field can influence the formation of singlet and triplet excitons depending on their generation rates. Increased formation of singlet excitons at the expense of triplet excitons would certainly benefit the OLED overall efficiency.

1.5. Organic spintronics

For the past decade the potential of organic spintronics has been recognized. Organic semiconductors can preserve the spin information over extremely long times, and therefore they can be used to carry information by means of the electron spin. In order to carry information via spin, three basic processes must take place. First, the spin of electron population must be polarized. Second, the spin polarized electrons must diffuse through the material. And finally the analysis of the spin polarization is conducted. The degree of spin polarization indicates the spin-relaxation time or the time required for the spin direction to change because of interaction with environment. The spin relaxation is affected by spin-orbit coupling and hyperfine interaction. Since both spin-orbit coupling and hyperfine interaction in organic semiconductors are relatively weak, the degree of polarization can be found through measuring of magneto-resistance of a spin-valve, where organic material is placed between two ferromagnetic electrodes.[9]

1.5.1. Spin-orbit coupling

The spin-orbit coupling is the interaction between the electron spin and its orbital motion around atomic nucleus. Spin-orbit coupling occurs when a particle with nonzero spin moves in an electric field. Even though there is no magnetic field in the restframe of

the nucleus, the electron, because of its velocity, feels a magnetic field, as shown in equation (1.10).

$$B = -\frac{v \times E}{c^2}. \tag{1.10}$$

From here we can see that the spin of an electron can be indirectly influenced by an electric field.

For hydrogen-like atoms spin-orbit interaction is proportional to Z^4. Since organic semiconductors have low atomic numbers, the spin-orbit coupling in them is generally small.

1.5.2. Hyperfine interaction

The hyperfine interaction is an interaction between electron spin and nuclear spins of the host material. Since the electron can interact with more than one nucleus, the hyperfine interaction can be described by the Hamiltonian expressed in equation (1.11).

$$H_{hyp} = \sum_i^N A_i \vec{I_\iota} \cdot \vec{S}. \tag{1.11}$$

where A_i is a coupling intensity between the spins, I_i is the nuclear spin operator and S is the electron spin operator.

Nuclear spins can also affect the spin relaxation and cause dephasing. For example, if an electron spin interacts with N nuclear spins, the statistical fluctuation scales with $1/\sqrt{N}$. From here we can conclude that as an electron interacts with more nuclei, or as it is more delocalized, the weaker the influence of nuclei on spin relaxation.

The nuclear spins in organics mostly originate from isotopes such as ^{1}H (I=1/2), ^{13}C (I=1/2), or ^{14}N (I=2). Consequently, the hyperfine interaction as well as spin relaxation time can be altered when an organic material is enriched with these isotopes, as it is the case with deutereted DOO-PPV discussed in Chapter 6.

.

CHAPTER 2

EXPERIMENTAL TECHNIQUES

This chapter introduces the experimental techniques applied in characterizing films of polymers, fullerene derivatives, or their blends that can be used in organic photovoltaics. Thin films are prepared using glass, sapphire, or cesium-iodide substrates by either drop casting or spin coating in inert nitrogen atmosphere inside a glove box with oxygen level less than 1ppm.

2.1. Absorption and emission

The absorption of light by conjugated polymers promotes an electron from a ground state S_0 to a higher singlet electronic state S_1 that is coupled to the ground state. Transitions from the ground state to higher electronic states S_n can occur where n represents higher laying state with appropriate parity, angular momentum and oscillator strength with respect to ground state.

Absorption in visible, ultraviolet and near infrared range is measured by using CARY 17 spectrophotometer. The film is deposited on glass substrate. In order to eliminate substrate effects and the system response, absorption of blank substrate is measured first and then automatically subtracted from the absorption spectrum of the sample. Scattering and reflection from the films are assumed to be small and therefore are not accounted for. Absorption is measured in units of optical density (OD), which is

related to transmission by $T=T_0 10^{-OD}$, where T_0 is transmission of the system without the film and $OD=\alpha d$, where α is absorption coefficient and d is the thickness of the film.

One of the excited states decay channels is radiative decay or photoluminescence (PL) where exciton relaxes to ground state S_0 by emitting a photon with appropriate energy $\hbar\omega$, corresponding to the optical transition. In order to measure emission (photoluminescence) we use CW laser with a minimum energy of S_1-S_0 optical transition, this way the excitons can be photogenerated in the film. The emission light is collected by a spherical mirror and dispersed by a grating monochromator enabling measuring of the spectrum. Dispersed light is detected by an appropriate solid state detector depending on wavelength range, such as Silicon photodiode ($\hbar\omega$ >1.1eV) or germanium detector ($\hbar\omega$>0.8eV). Photoluminescence spectra reported in this diesertation are done under vacuum and at low temperatures.

2.2. Continuous wave (CW) spectroscopy

CW spectroscopy is a powerful tool to study long lived species such as triplet and polaron excitations.

2.2.1. Photoinduced absorption

Photoinduced absorption (PA) is the experimental technique used to study long lived species (with life time of the order of 1ms at low temperatures) such as triplet and polaron excitations.[25-27] Ar+ ion laser is used in most cases as a pump to promote electrons from the ground to an excited state. Tungsten or Xenon lamps are used as probe light covering the wavelength range from 250nm to 4.2μm. Pump and probe beams are overlapped on the sample placed in vacuum inside of a cryostat. The light coming out of

the sample is collected in one of the spherical mirrors and focused onto 2mm wide slit of monochromator. The appropriate long pass filters are placed at the slit of monochromator to block the pump beam. The light is then collected at the exit of the monochromator with a suitable photodetector: Si 10D photodiode for wavelengths from 550nm to 1.05μm, Ge detector from 800 to 1.6μm, and InSb from 1μm to 4.2μm. The signal is then converted from current to voltage and amplified via preamplifier and sent to lock-in SR 830 amplifier. In order for the signal to be detected by the lock –in amplifier the pump light has to be modulated with a frequency corresponding to the lifetime of photoexcitation, usually around 300Hz. This experimental set-up is presented in Figure 11.

The absorption of the photoexcited species is essentially the difference in transmission (ΔT) when the sample is illuminated with both the pump and the probe (T_L) and when sample is not illuminated with the pump but only with the probe (T_D). The relation between the induced absorption coefficient (Δα) and difference in transmission (ΔT) is expressed the equations (2.1) through (2.4):

$$\Delta T = T_L - T_{D,} \tag{2.1}$$

$$1+\frac{\Delta T}{T_D} = e^{-\Delta\alpha d}, \tag{2.2}$$

$$\Delta\alpha = -\ln\left(1+\frac{\Delta T}{T_D}\right), \tag{2.3}$$

$$\Delta T \ll T_D \Longrightarrow \Delta\alpha \approx -\frac{\Delta T}{T_D}. \tag{2.4}$$

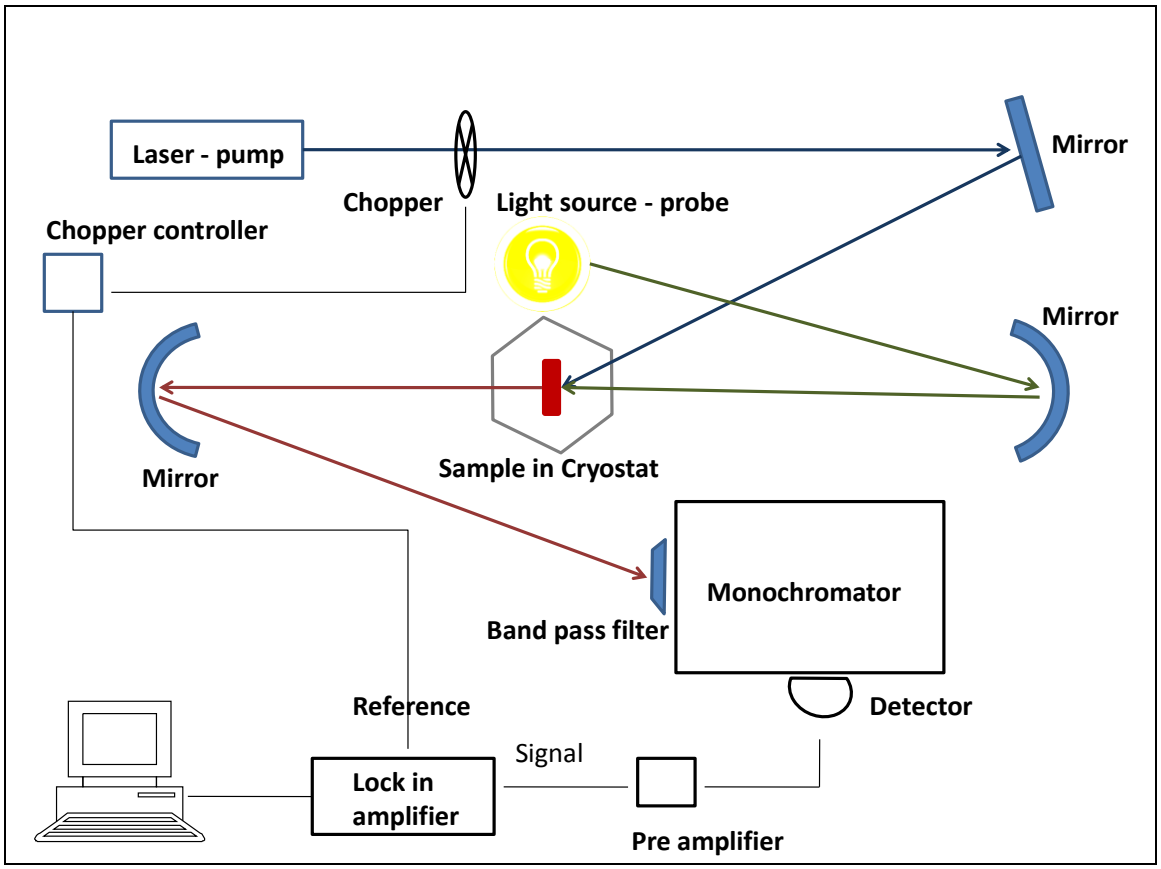

Figure 11 The photoinduced absorption experimental apparatus

Here we can distinguish between two signals: photoinduced absorption (PA) when $\Delta\alpha < 0$ and photoinduced bleaching (PB) or depletion of lower energy state involved in photonic transition, when $\Delta\alpha > 0$.

2.2.2. Doping induced absorption

In doping induced absorption (DIA) the change in transmission, ΔT of the film's optical transmission, T induced by doping is measured vs. photon energy using phase sensitive technique. The end result is the absorption-modulation spectrum, $\Delta T/T$.

In this experiment the films were doped by exposure to iodine (I_2) vapor for several seconds (~20s). First the transmission of undoped sample, T is measured. Then

the transmission of doped sample, T_D is measured. The $\Delta T/T$ spectrum is obtained by subtracting the transmission after doping from transmission before doping, and then normalizing it by transmission before doping.

In a one-dimensional model single charge carrier added to a polymer chain forms a spin ½ polaron with two localized states in the energy gap. As mentioned in the previous chapter polarons have two allowed optical transitions P1 and P2.

In this experiment large iodine ions may isolate polymer chains and cause quasi one-dimensional electronic properties. Furthermore, the iodine counter-ion may localize the induced polaron excitation. As a result a DIA spectrum consists of two polaron bands at low and high photon energy, P1 and P2.

2.3. Modulation spectroscopy

Modulation spectroscopy is used to understand the kinetics of the photogenerated species. The pump is modulated at a frequency f with a mechanical chopper or an acousto-optic modulator. PA is measured by lock-in amplifier tuned to the modulation frequency, f. The lock-in amplifier analyzes the first harmonics of the photoinduced signal defined as G(t).

$$G(t) = g(1 + \cos \omega t). \tag{2.5}$$

g represents the generation rate proportional to the pump intensity and $\omega=2\pi f$. Two phase components of the signal are detected by lock-in amplifier: in-phase and out -of- phase or quadrature. The in-phase means that signal- response is in phase with modulation

frequency ω. The out-of-phase component is π/2 relative to ω representing long-time response with respect to 2π/ω. The in-phase component can be written as $n_I(t)$.

$$n_I(t) = \frac{1}{2\pi}\int n(t)\cos\omega t\, dt, \tag{2.6}$$

The out-of-phase or quadrature is defined as $n_Q(t)$.

$$n_Q(t) = \frac{1}{2\pi}\int n(t)\sin\omega t\, dt, \tag{2.7}$$

$$n(t) = \frac{g\tau}{1+\iota\omega\tau}, \tag{2.8}$$

τ is the mean life time of a photexcitation.

2.3.1. Mono- and bimolecular recombination

Photoinduced absorption, PA (Δα) is proportional to excitation density N(t). Therefore to determine lifetimes and type of recombination, PA as a function of a modulation frequency, ω and laser intensity, I_L has been used. There are two relevant recombination mechanisms, monomolecular (MR) and bimolecular (BR) processes. Monomolecular kinetics points to a possible geminate generation, where the hole and electron polarons (P±) originate from a common excitation parent. Bimolecular kinetics, on the other hand, can indicate a distant pair recombination. [28] These processes can be described by a single rate equation for the photoexcitation density:

$$\frac{dN}{dt} = G(t)S(N_0) - U(N), \tag{2.9}$$

where G(t) is proportional to generation rate g:

$$G(t) = g(1 + \cos \omega t), \tag{2.10}$$

g is proportional to pump intensity I_L:

$$g \cong \eta \alpha_L I_L. \tag{2.11}$$

α_L and η represent the absorption coefficient at laser photon energy and a quantum efficiency in respective order. Equation (2.11) includes $S(N_0)$ function that includes defect limited cases in which due to trap filling N tends to saturate at high I. N_0 represents the trap density and U recombination mechanism.[28] However, for simplicity we assume that S=1 and equation (2.11) becomes

$$\frac{dN}{dt} = G(t) - U(N), \tag{2.12}$$

where for MR $U(N) = \frac{N}{\tau}$ and for BR $U(N) = bN^2$ and $\tau_{BR}^{-1} = \sqrt{gb}$. In CW measurements we assume steady state conditions, when

$$\left.\frac{dN}{dt}\right|_{SS} = g - U = 0. \tag{2.13}$$

In the case of monomolecular recombination the equation (2.15) becomes

$$\left.\frac{dN}{dt}\right|_{SS} = g - \frac{N_{SS}}{\tau} = 0, \tag{2.14}$$

with a solution:

$$N_{SS} = g\tau = \alpha I_L \tau. \tag{2.15}$$

According to the equation (2.17) if monomolecular recombination occurs, the PA signal depends linearly on laser excitation intensity. However, in the case of bimolecular recombination the recombination rate is proportional to population squared as mentioned above $U = bN^2$, where b is proportionality constant. The equation 2.16 becomes

$$\left.\frac{dN}{dt}\right|_{SS} = g - b{N_{SS}}^2 = 0, \tag{2.16}$$

$$N_{SS} = \sqrt{\frac{g}{b}} = \sqrt{\frac{\alpha I_L}{b}}. \tag{2.17}$$

In the bimolecular recombination the PA signal depends sublinearly on laser intensity.

2.3.2. Modulation frequency response

The dynamics of long-lived photoexcitations can be successfully studied by looking at their PA dependence of modulation frequency and the intensity of the pump. In the case of finite modulation frequency, the in-phase and quadrature components can be measured using phase sensitive lock-in technique and are given by equations (2.18) and (2.19)[28].

$$N_I(\omega) = \frac{g\tau}{(1+\omega^2\tau^2)}, \tag{2.18}$$

$$N_Q(\omega) = \omega\tau N_I. \tag{2.19}$$

If we replace τ with $\tau_{BR}=\sqrt{(gb)}$ we get expressions for bimolecular recombination. N_Q equals zero at zero frequency and has a maximum at

$$\omega_{max} = \frac{1}{\tau}, \tag{2.20}$$

where $N_I(\omega_{max})=N_Q(\omega_{max})$. At higher modulation frequencies $\omega > \omega_{max}$, both in-phase and quadrature component exhibit asymptotic behavior with a power law decrease $\omega^{-\beta}$, where $\beta=2$ for in-phase and $\beta=1$ for quadrature component. In this measurement is very important to take into account the system response and to phase the measurement results relative to the laser phase. In order to do that, before each measurement the laser should be scattered at monochromator slit without any optical filters while the probe is blocked. The lock-in amplifier should be auto-phased so that the signal is completely in the in-phase component. Since the measurement consists of collecting in-phase and quadrature components while with help of acusto-optic modulator the modulation frequency is changed, signal tends to get out of phase in respect to the pump. This offset can be accounted for in the following way:

Complete frequency scans, both in-phase and out-of-phase are taken of PA, PL, and of the modulated laser ($L_{in}(f)$ and $L_{out}(f)$). Then,

$$R_L = \sqrt{L_{in}^2 + L_{out,}^2} \tag{2.21}$$

$$\Delta A_{in} = \frac{PA_{in} - PL_{in}}{R_L}, \tag{2.22}$$

$$\Delta A_{out} = \frac{PA_{out} - PL_{out}}{R_L}, \tag{2.23}$$

$$R = \sqrt{\Delta A_{in}^2 + \Delta A_{out}^2}, \tag{2.24}$$

$$\tan\alpha = \frac{\Delta A_{out}}{\Delta A_{\mathrm{in}}} = \tan(\phi_{\Delta A} - \phi_{\mathrm{L}}) = \tan\left[\tan^{-1}\left(\frac{\Delta A_{out}}{\Delta A_{in}}\right) - \tan^{-1}\left(\frac{L_{out}}{L_{in}}\right)\right]. \tag{2.25}$$

R(f) is modulus of measured PA and α(f) is relative phase between the measurement, $\varphi_{\Delta A}$ and the modulated laser response, φ_L. Based on equations (2.18) through (2.22) we can calculate actual PA frequency response for both in-phase and out-of-phase components.

$$PA_{in}^{actual} = R\sqrt{\frac{1}{1+\tan\alpha}}, \tag{2.26}$$

$$PA_{out}^{actual} = PA_{in}^{actual}\tan\alpha. \tag{2.27}$$

2.3.3. Dispersive kinetics

The equations presented above can be used to describe kinetics in ordered materials. However, in this study we concentrate on polymers which are disordered materials so most processes are temporarily dispersed. Therefore the recombination processes can be described more accurately by the simple Cole-Cole model for amorphous materials [29]:

$$N(\omega) = \frac{g\tau_0^{eff}}{1+(i\omega\tau_0^{eff})^{\alpha}}, \quad (2.28)$$

where α is dispersive parameter α<<1, and τ^{eff} is mean lifetime. The in-phase and quadrature are given by N_I = Re(N) and N_Q = Im(N). In ordered material photoexcitations have a single lifetime and α=1. In polymers (disordered medium) dispersive parameter, α is less than 1 and τ becomes τ^{eff}.

PA response at high modulation frequencies distinguishes dispersive kinetics from the single lifetime processes. Figure 12 shows PA dependence from modulation frequency for a polymer/fullerene blend. Using equations (2.23) through (2.29) to process collected data and fitting with equation (2.30) we can find the lifetime of the photoexcitaion and the recombination mechanism.For dispersive kinetics, described by Equation (2.30) the in-phase and the quadrature components decrease sublinearly with ω: $N(\omega_{I,Q}) \propto \omega^{-\beta}$, where $\beta \approx \alpha$.

2.1.1. FTIR photomodulation spectroscopy

Fourier transform infrared (FTIR) spectroscopy is used to measure photoinduced absorption in mid and far infrared photon energy range. This technique is based on Michelson interferometer, depicted in Figure 13. Beam I_0 coming from an appropriate light source is split by a beam splitter into two, I_1 and I_2. Beam I_1 is reflected from a stationary mirror and I_2 from a movable mirror causing the change in optical travel length denoted by x. The two reflected beams pass through the sample generating an interferogram spectrum that can be described by the equation (2.29).

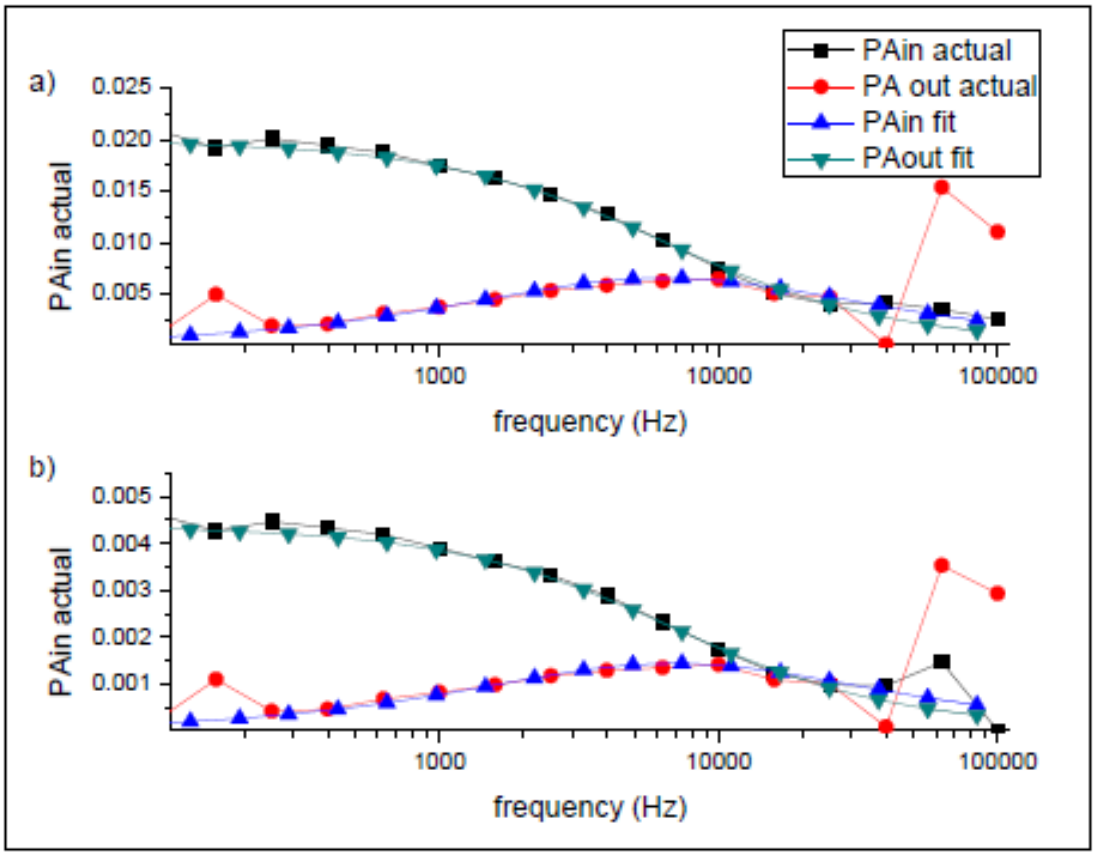

Figure 12 Frequency dependant PA of LYON:PC70BM blend.

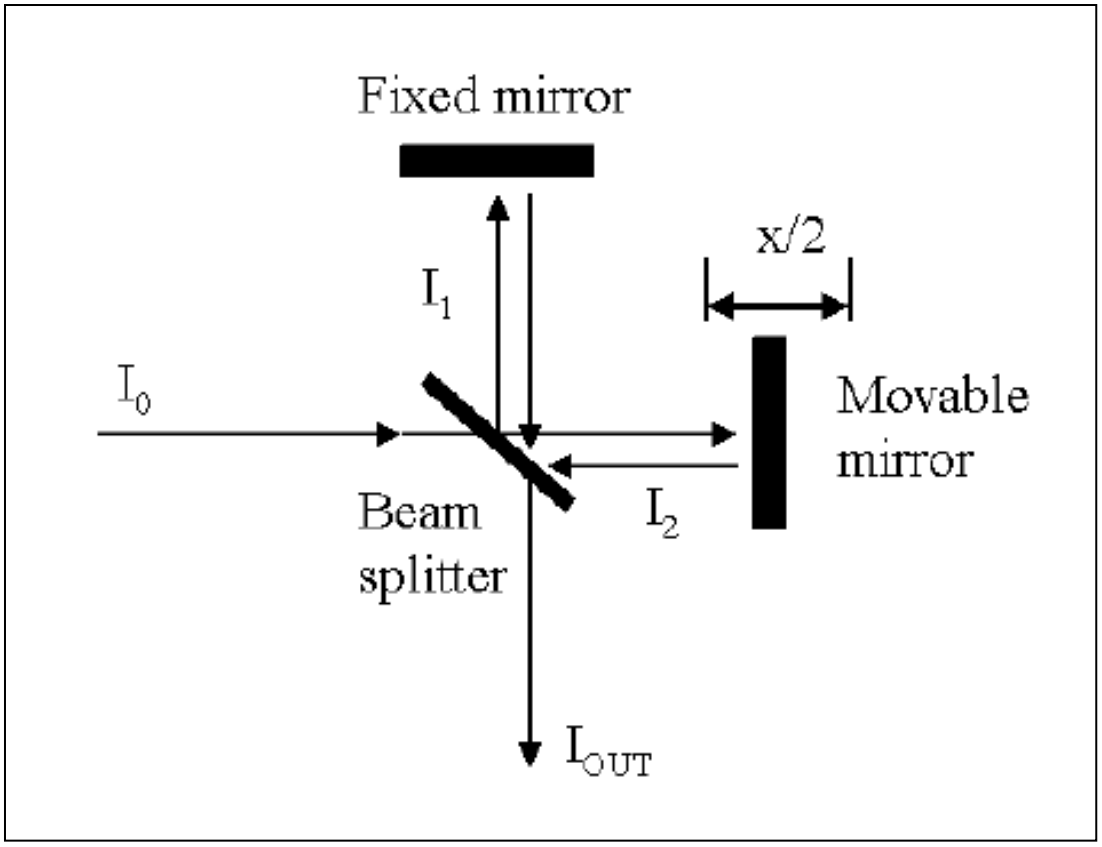

Figure 13 Schematics of Michelson interferometer

$$I_{out}(x) = \frac{1}{4}\int_{-\infty}^{+\infty} I_0(\bar{\nu})\,[1 + \cos(2\pi\bar{\nu}x)]d\bar{\nu} = const + \frac{1}{4}\int_{-\infty}^{+\infty} I_0(\bar{\nu})\cos(2\pi\bar{\nu}x)\,d\bar{\nu}, \tag{2.29}$$

where $I_{out}(x)$ is interferogram spectrum as a function of displacement x. The inverse Fourier transform of the second part of Equation(2.31) describes the interference spectrum as a function of wavenumber $\bar{\nu}$, given by

$$I_0(\bar{\nu}) = \frac{2}{\pi}\int_{-\infty}^{+\infty} I_{out}(x)\cos(2\pi\bar{\nu}x)dx. \tag{2.30}$$

FTIR spectroscopy uses the fast Fourier transform (FFT) to convolute spectrum with a limitation on resolution, $\Delta\nu_{max}$. Here FTIR spectroscopy is used to construct PA spectrum in range of mid- to far- IR, so that:

$$-\frac{\Delta T}{T} = \frac{(T_{off} - T_{on})}{T_{off}}, \tag{2.31}$$

where T_{on} and T_{off} are transmitted spectrum with and without illumination by the pump laser. Ar+ ion laser was used as the pump. The laser beam was directed through a shutter that is controlled by the computer. The globar lamp with emission in IR spectrum was used as a probe. The IR beam was split by KBr beam splitter that is fit to a range 400 cm^{-1} to 5000 cm^{-1}.The Light beam that passed through the sample is collected by a MCT (mercury-cadmium-telluride) detector that must be cooled with liquid nitrogen. The FTIR experimental setup is shown in Figure 14

2.1. Electroabsorption

In electroabsorption or EA measurement an electric field is applied on the sample and then the change in transmission is measured with the probe similarly to previously described PA experiment. Transmitted light intensity ΔI/I decreases exponentially with absorption constant α and film thickness d. Therefore, change in absorption constant, Δα can be derived from the change in transmittance:

$$\Delta\alpha = -\frac{1}{d}\frac{\Delta I}{I} \tag{2.32}$$

.

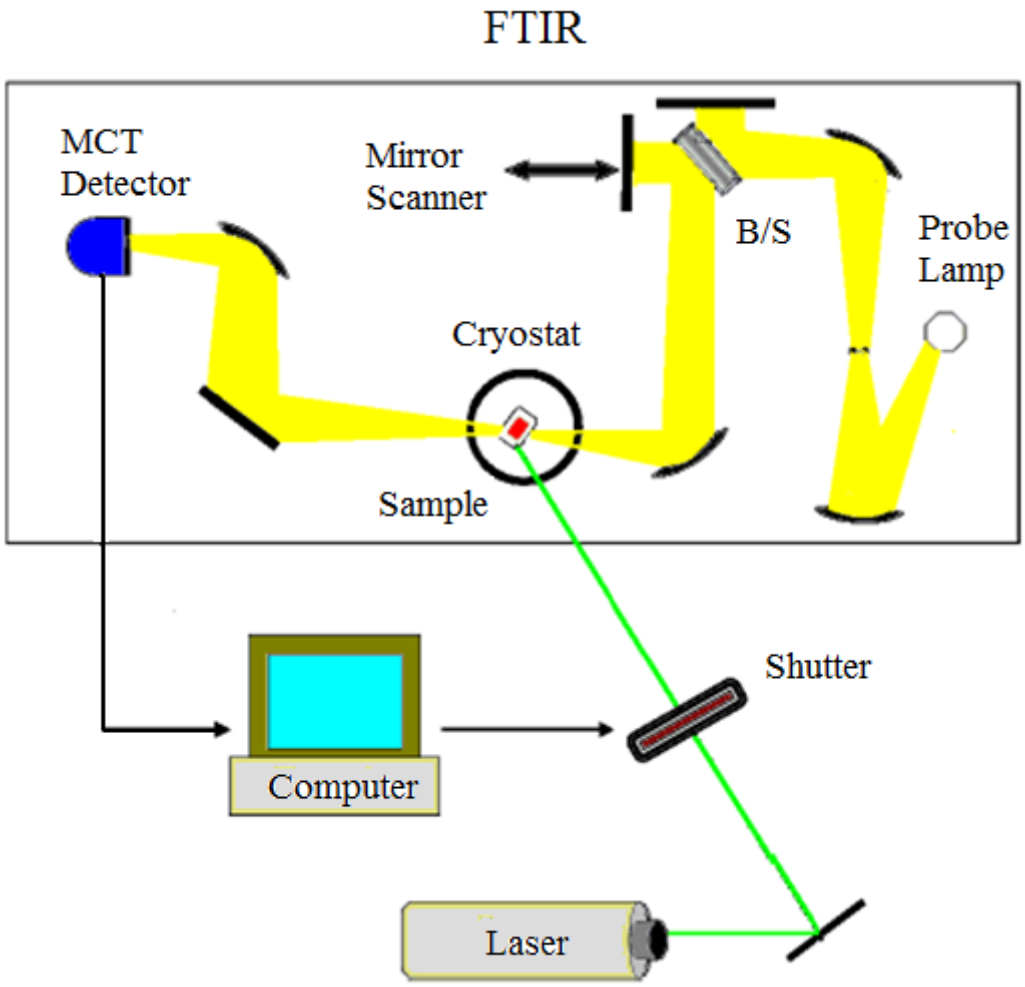

Figure 14 The photomodulation experimental set-up using FTIR spectrometer

Since in the electroabsorption experiment electric field is applied, a sample/film was deposited on a special substrate prepared in the following way: A 0.5nm titanium film followed by 150nm gold film was RF sputtered on a 1 inch in diameter and 2mm thick sapphire substrate. Then an interdigitated gold electrode array was photo lithographically patterned and etched with a 40μm gap between the electrode fingers as shown in Figure 15.

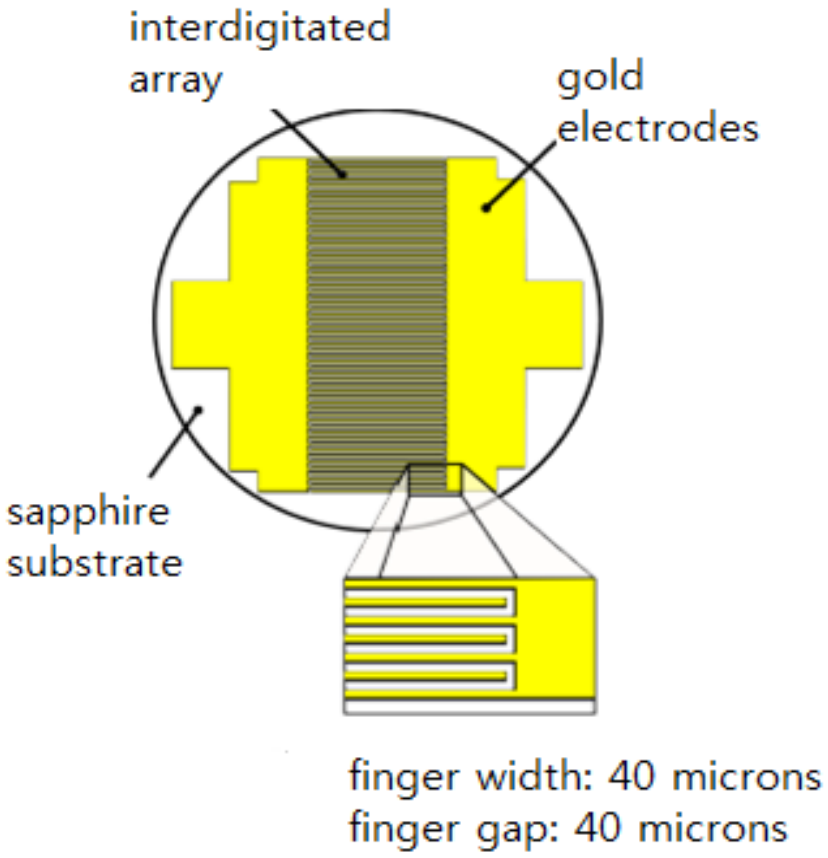

Figure 15 Electroabsorption substrate architecture.

Figure 16 illustrates the EA experimental set-up. The applied electric field was produced using signal generator (Tekttronix –FG503, 3MHz) and transformed using a step-up transformer. The deposited film on the EA substrate was supplied with 200-300V AC that generated an AC field of the order of 10^5V/cm at frequency of 500Hz. Depending on desired wavelength range either xenon or tungsten lamp was used as a probe light. Probe light was dispersed through a grating monochromator and guided with mirrors through the sample into a solid state detector. The sample holder was mounted on

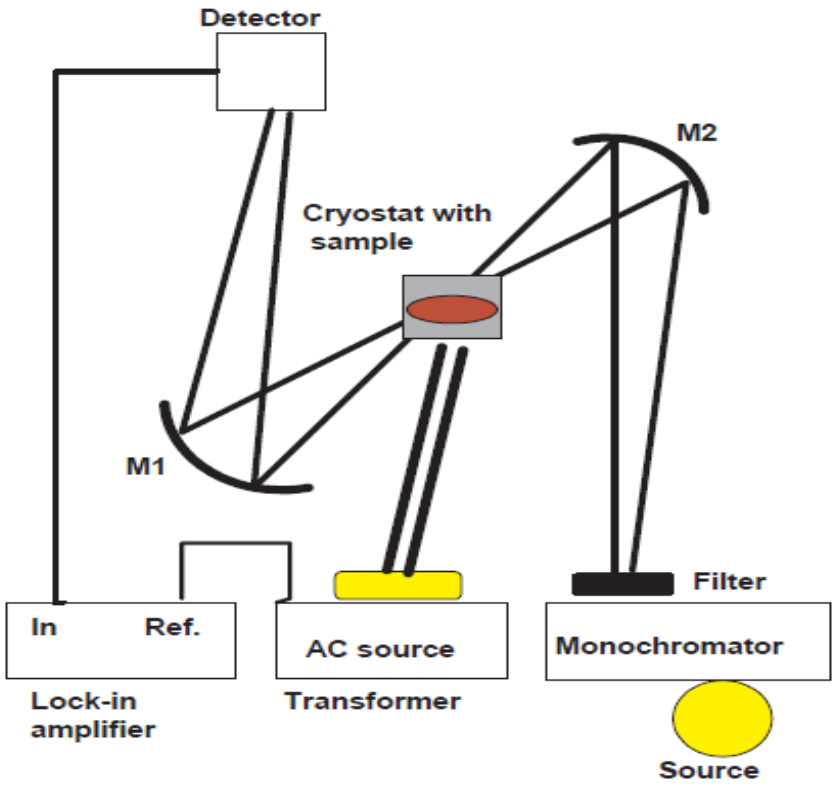

Figure 16 Schematic representation of EA experimental set-up

a cold-finger cryostat and its electrodes connected to the leads from the transformer. Using a phase sensitive modulation technique, a reference signal is taken from the signal generator and the signal from the detector was connected to the input of the lock-in. Because conjugated polymers have mirror symmetry, they respond to a sinusoidal field of frequency with signals at 2ω, where fundamental frequency is significantly suppressed. Nonzero signal at fundamental frequency indicates existence of asymmetry, possibly due to internal fields. Therefore, an EA signal was detected at a second harmonic frequency, indicating transitions due to the change of electronic states.

2.2. Photoluminescence quantum efficiency

Photoluminescence quantum efficiency (PLQE) can be defined as number of emitted photons per absorbed photon. PLQE provides useful information for better understanding of radiative and nonradiative processes in organic materials. The measurement presented in Figure 17 is performed using Ar+ ion laser as a source of excitation and integrated sphere (IS) that distributes light homogenously. The sample is placed inside the sphere and the light emission is collected at the exit of IS with a solid state detector. The signal is amplified and analyzed using lock-in technique. Before starting the actual PLQ E measurement optical density (OD) of the thin spincoated film is measured. The OD should be below 1. The PLQE can be calculated using the equation (2.33).

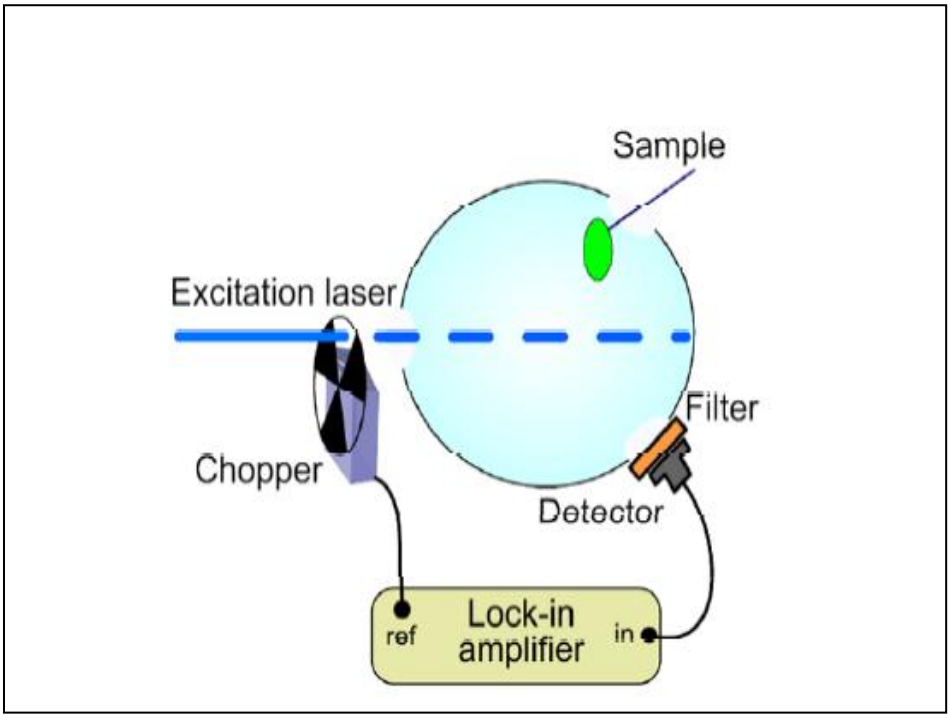

Figure 17 PLQE experimental set up done at room temperature in air

$$PLQE = \frac{I_{PL}-(R+T)I_{PL,corr}}{(1-R-T)I_L}\frac{D_L}{D_{PL}}\frac{S_L}{S_{PL}}\frac{E_L}{E_{PL}}\frac{1}{T_{F(PL)}}. \quad (2.33)$$

I_L, I_{PL} and $I_{PL,corr}$ are measured and represent: the reflected laser intensity without the sample inside IS, the uncorrected PL intensity with sample inside the laser path, and the corrected PL intensity with the sample inside IS but out of the laser path. Correction term, $I_{PL,corr}$ is measured to eliminate the contribution of reflected photons (from IS walls) to collected light emission. R and T are reflection and transmission coefficients at laser wavelength. D_L and D_{PL} are detector sensitivities at laser and the PL wavelengths. S_L and S_{PL} are IS sensitivities at laser and PL wavelengths. E_L and E_{PL} are photon energies of laser and PL emission. T_F(PL) is transmission of optical long pass filter used in the experiment at PL wavelength.

2.3. Electron spin resonance spectroscopy

2.3.1. Introduction to theory

The physics of electron spin resonance is the basis for two major experimental techniques used in this study, ESR and ODMR.

2.3.1.1. Spin and orbital moments

Electron spin resonance (ESR) studies the interaction between electronic magnetic moments and magnetic fields.

The magnetic moment of an electron spin, μ_s and magnetic moment associated with its orbital momentum μ_L can be expressed as:

$$\mu_S = 2\beta \boldsymbol{S}, \tag{2.34}$$

$$\mu_L = \beta \boldsymbol{L}, \tag{2.35}$$

where **S** is the spin angular momentum operator, **L** is the angular momentum operator, and, β is Bohr magneton, defined by

$$\beta = \frac{e\hbar}{2m}, \tag{2.36}$$

If an electron has a both spin and orbital motion, then the total angular momentum **J** is obtained by the vector addition as in equation (2.37).

$$\boldsymbol{J} = \boldsymbol{L} + \boldsymbol{S}, \tag{2.37}$$

where J has possible magnitudes |L-S|, |L-S+1|,…,|L+S|. As a result of the vector addition of the spin and orbital components the overall magnetic moment can be expressed as:

$$\boldsymbol{\mu} = g\beta \boldsymbol{J}, \tag{2.38}$$

where g is the Landè factor

$$g = \frac{3}{2} + \frac{S(S+1) - L(L+1)}{2J(J+1)}. \tag{2.39}$$

In the solids the electrical orbital motion interacts strongly with the crystalline electric fields and becomes decoupled from the spin or quenched. The stronger the

quenching the closer the g factor to the free electron value, 2.0023. [30] The value of g factor depends on the environment of the unpaired electron. It depends on the orientation of the molecule containing the unpaired electron in respect to applied electric field, as well as the phase of the sample (solid, liquid, or gas). In the gas and liquid phase the molecules have free motion and value of g is averaged over all orientations. In the case of paramagnetic ion inside of a perfect cubic crystal the g value does not vary with orientation. [31]

However, in most cases such as a radical ion in a crystal with low symmetry, the g factor is very often anisotropic and varies with the direction (x',y'z') in a single crystal. Generally, the g factor may be a symmetric tensor **g'** with components g'_{ij}

$$\boldsymbol{g}' = \begin{bmatrix} g'_{x'x'} & g'_{x'y'} & g'_{x'z'} \\ g'_{y'x'} & g'_{y'y'} & g'_{y'z'} \\ g'_{z'x'} & g'_{z'y'} & g'_{z'z'} \end{bmatrix}, \tag{2.40}$$

where $g'_{ij}=g'_{ji}$. However, it is possible to find principal axes (x,y,z) where the **g** tensor is diagonal.

$$g = \begin{bmatrix} g_x & 0 & 0 \\ 0 & g_y & 0 \\ 0 & 0 & g_z \end{bmatrix}. \tag{2.41}$$

Very often the g tensor has axial symmetry where

$$g_{\parallel} = g_{zz}, \tag{2.42}$$

$$g_{\perp} = g_{xx} = g_{yy}, \tag{2.43}$$

where the z axis is taken as the symmetry axis. For an arbitrary orientation of a crystal in a magnetic field, the resonance is characterized by the g factor

$$g = \sqrt{g_{xx}^2(\cos\theta_x)^2 + g_{yy}^2\left(\cos\theta_y\right)^2 + g_{zz}^2(\cos\theta_z)^2}, \tag{2.44}$$

where θ represents the angle between an axis and direction of magnetic field. Since the three direction cosines obey the relation

$$(\cos\theta_x)^2 + \left(\cos\theta_y\right)^2 + (\cos\theta_z)^2 = 1 \tag{2.45}$$

Using equation (2.45) and assuming that θ is the angle between the symmetry axis and magnetic field equation (2.44) can be simplified to

$$g = \sqrt{g_{\perp}^2(\sin\theta)^2 + g_{\parallel}^2(\cos\theta)^2}. \tag{2.46}$$

2.3.1.2. Spin Hamiltonian

The interaction energy of a paramagnetic atom in a constant magnetic field H_0 is represented by the spin Hamiltonian $\mathcal{H}$:

$$\mathcal{H} = \mathcal{H}_e + \mathcal{H}_{cf} + \mathcal{H}_{LS} + \mathcal{H}_{SS} + \mathcal{H}_Z + \mathcal{H}_{hfs} + \mathcal{H}_Q + \mathcal{H}_N, \tag{2.47}$$

$\mathcal{H}_e$ represents electronic energy of the paramagnetic ion in free state, $\mathcal{H}_{cf}$ crystal field energy or interaction energy of the free ion's electronic structure with the crystalline electric field , and $\mathcal{H}_{LS}$ spin orbit coupling, $\mathcal{H}_{SS}$ spin-spin interaction, $\mathcal{H}_Z$ Zeeman energy, $\mathcal{H}_{hfs}$ hyperfine structure, $\mathcal{H}_Q$ quadrupole energy, and $\mathcal{H}_N$ nuclear spin energy.

However, in our studies of ESR, LESR and ODMR the most important components are Zeeman, hyperfine interaction and to some degree spin-spin and spin-orbit interaction.

Spin-orbit interaction is defined by the equation (2.48).

$$\mathcal{H}_{LS} = \lambda \boldsymbol{L} \cdot \boldsymbol{S}, \tag{2.48}$$

where λ is the spin-orbit coupling constant. The spin-spin interaction $\mathcal{H}_{SS}$ is defined by the equation (2.49).

$$\mathcal{H}_{SS} = D(S_z^2 - \tfrac{1}{3}S(S+1)), \tag{2.49}$$

where D is the zero field splitting parameter and Sz is the z component of the spin angular moment.

$\mathcal{H}_Z$ is Zeeman energy

$$\mathcal{H}_z = \beta \boldsymbol{H} \cdot (\boldsymbol{L} + 2\boldsymbol{S}) = \beta\left(g_x H_x S_x + g_y H_y S_y + g_z H_z S_z\right), \tag{2.50}$$

Hyperfine structure $\mathcal{H}_{hfs}$ is given by

$$\mathcal{H}_{hfs} = A\boldsymbol{I}\cdot\boldsymbol{S} = \left(A_x S_x I_x + A_y S_y I_y + A_z S_z I_z\right), \quad (2.51)$$

where A_x, A_y, and A_z are components of hyperfine coupling constant A, and I_x, I_y, and I_z are components of nuclear spin I.

The ESR measurement in essence studies Zeeman energy, and the way in which the other Hamiltonian terms perturb or are perturbed by Zeeman energy.

Spin orbit interaction $\lambda\mathbf{L}\cdot\mathbf{S}$ further splits the optical energy levels and influences g factor.

The spin-spin interaction can in some cases be the same order of magnitude as the Zeeman energy causing the energy levels to be strongly dependant on orientation of crystal in magnetic field.

The hyperfine structure is caused by the interaction of the nucleus with an unpaired electron. In some systems such as aromatic molecules, where electron is delocalized hyperfine structure can be expressed as:

$$\mathcal{H}_{hfs} = \sum A_i m_i. \quad (2.52)$$

where the projection m_i of the nuclear spin on the direction of the magnetic field can have the following values: I_i, I_i-1, …, -I_i+1, -I_i. Hyperfine coupling constant A_i varies with the type of nucleus and represents the strength of the interaction between spins of nucleus and electron. Hyperfine interaction causes further splitting of energy levels (Figure 18). In the case of several nuclei with spin ½ with the same hyperfine constant A, they

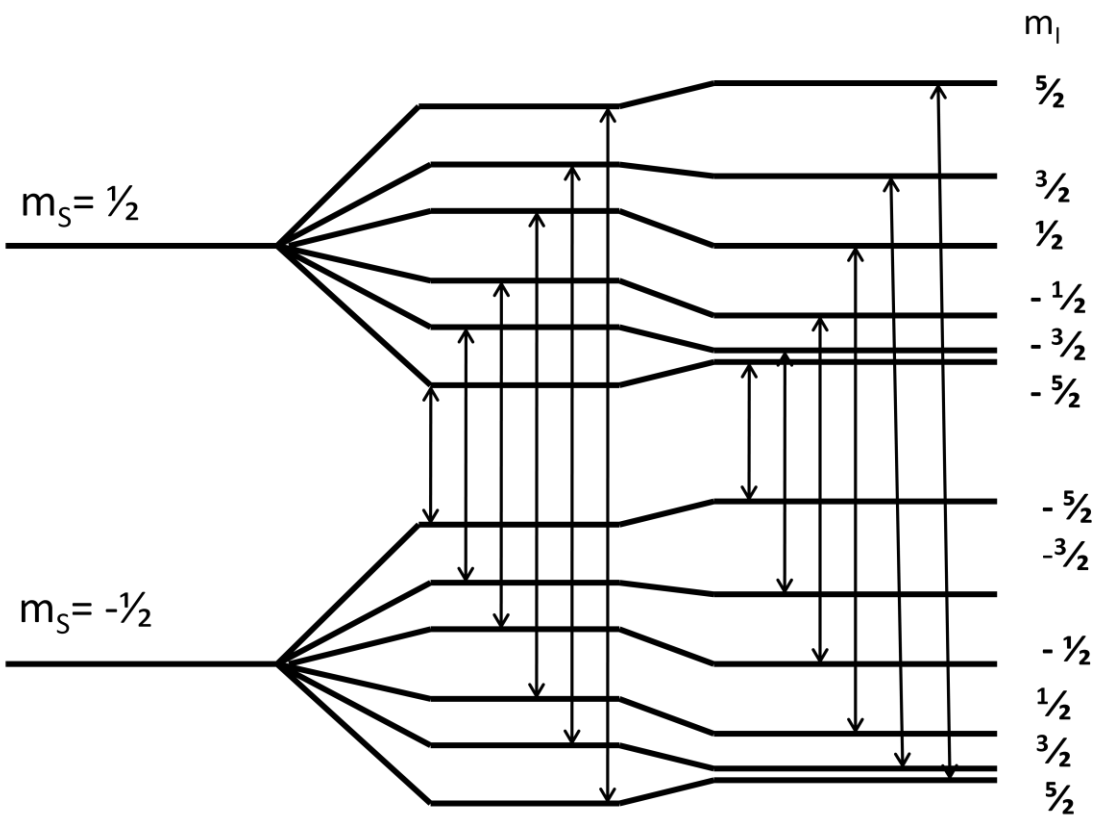

Figure 18 Due to the Zeeman Effect in the presence of an external magnetic field the electronic energy level splits into two ±gβH energy sublevels. Each of the two electronic energy levels is split into six equally spaced energy levels by hyperfine interaction for I=5/2. Quadrupole interaction shifts these levels according to selection rule $\Delta m_I=0$ causing asymmetry.

produce an ESR spectrum whose intensity follows the binomial coefficient distribution. If the width of spectral lines is smaller than their separation they are well resolved. However if their width exceeds the separation, spectral lines merge into one line. If there are n nuclei with spin I then the energy level will be split into $(2I+1)^n$ lines. If all of the coupling constants are different then no degeneracy occurs. If some nuclei have the same coupling constant then resulting degeneracy decreases the number of lines but increases their amplitude. Usually all of the hyperfine components have the same line width and shape except in the case of overlapping resonances.

2.3.1.3. Information obtained from ESR

ESR gives us information about the various parts of Hamiltonian. The Zeeman and hyperfine structure Hamiltonian can be evaluated directly from ESR spectra. Crystal field and spin orbit energies are evaluated from optical spectra and then correlated with ESR data. In this study, ESR data are used to evaluate the g factor of various organic materials used in photovoltaic applications. ESR can be used to determine concentration of paramagnetic species. Therefore, in the studies of the blends, ESR proved to be very useful in comparing concentrations of paramagnetic species in donor and acceptor materials.

In order to obtain the most of information ESR is done at different temperatures and different microwave powers.

2.3.2. ESR kinetic studies

2.3.2.1. Bloch equations

In ESR studies magnetic field is applied to an electron causing spin magnetic moment to align parallel or antiparallel to direction of the magnetic field. The spins that are aligned parallel to the applied magnetic field have lower energy than the antiparallel spins. For an ensemble of spins the nonzero net magnetic moment (macroscopic magnetization) **M** can be expressed by the following equation

$$\boldsymbol{M} = \sum_i \mu_i, \tag{2.53}$$

In equilibrium **M** is in direction of magnetic field **B**. However if **M** is not in direction of **B** then there will be a net torque that causes **M** to precess about direction of **B** according to the equation (2.54).

$$\frac{d\boldsymbol{M}}{dt} = \gamma \boldsymbol{B} \times \boldsymbol{M}, \tag{2.54}$$

In addition to precession there two relaxation processes, spin-lattice and transverse relaxation.[32, 33] Spin –lattice relaxation involves transfer of energy from the spin system to the surroundings or lattice. The time that is required for this process is called spin-lattice relaxation time, T1.

$$\frac{dM_z}{dt} = \frac{M_z - M_0}{T_1} \tag{2.55}$$

where M_z is z component of magnetization under nonequilibrium conditions, and M_0 is equilibrium magnetization along **B**. According to the equation above M_z approaches M_0 (equilibrium) in characteristic time T_1.

If we assume that **M** is not exactly in the z direction but tilted toward the x direction of the magnetic field, each individual spin will precess under a different rate. So an ensemble of spins will start a precession in phase but with time it will lose its coherence. The characteristic time for this process is called the transverse relaxation time, T_2. The transverse components of magnetization, Mx, and My, decay to zero (equilibrium) according to the equation (2.56).

$$\frac{dM_x}{dt} = -\frac{M_x}{T_2}\frac{dM_y}{dt} = -\frac{M_y}{T_2}, \tag{2.56}$$

Based on the equation (2.56) the transverse relaxation does not involve energy transfer from spin to lattice, but it does increase entropy of the system. However, the spin-lattice relaxation process where M_z goes to zero causes both transverse components to become zero. Therefore, transverse relaxation time includes both spin-relaxation time as well as spin dephasing relaxation time T_2*.

$$\frac{1}{T_2} = \frac{1}{T_1} + \frac{1}{T_2^*}. \tag{2.57}$$

Relaxation processes can be classified by their effects on electron spin. Nonsecular process is a process that involves spin flip and energy transfer between the spin system and the lattice, and therefore involves T_1. Secular process does not involve spin flip but results in the loss of spin coherence.

2.3.2.2. CW ESR

In an ESR experiment beside a static magnetic field B_0 in z direction another oscillating magnetic field B_1 in xy plane is applied. If B_1 is a circularly polarized field rotating around the z axis then the total magnetic field can be expressed with the equation (2.58).

$$\boldsymbol{B} = \hat{\boldsymbol{\imath}} B_1 cos\omega t + \hat{\boldsymbol{\jmath}} B_1 sin\omega t + \hat{\boldsymbol{k}} B_0. \tag{2.58}$$

Combining equations (2.54) – (2.56) we obtain equation (2.59).

$$\frac{d\boldsymbol{M}}{dt} = \gamma \boldsymbol{B} \times \boldsymbol{M} - \hat{\boldsymbol{i}}\frac{M_x}{T_2} - \hat{\boldsymbol{j}}\frac{M_y}{T_2} - \hat{\boldsymbol{k}}\frac{M_z - M_0}{T_1}, \tag{2.59}$$

Taking the vector product **B** × **M** and manipulating equations (2.58) and (2.59) we can obtain the expressions for dM_x/dt, dM_y/dt, and dM_z/dt. However, it is very convenient to write:

$$M_x = u cos\omega t + v sin\omega t, \tag{2.60}$$

$$M_y = u sin\omega t - v cos\omega t, \tag{2.61}$$

or

$$u = M_x cos\omega t + M_y sin\omega t, \tag{2.62}$$

$$v = M_x sin\omega t - M_y cos\omega t. \tag{2.63}$$

In the equations (2.60) through (2.63), *u* represents the component of M_x that is in phase with B_1 and *v* is 90° out of phase with B_1. Differentiating these equations we obtain

$$\frac{du}{dt} = -(\omega - \gamma B_0)v - \frac{u}{T_2}, \tag{2.64}$$

$$\frac{dv}{dt} = (\omega - \gamma B_0)u - \frac{uv}{T_2} + \gamma B_1 M_z, \tag{2.65}$$

$$\frac{dM_z}{dt} = -\gamma B_1 v - \frac{M_z - M_0}{T_1}. \tag{2.66}$$

These equations express magnetic resonance in rotating coordinate frame. However, in this study we focus on the CW magnetic resonance experiment where radiation field B_1 is continuous and B_0 changes slowly compared to relaxation rates (slow passage condition). Therefore, we can assume steady-state conditions and set derivatives to 0.

$$u = \frac{\gamma B_1 M_0 (\omega_0 - \omega) T_2^2}{1 + T_2^2 (\omega_0 - \omega)^2 + \gamma^2 B_1^2 T_1 T_2}, \tag{2.67}$$

$$v = \frac{\gamma B_1 M_0 T_2}{1 + T_2^2 (\omega_0 - \omega)^2 + \gamma^2 B_1^2 T_1 T_2}, \tag{2.68}$$

$$M_z = \frac{M_0 \left[1 + (\omega_0 - \omega)^2 T_2^2\right]}{1 + T_2^2 (\omega_0 - \omega)^2 + \gamma^2 B_1^2 T_1 T_2}. \tag{2.69}$$

where $\omega_0 = \gamma B_0$ is the Larmor frequency that corresponds to the frequency of the energy level transition. According to equations (2.67 - 2.69) as B_1 approaches to 0 so do u and v as well and M_z approaches to M_0, the equilibrium value. In the opposite case when B_1 increases M_z decreases moving away from the equilibrium.

As mentioned earlier, u represents the transverse magnetization that is in-phase with B_1 and therefore corresponds to dispersion. The out-of-phase response, v corresponds to the absorption. In magnetic resonance experiments, it is usually out-of-phase or v-mode detected. When microwave power proportional to B_1^2 is small so that $\gamma^2 B_1 T_1 T_2 \ll 1$, then the equation (2.68) can be simplified.

$$v = \frac{\gamma B_1 M_0 T_2}{1 + T_2^2 (\omega_0 - \omega)^2}. \tag{2.70}$$

Absorption represented by the equation (2.70) corresponds to a Lorentzian line shape as seen in Figure 19. In the continuous wave electron spin resonance (CW ESR) experiments where the magnetic field B_0 is changed while the microwave (MW) frequency is kept constant, half width at half maximum, ΔB_0 corresponds to equation (2.71).

$$\Delta B_0 = \frac{\hbar}{g\beta T_2}. \tag{2.71}$$

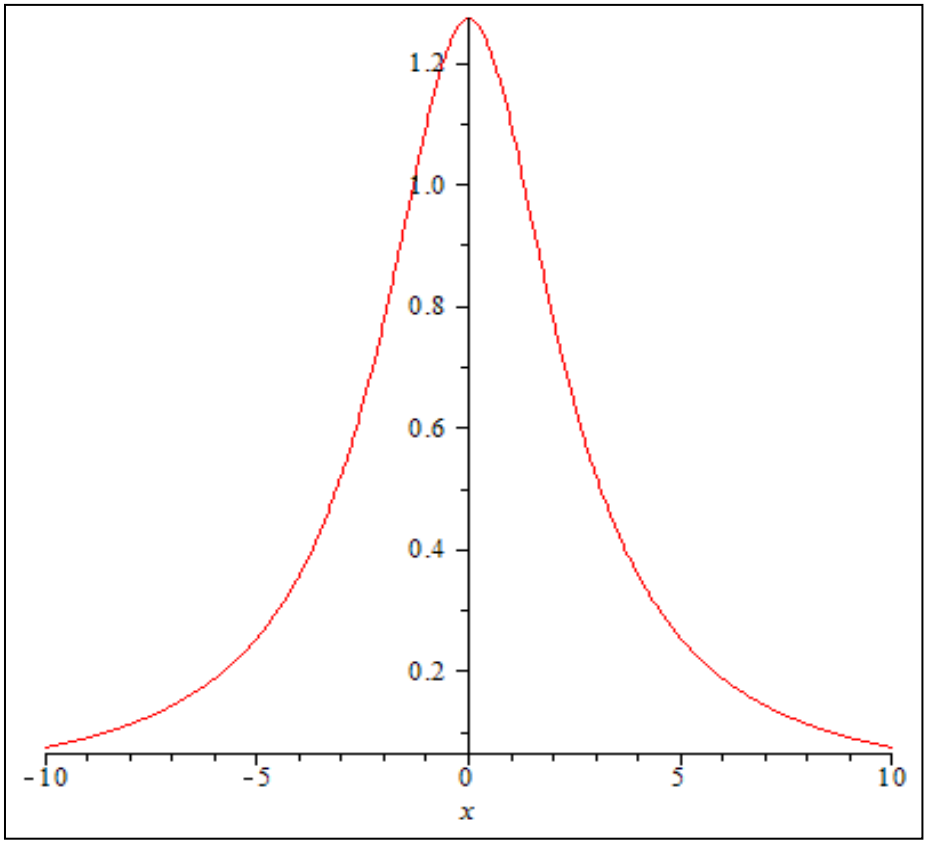

Figure 19 Absorption corresponding to Lorentzian line shape

In these studies absorption is detected via small field modulation (1G) so the signal is proportional to first derivative of absorption corresponding to first derivative of Lorentzian line shape shown in Figure 20 and represented by equation (2.72).

$$\frac{dv}{d\omega} = \frac{2\gamma B_1 M_0 T_2^3(\omega_0-\omega)}{\left[1+T_2^2(\omega_0-\omega)^2\right]^2}. \tag{2.72}$$

Here the line width can be described as a distance between two extremes of the first derivative of absorption. It can be calculated by taking a second derivative and finding zeros.

$$\Delta B = \frac{2}{\sqrt{3}}\frac{\hbar}{g\beta T_2}. \tag{2.73}$$

Since both amplitude and line width of the absorption derivative are dependent on T_2, the product of the amplitude and square of the line width (independent of T_2 and proportional to M_0) is taken as a measure of strength of ESR signal. In the regime of the small B_1, line width is independent and amplitude is linearly proportional to B_1. Neither of them is dependent on T_1. However, at high microwave power the term $\gamma^2 B_1 T_1 T_2$ cannot be neglected. The amplitude of ESR is not linear in B_1 anymore, and both amplitude and line width depend on T_1. At high microwave power amplitude starts to decrease with increasing B_1. This phenomenon is known as resonance saturation. It can be understood as population equalization of energy levels that causes net absorption to decrease.

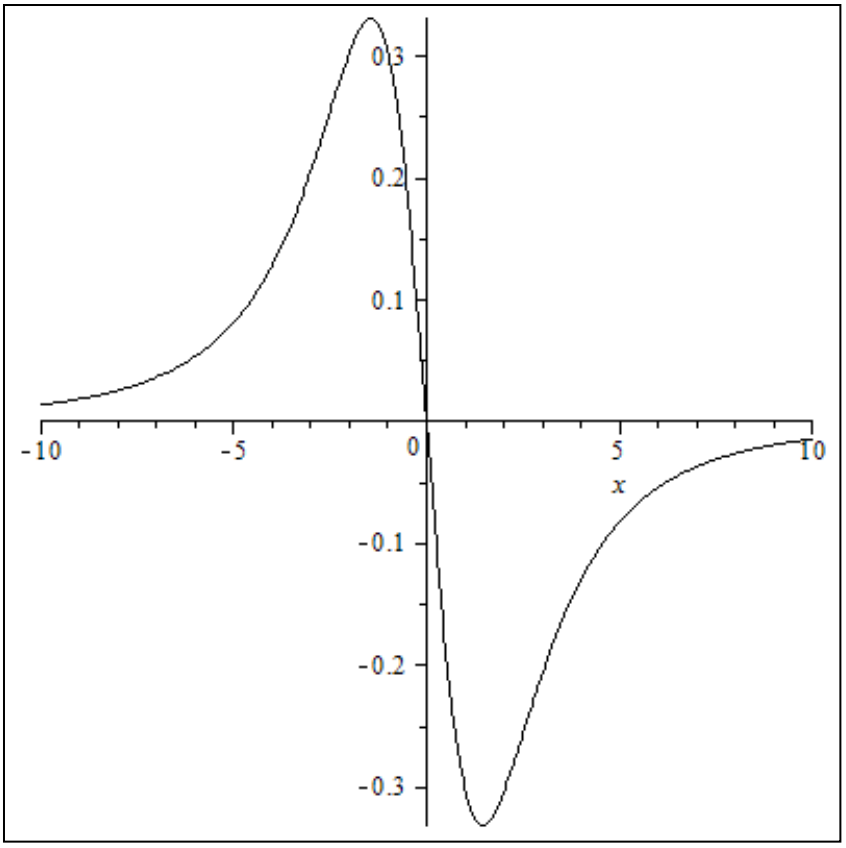

Figure 20 Detected ESR signal corresponding to first derivative of absorption

2.3.2.3. Line shape

In a perfect scenario, the ESR signal should look like a first derivative of a Lorentzian line. However, when the magnetic field is not homogeneous and varies over the sample, not all of the molecules are in resonance at the same value of the magnetic field. This as well as unresolved hyperfine coupling might cause inhomogeneous broadening and the resonance looks more like a Gaussian line shape than a Lorentzian. In this study we work with the films of blend of polymers with fullerene derivatives and it is

common to see a Gaussian line shape of an ESR resonance that can be described by the equation (2.76).

$$S(\omega) = e^{-\frac{(\omega_0-\omega)^2}{2\delta^2}}, \quad (2.74)$$

where half width at half maximum (HWHM) can be expressed as

$$HWHM = \sqrt{2}\ln 2\delta. \quad (2.75)$$

2.3.3. Experimental setup for ESR

ESR or electron paramagnetic resonance (EPR) technique is based on measuring the absorption of electromagnetic radiation (microwave) by an electron spin system. The sample is placed in magnetic field and transitions between Zeeman levels are monitored. Principles of ESR have been described previously in the introduction. However, the ESR measurement can be simplified by considering first only spin angular momentum S=1/2. When an electron is placed in magnetic field, the projection of its magnetic moment on the axis defined by the magnetic field, takes on two values -1/2 and +1/2. The separation ΔE between these two energy levels is linearly proportional to strength of magnetic field B. When an incoming microwave photon has energy equal to ΔE transition between the spin levels occurs as shown in Figure 21. These transitions are magnetic-dipole allowed, and are affected by the microwave magnetic field vector B_1, that is perpendicular to the external magnetic field generated by the electromagnet. The sample is placed in a resonator that maximizes the B_1 field at the sample. The matching of the photon energy

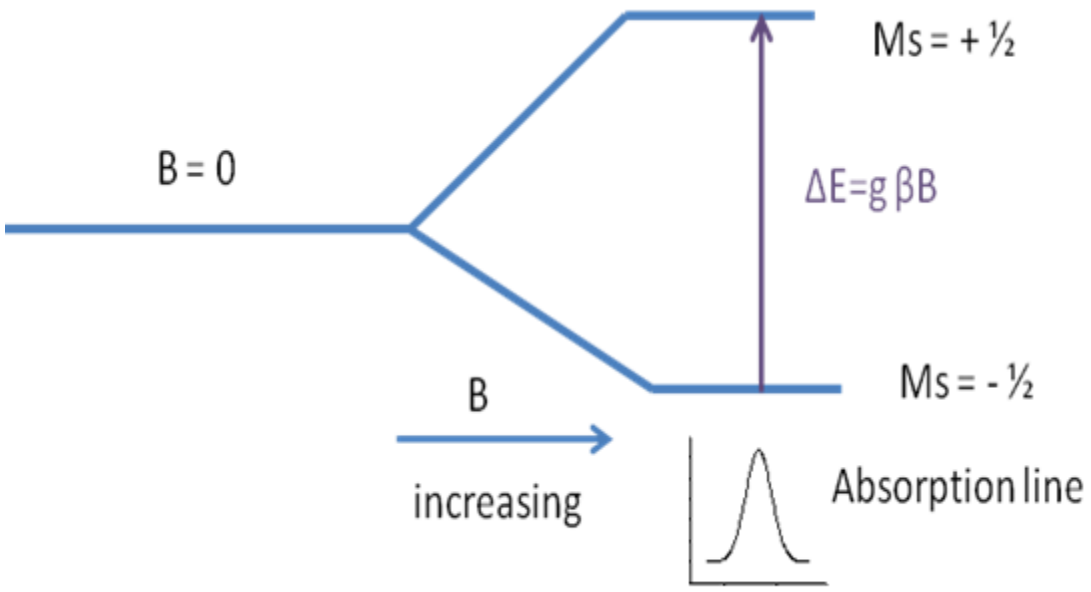

Figure 21 Zeeman energy splitting for an electron in magnetic field

of the microwave, ħω, to separation of electronic levels is called resonance.[34] The simplest ESR spectrometer has three basic parts: a source of electromagnetic radiation, a sample, and a detector. In the most basic terms, the spectrum is acquired by changing the frequency of the electromagnetic radiation and measuring with a detector the amount of radiation that passes through or gets reflected from the sample in order to observe the spectroscopic absorptions. In this study we used Bruker Elyxis 580 spectrometer. The general schematic of a Bruker EPR spectrometer is shown in Figure 22.

The microwave source and detector are placed inside of a microwave bridge. The sample is placed inside of a metal microwave cavity with the purpose to amplify weak signals coming from the sample. The cavity with the sample is placed inside of a cryostat because most of the measurements take place at cryogenic temperatures. The electromagnet is placed around the cryostat. The console contains signal processing and

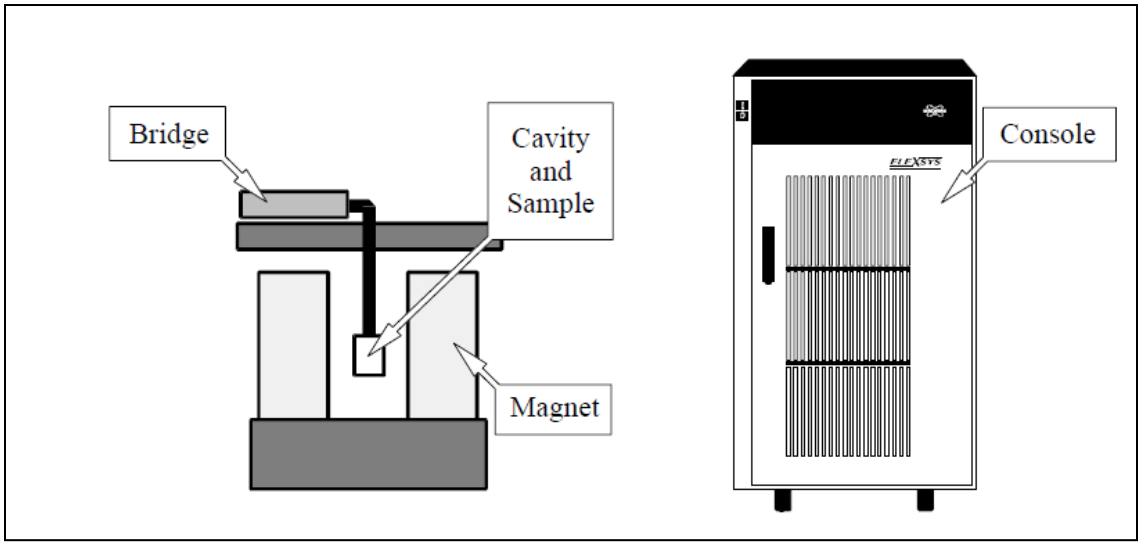

Figure 22 General schematics of a ESR Spectrometer

control electronics as well as a computer that is used for analyzing data and coordinating all of the units for acquiring a spectrum.

2.3.3.1. The microwave bridge

As mentioned previously the most import parts in the microwave bridge are the microwave source and the detector. The microwave power that the sample sees is varied via an attenuator that blocks the flow of microwave radiation. Most ESR spectrometers are reflection spectrometers, meaning they measure changes in reflection from the microwave cavity (together with the sample) due to spectroscopic transitions.The Shotky barrier diode is used as a microwave detector. It converts microwave into current. At low power levels less than 1μW, the diode works in a square region where the diode current is proportional to microwave power. At powers larger than 1mW, the diode works in a linear region where the diode current is proportional to the square root of microwave power. To achieve reliable results the diode should work in a linear region, and the diode

current should be around 200μA. To ensure that detector operates in that region the reference arm supplies the detector with some extra microwave power or bias. Some of the source power is tapped off into the reference arm where the second attenuator controls the power level and consequently the diode current for optimal performance. The phase shifter ensures that reference arm microwave is in phase with reflected microwave when they combine at the detector.

2.3.3.2. The ESR cavity

The microwave cavity is a metal box of rectangular or cylindrical shape that resonates with microwaves. At resonance, the microwave cavity stores microwave energy¸ no microwave will be reflected back but will remain inside of the cavity. Cavities are characterized by their quality factor or Q, which describes how well a cavity stores microwave energy. As the Q factor increases so does the sensitivity of spectrometer.

$$Q = \frac{2\pi\ (energy\ stored)}{energy\ dissipated\ per\ cycle}, \tag{2.76}$$

Energy can get lost due to the walls of the cavity because microwaves generate current in the walls of cavity which then generate heat. Q can be measured and calculated according to the equation (2.77):

$$Q = \frac{\nu_{res}}{\Delta\nu}, \tag{2.77}$$

where ν_{res} is the resonant frequency of the cavity and $\Delta\nu$ is the width at half height of the resonance. Due to the resonance a standing electromagnetic wave will be formed inside of the cavity, meaning that the magnetic and electric field will be exactly out of phase. The best ESR signal and highest sensitivity of spectrometer is achieved when magnetic field is maximum and electric field as at its minimum.

Microwave is coupled into the cavity via a hole called iris. With changing the size of iris it is possible to control the amount of microwave that will enter the cavity and be reflected back from the cavity.

The ESR signal is basically a result of reflected microwave caused by absorption of microwave by sample and consequently lowering Q of the cavity.

2.3.3.3. Signal channel

The signal channel unit located inside the console uses phase sensitive signal detection or lock-in amplifier to enhance sensitivity of spectrometer. The magnetic field strength that the sample sees is modulated sinusoidally at a modulation frequency usually 100 kHz. Field modulation sweeps through part of the ESR signal and reflected microwave is then amplitude modulated at the same frequency. The modulation amplitude should be much smaller than the width of the ESR signal, so that the signal is approximately linear over an interval of the same width as the modulation amplitude. The ESR signal is then transformed into sine wave with amplitude proportional to the slope of the signal as shown in Figure 23. The signal channel produces a DC signal proportional to the amplitude of the modulated ESR signal. Then it compares the modulated ESR signal to the reference signal and suppresses everything else that has a different frequency or phase than the field modulation. To improve sensitivity even more time

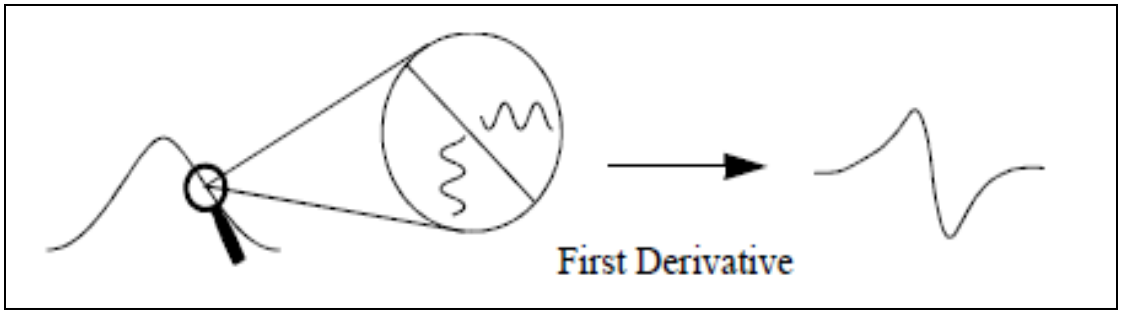

Figure 23 Field modulation and phase sensitive detection

constant is used to filter out the noise. This way sensitivity can be increased by several orders of magnitude, but modulation amplitude, frequency and time constant must be appropriate or the signal will be distorted. The magnetic field amplitude must be smaller than the width of the ESR signal or the signal will be broadened.

The time constant filters out the noise by slowing the response of spectrometer. However, if the time constant is too long, the ESR signal itself can get filtered out. Also the magnetic field at which resonance occurs can become shifted as well, preventing us from finding the correct g value. Sometimes it is necessary to use a long time constant to detect a very weak signal. In this instance the sweep time must be about 10 times longer than the time constant.

Distortion of the signal (broadening) can occur if the modulation frequency is too high. However, this is a only concern when dealing with dilute solutions and samples that have very narrow or closely spaced resonances.

2.3.3.4. Magnetic field controller

The magnetic field controller consists of two parts. The first part sets the magnetic field value and timing of the field sweep. The second part regulates the current in magnet

windings to reach the requested magnetic field value. Magnetic field regulation occurs via a Hall probe placed in the gap of the magnet. It produces voltage that depends on magnetic field perpendicular to the probe. Regulation of the magnetic field is achieved by comparing the voltage from the Hall probe to the voltage given by the first part of controller

2.3.4. Light induced ESR (LESR)

This study focuses on photogenerated species, so rather than studying ESR we study light induced ESR. The experimental set up is identical except for introduction of a laser. The experiment consists of two parts. First we measure the ESR before illumination of the sample with the laser light. Then we measure the ESR again while illuminating the sample with the laser. We call this measurement light on measurement. The final result or LESR spectrum is obtained by subtracting ESR from **l**ight-on measurement.

2.4. Optically detected magnetic resonance (ODMR) spectroscopy

The LESR technique is very successful in studying the blends of polymers and fullerenes. However, the LESR signal in pristine π-conjugated polymers is very low because of the low density of excited states and the sensitivity of shotky barrier diode used to detect the reflected microwave.

The optical transitions change with magnetic resonance, so rather than observing changes in reflected microwave that are in order of meV we can observe changes in transmission light intensity that are in order of eV. So using optically detected magnetic resonance (ODMR) we enhance spin detectability by orders of magnitude.

There are two main techniques: PLDMR- the detection of changes in PL under magnetic resonance and PADMR – the detection of changes in photoinduced absorption under magnetic resonance.

2.4.1. PADMR

Excited state recombination is a spin dependant process. The resonant absorption of microwave induces a spin flip, redistributes excited state populations among magnetic sublevels changing the recombination rate. This results in a change of the optical properties, namely the absorption and the emission. PADMR is a desired technique when dealing with materials that have low photoluminescence, such as blends of polymers and fullerene derivatives. However, since PADMR is based on a change of the recombination rate we can only observe spin pairs and not individual spins as in the case of LESR.

The photoinduced absorption spectrum shows the optical transitions and PADMR distinguishes if these transitions are due to spin ½ (polarons) or spin 1 (triplet exciton).

For spin ½ species PADMR, the change of excited states, δN due to magnetic resonance can be expressed as in the equation (2.78).

$$\delta N = \widetilde{N} - N = \left(\widetilde{N}_P + \widetilde{N}_{AP}\right) - (N_P + N_{AP}), \qquad (2.78)$$

Subscripts P and AP mean parallel and antiparallel spin pairs; tilde above N, the number of spin carriers denotes the resonant condition. The number of excited states N can be expressed in terms of generation rate, G and recombination rate, R.

$$N = \frac{G}{R}, \tag{2.79}$$

Under microwave saturation the number of parallel and antiparallel spins is equal.

$$\widetilde{N}_P = \widetilde{N}_{AP} = \frac{G_P}{R_P} = \frac{G_{AP}}{R_{AP}} = \frac{G_P + G_{AP}}{R_P + R_{AP}} = \frac{\sum G}{\sum R}, \tag{2.80}$$

It follows that

$$\frac{\partial N}{N} = \frac{N_{AP} - N_P}{N} \frac{R_{AP} - R_P}{R_{AP} + R_P}, \tag{2.81}$$

In the case of geminate recombination where all of the spins are generated in antiparallel configuration N_P=0 and N_{AP}=N, equation 2.91 becomes

$$\frac{\partial N}{N} = \frac{R_{AP} - R_P}{R_{AP} + R_P} > 0, \tag{2.82}$$

In the case of distant pair recombination where all of the spin ½ pairs are randomly generated, we can assume that G_{AP}=G_P and therefore

$$\frac{N_{AP} - N_P}{N} = \frac{\frac{G_{AP}}{R_{AP}} - \frac{G_P}{R_P}}{\frac{G_{AP}}{R_{AP}} + \frac{G_P}{R_P}} = -\frac{R_{AP} - R_P}{R_{AP} + R_P}, \tag{2.83}$$

From here the equation (2.82) becomes

$$\frac{\partial N}{N} = -\left(\frac{R_{AP}-R_P}{R_{AP}+R_P}\right)^2 < 0, \tag{2.84}$$

From equation (2.84) we can conclude that the sign of PADMR can tell us more about the recombination of the spin species. However, the geminate pairs have too short a lifetime to significantly contribute to CW PADMR. For spin 1, triplet exciton, we have to consider spin-spin interaction. So the spin Hamiltonian can be expressed with equation (2.85).

$$H_s = g\beta HS + D\left(S_z^2 - \frac{1}{3}S^2\right) + E\left(S_x^2 - S_y^2\right), \tag{2.85}$$

where S is the sum of two interacting spins, D and E are zero-field splitting (ZFS) parameters derived from coupling of two spin ½ particles responsible for triplet energy splitting at zero magnetic field. The spin 1 PADMR is a consequence of microwave induced changes in population of the triplet energy sublevels. There are three transitions occurring, two full-field transitions for Δm=1 and one half-field transition corresponding to Δm=2 that is only possible because of the anisotropic spin exchange interaction that mixes the triplet sublevels as depicted in Figure 24.The magnetic resonance satisfies equation (2.86):

$$2D\left(E^2 - \frac{D^2}{9}\right) \pm \frac{1}{\sqrt{3}}\left[\hbar^2\omega^2 - \frac{D^2}{3} - E^2 - (g\beta H_0)^2\right] \times \frac{\left[4(g\beta H_0)^2 - \hbar^2\omega^2 + \frac{4D^2}{3} + 4E^2\right]}{(g\beta H_0)^2} = D(1 - 3\sin^2\theta\cos 2\phi), \tag{2.86}$$

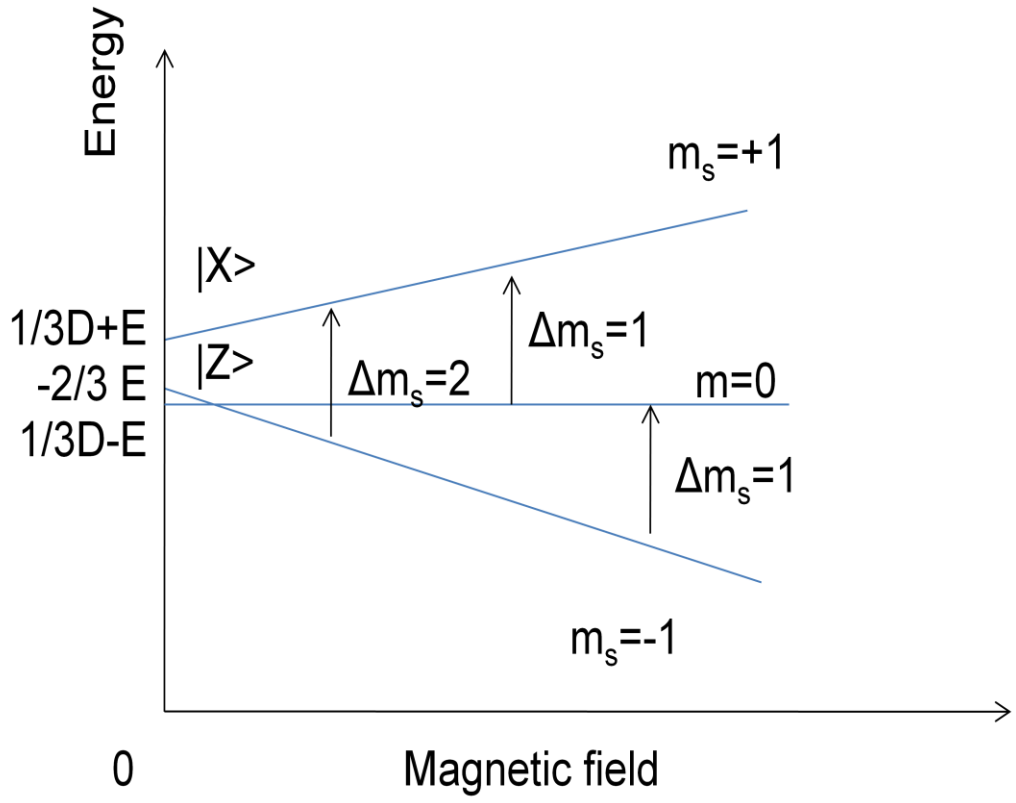

Figure 24 Spin 1 resonance transitons

where θ and ϕ are the Eulers angles for the principal axis of triplet's zero field splitting **D** tensor with respect to the magnetic field coming from spin-spin dipolar interaction. H_0 is ħω/gβ. At zero magnetic field, the degenerate energy states corresponding to m_s=1, m_s=0, and m_s=-1 are related to ZFS parameters in the following way:

$$E_1 = \frac{D}{3} + E, \tag{2.87}$$

$$E_0 = \frac{D}{3} - E, \tag{2.88}$$

$$E_{-1} = -\frac{2D}{3}, \tag{2.89}$$

where zero field splitting parameters can be expressed by means of the triplet wavefunction, Ψ and single particle operators r_{12}, x_{12}, y_{12}, and z_{12}.

$$D = \frac{3g^2\beta}{4}\left\langle \Psi \left| \frac{r_{12}^2 - 3z_{12}^2}{r_{12}^5} \right| \Psi \right\rangle, \tag{2.90}$$

$$E = \frac{3g^2\beta}{4}\left\langle \Psi \left| \frac{y_{12}^2 - 3x_{12}^2}{r_{12}^5} \right| \Psi \right\rangle. \tag{2.91}$$

In polycristaline and amorphous materials the D tensor is randomly oriented resulting in a PADMR spectrum called a triplet powder pattern that is the integration average over resonance conditions for all possible orientations.

2.4.2. PLDMR

PLDMR is very successfully used in systems with strong photoluminescence because when the spin carriers recombine radiatively, the direct changes in PL can be observed. PLDMR for spin ½ can be expressed as:

$$\frac{\partial I}{I} = \frac{I_{ON} - I_{OFF}}{I_{OFF}}, \tag{2.92}$$

where I is intensity of PL and ON and OFF subscripts denote microwave being on and off.

$$I_{OFF} = R_P^{'} N_P + R_{AP}^{'} N_{AP}, \tag{2.93}$$

$$I_{ON} = R_P^{'} \widetilde{N}_P + R_{AP}^{'} \widetilde{N}_{AP}, \tag{2.94}$$

R is the recombination rate and R' is the radiative recombination rate. From here we can calculate that

$$\frac{\partial I}{I} = \frac{R_{AP}R_P(N_{AP}-N_P)\left(\frac{R'_{AP}}{R_{AP}}-\frac{R'_P}{R_P}\right)}{(R_{AP}+R_P)I}, \tag{2.95}$$

PLDMR for spin 1, triplet excition is very similar to spin 1 PADMR. Its spectrum is a triplet powder pattern with half-field and full-field transitions and can be expressed as

$$\left(\frac{\delta I}{I}\right)_{i,j}(\theta,\phi,H) = \frac{R_i R_j \Delta N_{i,j}\Delta_{\mathrm{i,j}}\left(\frac{\mathrm{R}'}{\mathrm{R}}\right)}{(R_i+R_j)(I_i+I_j)}. \tag{2.96}$$

2.4.3. Experimental setup

The ODMR experimental set-up is identical to PA experimental set-up with addition of superconducting magnetic and microwave as presented in Figure 25. The sample is mounted in 3GHz coaxial microwave cavity with windows for optical access that is placed between poles of the superconducting magnet. The structure of the microwave cavity is shown in Figure 26. The electromagnetic field inside of the cavity can be described by the Maxwell equations:

$$E_{TEM}(x,y,z,t) = E_{TEM}(r,z,t) = \frac{b}{r}\sin\omega t \sin kz\hat{e}_z \tag{2.97}$$

$$B_{TEM}(x,y,z,t) = B_{TEM}(r,z,t) = \frac{b}{r}\cos\omega t \cos kz\hat{e}_\phi \tag{2.98}$$

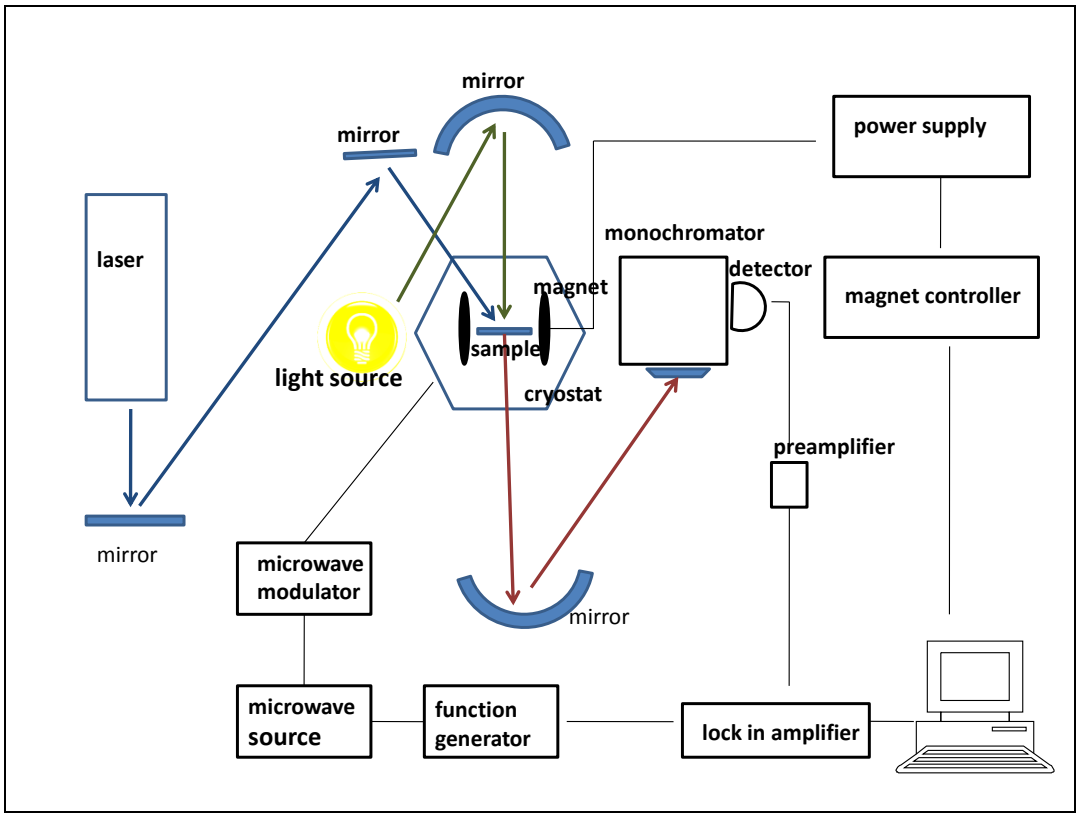

Figure 25 ODMR experimental set-up

where $k = \frac{mP}{L}$ (m=1,3,5,…), $k = \sqrt{\frac{8PQ}{\omega_{res} L \ln\frac{r_2}{r_1}}}$, r_1 and r_2 are the inner and outer radii of coaxial resonant cavity, P is microwave power, Q is quality factor of resonant cavity, L is the length of cavity, resonant frequency is $\omega_{res} = \frac{m\pi}{L}\frac{c}{\sqrt{\mu\varepsilon}}$. In the system used r_1=0.627cm, r_2=2.2cm, L=9.9cm, ω_{res}=2P×2946MHz, and Q=1000. The maximum power of the microwave is 100mW which produces inside of the cavity electric field of 90V/cm and magnetic field of 0.3G. The temperature in the cavity is adjusted manually by changing the flow of liq. He into sample chamber or via heater placed on the sample holder. The superconducting magnet provides a slowly swept DC magnetic field reaching 3T (30,000 G). The magnet is powered by a HP6260B DC power supply controlled by AMI 400A

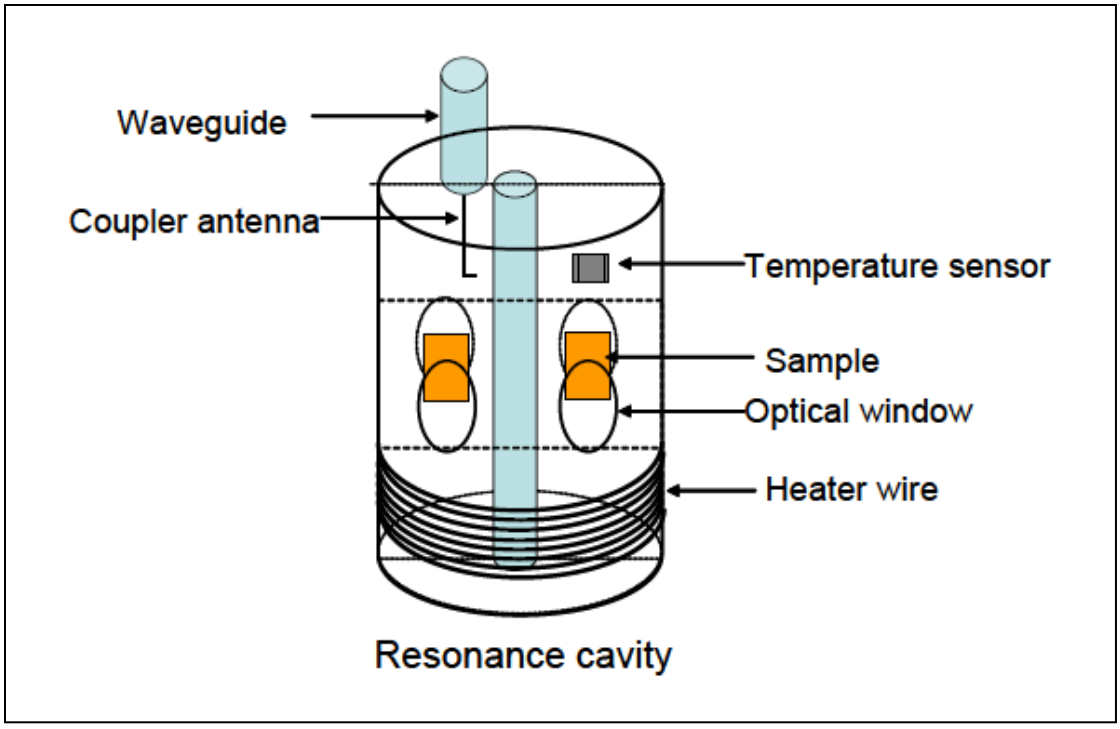

Figure 26 The 3 GHz coaxial resonant cavity

programmer that is in turn controlled by Keithley 236, a stable voltage source with computer interface (GPIB).

As the microwave source a HP616B UHF high frequency signal generator is used. Microwave is amplified by minicircuit ZHL-42 amplifier, modulated by a HP 11720A pulse modulator which is controlled by TTL signal from a function generator. Amplified microwave is transmitted through a Raytheon CSL71 bridge via a coaxial wave guide and it is coupled in resonant cavity via a copper antenna. The reflected microwave converted in voltage is monitored by an oscilloscope. The reflected signal is then compared to the ground signal to examine weather the optimum resonance conditions are achieved as shown in Figure 27.

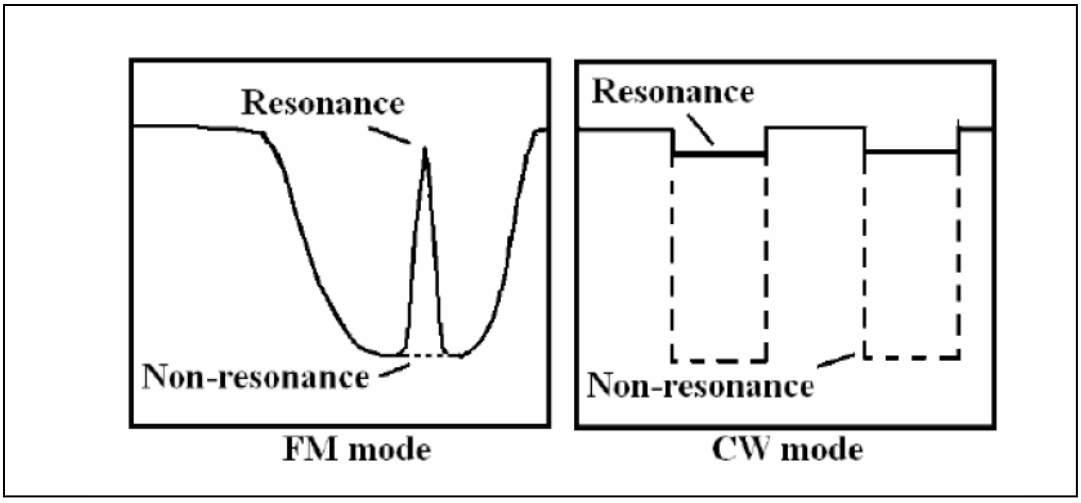

Figure 27 Oscilloscope display – achieving optimum resonance conditions, the maximum reflected microwave signal

2.5. Polaron pair mixing under magnetic resonance

In this study we pay special attention to the blends of polymers and fullerene derivatives where the dominant photoexcitations are due to polarons. It is important to discuss what happens to polaron pairs under the influence of magnetic field and microwave, as is the case in magnetic resonance experiments. In polaron pair triplet (PP_T) manifold due to Zeeman splitting there are three spin sublevels corresponding to m=+1,0,-1that are in resonance with microwave energy, ħω. Consequently transitions between m=0 and m=±1are induced as shown in Figure 28. The triplet m=0 sublevel is coupled with singlet PP_S spin sublevel via intersystem conversion interaction that is mainly determined by the hyperfine interaction. Through the resonant microwave all of the spin sublevels S, T_{-1}, T_0, and T_{+1} of PP are interconnected. At off resonance conditions triplet spin sublevels with m=±1 mix strongly with singlet spin sublevel. However, the population of triplet and singlet spin sublevels with m=0 is governed by their own generation and decay rates.

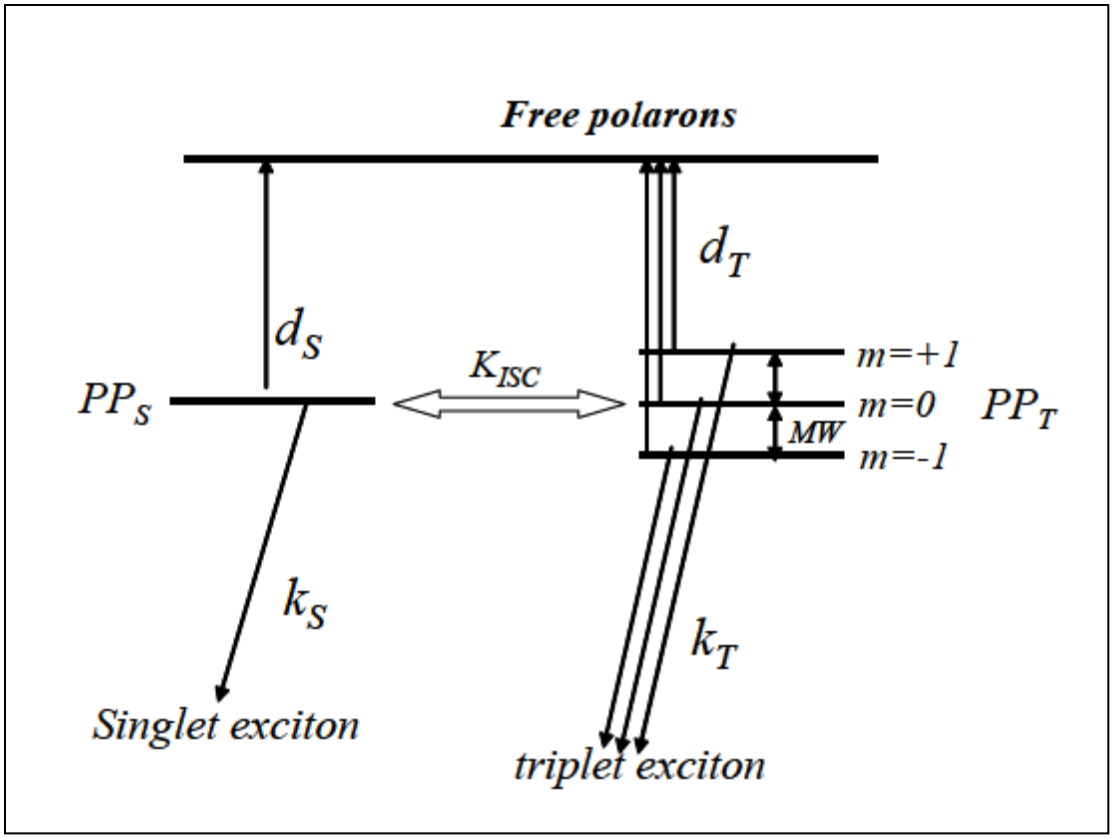

Figure 28 Transitions within polaron pair spin sublevels under the influence of a magnetic field. Microwave induced transitions under the magnetic field are depicted by the arrows between spin sublevels. K_{ISC} represents mixing of spin states within polaron pairs.

CHAPTER 3

STUDY OF PHOTOEXCITATIONS IN DONOR MATERIALS

3.1. Poly(3-hexylthiophene)

3.1.1. Introduction

Since the 70s, conjugated polymers have been extensively studied driven by possible applications in electronic, spintronics and optoelectronic devices. Polythiophenes form very environmentally and thermally stable materials, making them desirable for use in many applications such as donor materials in organic photovoltaic cells.[35] A very promising characteristic of the polythiophenes is that their structure and properties can be controlled by their synthesis. The polymer chain structure especially plays a critical role in determining the physical properties of this conducting polymer class. Their asymmetrical structure causes the polymerization to produce a mixture of three possible regio-chemical linkages between the repeat units: head-to-head, tail-to-tail (these are known as regio-random coupling), and head-to-tail or regioregular coupling. Regio-random couplings are considered to be less pure because they somewhat disrupt conjugation, and prevent ideal solid state packing, thereby diminishing the polymer electronic and photonic properties. On the other hand, regioregular coupling allows access to low energy planar conformation that results in highly conjugated polymers that provide flat, stacking macromolecular structures that can self-assemble into lamellas perpendicular to the substrate, and therefore providing efficient interchain and intrachain

conductivity pathways. In other words regioregularity maximizes the electronic and photonic properties of many conducting polymers and in particular the polythiophenes [36]. Regioregular poly-(3-hexylthiophene) or RR P3HT has been successfully used in organic photovoltaic cells as a donor material. It has been demonstrated that the degree of regioregularity [37], as well as the architecture of an organic solar cell [38] affect the solar power conversion efficiency.

In this study we concentrate on the effect of regioregularity on the photophysics and electrical properties of P3HT. It has already been shown that regioregularity increases with molecular weight and that charge transport amplifies with regioregularity (MW). [39],[40],[41],[42],[43] We will show that the photoinduced absorption spectrum can be used to differentiate between low and high molecular weight RR P3HT polymer chains, by tracking the appearance of a polaron band at low photon energy. Photo induced detected magnetic resonance (PADMR) is used as a complementary technique to understand the spin nature of the various PA bands in the spectrum. PADMR shows that the PA band in RRa P3HT is of excitonic (spin 1) nature. In the highest molecular weight RR P3HT the dominant PA band is due to delocalized triplet exciton. Moreover ultrafast transient PA shows that as the MW of P3HT chains decreases, a new PA band with different dynamics appears in the spectrum at 0.55 eV. Moreover, in high MW RR P3HT we also see stimulated emission and laser action that is absent in low MW polymer. Consequently it is possible by using these optical and magnetic probes to evaluate and predict the suitability of the P3HT polymer batches for their use in photovoltaic cells.

3.1.1. Study of absorption and emission spectra

In Figure 29 the absorption and photoluminescence (PL) spectra of RR P3HT and RRa P3HT are shown. The absorption band over the optical gap is due to π-π^* transitions. According to the normalized absorption spectra of the superior high molecular weight RR P3HT (50kDa) and RRa P3HT it is noticeable that RR P3HT has stronger absorption in the near IR and visible spectral region. According to Kasha's rule the PL emission comes from the lowest exciton in the system. In agreement with previous studies [44] we detect red shift of both absorption and PL of RR P3HT comparing to RRa P3HT, that may be assigned to the better order in lamellae and longer conjugation lengths [45]. The absorption and PL spectra of RR P3HT show pronounced structures due to phonon replica suggesting more homogeneity of polymer chains in the film[44]. The ratio of 0-0 to 0-1 vibronic side band in the PL spectra of RR P3HT is smaller than in RRa P3HT, suggesting a higher degree of aggregation of the former polymer.[46, 47]

The PL intensity of RR P3HT is much lower compared to that of RRa P3HT. This is also reflected in the PL quantum efficiency (PLQE), which we measured to be approximately 4% for high molecular weight RR P3HT and 13% for RRa P3HT. This could be explained by a weaker radiative transition of the lowest lying excitons that may be due to a larger interchain contribution compared to intrachain excitons in RRa P3HT. On the other hand, comparing the latest high molecular weight RR P3HT to RR P3HT from 2001/2002 that had PL QE less than 0.5% [44, 48] we may conclude that our new RR P3HT polymer might have fewer defects, and therefore yielding higher PLQE.

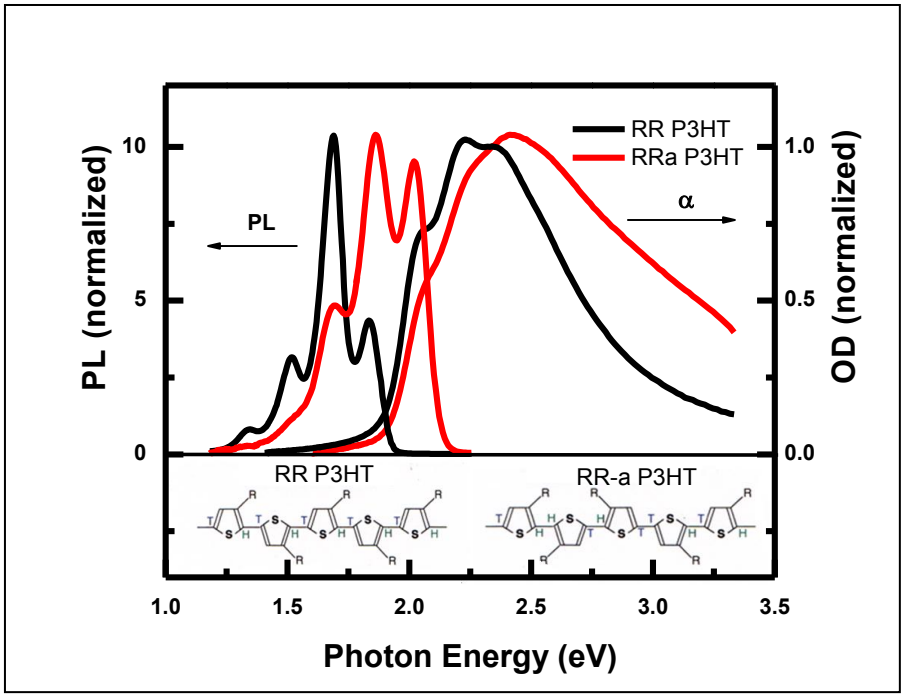

Figure 29 Normalized absorption and PL spectruas of RRa P3HT and RR P3HT thin films. The PL was measured at 80 K whereas the absorption was obtained at 300 K.

3.1.2. Studies of photoinduced and doping induced absorption spectra

In order to understand the excitonic nature in the polymer, we studied ps photo modulation spectra of thin films of RR P3HT from ADS, and from Plextronics, Inc. with different molecular weights, as well as RRa P3HT, as shown in Figure 30. These studies were carried out by Mr. Bill Pandit in our group. In RR P3HT film we can notice a blue shift of the excitonic PA band at ~1eV (referred to as PA1). However, with lowering molecular weight (to ~15 kDa) we observed the formation of a new PA band at ~0.6 eV that we dub PA*; this PA band is very pronounced and red shifted to 0.55 eV in the ADS RR P3HT film. When comparing the dynamics of the two PA bands, namely PA1 and PA* (Figure 30 inset (a)), it is obvious that they are not exactly the same. The decay of PA1 is faster than that of PA* indicating that they belong to different photogenerated

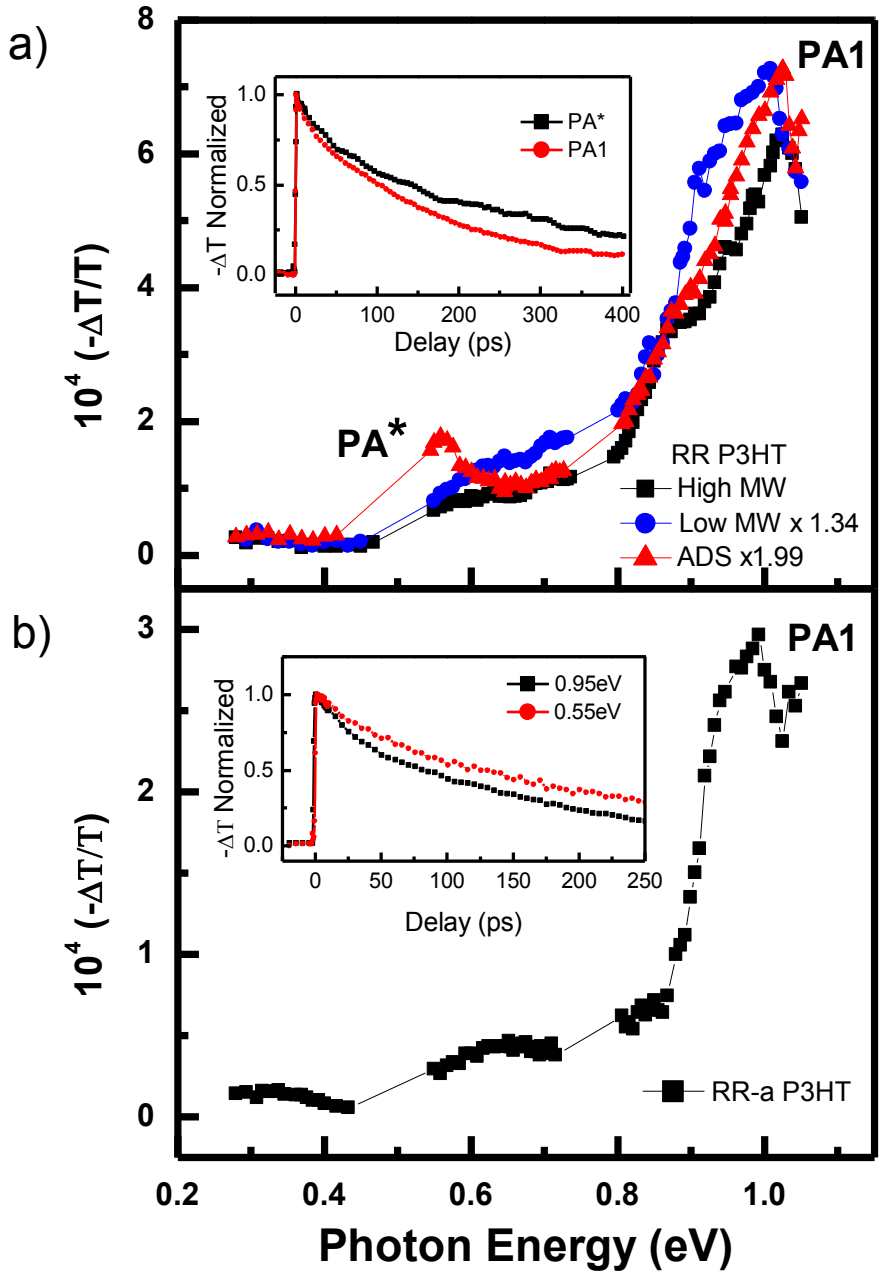

Figure 30 Transient PA spectra of a) RR P3HT with three different molecular weights; b) RRa P3HT. The insets show time decay at 0.95eV and 0.55eV, respectively.

species. The transient PA of RRa P3HT shows two PA bands at 0.95 eV and 0.55 eV, respectively, that also do not share the exact dynamics. Similarly to RR P3HT, the PA band at 0.95 eV has a faster decay than that of the 0.55 eV band. We tentatively assign the PA band at 0.55 eV to instantaneously formed polarons since it is longer lived than the excitonic PA band at ~1 eV. [49]

In Figure 31(a) we show the photoinduced absorption spectrum of RR P3HT film at 80 K. It is seen that the high molecular weight (50kDa) RR P3HT film does not have a PA band at low photon energy (assigned as P1) as observed in the literature [44, 48, 50]. In contrast the PA spectrum is dominated by a PA band at ~1.08 eV with a shoulder at about 1.2eV. This PA band has been previously assigned as P2, related to a photogenerated polaron species. However, the DIA spectrum of high MW RR P3HT presented in Figure 32 does not show any bands at this photon energy. The polaron DIA bands occur at ~0.2 eV and ~1.8 eV, respectively. From here we can infer that the PA band at 1.08 eV is not due to charge excitation, but may be due to delocalized triplet excitons. The PA spectrum of lower MW RR P3HT (that yields lower power conversion efficiency) shows the P1 band at 0.2 eV, somewhat smaller PA band at 1.08 eV and stronger shoulder at 1.2 eV that may be assigned to localized triplet exciton. ADS RR P3HT spectrum has even stronger P1 band at low photon energy and the localized triplet exciton band dominates the PA spectrum at 1.2 eV. The PA spectrum of RRa P3HT is dominated by only one PA band at around 1.36 eV that is assigned to be due to localized triplet excitons, which is in agreement to DIA spectrum presented in Figure 33, where we do not see any clear polaron bands at this photon energy.

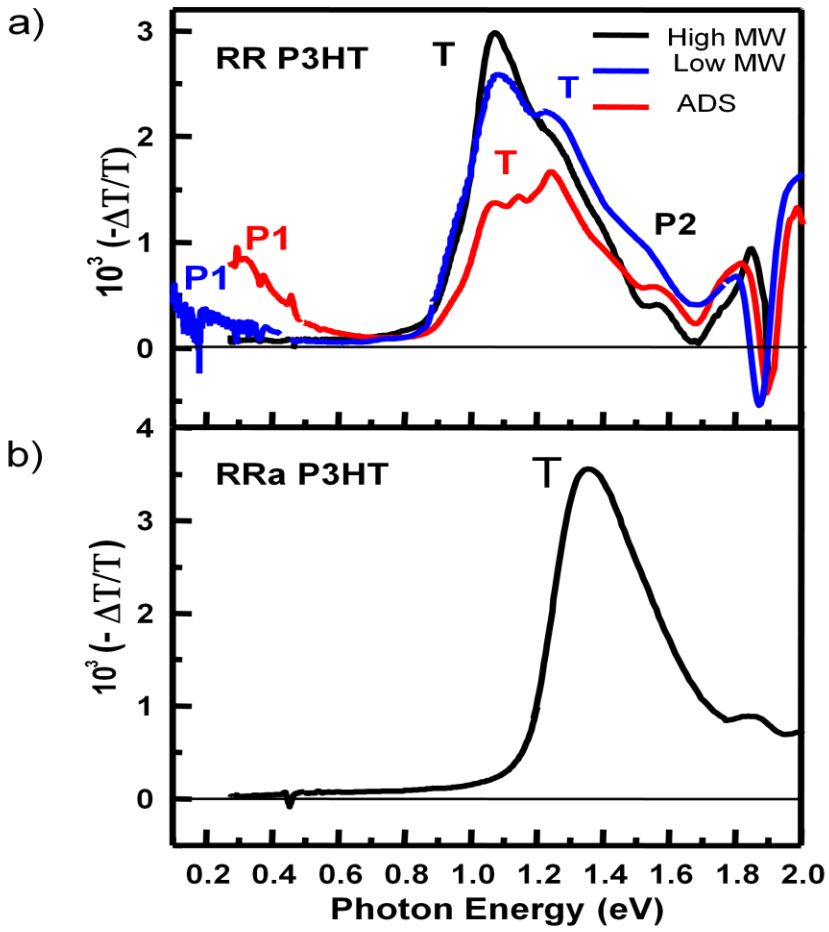

Figure 31 CW PA spectra of a) RR P3HT with three different MW; b) RRa P3HT. The PA bands P1 and P2 of polarons, PP for polaron pairs, and T for triplets are assigned.

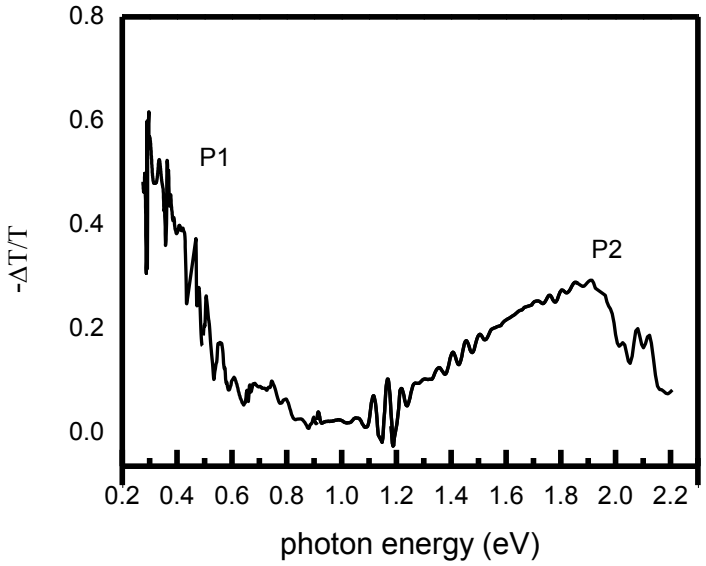

Figure 32 DIA spectrum of RR P3HT thin film doped with I2 for ~20 s.

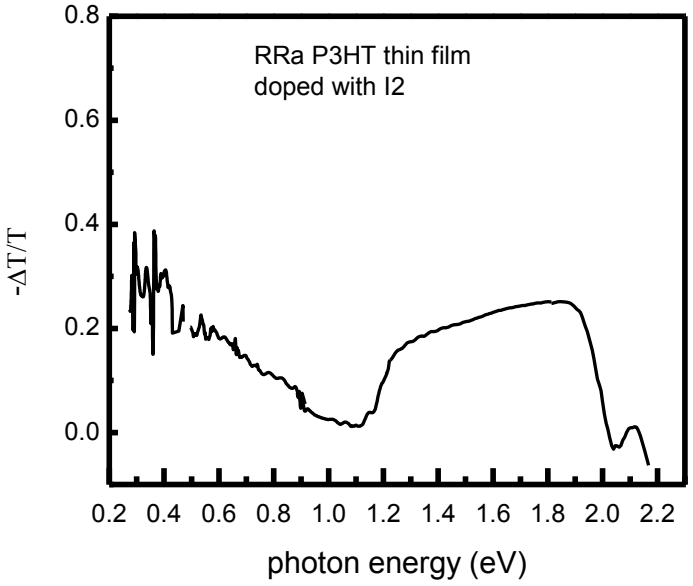

Figure 33 DIA spectrum of RRa P3HT thin film doped with I2.

3.1.3. PADMR spectroscopy

The PADMR of RR P3HT film measured at ħω=1.08 eV (Figure 34(a)) shows a 9 Gauss narrow asymmetric band at H_0=1000 Gauss, corresponding to g=2, with shoulders similar to triplet powder pattern.[51] The inset of Figure 34 (a) presents the closer look at the resonance at 1000 Gauss. Even though the resonance is very narrow it does not have a typical shape of a spin -½ resonance. This can be explained by delocalized triplet excitons. According to equations 2.90 and 2.91 with increasing distance, r between the electron and hole that form the delocalized triplet exciton, its zero field splitting parameters, D and E decrease. For very small D and E the zero field splitting between the spin sublevels can be negligible due to the weak magnetic dipole interaction between the spin ½ carriers comprising the triplets. Therefore the two full field transitions occur at very close magnetic field values, as depicted in Figure 35 that results in a narrow, asymmetric resonance. Based on the broader range of PADMR that does not show the typical 'half field' triplet resonance, we may question that the PA band in high molecular weight RR P3HT is due to the triplet excitons. The lack of 'half field' transition can be explained by very small values of zero field splitting parameter D and E, which based on the equation (3.1) (the FF resonance steps) and the equation (3.2) (the FF resonance shoulders) were calculated to be 12 G and 6 G, respectively.

$$H_{1,2} = H_0 \pm D \tag{3.1}$$

$$H_{3,4} = H_0 \pm \frac{(D+3E)}{2}, \tag{3.2}$$

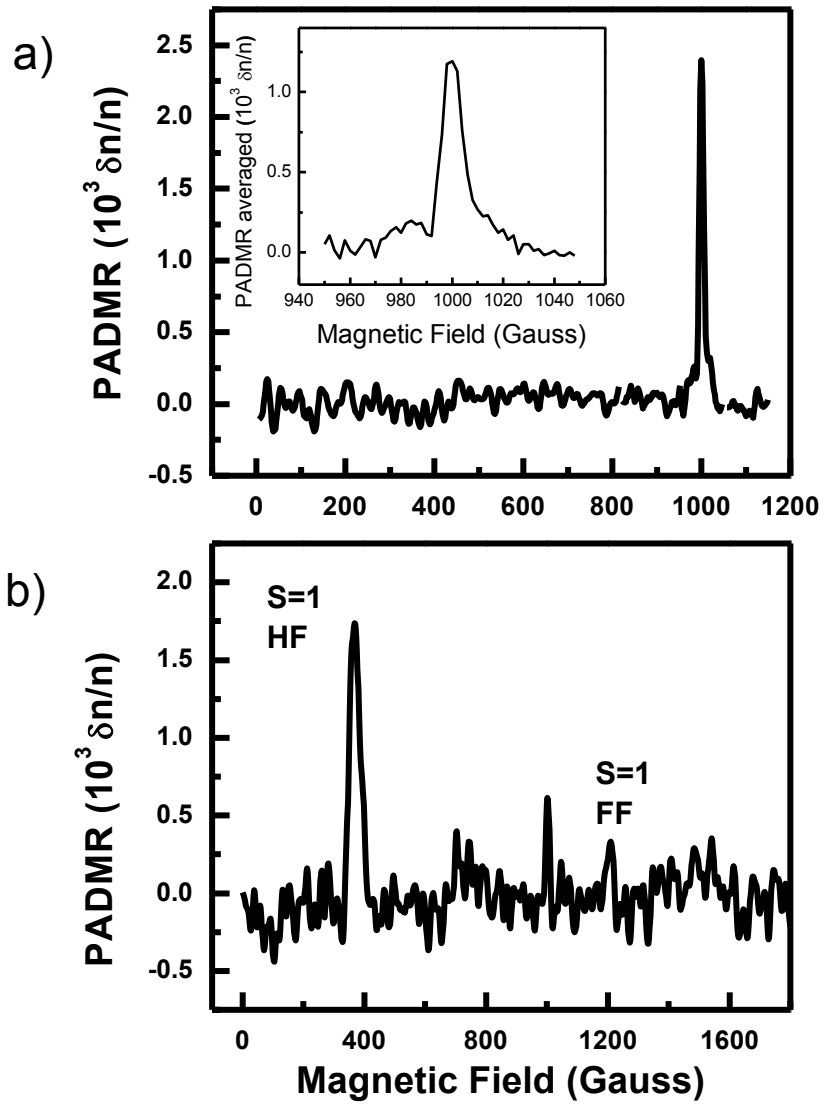

Figure 34 PADMR of: a) RR P3HT film showing delocalized triplet exciton resonance; and b) RRa P3HT with spin -1triplet powder pattern. FF and HF powder patterns are assigned. The inset in a) shows a closer look at spin-1 resonance due to delocalized triplet exciton with small zero field splitting parameters D and E.

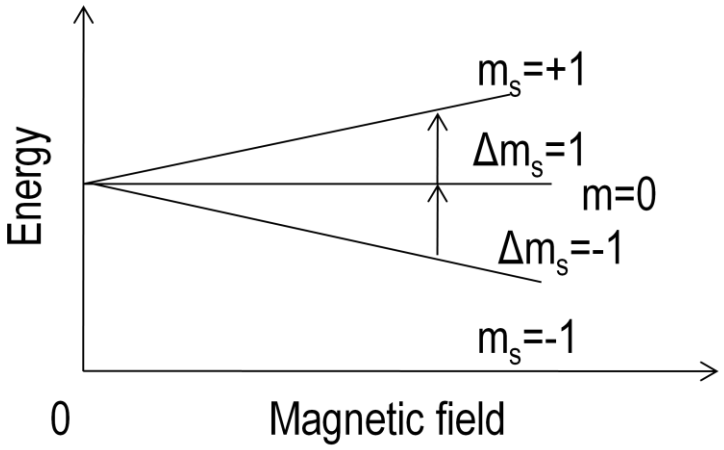

Figure 35 Resonant transitions for delocalized triplet exciton with very small zero field splitting parameters D and E.

In contrast, the PADMR of RRa P3HT at ħω=1.36 eV consists of a weak 13 G narrow spin 1/2 resonance at H_0=1002 G, and characteristic spin 1 triplet powder pattern with strong 'alf field' resonance H_1=368 G and 'full-field' resonance powder patter between 800 and 1200 Gauss. The anisotropic spin exchange mixes the triplet sublevels, permitting both $\Delta m_s = \pm 1$ and $\Delta m_s = \pm 2$ transitions at 3 GHz. That is the reason that both full field (FF) and half field (HF) powder pattern resonances are observed. We can calculate the zero filed splitting parameters from the HF and FF powder pattern singularities.

$$H_{1,2} = \frac{1}{2} H_0 \sqrt{1 - \left(\frac{D+E}{H_0}\right)^2} \tag{3.3}$$

$$H_{5,6} = H_0 \pm \frac{(D-3E)}{2}, \tag{3.4}$$

where D and E are zero field splitting parameters. Using the equations (3.3) and (3.4) we calculate D=607 G and E=70 G.

3.1.4. Conclusion

Based on our results, the power conversion efficiency of organic solar cell does not depend on the architecture of a device alone, but also on the synthesis of the organic materials used for the active blend. In the past 10 years the RR P3HT regioregularity continuously improved, yielding higher power conversion efficiencies.

PLQE of the newest RR P3HT increased almost 10 times, which can be attributed to fewer defects. The PA spectrum of high MW (superior regioregularity) RR P3HT does not show a PA band at low photon energy, previously assigned to P1 of separated polarons. The PADMR and DIA show that the dominant PA band in this polymer is due to delocalized triplet excitons. Ultrafast photomodulation shows that with decreased MW a new band at 0.55 eV appears in the PA spectrum that does not share the same dynamics as the band at 0.95 eV that belongs to excitons. We thus conclude that this PA band is either due to trapped excitons in defects, or to excitons in the polymer aggregates.

3.2. TAES-V polymer

3.2.1. Introduction

The bulk heterojunction organic photovoltaic cells (OPVC) based on RR P3HT/PCBM blend have been reported with power conversion efficiency (PCE) around 4%. [38] However, it seems that with this particular donor/acceptor blend the PCE limits have been reached. There are many factors that limit performance of OPVC; one of them is absorption of the polymer donor. It seems that narrow absorption of RR P3HT in the

spectral range of 300-650 nm is the main factor that hinders further improvement of OPVC based on RR P3HT.[52]

In general, the performance of OPVC is directly proportional to three parameters: open-circuit voltage (Voc), short –circuit current density (Jsc), and fill-factor (FF). Jsc depends on the absorbance of the donor material; thus so to increase Jsc low –band gap polymers have been successfully synthesized.[53-56]

To achieve high PCE, in addition to the low band gap (<1.6 eV), the ideal donor material need also to show have high hole mobility and well-matched HOMO/LUMO levels with the acceptor material [57] in order to enhance Voc. For this reason, building blocks with lower-lying HOMO are introduced in the donor polymers.

TAES-V is a novel low-band gap polymer composed of three co-polymers of the structure D-A-D (where D stands for donor and A for acceptor) synthesized by Plextronics, Inc, which when blended with $PC_{70}BM$ in OPVC gives record power conversion efficiency of 7%. In this study we used optical and magnetic resonance spectroscopy in order to better understand the nature of photoexcitations in this new polymer.

3.2.2. Optical study of TEAS-V copolymer

As shown in Figure 36 the absorption onset of TAES-V is at ~1.6 eV (the optical gap is~1.75 eV) indicating the existence of some low band gap building blocks in this polymer. The absorption spectrum peaks at approximately 2.08 eV, which is closer to peak of photon flux irradiation at ~1.82 eV [56] than that of RR P3HT (having absorption peak at ~2.4 eV). Comparing to RR P3HT, the absorption spectrum of TAES-V is dramatically red shifted by ~0.3 eV; this shift improves sun light absorption of this

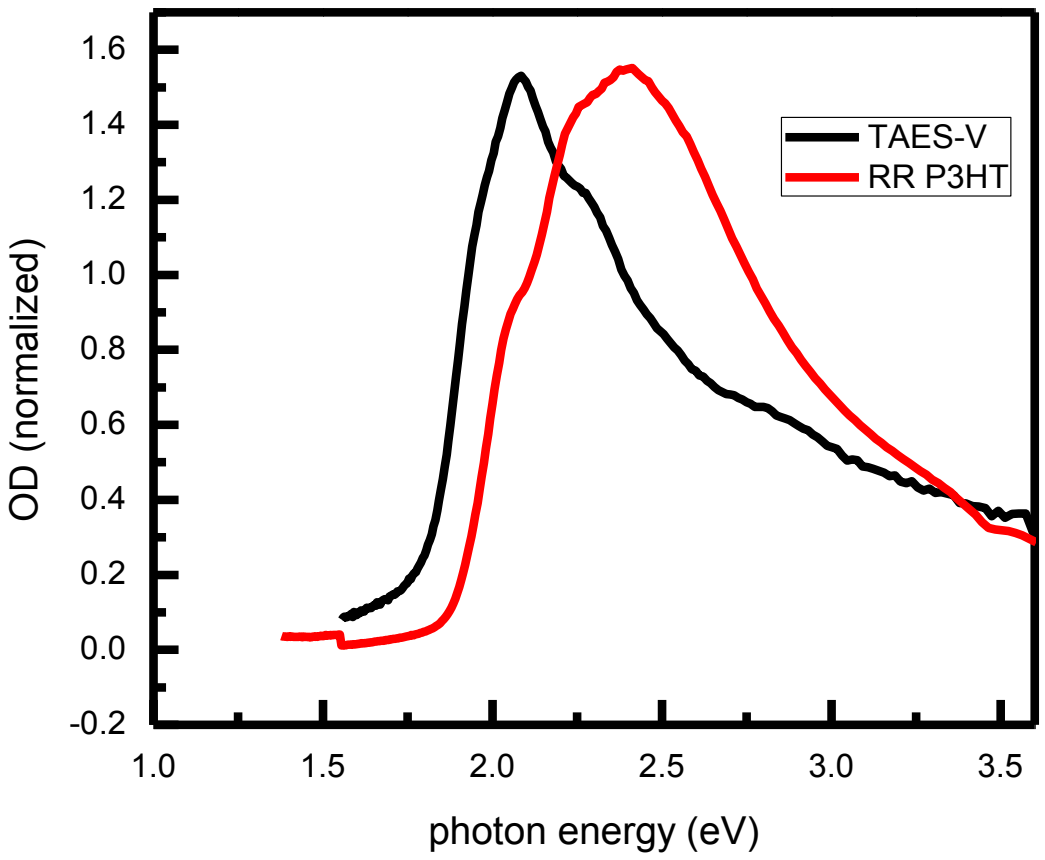

Figure 36 Normalized optical density (absorbance) spectra of TAES-V and RR P3HT.

copolymer and consequently Jsc also increases, resulting in better PCE of OPVC based on this material donor.

PL measurements were done with the pump excitation wavelength of 514 nm and 100mW power at 50 K (Figure 37). The PL spectrum is very well structured suggesting long conjugation lengths and higher regioregularity with the primary exciton emission (or 0-0 emission line) at ~1.75 eV. However, the PL spectrum shows very strong and almost equal in intensity 0-0 and 0-1 vibronic transitions; this indicates lack of polymer chain

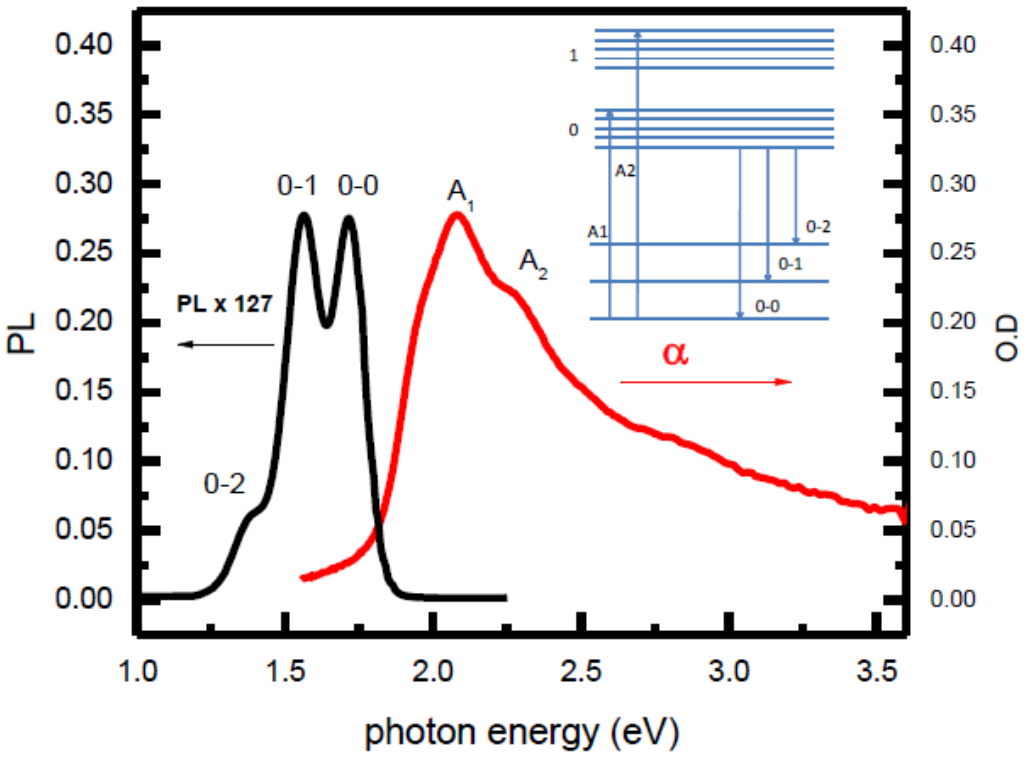

Figure 37 Normalized PL and absorption spectra of TAES-V thin films. Inset shows the vibronic energy level diagram with the optical transitions corresponding to absorption peaks (A_1,A_2) and PL peaks (0-0, 0-1,0-2) .

aggregation, and contribution of intrachain excitons to PL. The ratio of 0-0 to 0-1 transition, Sr is close to unity, almost its maximum value; that is characteristic of single molecule emission. Consequently, the PL spectrum could be described with Franck Condon model giving relative intensity of vibronic replica [46].

$$I_{0\to m} \propto (\hbar\omega)^3 n_f^3 \frac{S^m e^{-S}}{m!}. \quad (3.5)$$

where n_f is the real part of the refractive index that is usually taken as constant over the spectral range, m is the index of the vibrational level, and S is the Huang-Rhys factor, which gives a measure of the coupling between the electronic transition and the most strongly coupled vibration. The PL spectrum of TAES-V was fit with equation (3.5) using Gaussian line shape with the same width for each vibronic transition resulting in S=0.98±0.06 as shown in Figure 38) [46, 47, 58].

The photoluminescence quantum efficiency of this polymer films is relatively high ~17% compared to 4% of the best (highest molecular weight) RR P3HT . This gives further evidence for the intrachain exciton recombination and the lack of aggregation.

Photoinduced absorption (Figure 39) was measured on a drop-casted film of TEAS-V with concentration of 3 mg/ml in chloroform. Sapphire was used as a substrate. The pump wavelength was 514 nm with100 mW power. A lamp was used as a probe light. The photoinduced absorption spectrum shows no band due to polaron P1 at the low photon energy suggesting fewer defects. At ~1.06 eV there is a broad PA band and photobleaching starting at ~1.8 eV due to depletion of ground state population due to the

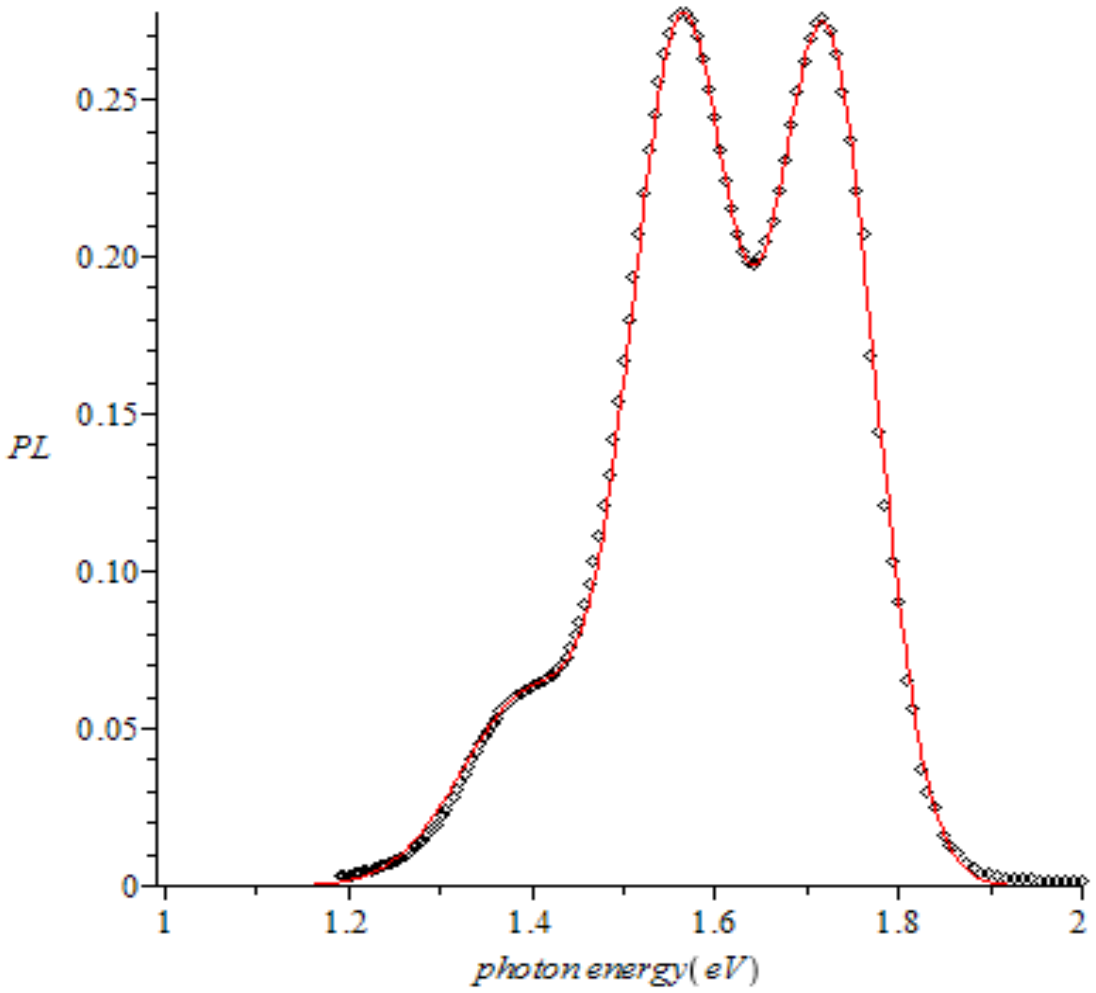

Figure 38 The fit of the PL spectrum using the Franck-Condon model (the equation (3.5)). The empty rhombs represent experimental data, and the red line is the fit.

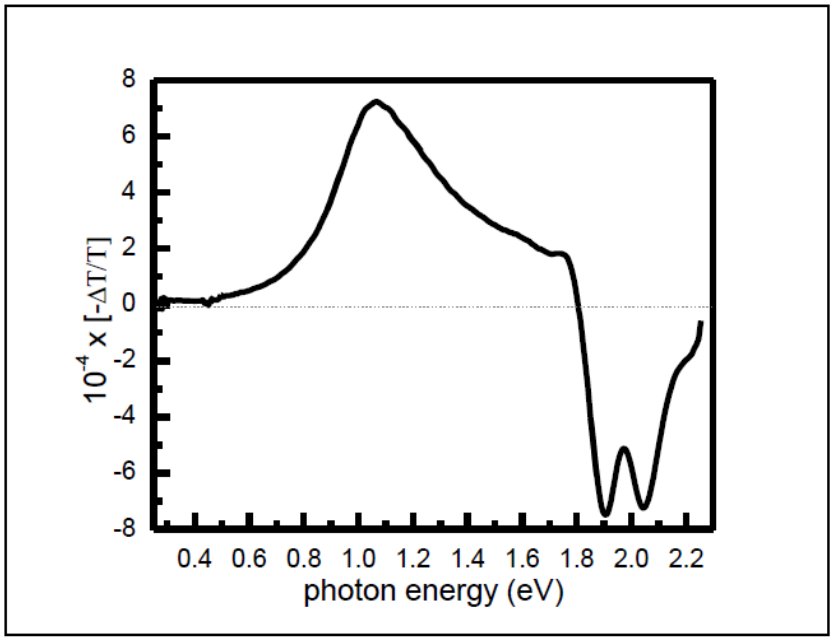

Figure 39 Photoinduced absorption spectrum of TAES-V thin film with only one PA band at ~1.06 eV and photobleaching starting at 1.8eV.

photogeneration of long-lived excitations. In order to distinguish the nature of PA peak at 1.06 eV additional experiments involving magnetic resonance need be done.

Frequency dependent PA was done by changing the pump beam modulation frequency from 10 Hz to 100 kHz at a fix photon energy of 1.06 eV, and at two different pump powers, namely 100 mW (Figure 40) and 400 mW (Figure 41). The measured photoexcitation lifetime, τ =0.14 ms ± 0.05 ms does not significantly change with the pump power suggesting monomolecular recombination kinetics, as explained in chapter 2. Using Equation(2.30) a dispersive parameter, α may be obtained as~0.89.

The PA intensity dependence is linear (Figure 42) which further proves monomolecular recombination kinetics. The decrease of PA intensity with increasing temperature (Figure 43) is related with a parallel decrease in the photoexcitation mean lifetime with the temperature.

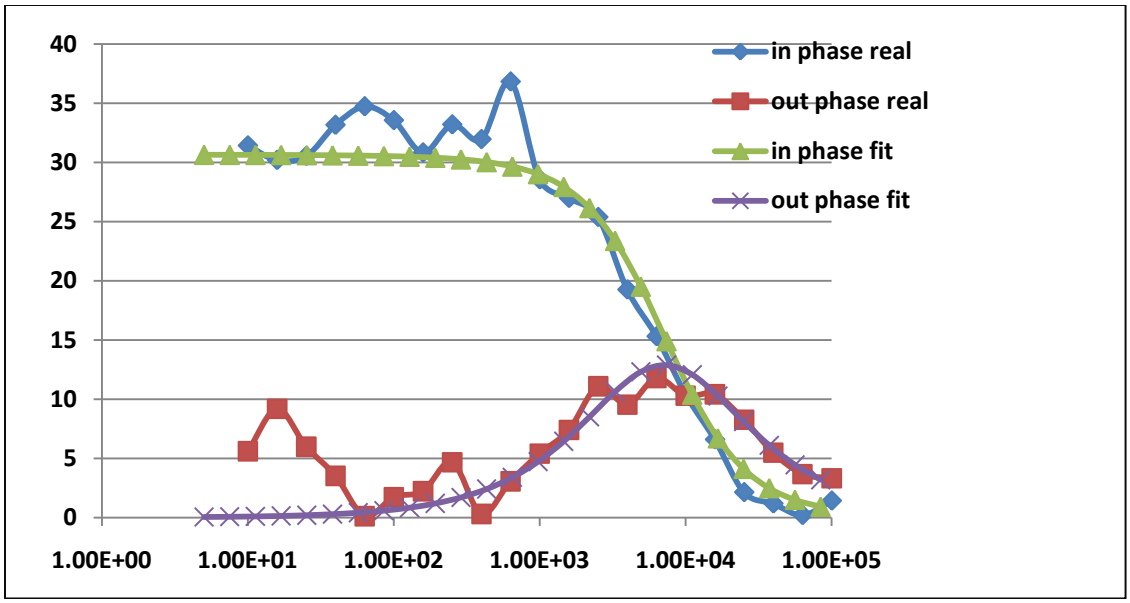

Figure 40 Frequency dependent PA measured at a fixed photon energy of 1.06 eV, with laser power of 100 mW at 50 K.

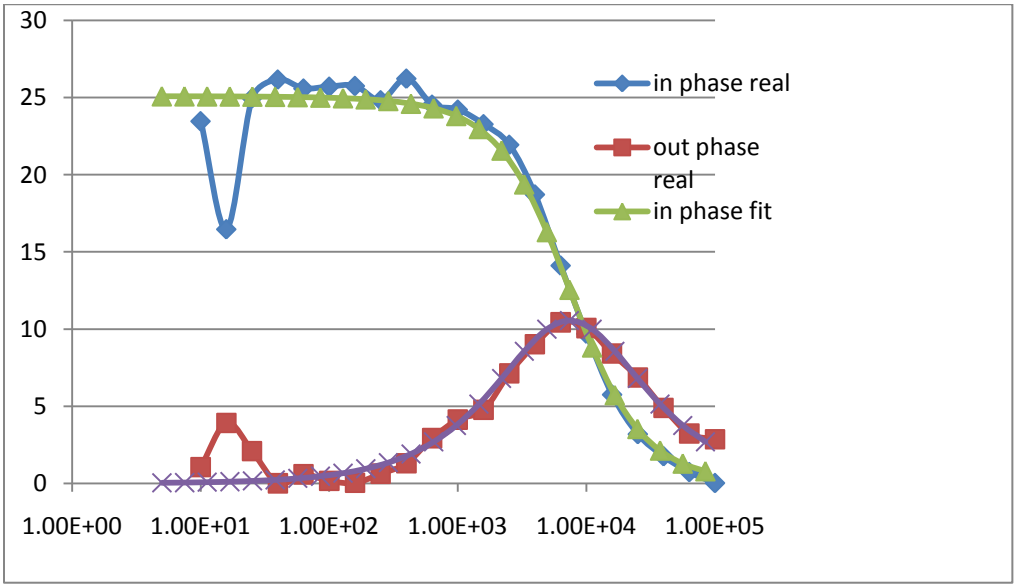

Figure 41 Frequency dependent PA measured at fixed probe photon energy1.06 eV with laser power of 400 mW at 50K.

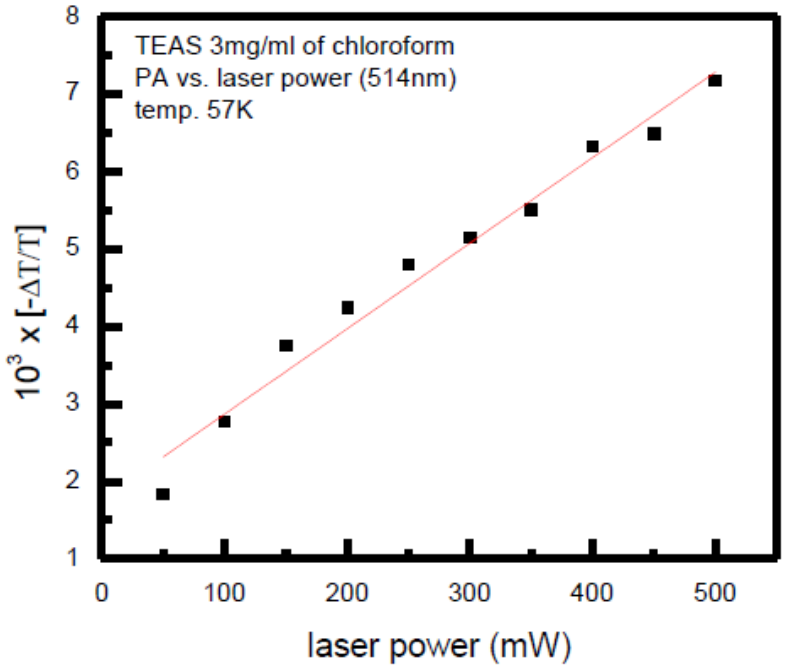

Figure 42 PA of TAES-V at 1.06 eV vs. the excitation laser power. The line through the data is a linear fit.

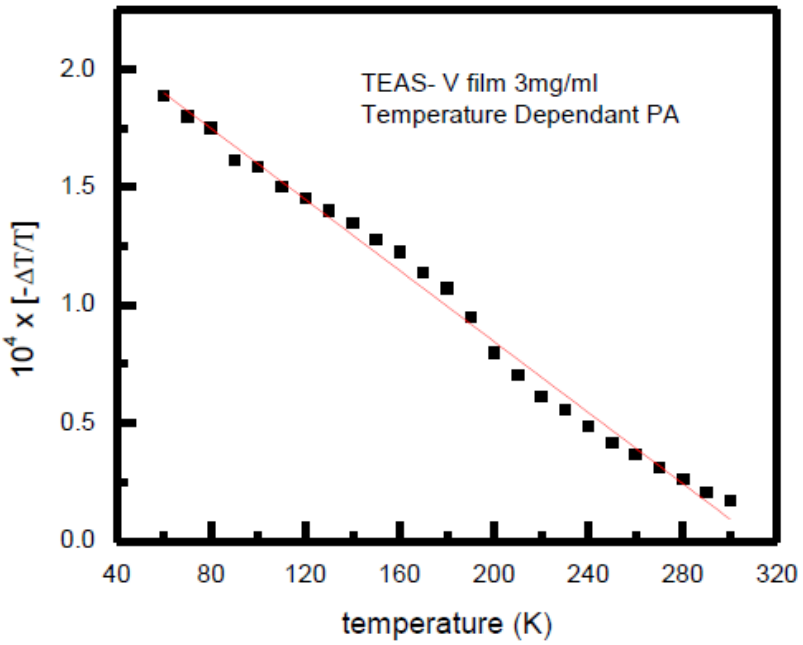

Figure 43 PA of TAES-V vs. the temperature; the line through the data points is a linear fit to guide the eye.

From electroabsorption spectrum shown in Figure 44 we can identify the exciton at ~1.93 eV, lowest exciton state 1Bu. At ~2.45 eV we can recognize an induced absorption feature, assigned mAg. According to the separation of EA exciton contribution (1Bu) and continuum band (mAg) we can conclude that the exciton binding energy is ~ 0.5 eV. However, this spectrum does not show the signature of charge transfer (CT) exciton.

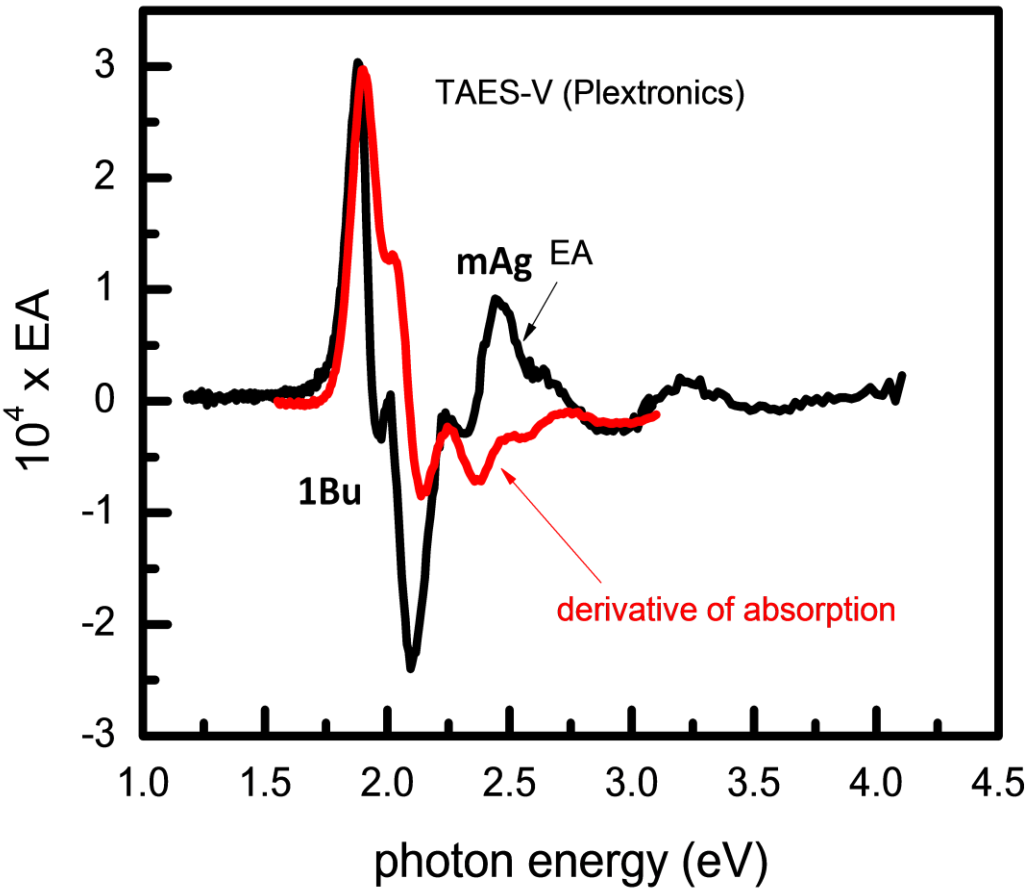

Figure 44 Electroabsorption of TAES-V film (black line) follows the derivative of absorption (red line).

3.2.3. Magnetic resonance study of TAES-V copolymer

Optically detected magnetic resonance (ODMR) in Figure 45 was measured at 10 K, with microwave power of 100 mW, laser wavelength 514 nm and power of 600 mW. The PLDMR was obtained with very good signal to noise ratio, which was not possible with PADMR measurement. The PLDMR measurement was done at fixed photon energy 1.06 eV, where we observed a broad PA band. PLDMR consists of a 9 G narrow spin-1/2 resonance at 1011 G and a spin-1 triplet powder pattern with over 500 G wide full field and ~20 G wide half field resonances.

The H-PLDMR of TAES-V is reminiscent of PLDMR of an anisotropic exchange coupled polaron pair with the Hamiltonian expressed in equation (3.6)[59]:

$$\mathcal{H}_{SS} = g_e \boldsymbol{H}\cdot\boldsymbol{S_e} + g_h \boldsymbol{H}\cdot\boldsymbol{S_h} + J\boldsymbol{S_e}\cdot\boldsymbol{S_h} + \boldsymbol{S_e}\cdot\overleftrightarrow{\boldsymbol{D}}\cdot\boldsymbol{S_h} = \overline{g\beta}Hm_s + J\left[S^2 - \frac{3}{2}\right] + \frac{1}{2}\left(J_x' S_x' + J_y' S_y' + J_z' S_z'\right), \quad (3.6)$$

where S and m_s are the spin quantum numbers and $J_x' = J_x - J$. Equation (3.6) has one singlet or even solution and three odd or triplet solutions. HSS can be written in terms of zero-field splitting (ZFS) parameters, D' and E', where $D' = \frac{3}{4}J_z' \; and \; E' = \frac{1}{4}\left(J_x' - J_y'\right)$. Triplet Hamiltonian can be expressed as:

$${}^3\mathcal{H}_{SS} = \overline{g\beta}Hm_S + J\left[S^2 - \frac{3}{2}\right] + D'\left[S_z^2 - \frac{1}{3}S^2\right] + E'\left(S_x^2 - S_y^2\right), \quad (3.7)$$

The anisotropic spin exchange interaction mixes the triplet sublevels therefore permitting transitions corresponding to $\Delta m_s = \pm 1$ and $\Delta m_s = \pm 2$ as shown in Figure 46.

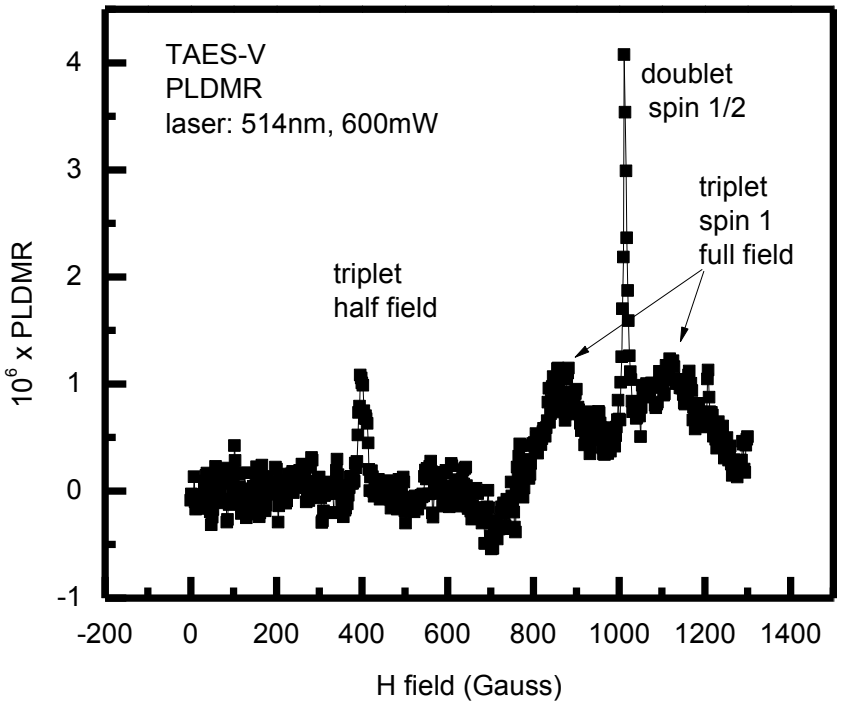

Figure 45 H-PLDMR spectrum of TAES showing spin1/2 resonance at 1011 G, and FF and HF triplet spin-1 powder patterns, as indicated.

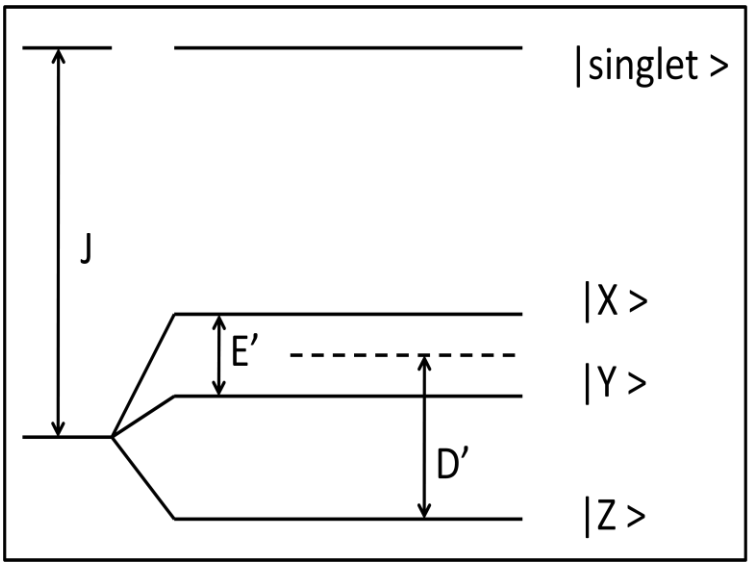

Figure 46 Schematic diagram of polaron pair energy levels with anisotropic exchange interactions.

Consequently, exchange triplet powder pattern has both full field (FF) and half field (HF) resonances. The following equation can give us singularities, shoulder, and steps of FF powder pattern:

$$\text{singularities: } H = H_0 \pm \frac{(D' - 3E')}{2}, \tag{3.8}$$

$$\text{shoulder: } H = H_0 \pm \frac{(D' + 3E')}{2}, \tag{3.9}$$

$$\text{steps: } H = H_0 \pm D', \tag{3.10}$$

The HF powder pattern consists of a singularity and shoulder that can be calculated as well.

$$\text{singularity: } H = \frac{1}{2} H_0 \sqrt{1 - \left[\frac{D+E}{H_0}\right]^2}, \tag{3.11}$$

$$\text{shoulder: } H = \frac{1}{2} H_0 \sqrt{1 - \left[\frac{D-E}{H_0}\right]^2}. \tag{3.12}$$

Using equations (3.11) and (3.12) we calculate ZFS parameters D≈635G and E≈62G.

A closer look at the spin 1/2 resonance reveals that it is asymmetric consisting of at least two contributions, possibly holes and electrons on the polymer chain, which confirms that an electron-withdrawing moiety has been added to this polymer backbone in order to lower HOMO level (Figures 47 and 48).

PLDMR at various MW power was measured for both the spin-½ and HF spin-1 resonance (Figure 49), and the area under the resonance peak was plotted vs. MW power. The saturation behavior of the two resonances is different; the spin 1 HF

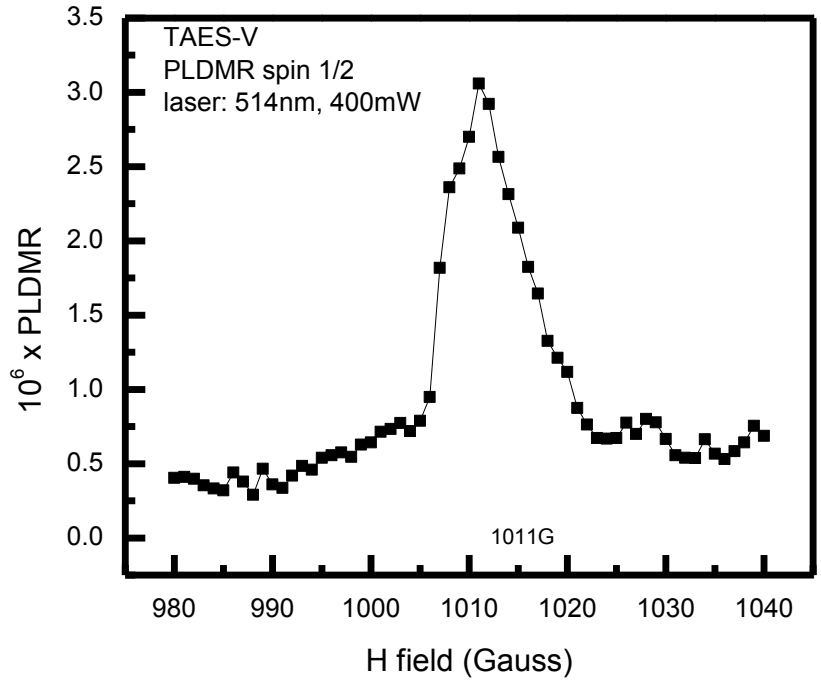

Figure 47 PLDMR of TAES-Vfilm showing asymmetric spin-1/2 resonance.

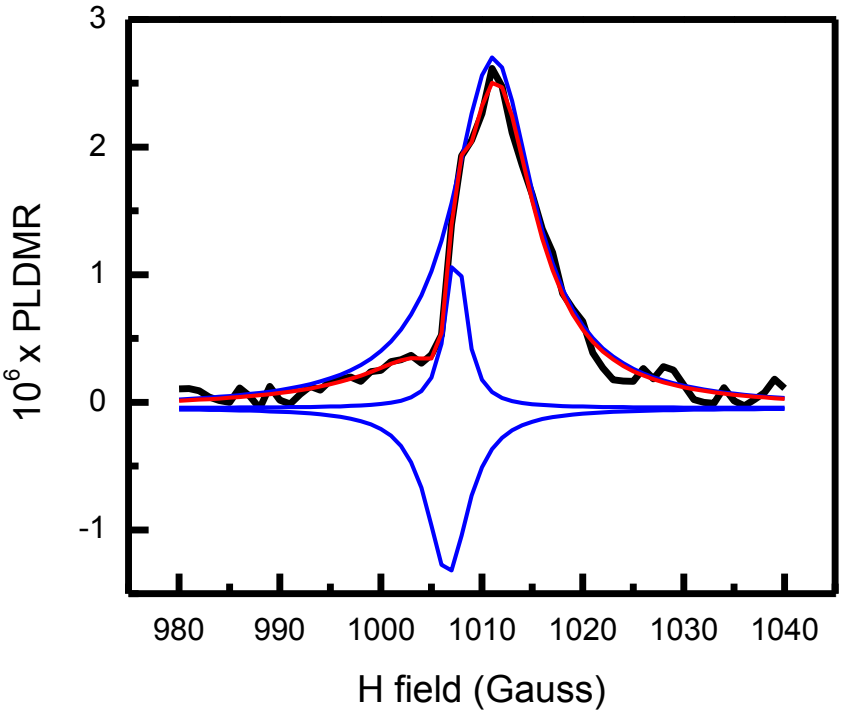

Figure 48 Fitting spin ½ resonance with three Lorentzians indicating positive and negative contributions to the resonance

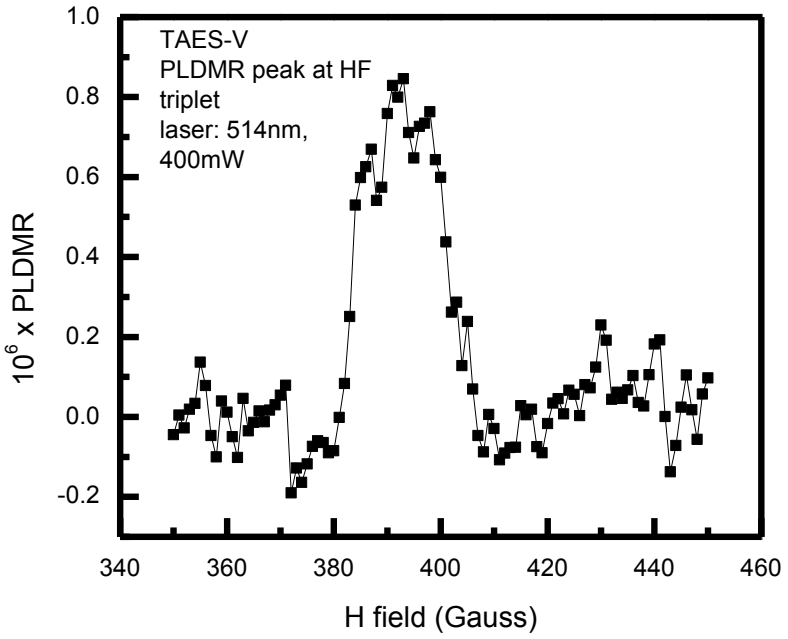

Figure 49 HF resonance of TAES-V film due to Δm=±2 transition

resonance saturates faster than the spin ½, which indicates two different photoexcitation species having different spin relaxation lifetimes (Figure 50). The data were fit with the saturation equation: $\int \boldsymbol{PADMR} \sim \frac{\boldsymbol{P_{MW}}}{\boldsymbol{P_{MW}+P_S}}$, where Ps indicates the spin relaxation rate. And according to our results the Ps for spin ½ resonance is ~14, and for spin 1 HF resonance Ps is ~2. Since the spin relaxation time is reciprocally proportional to spin elaxation rate, we can conclude that triplet has much longer spin relaxation time than the polarons.

Spin- ½ resonance is best fit with three Lorentzian curves as shown in Figure 48. We see two strong positive contributions and one negative contribution to the resonance. Since the ~3 GHz microwave frequency of our system does not allow us to clearly resolve these three contributions to the sharp spin ½ resonance, then LESR with microwave frequency of ~9 GHz proves to be a useful technique that also allows us to find the exact values of g-factors.

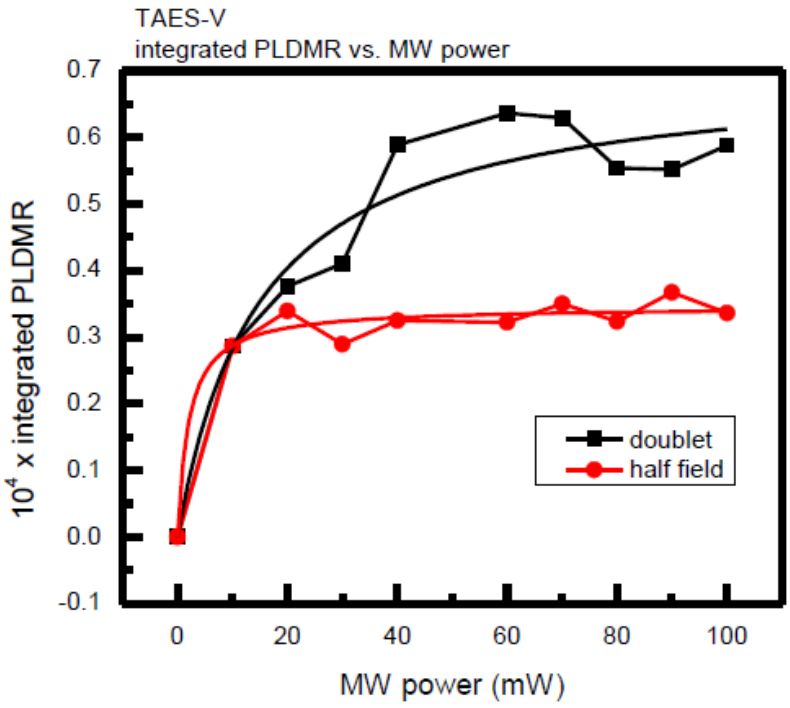

Figure 50 Integrated PLDMR resonance vs. MW power for spin1 and spin1/2 resonances. The lines through the data points are fits using the saturation equation: $\int \boldsymbol{PADMR} \sim \frac{\boldsymbol{P_{MW}}}{\boldsymbol{P_{MW}+P_S}}$.

LESR of TAES-V film was measured at 10 K, using the Bruker Elyxis 580 X-band spectrometer. Ar+ ion laser was used as a pump with excitation wavelength of 514 nm and ~200 mW power. Microwave in this experimental apparatus is approximately ~9.67 GHz with power of 0.39 mW. First, we measured ESR at 10K. After that we directed the laser light onto the sample using fiber optics; we dub this measurement as 'Light On'. Intensity of ESR is very large, ~50% of the intensity of Light On measurement, as can be seen in Figure 51. The ESR signal is broader than Light On signal confirming a negative contribution to the resonance. Light Off measurement was done in the dark after the sample was already exposed to the excitation with the laser,

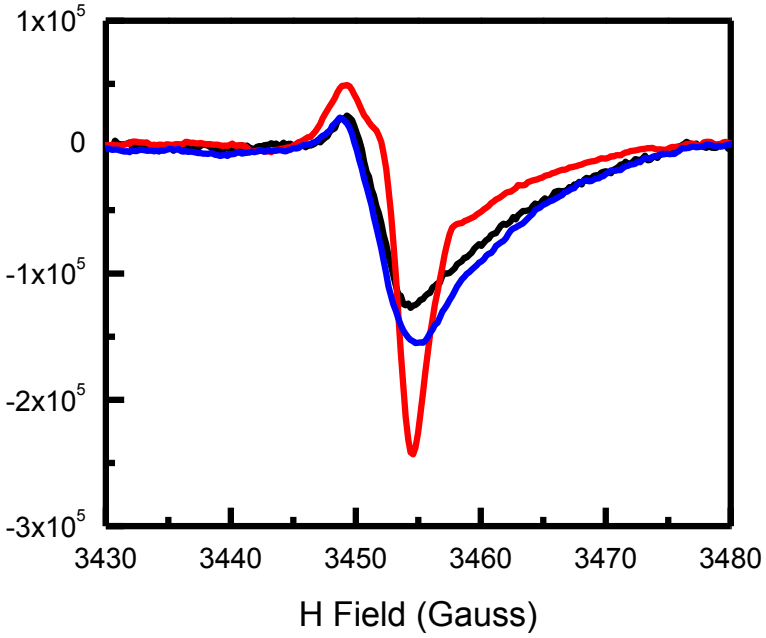

Figure 51 ESR, 'Light On', and 'Light Off' measurements of TAES-V film at 10 K using ~9 GHz microwave frequency

and the laser was turned off. The long-lived LESR is slightly larger than the ESR signal, indicating the existence of metastable states. LESR is obtained by subtracting ESR from Light On measurement, showing only the contribution of photogenerated specie (Figure 52). Integrating LESR as shown in Figure 53 we obtain a graph similar to ODMR that has well resolved resonances. Transforming x axis from magnetic field into g-factor values we obtained the following g-factor for each contribution: 2.00078 ± 0.00008, 2.00214±0.00002, and 2.00537±0.00004. This measurement was done before we realized that we can calibrate system with DPPH to get exact g-factors. So the g-factors might be as well 1.998, 1.999, and 2.00237. The origin of negative contribution with g-factor of 2.00214 seen in both PLDMR and PADMR can be due to spin-dependant nonradiative trapping of photogenerated polarons by negative radical ions on acceptor moiety that might be responsible for large ESR signal[51, 60] .

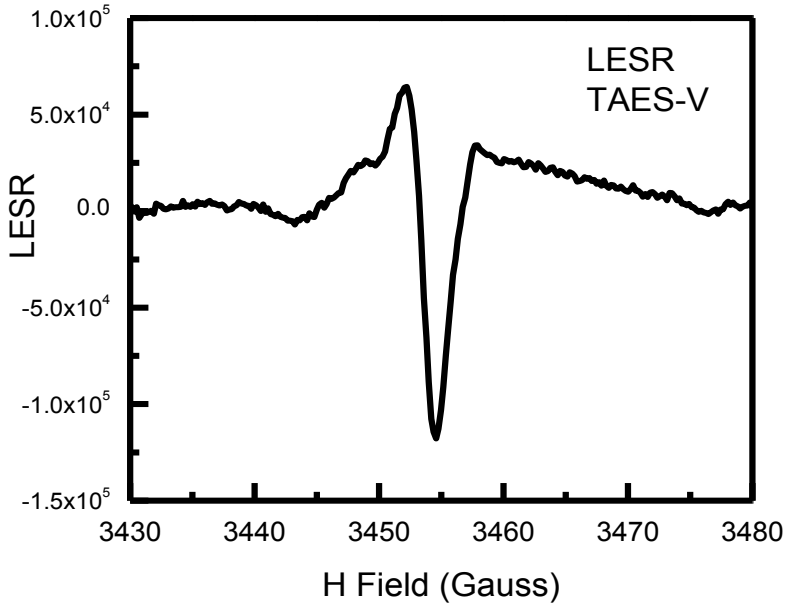

Figure 52 LESR of TAES-V film at 10K, obtained by subtracting the Light On ESR from the ESR in the dark

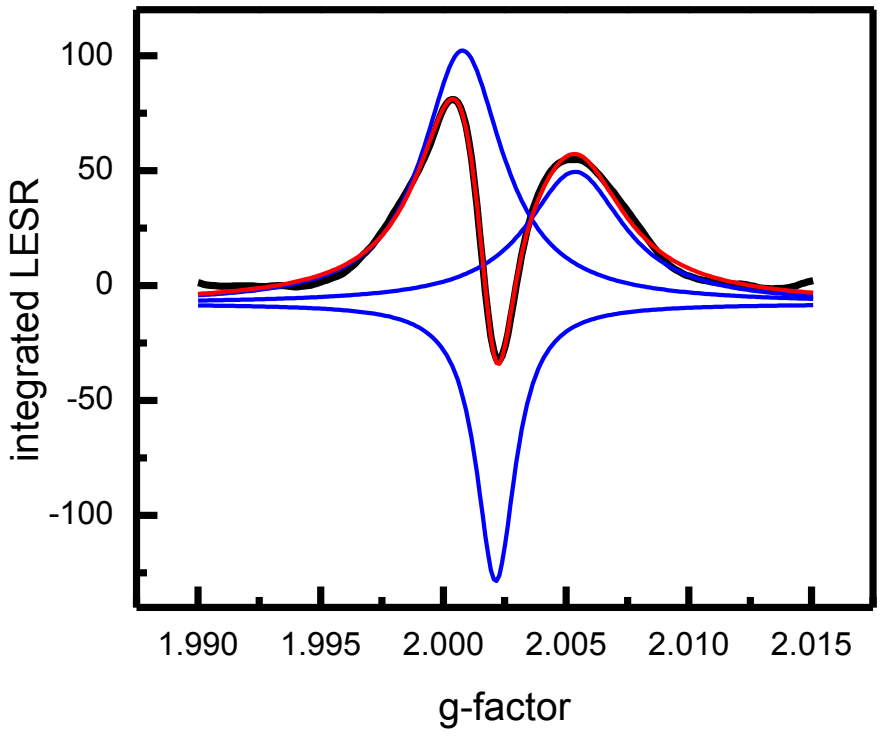

.

Figure 53 Integrated LESR fit with three Lorentzian curves, showing two positive and one negative contribution with different g-factors.

3.2.4. Conclusion

TAES-V is a novel low band gap (~1.7 eV) polymer composed of three copolymers of the structure D-A-D. When used in OPVC it gives 7% power conversion efficiency that can be partially due to its red shifted absorption. PL of this polymer is very well structured indicating long conjugated chains and high regioregularity. The 0-0 vibronic transition is very strong, almost equal to the 0-1 transition that is typical of single molecules, suggesting low aggregation of the undoped pure polymer. PLQE is very high, 17%, which can be attributed to intrachain exciton recombination. Photoinduced absorption shows only one PA peak at ~1.06 eV that is due to triplets. PLDMR clearly shows spin-1 triplet powder pattern with both full field and half field resonances. At 1011 Gauss there is another sharp asymmetric resonance due to spin-1/2, but we do not see it in PA. The PLDMR can be the result of both triplet and polaron pair resonances, where shoulders of polaron-pair might be buried in triplet powder pattern, giving us very large D and E zero field splitting parameters. Different saturation behavior of PLDMR with increase microwave power of half field resonance as opposed to the resonance at 1011 G confirms that they are due to different photogenerated species. Under closer inspection of the narrow spin-1/2 resonance we see that it consists of two positive and one negative contribution. Due to the small microwave frequency of our apparatus these contributions cannot be clearly resolved using PLDMR. When using LESR we are able to clearly resolve these contributions and confirm the negative resonance. The negative resonance may be due to nonradiative trapping of polarons by radical ions on the acceptor copolymer, which can be the cause of a large ESR signal.

CHAPTER 4

ACCEPTOR MATERIALS IN ORGANIC PHOTOVOLTAICS

4.1. Introduction

Some of the main requirements for good electron acceptor materials used in bulk heterojuction organic solar cells are large charge carrier mobility, large LUMO energy, and fast interfacial charge separation rates. Fullerene based materials have been thoroughly investigated since their discovery in 1985. The use of C60 as an acceptor in organic solar cell was first reported in 1993 by Sacriftci et al.[5, 61] Fullarenes have many attractive characteristics for OPV, such as a good electron transport and LUMO energy level that is both high enough to support a large Voc but also low enough to provide ohmic contacts for electron extraction and injection from common cathodes. Consequently, they became the acceptor materials of choice for the best performing organic solar cells.[2, 62, 63]

C_{60} exhibits all the desirable characteristics mentioned above, but it is insoluble in common organic solvents. In order to improve its solubility and tune its electronic properties, functional groups such as butyric acid methyl ester are added to its cage structure. Each functional group attached lowers the electron affinity or increases the LUMO energy level of the acceptor by ~100 meV. Like C_{60}, fullerene derivatives tend to aggregate and thereby assist phase segregation in blends with donor materials that is essential for charge separation

in OPVC. In this chapter our studies of PCBM, bis-[60]PCBM, and indene-C60 bisadduct will be presented.

4.2. PCBM

4.2.1. Introduction

In an organic photovoltaic device excitons (usually Frenkel excitons) are formed in the donor materials following light absorption[18]. Exciton dissociation at the donor/acceptor interface is the critical step in harvesting electricity from light [2, 18, 38, 64]. However, it has been shown in the literature that charge separation in an organic material can be achieved without the donor/acceptor interface [18, 65]. Consequently, it is possible to produce OPVC with an active material consisting of PCBM only [66] with the power conversion efficiency up to 2.64%. [67] This is possible if PCBM itself shows phase separation that causes exciton dissociation, or excitons in PCBM dissociate at the interface with the electrodes or the hole transport layer (PEDOT-PSS). In this section we study aggregation of PCBM using optical and magnetic resonance studies of PCBM films and PCBM isolated in polystyrene matrix.

4.2.2. Sample preparation

In order to make a PCBM film 18 mg of PCBM (supplied by Plextronics, Inc.) was dissolved in 1 ml of ortho-dichlorobenzene (ODCB) solvent. The PCBM dispersed in polystyrene was prepared in the following way: 100 mg of polystyrene was dissolved in 10 ml of toluene; and 10 mg of PCBM was dissolved in 10 ml of toluene. Subsequently the polystyrene solution was mixed with the PCBM solution achieving a ratio of 100:1. Samples were prepared by drop casting of the proper

solution on a sapphire substrate for PA measurement, and on a glass substrate for ODMR measurement. The annealing of chosen samples was done in inert nitrogen atmosphere at 150ºC for 30 min.

4.2.3. Optical studies of PCBM film and isolated molecules

PCBM absorbs mainly in the UV region, as shown in Figure 54 resulting in a limited role in light harvesting in an OPVC. The absorption spectrum is mostly featureless.

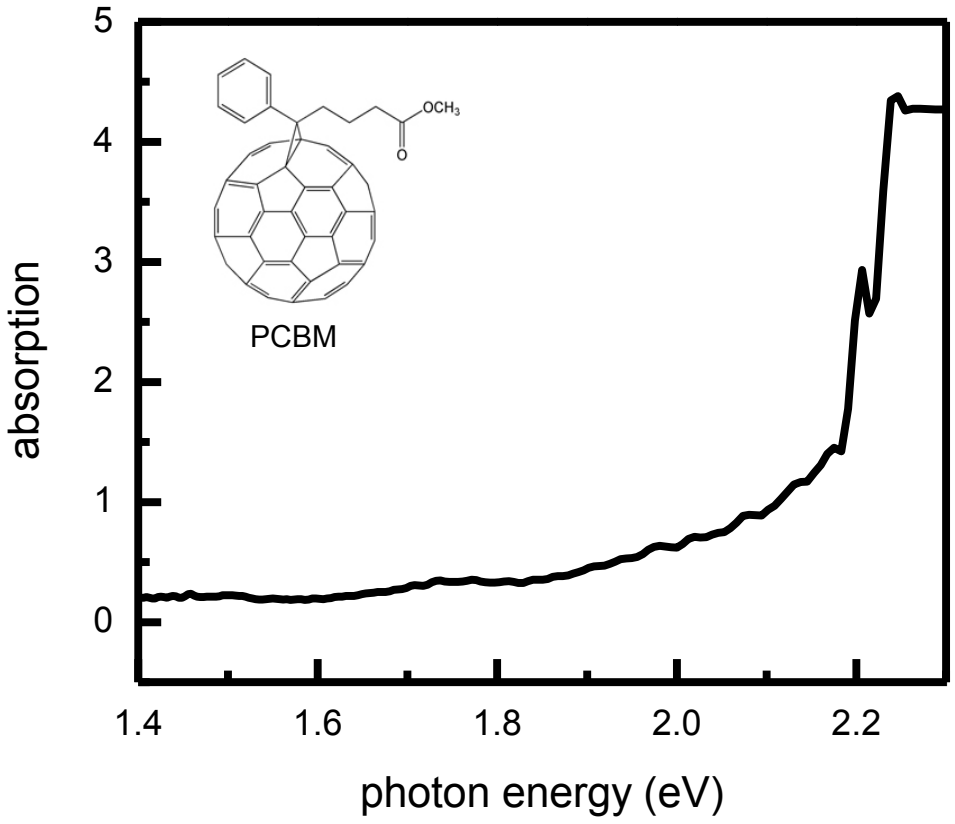

Figure 54 Absorption spectrum of PCBM film at room temperature, and PCBM molecular structure in the inset

Figure 55 shows the PL spectrum of PCBM dispersed in polystyrene. Since the ratio between PCBM and polystyrene is 1:100, this sample can be treated as containing isolated molecules. The PL spectrum confirms this, because the 0-0 vibronic side band is very strong suggesting the lack of aggregation [46, 47]. At ~2.0 eV we see an emission that can be attributed to the interaction of PCBM molecules and polystyrene, as it will be discussed later in this chapter. Consequently, we do not see this emission band in the PCBM film.

Figure 56 shows the PL spectrum of the annealed sample of PCBM isolated molecules. The 0-0 vibronic side band became significantly weaker, causing the ratio between 0-0 and 0-1 vibronic sidebands to decrease, which is an indicative of the formation of aggregates [47]. The emission at 2.0 eV decreases as well.

The well structured PL spectrum of the PCBM film has a dominant 0-1 vibronic side band and almost completely diminished 0-0 band. This provides further evidence for the formation of aggregates, as depicted in Figure 57. Moreover, the PL spectrum of PCBM film has red shifted and has become narrower compared to isolated PCBM molecules as can be seen in Figure 58 , suggesting increased order [47].

In addition to PL, XRD experiment on annealed film of PCBM was done by Dr. Tho Nguyen. The result (Figure 59) further supports the formation of aggregates in the PCBM film.

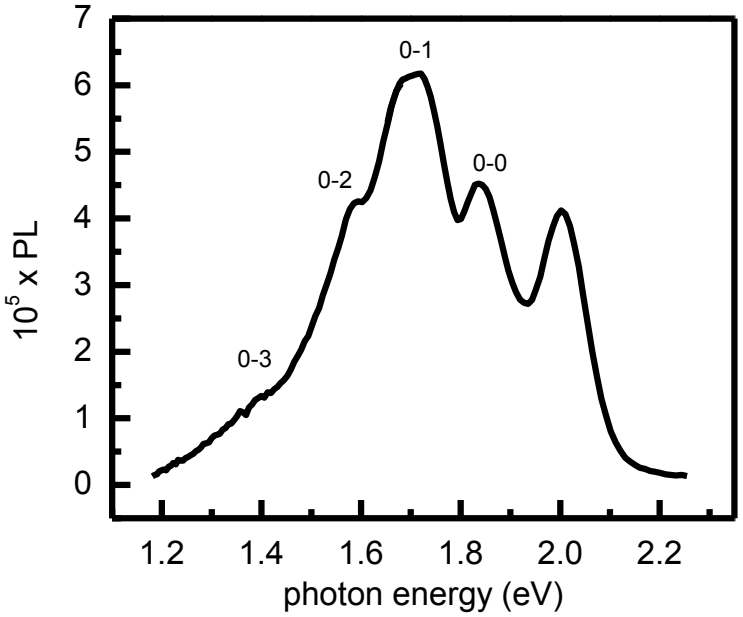

Figure 55 PL spectrum of PCBM dispersed in polystyrene at 45K with assigned vibronic side bands. The ratio between PCBM and polystyrene is 1:100 and therefore PCBM can be treated as isolated molecules. The excitation wavelength was 488 nm and laser power was 100 mW.

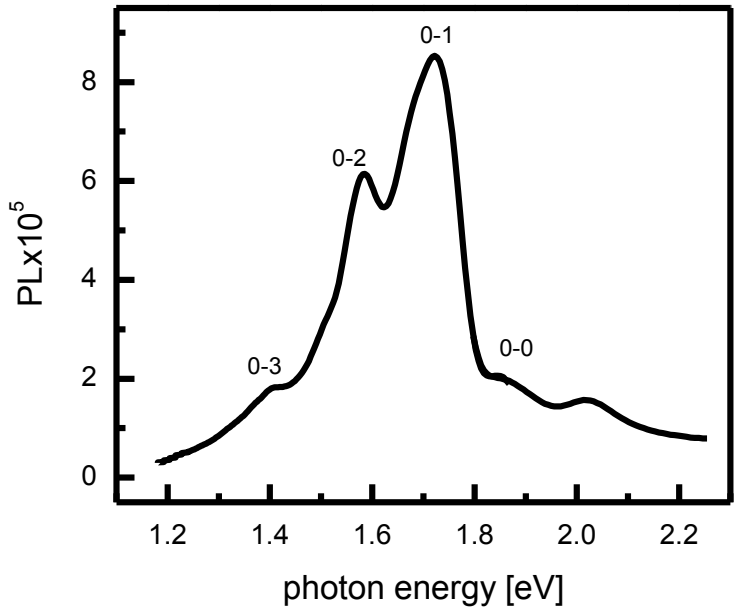

Figure 56 PL spectrum of isolated PCBM molecules in polystyrene, at 45K with the excitation wavelength of 488 and laser power of 100 mW. The sample was annealed at 150ºC for 30 min.

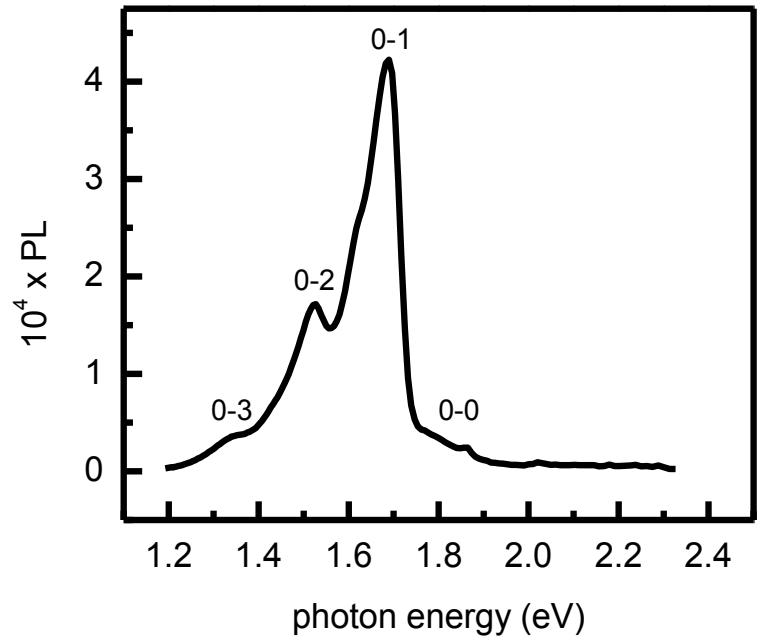

Figure 57 The well resolved PL spectrum of PCBM film at 45K with the excitation wavelength of 457 nm and laser power of 80 mW.

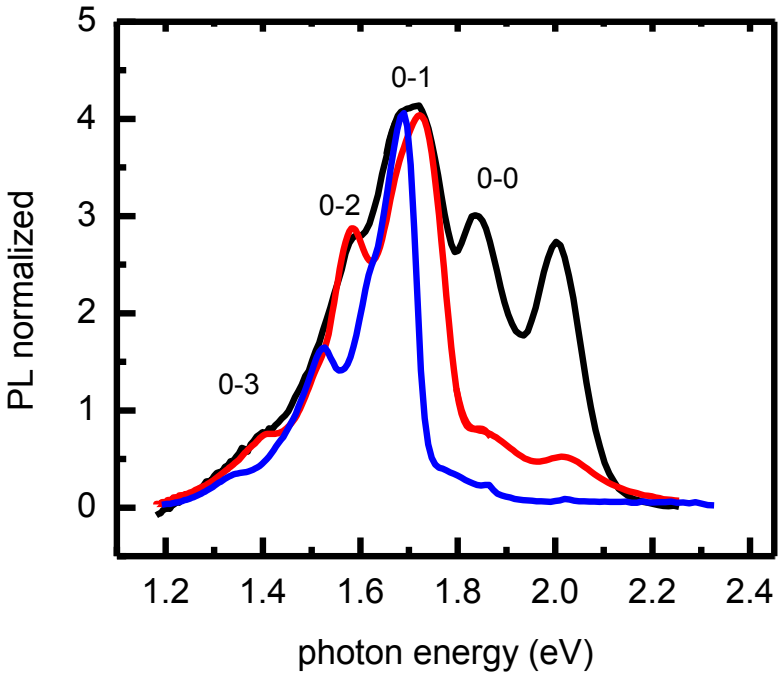

Figure 58 PL spectra of PCBM isolated molecules (black line), annealed sample of isolated PCBM (red line), and PCBM film (black line).

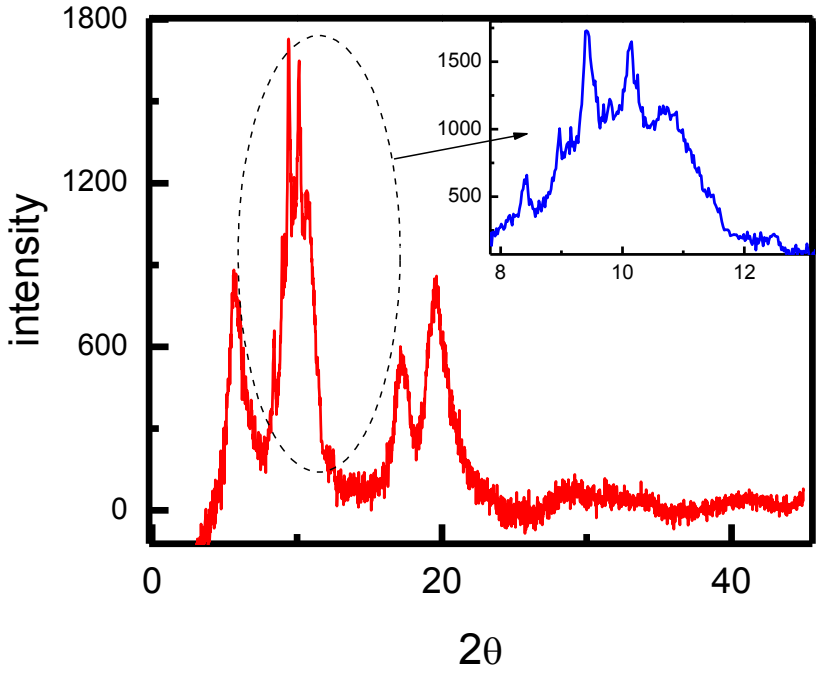

Figure 59 The XRD of annealed film of PCBM supports formation of ~8.5 nm large crystals. Experiment and calculation were done by Dr. Tho Nguyen.

Figure 60 depicts the PA spectrum of PCBM in both isolated and film forms. In isolated PCBM (Figure 60(a)) the spectrum is dominated by a PA band (T1) at ~ 1.7 eV. In the PCBM film, however, the T1 band at ~1.7 eV is accompanied by another PA band (P1) at ~1.2 eV. Based on these measurements we argue that P1 in PCBM film is caused by the aggregation of the PCBM molecules. This indicates that the T1 band is due to a neutral, long-lived excitation specie, which is isolated on the fullerene molecule; thus we conclude it must be due to an exciton. The singlet exciton in fullerene decays in few ns (~5ns in C60) [68] and hence the triplet exciton specie dominates the long-lived photoexcitations [68]. We therefore conclude that the T1 band is due to triplet excitons. The following PADMR measurements give further evidence for this assignment.

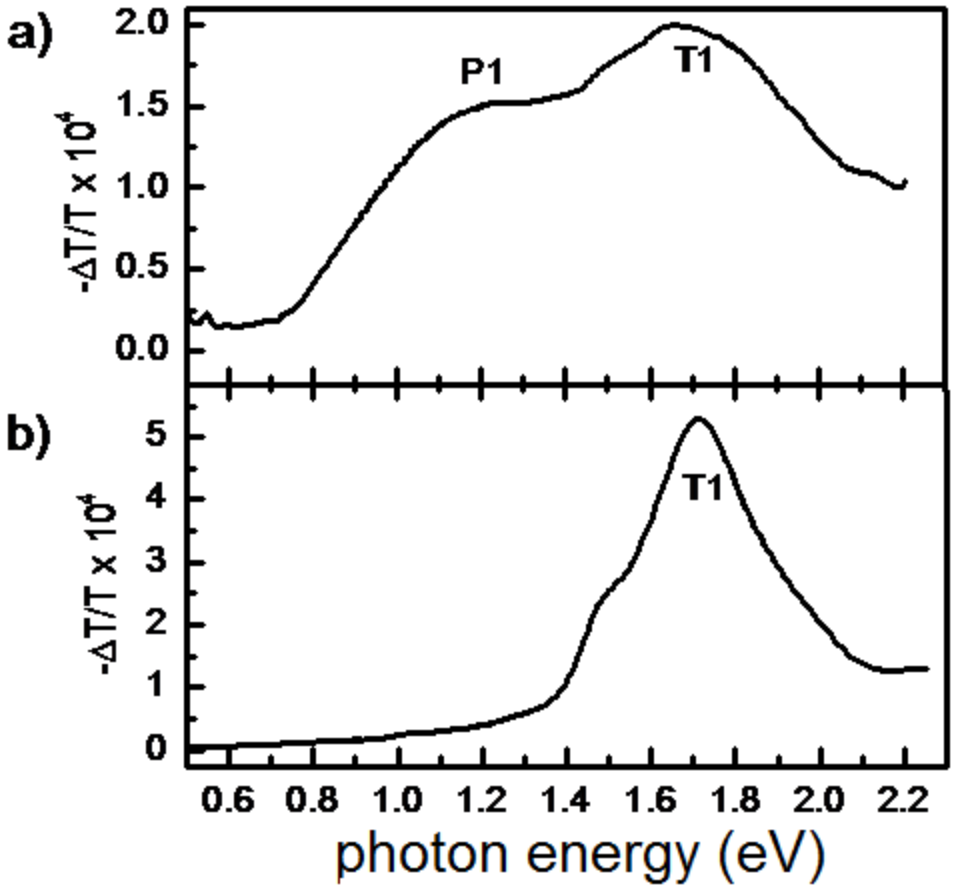

Figure 60 Photoinduced absorption spectrum of PCBM measured at 45 K, excitation photon energy of 2.5 eV, and modulation frequency 300 Hz. a) PCBM film; b) PCBM dispersed in polystyrene matrix.

The frequency dependent PA measurement at 1.7 eV was done at two different laser powers, namely 80 mW (Figure 61) and 400 mW (Figure 62). The dispersive parameter α was found to be ~0.9, and the mean lifetime, τ of triplet exciton changes with the laser power. At 80 mW of the laser power $\tau \approx 0.17$ ms, whereas at 400 mW $\tau \approx 0.084$ ms; the lifetime power dependence suggests bimolecular recombination kinetics due to triplet-triplet annihilation.

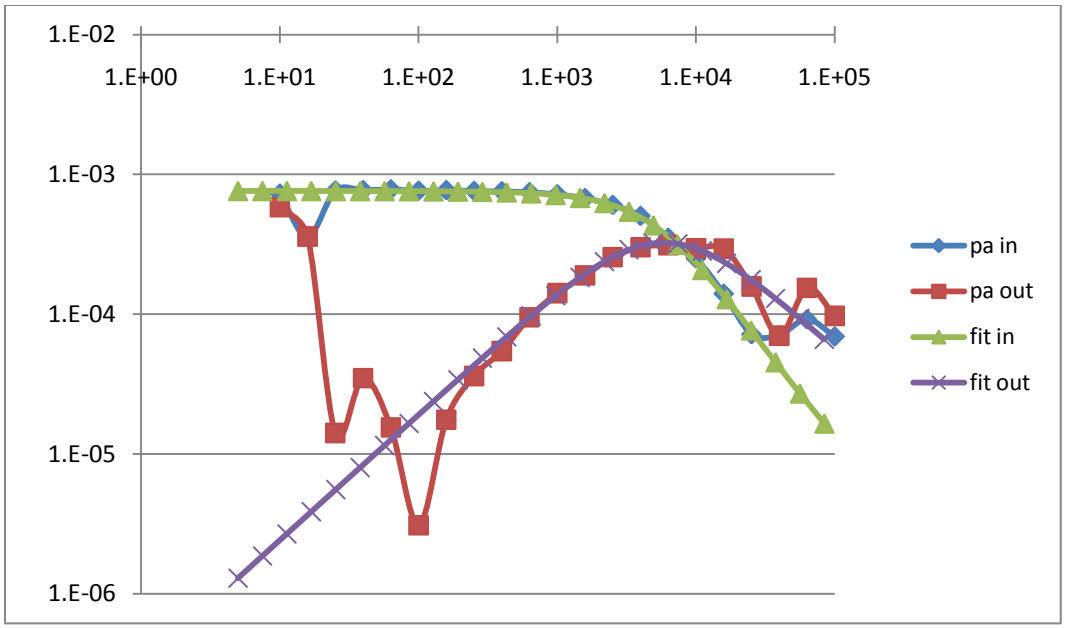

Figure 61 The frequency dependent PA of PCBM film at 1.7 eV. The measurement was done at 45K with excitation wavelength of 488 nm and laser power of 80 mW. The blue and the burgundy curves represent collected data where the green and the purple curves represent the fit according to equation (2.30)

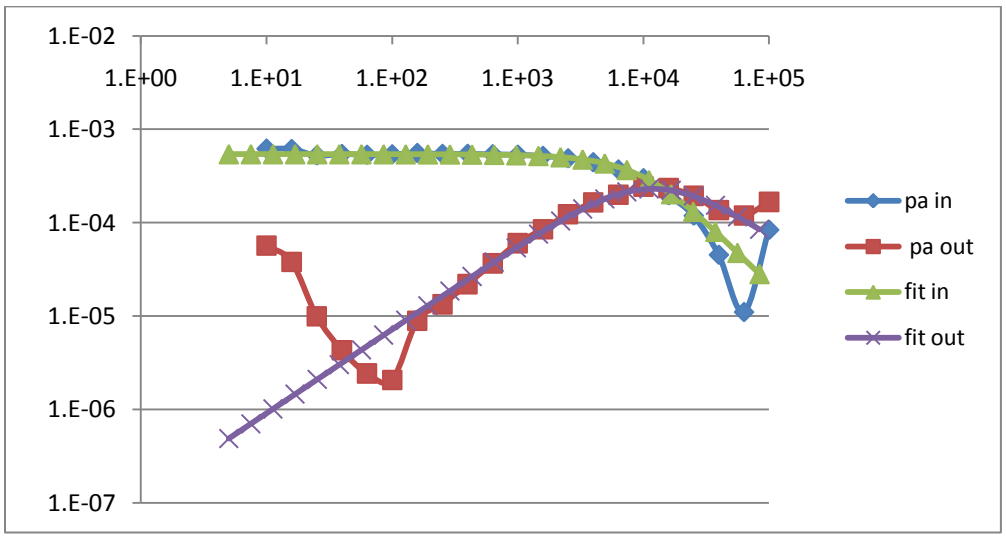

Figure 62 The frequency dependent PA of PCBM film at 1.7 eV, as in Fig. 4.7 but at higher laser power. The measurement was done at 45K with excitation wavelength of 488 nm and laser power of 400 mW. The blue and the burgundy curves represent collected data where the green and the purple curves represent the fit according to Equation (2.30)

4.2.4. Magnetic resonance studies

The H-PADMR spectra (Figure 63) were obtained at 12 K at the probe photon energy of 1.7 eV. The H-PADMR spectrum of PCBM in polystyrene matrix (Figure 63(b)) consists of a 130 Gauss wide triplet powder pattern around g ~ 2. The two observed peaks in the pattern are separated by ~ 84 Gauss, from which we may calculate a zero-field-splitting parameter D ~ 40 Gauss. As expected this H-PADMR corresponds to full field triplet powder pattern, similar to what was observed in C_{60} that was also dispersed in polystyrene[68].

In Figure 63 (a) we see that the full field H-PADMR triplet powder pattern is different from that of isolated PCBM. This is likely due to the spin dynamics that are now allowed in this PCBM form. We can also distinguish a ~ 14 Gauss narrow band at about 1004 Gauss (g ~ 2), which we attribute to polarons having spin ½ [69]. An alternative explanation is that the spin dynamics in the PCBM aggregates conspire to form a triplet powder pattern that contains a sharp peak in the middle. To discern between these two possible explanations we measured the triplet powder pattern at various probe wavelengths. We observed that the broad powder pattern retains its shape; however the narrow superimposed peak changes its amplitude in respect to the broad band as shown in Figure 64. Thus we conclude that the two resonance features do not originate from the same species. We infer that the broad resonance is due to triplet exciton, whereas the narrow resonance is the result of spin ½ polarons, consistent with the appearance of the second PA band (P1) in the photomodulation spectrum.

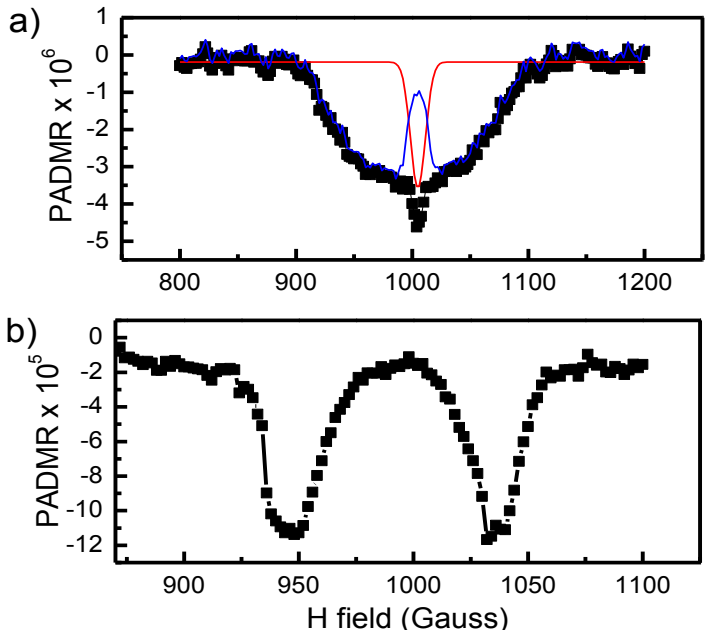

Figure 63 PADMR at 12K, probe energy 1.7eV, 3 GHz microwave cavity modulated at 200 Hz, a) PCBM film; where black squares represent the actual data, red line represents possible fit for spin ½ contribution to the resonance and blue line represents possible spin 1 resonant contribution b) isolated PCBM in polystyrene matrix.

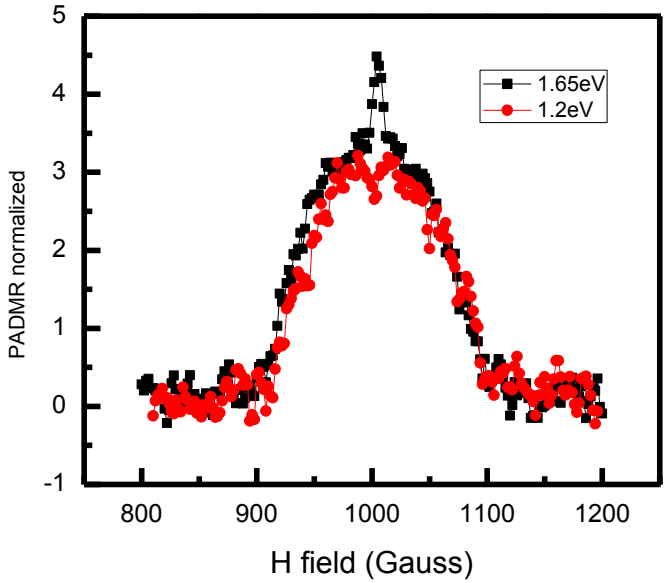

Figure 64 PADMR of PCBM film at two different photon energies, 1.65 and 1.2 corresponding to triplet exciton and polaron PA band, respectively.

4.2.5. Conclusion

In both PCBM film and PCBM dispersed in polystyrene the cw photomodulation spectrum is dominated by a triplet excitons having a PA band at around 1.7 eV. However, we also noticed a distinct polaron band in PCBM film with a PA band at around 1.2 eV. In PADMR we clearly identified spin1 resonance at 1000 Gauss with characteristic triplet powder pattern in both PCBM film and PCBM dispersed in polystyrene; with the addition of a sharp 14 Gauss wide peak in PCBM film, which can be attributed to spin ½ polarons. The PL spectrum of PCBM film shows increased order and aggregation manifested in a narrower spectrum than in PCBM dispersed in PS matrix and diminished 0-0 vibronic side band, respectively. According to our results we can conclude that charge separation can be achieved in a pure PCBM film thanks to the formation of aggregates.

4.3. Bis-PCBM

4.3.1. Introduction

In Chapter 3 we introduced TAES-V, low band gap copolymer, which yields a power conversion efficiency of OPVC up to 7%, when used as a donor material. As previously mentioned, when a low band gap polymer with deeper HOMO is used, it is possible to improve the matching of HOMO-LUMO levels between the donor and the acceptor materials and consequently improve Voc [53, 56, 70-74].

In this chapter the focus will be shifted to the study of acceptor materials. Various strategies have been applied to improve performance of acceptor materials based on fullerene derivatives, such as increasing the optical absorption; improving solubility; improving miscibility with donor materials; and increasing the energy level of the lowest

LUMO [75-78]. Since Voc is a function of the energy difference between HOMO of the donor and LUMO of the acceptor, it is possible to improve performance of an OPVC by raising LUMO of the acceptor. This can be achieved when altering the fullerene cage by the direct addition of multiple functional groups.[62, 79] Figure 65 shows one form of bis-[60] PCBM that has two side-groups, namely two 4-phenyl butyric acid methyl ester groups, added to the fullerene cage.[63] Different forms (regioisomers) are possible when the side-groups are attached to different regions relative to each other. Thus we note that bis-[60]PCBM is actually a mixture of different regioisomers.[80] The LUMO of bis-[60]PCBM is about 100 meV higher than the LUMO of [60]PCBM resulting in higher PCE: 4.5% for bis-[60]PCBM based device compared to 3.8% for [60]PCBM based device [80].

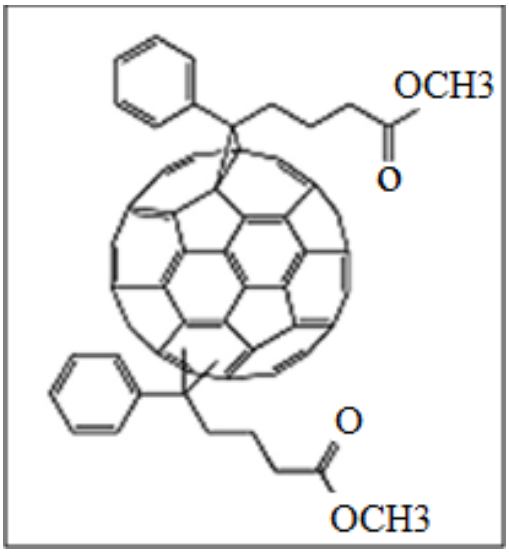

Figure 65 The chemical structure of a regio-isomer of bis-[60]PCBM

4.3.2. Optical and magnetic resonance studies of bis-[60]PCBM

Sample preparation was identical to that of PCBM described above. The bis-PCBM film was dropcasted from a solution made with 18 mg of bis-PCBM (supplied by Plextronics, Inc.) dissolved in 1 ml of ortho-dichlorobenzene (ODCB) solvent. The bis-PCBM dispersed in polystyrene sample was prepared in the same way as PCBM, achieving 1% of bis-PCBM and 99% of PS.

Figure 66 shows the normalized PL spectra of 1% bis-PCBM dispersed in polystyrene (PS) matrix and bis-PCBM film. As expected the PL spectrum of bis-PCBM dispersed in PS is much broader and featureless compared to bis-PCBM film. This phenomenon is consistent with the appearance of aggregation and increased order in films as previously seen in PCBM. However, because of the disorder that caused broadening of the PL spectrum of isolated bis-PCBM molecules the 0-0 and the 0-1 vibronic side bands are not resolved. Using the Franck-Condon principle, equation (3.2) it is possible to resolve these vibronic side bands with the same value of Huang-Rhys factor, S=0.99 for each vibronic side band. Accordingly, we can clearly see that the ratio of the 0-0 to the 0-1 vibronic side bands is larger in the isolated bis-PCBM molecules than in the bis-PCBM film.

Figure 67 shows the PL spectra of bis-PCBM and PCBM films. Compared to the PL of PCBM film, vibronic side bands are not well resolved and the 0-0 vibronic side band is stronger. For this reason, we can conclude that bis-PCBM is less ordered than PCBM, namely forms aggregate to a lesser degree.

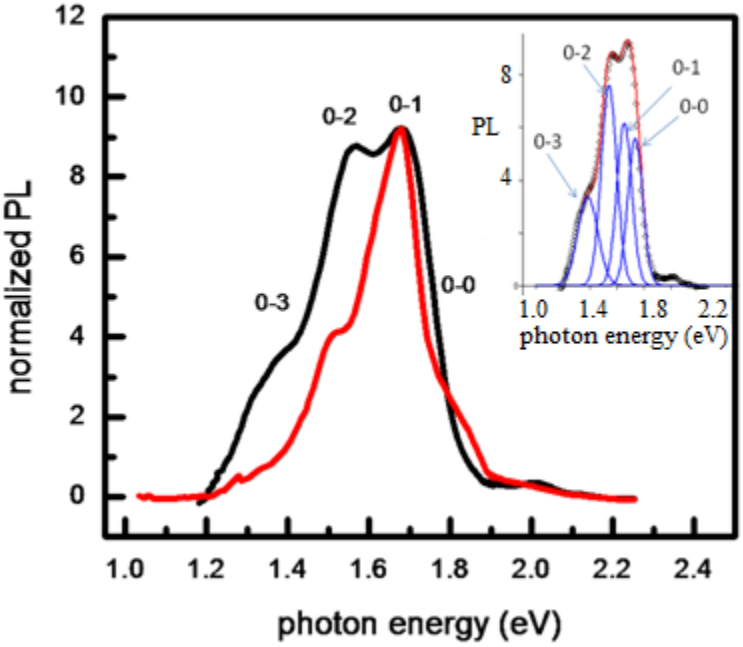

Figure 66 The normalized PL spectra of bis-PCBM dispersed in PS matrix (black) and bis-PCBM film (red). Inset shows the PL spectrum and resolved vibronic side bands of bis-PCBM, fit according to Franck-Condon principle.

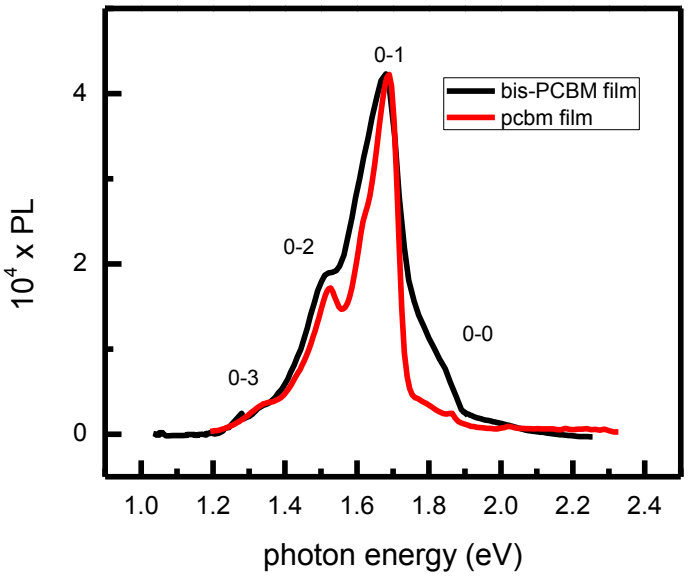

Figure 67 Normalized PL spectra of bis-PCBM (black) and PCBM (red) films at 488 nm excitation wavelength, 100 mW laser power at 50K

The PA spectrum of bis-PCBM dispersed in PS matrix (Figure 68) is dominated by a PA band at ~1.65 eV. We suspect this is due to triplet exciton. Similarly to PCBM film, the PA spectrum of bis-PCBM film has one more PA band that appears at ~1.2 eV (Figure 69). Based on this similarity, the PA band at ~1.2 eV is attributed to spin ½ polaron. PADMR of bis-PCBM confirms this assignment, as seen in Figure 70. Accordingly, PADMR consists of ~200 Gauss wide full field triplet powder pattern and one more resonance contribution due to spin ½, as suggested in the inset of Figure 70. Hence the triplet exciton is the dominant feature of the PA spectrum in both isolated molecules and film.

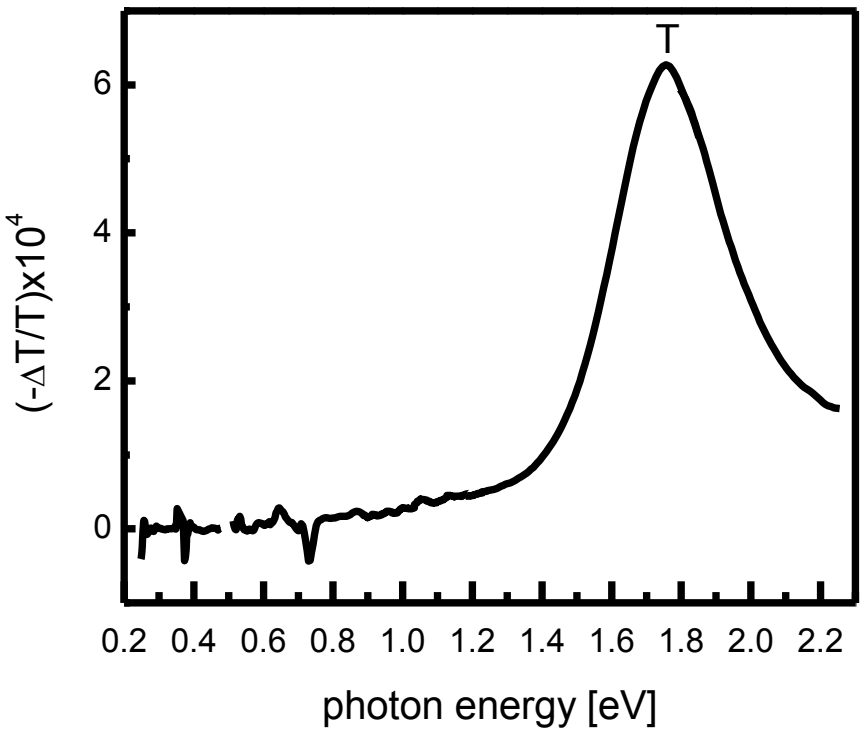

Figure 68 The PA spectra of bis-PCBM dispersed in PS matrix (1:100 weight ratio) with a dominant triplet exciton PA band at 1.75 eV. The measurement was done at 45K with 488 nm excitation wavelength and 150 mW laser power.

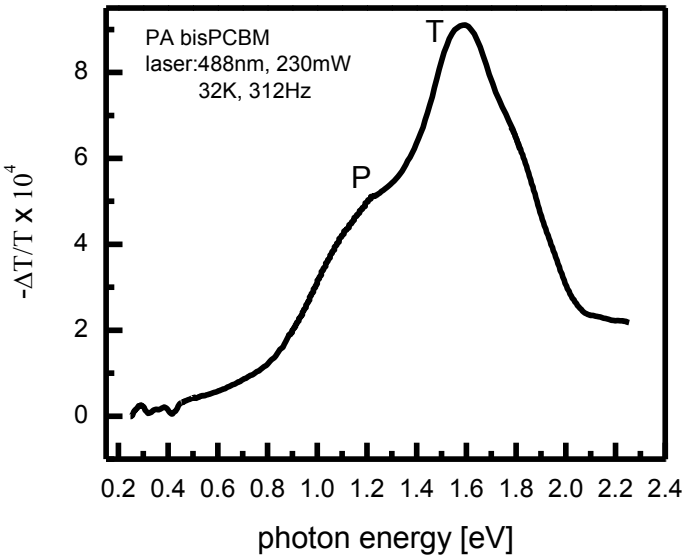

Figure 69 The PA spectrum of bis-PCBM film with additional PA band at ~1.2 eV. The measurement was done at 32 K, with 488 nm excitation wavelength, and 230 mW laser power.

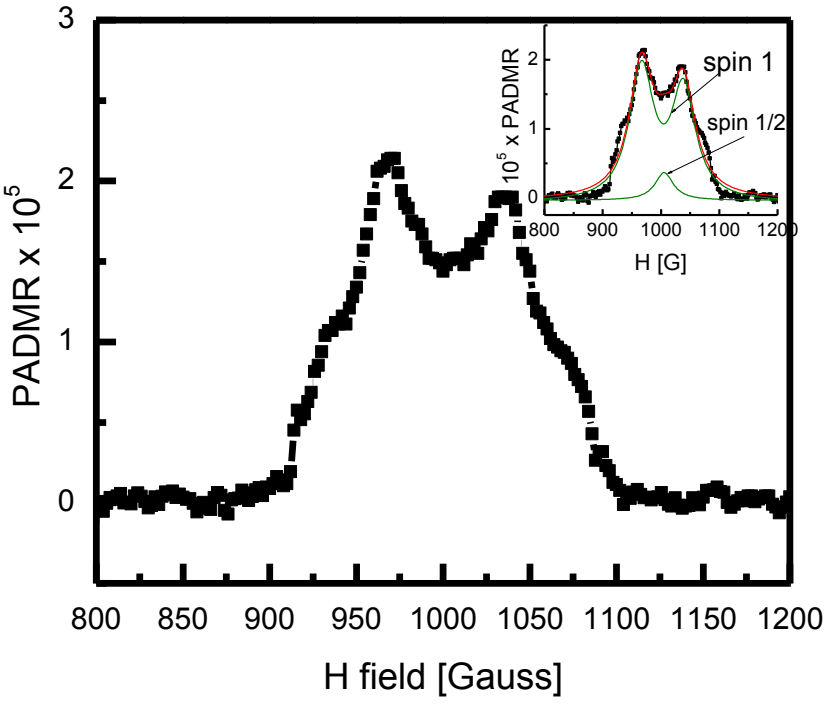

Figure 70 **H**-PADMR spectrum of bis-PCBM film measured at 1.65 eV. The inset shows the possible contributions of the spin 1 and spin ½ resonances.

The frequency dependent PA measurement at ~1.65 eV was taken at two laser powers, namely 100 mW (Figure 71) and 400 mW (Figure 72). Using equation (2.30) we found that the dispersive parameter in bis – PCBM is $\alpha \approx 0.92$, which is close to that in PCBM films. Furthermore, we found that the triplet exciton mean lifetime changes with the laser power. As the laser power is increased from 100 mW to 400 mW, the triplet mean lifetime decreases from $\tau = 0.17$ ms to $\tau = 0.054$ ms, showing that there is a large component of bimolecular recombination kinetics in bis-PCBM films.

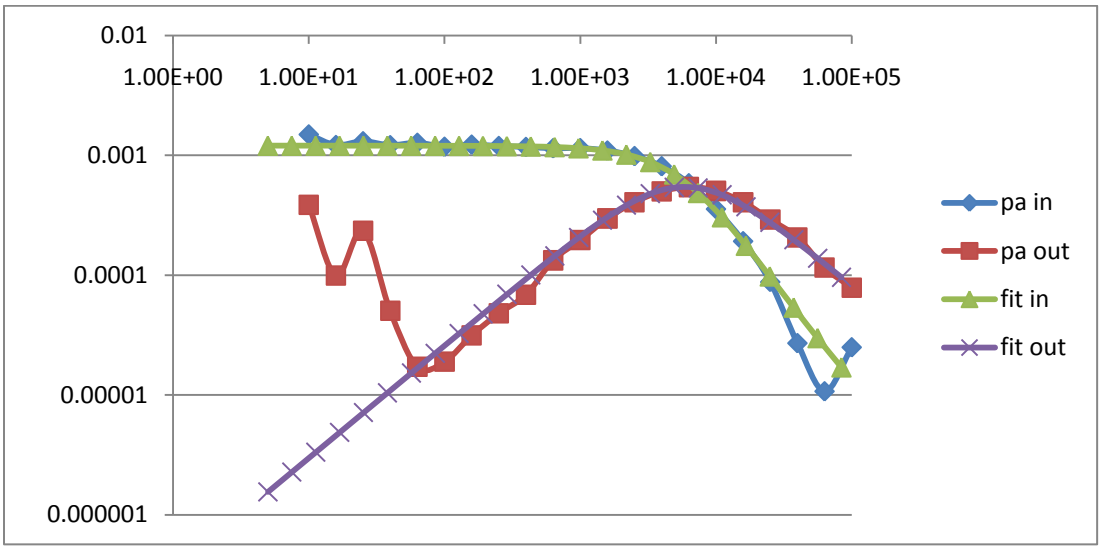

Figure 71 The frequency dependent measurement of the PA band at ~1.65eV. Laser power was 100mW and the excitation wavelength used was 488nm and temperature was 32K . The blue and the burgundy curves represent the measured data and the green and the purple lines represent the fit. The mean lifetime of triplet exciton was calculated $\tau = 0.17$ms.

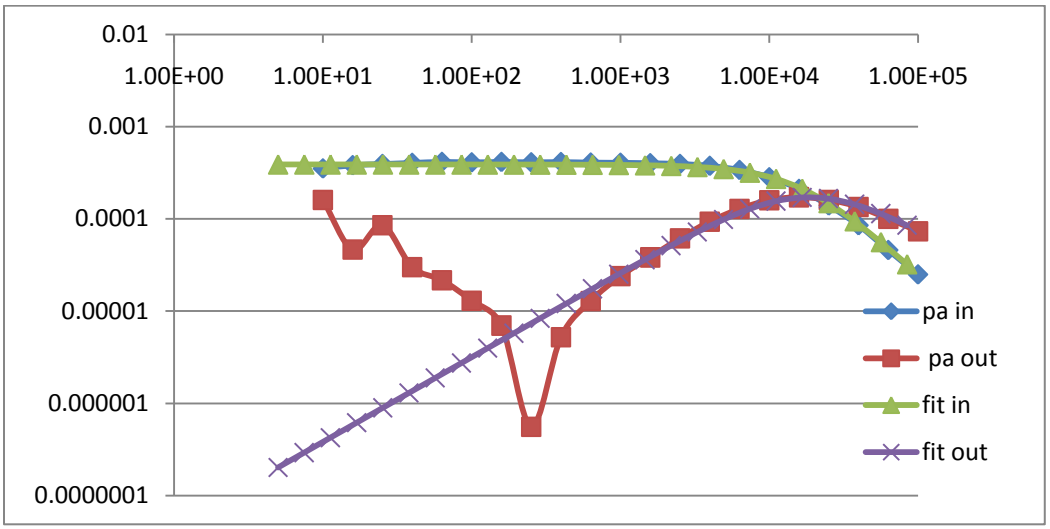

Figure 72 The frequency dependent measurement of the PA band at ~1.65 eV. The laser power was 400 mW and the excitation wavelength was 488 nm at 32 K. The blue and the burgundy lines represent the measured data and the green and the purple lines represent the fit. The mean lifetime of triplet exciton was calculated to be τ=0.054ms and α=0.9.

4.3.3. Conclusion

With the addition of two functional groups to the C_{60} cage and synthesizing a new fullerene derivative bis-PCBM, it is possible to raise LUMO level by 100 meV and improve the performance of organic solar cells. Our optical and magnetic resonance studies show that bis-PCBM is very similar to PCBM. The PM spectrum is dominated by triplet excitons, but in films, because of the formation of aggregates, we see an additional band due to photogeneration of polarons. The PADMR results confirm the assignment of the PA bands.

However, the PL spectrum of bis-PCBM shows a lower degree of order than in the PCBM film. This indicates that the additional side-chains might disrupt building of aggregates to some degree. Consequently, the field effect electron mobility in bis-PCBM,

$(2.7\pm0.3)\ x10^{-3}\ cm^2/Vsec$ is somewhat lower than in PCBM film $(4.0\pm0.4)\ x10^{-2}\ cm^2/Vsec$. [62] Moreover, bis-PCBM is a mixture of different isomers with a large variation of energy levels, which might result in a LUMO that is not well defined. [81] This energetic disorder decreases charge carriers' mobility through trapping and directly hinders performance of organic solar cell.

4.4. Indene-C_{60} bisadduct

4.4.1. Introduction

PCBM has many advantages, such as good solubility in organic solvents, considerably high electron mobility and electron affinity, that make it a preferable acceptor in organic photovoltaic applications [2, 82-84]. However, PCBM has a weak absorption in the visible and near IR region that limits its role in light harvesting. In addition, PCBM has a relatively low LUMO energy level resulting in lower than optimal Voc[85].

For this reason, many methods were used to synthesize a fullerene derivative that would have stronger absorption in the visible region and a higher LUMO level than PCBM [62, 63, 86, 87]. One of the approaches to raising the LUMO levels is the addition of functional side groups to the fullerene cage. As discussed above, the addition of just one functional group can increase LUMO energy level by 100 meV. Consequently, bis-PCBM yields higher Voc and significantly better performing organic solar cells. However, if we would like to further increase the LUMO level, adding more than two functional groups is not the solution. In the case of tris-PCBM, three functional groups affect the microstructure of the film. As a result, the electron transport is significantly reduced, [mobility of $(5.5\pm0.5)\ x\ 10^{-6}$] , due to high disorder of the fullerene phase[63].

Indene – C_{60} bisadduct (ICBA) has been introduced to us by our collaborators Plextronics, Inc. This is a fullerene derivative that has a 170 meV higher LUMO than PCBM. The OPVCs with an active material consisting of RR P3HT and ICBA blend yield high Voc of ~0.84 V and a PCE as high as 6.48%. [63, 88] ICBA is easily synthesized from C60 and indene as shown in Figure 73 and reported by Y.J. He et al.[89, 90].

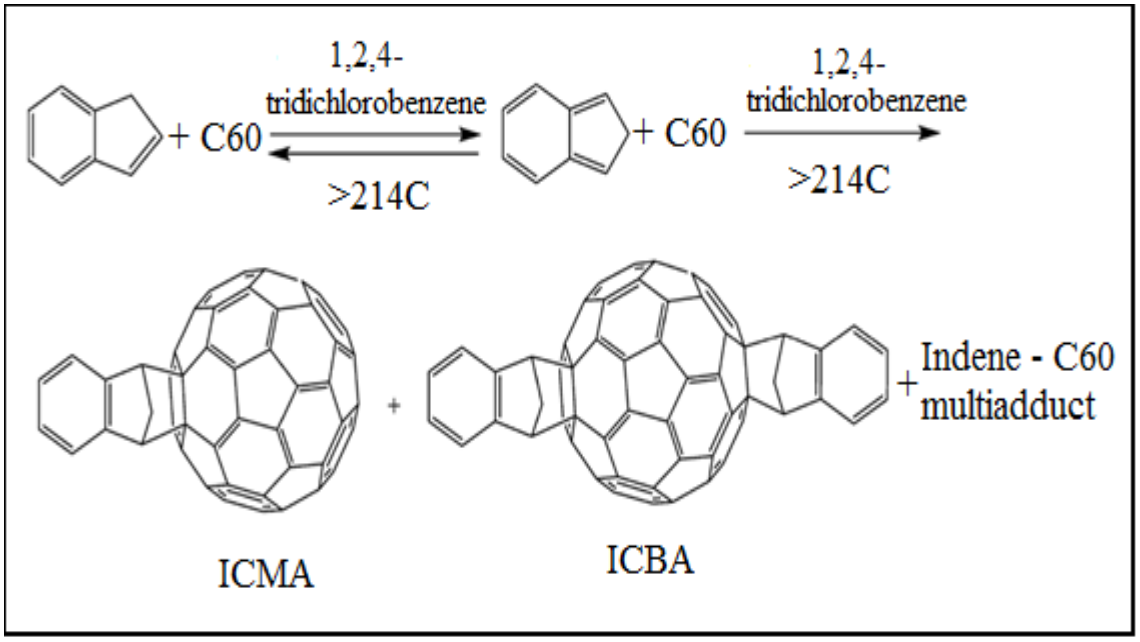

Figure 73 Synthesis of ICBA molecule from C_{60} and indene. Figure adopted from reference [89].

4.4.3. Optical and magnetic resonance studies

Besides the higher LUMO, ICBA also exhibits better solubility in organic solvents and has stronger absorption in the visible region compared to PCBM. The absorption spectra of ICBA, ICMA (Indene-C60 monoadduct), and PCBM are shown in Figure 74. The inset shows that ICBA has much stronger absorption above ~ 300 nm than PCBM, and an absorption tail up to 750 nm. This definitely plays a significant role in the light harvesting.

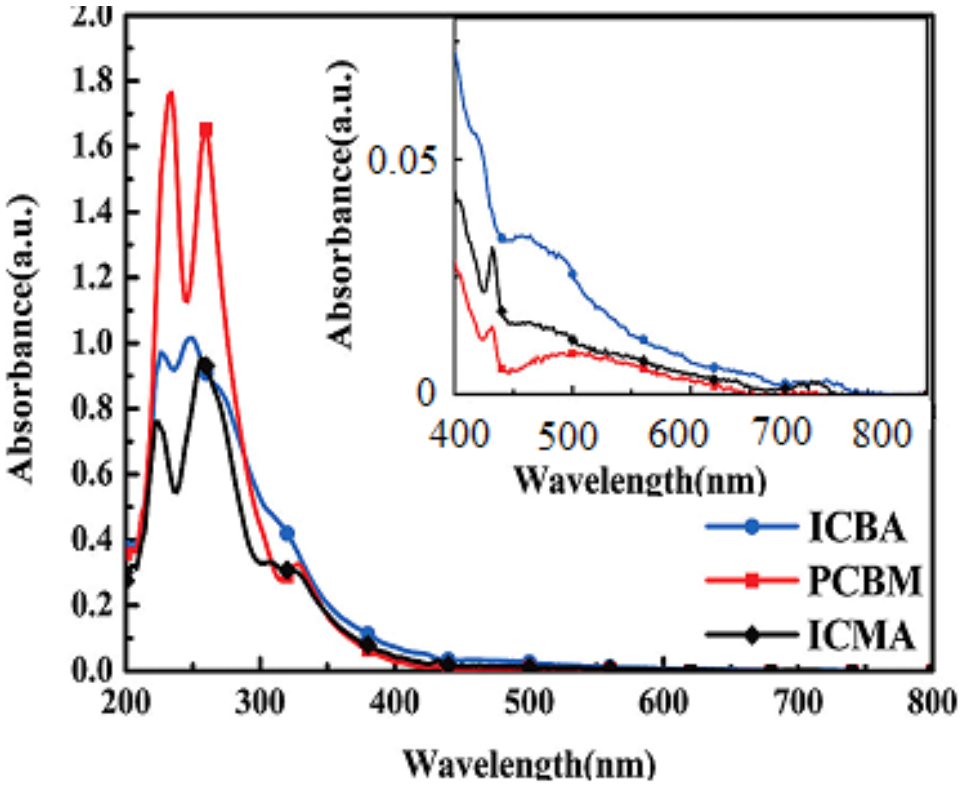

Figure 74 Absorption of ICMA (Indene-C60 monoadduct), ICBA, and PCBM. Figure adapted from reference[89].

The photoluminescence spectrum of the ICBA film (Figure 75)is similar to that in PCBM film, except that the spectrum is somewhat narrower and is just slightly red shifted (0.01-0.02 eV) . The ICBA film might have a higher degree of order than the PCBM film due to the geometry of its molecule and ability for closer packing than in PCBM. Consistent with previous measurements the photoluminescence spectrum of the film is narrower and slightly more red shifted than in ICBA dispersed in PS matrix (Figure 76). In contrast to Bradley et al. [65], we see the beginning of an additional high-energy emission at ~1.95 eV in ICBA dispersed in polystyrene, and surprisingly not in the film. Bradley sees this additional emission band peaking at ~2.5 eV in films of PCBM and attributes it to emission of CT state that arises from the formation of aggregates in the PCBM films. [65] From literature it is known that C_{60} molecules do interact with polystyrene. [91, 92] Bis-PCBM has two functional groups attached to C_{60} cage that prevent hybridization of the molecules with polystyrene, and interestingly enough we see considerably weaker emission than in PCBM molecules at ~2 eV. However, ICBA has different geometry. From comparison of the PL spectra we see that ICBA molecules have the capability of closer packing than PCBM molecules, so it is very likely that this additional emission is due to interaction between ICBA and polystyrene. Furthermore, in work of Polotskaya et al., it was suggested that at the temperature when PS is in a high-elastic state, the destruction of fullerene clusters facilitates the formation of PS–C_{60} aggregates.[93] This is consistent with our preparation of isolated molecules of a fullerene derivative; we dissolved PS in toluene at a high temperature, and then mixed it with fullerene solution at 50ºC.

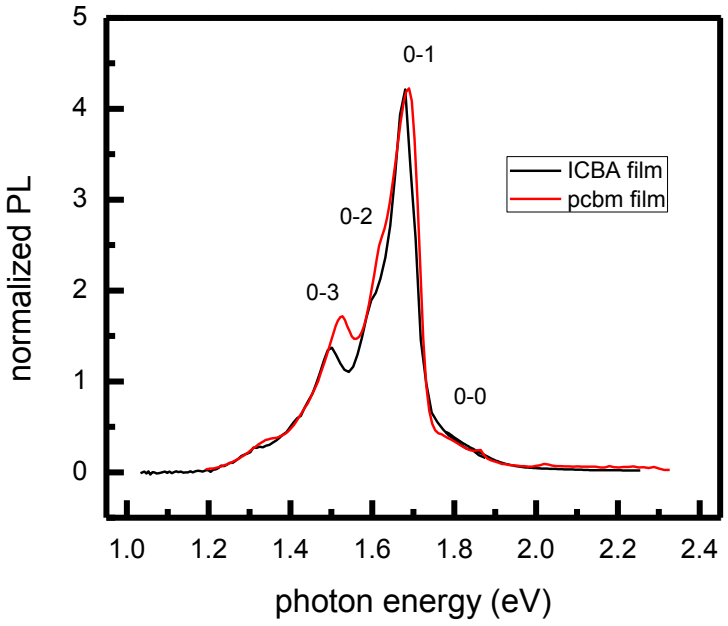

Figure 75 The normalized PL spectra of the ICBA film (black) compared to that in PCBM film (red) at 40 K with vibronic side bands as assigned.

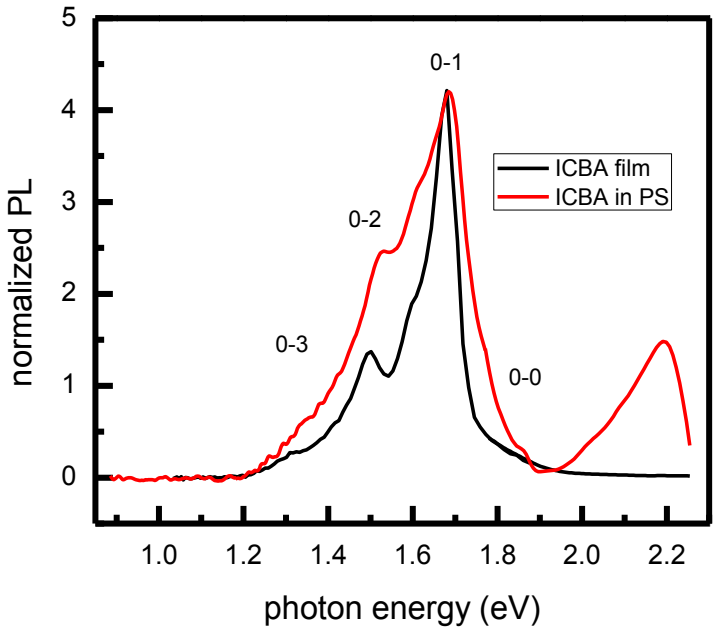

Figure 76 The normalized PL spectra of the ICBA film and ICBA dispersed in PS matrix measured at 50 K.

The PA spectra of the ICBA film and dispersed in PS are shown in Figure 77. Similarly to PCBM and bis-PCBM the PA spectrum of the ICBA dispersed in PS is dominated by a triplet PA band. This PA band assignment is confirmed by PADMR measurement where we see spin 1 triplet powder pattern resonance (Figure 78). The separation between two triplet resonance peaks is ~54 Gauss resulting in zero-field splitting parameters D≈27 Gauss and E≈6 Gauss. The smaller value of D for ICBA is consistent with higher lying excited triplet state (~1.8 eV) compared to PCBM (~1.72 eV)[94] . The PADMR of the ICBA film has two resonance contributions: the broad ~200 Gauss wide resonance coming from spin 1 triplet exciton and ~15 Gauss narrow spin ½ resonance centered at ~1000 Gauss due to polaron. The intensity of the narrow resonance changes with probe energy as shown in the inset of Figure 79, further confirming that these two resonances are not due to the same species.

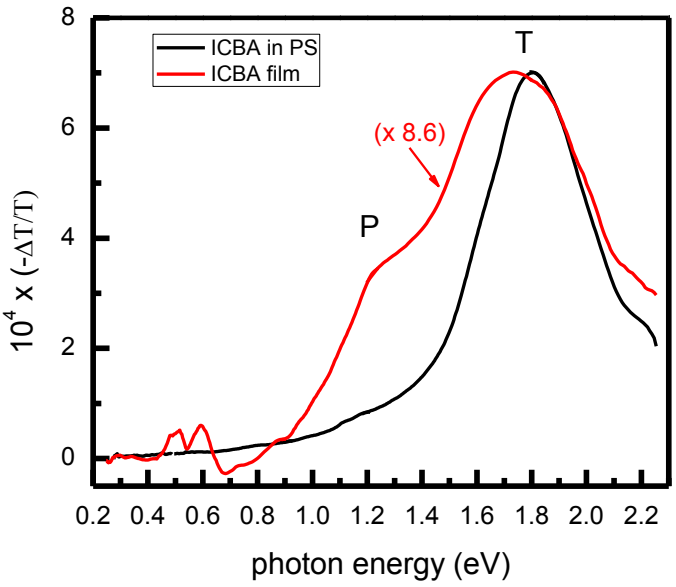

Figure 77 The PA spectra of ICBA film (black) and dispersed in PS (red) at 50 K. The excitation wavelength was 488 nm at power of100 mW.

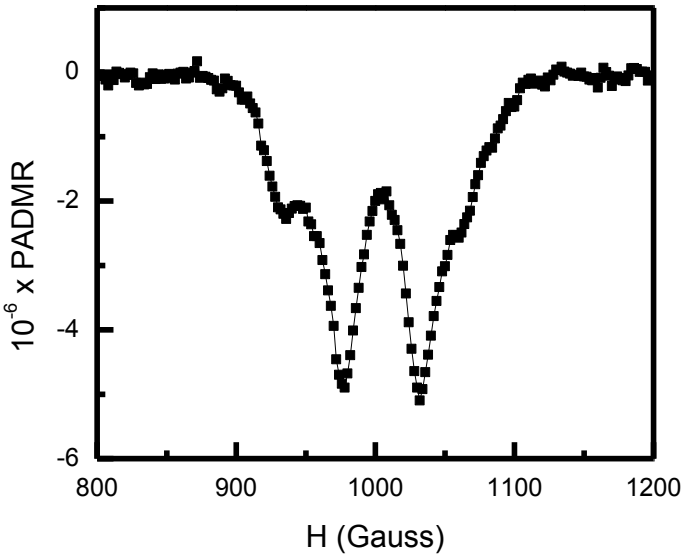

Figure 78 The H-PADMR spectrum of ICBA dispersed in polystyrene measured at 1.65 eV that shows the spin 1 triplet powder pattern at 10K.

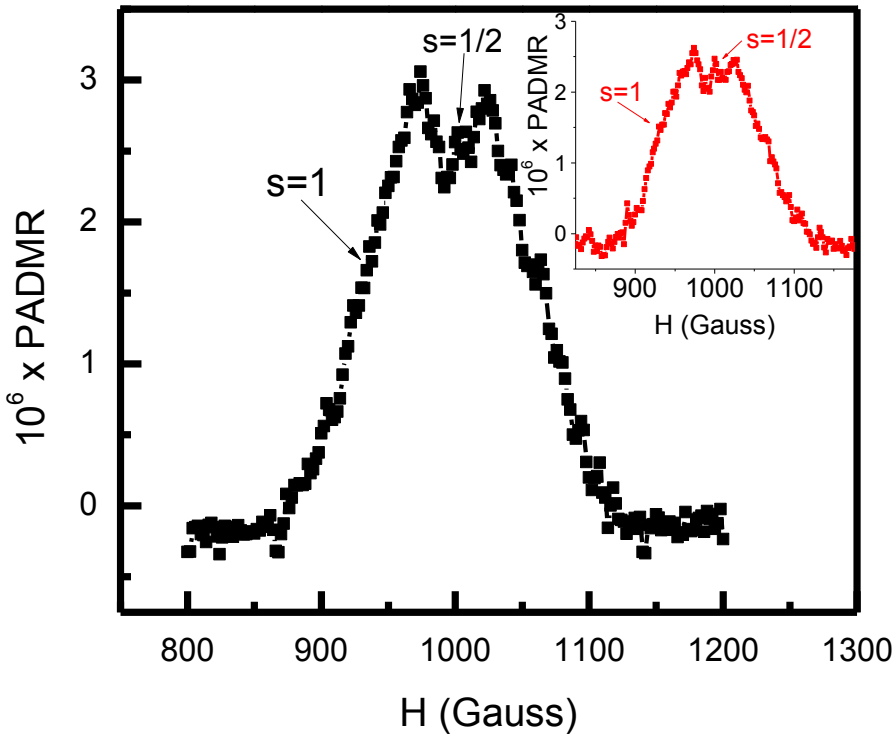

Figure 79 The H-PADMR resonance of ICBA film at 1.8 eV (1.25 eV in the inset). Measurements were done at 10K.

To analyze the dynamics of these two photoexcitations, namely the triplet exciton and polaron that appear in the PA of the ICBA film, we performed frequency dependent PA at two different excitation powers, namely 88 mW (Figure 80) and 300 mW (Figure 81). The triplet mean lifetime decreases from 0.012 ms to 0.009 ms, and the polaron lifetime decreases from 0.013 ms to 0.009 ms. The dispersive parameter, α of ICBA film, was calculated to be ~ 0.86.

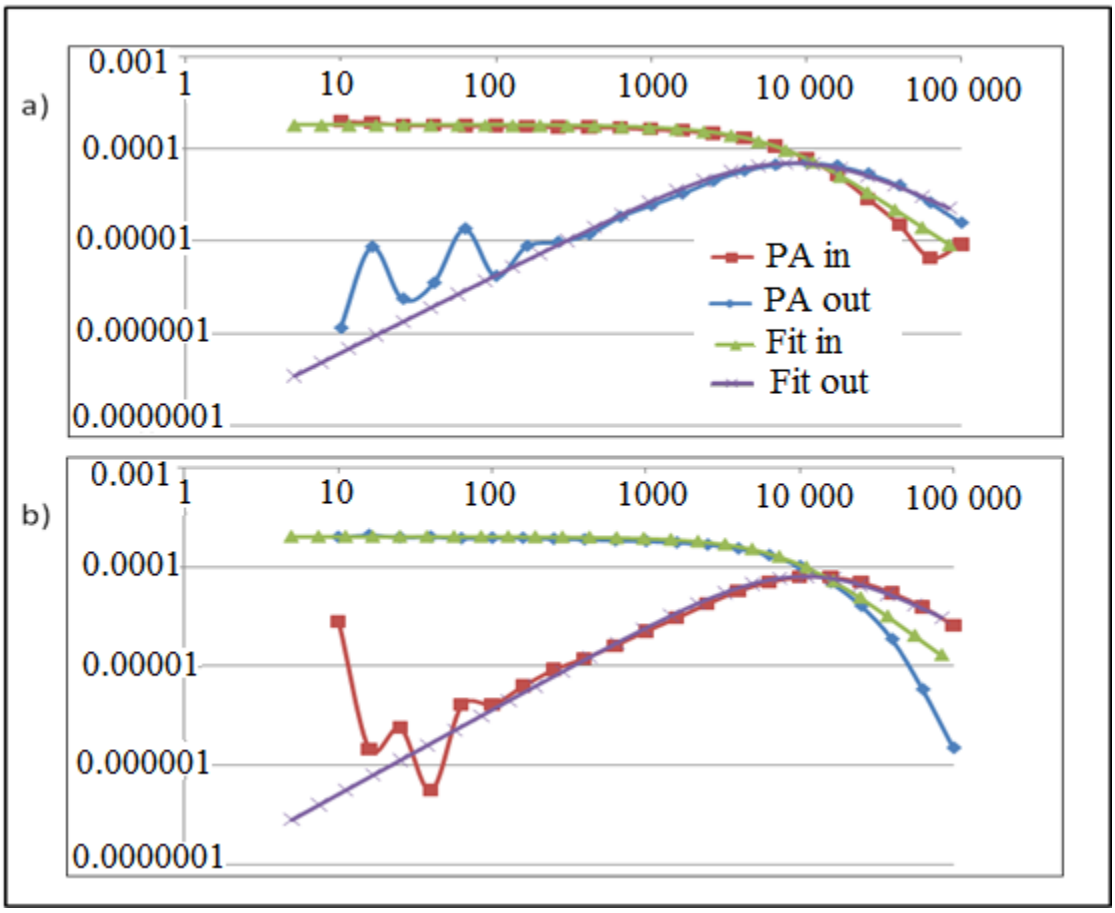

Figure 80 The PA at 1.73 eV as a function of frequency at different laser powers, a) 88 mW and b) 300 mW.

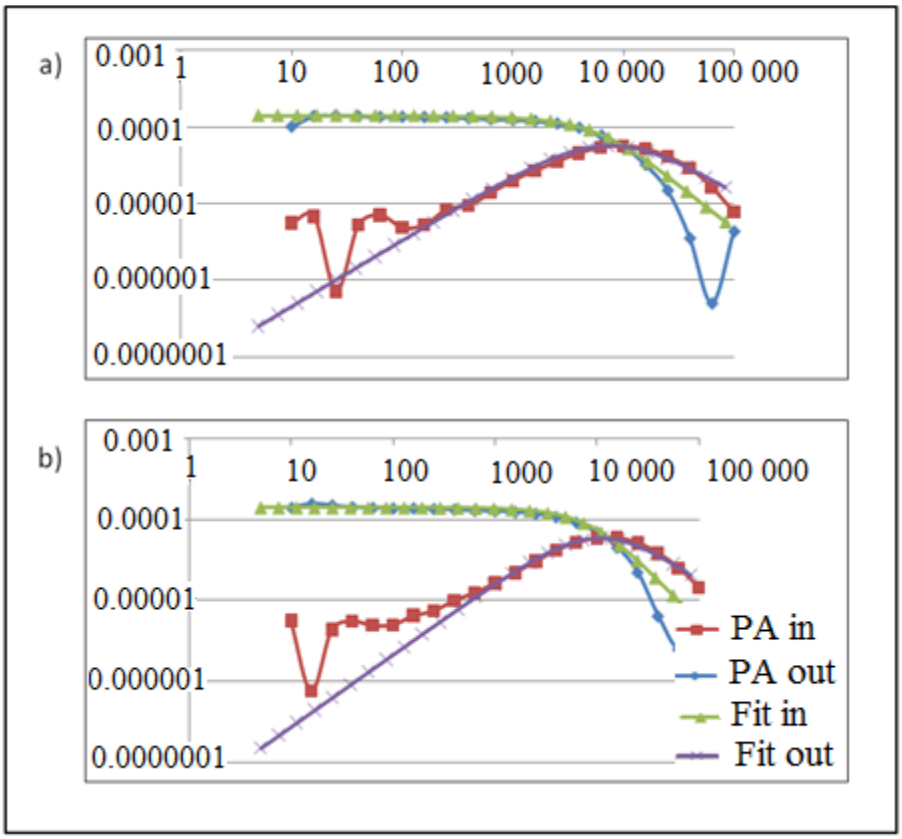

Figure 81 The PA at 1.24 eV as a function of frequency at different laser powers, a) 88 mW and b) 300 mW.

4.4.3. Conclusion

ICBA is an easily synthesized fullerene derivative that has a better absorption in the visible region and significantly higher LUMO energy level than PCBM. Consequently, it yields better performing organic solar cells. According to its well structured and narrow PL spectrum, ICBA forms the aggregates to a greater degree than PCBM because of the geometry of the ICBA molecule, which enables closer packing in films. The PA of ICBA is dominated by the triplet exciton PA band. Formation of aggregates in films results in another long lived excitation due to polaron. The PADMR results support this PA bands assignment. We found that there are two contributions to

PADMR resonance, a broad ~200 wide Gauss resonance due to the spin 1 triplet exciton and a narrow ~15 Gauss wide spin ½ resonance due to the polaron. At different probe energies the broad resonance stays the same, whereas the narrow resonance changes its intensity. This further supports our claim that these two resonances do not originate from the same species.

4.5. General Conclusion

In this chapter we presented our results of optical and magnetic resonance studies of three fullerene derivatives: PCBM, bis-PCBM and ICBA. Depending on their absorption and LUMO energy level they produce OPVCs with largely different PCE. We learned that the absorption and the LUMO of a fullerene derivative can be changed by altering its molecular structure. The addition of functional side groups to the PCBM cage can significantly raise its LUMO level; however, it affects the film morphology. The addition of more than two functional groups hinders the aggregation in films, and consequently also the charge transport. The drawback of PCBM multiadducts is that they form a mixture of few isomers, and therefore the LUMO level is not well defined. It is possible to decrease the number of isomers in bis-PCBM but it is a complicated and expensive task [81, 95]. The easier approach is to synthesize a new fullerene derivative with shorter side chains that would not disrupt the packing of molecules and the aggregation[81] such as ICBA. ICBA is a fullerene derivative where two indene side groups are added to the C60 cage. Its superiority over PCBM is reflected in better solubility, broader absorption in the visible region, the higher LUMO energy level, the capability in closer molecule packing and the more distinct phase separation.

CHAPTER 5

POLYMER / FULLERENE BLENDS

5.1. Introduction

The active organic layer in bulk heterojunction (BHJ) solar cells consists of a blend of an organic donor and acceptor materials. One of the reasons for BHJ architecture is the relatively high exciton binding energy in π-conjugated polymers. Thus upon light illumination and absorption, rather than formation of free charge carriers (like the case for inorganic semiconductors), intrachain excitons are photogenerated. By blending acceptor with donor materials, it becomes energetically favorable for electrons to transfer from the donor to the acceptor material, thereby overcoming the exciton binding energy. For a successful electron transfer reaction, the LUMO of the acceptor should be lower by 0.3-0.5 eV than the LUMO of the donor [79, 96].

The RR P3HT/PCBM blend has been one of the most successful active blend materials giving one of the best power conversion efficiencies of organic solar cells[3]. Irwin et al. achieved the best power conversion efficiency for this blend based solar cell of 5.2%.[97] However, the offset between the LUMO of RR P3HT and the LUMO of PCBM is 1.1 eV, and this results in less than optimal open circuit voltage. There are two main approaches to reduce this energy offset, either by lowering LUMO of the donor, or raising it at the acceptor side (as discussed in Chapters 3 and 4).

In this chapter we will present the study of RR P3HT/PCBM blend, and also the investigation of three different blends, where either the donor or the acceptor has been chosen to achieve the optimal energy offset as required for obtaining large V_0.

5.2. P3HT / PCBM blend

5.2.1. Introduction

In the last 10 years the blends of polythiophenes and fullerenes have received a lot of attention [57]. Poly-alkyl-thiophenes were one of the first conjugated systems studied for use in organic solar cells. [98] Schilinsky et al. in 2002 made considerable progress with an OPVC based on the RR P3HT/PCBM blends achieving a PCE of 2.8% [99]. Since then a lot of efforts were spent on understanding the photophysics of this blend in order to improve performance of solar cells. Within three years, the efficiency of RR P3HT/PCBM cell was increased to the 5% level [84].

This large increase in PCE was partially caused by changing the morphology of the film by annealing [100]. The annealing process enhances the charge carrier mobility [101], and changes the recombination process from Langevin type into a non-Langevin type, which is about 10^3 times slower[102]. This is because of two-dimensional Langevin recombination taking place in the lamellar structure of RR P3HT [103]. The annealing process is considered to take place in the following way: the high temperature softens the P3HT matrix, which allows PCBM molecules to diffuse out of disordered P3HT clusters, to form larger fullerene aggregates. The PCBM-free P3HT matrix recrystallizes into larger fibrillar type crystalites, that are embedded in a matrix consisting of PCBM nano-crystals and amorphous P3HT.[3] Our X-ray investigation supports this microscopic picture of the annealing process (Figure 82).

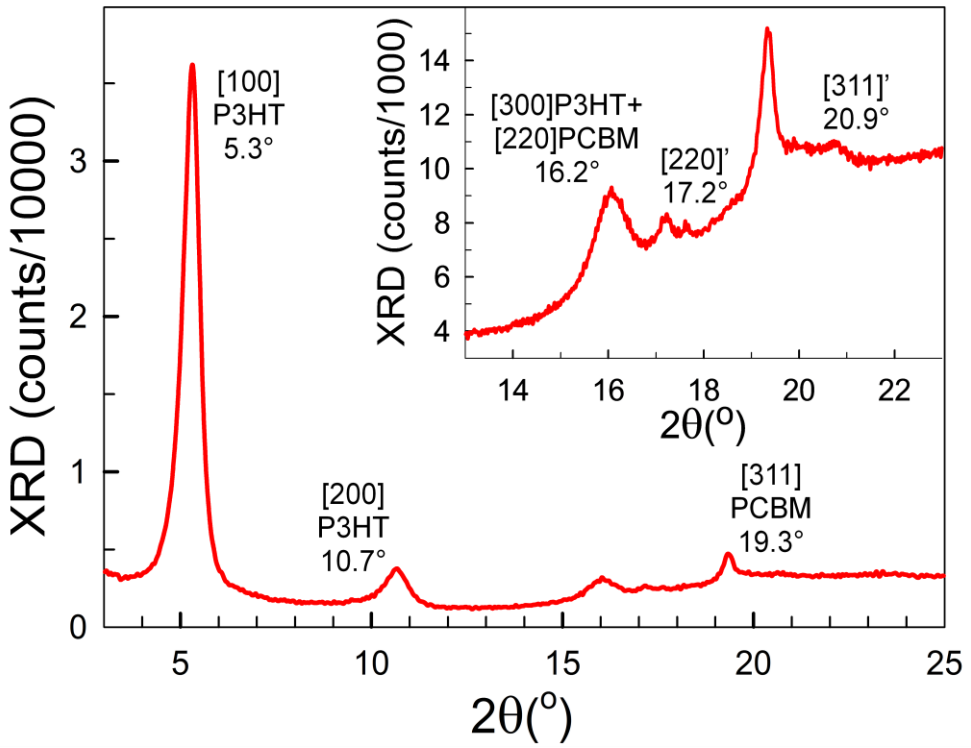

Figure 82 The XRD of RR P3HT/PCBM blend after annealing supports the formation of PCBM aggregates and P3HT fibrillar crystals.

Another large push for increasing PCE in this blend has come from increasing the regioregularity of P3HT [37], which will be the topic of our investigation in this section.

5.2.2. Optical studies

In this section we study RR P3HT/PCBM blend films in comparison to the blend of PCBM with RRa P3HT that does not form lamellas to the same degree. [37] Figure 83 represents the normalized absorption spectra of RR P3HT/PCBM and RRa P3HT/PCBM blends. The absorption spectrum of the blend consists of absorption bands due to the acceptor and the donor. The band at ~3.7 eV is due to PCBM and the band at lower photon energy is due to P3HT. We observe a 0.4 eV red shift in the absorption spectrum

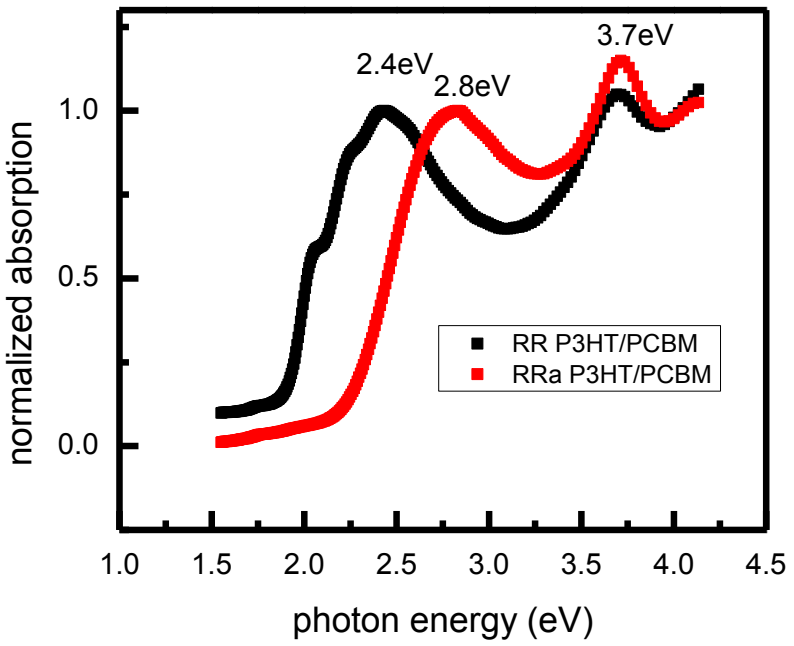

Figure 83 The normalized absorption spectra of RR P3HT:PCBM blend (black) and RRa P3HT:PCBM blend (red)

of RR P3HT blend that is the result of higher regioregularity [37] and phase segregation, as seen in TEM images (Figure 84). Due to this red shift in the absorption spectrum, Jsc in organic solar cell considerably increases from ~0.12 mA/cm^2 for RRa P3HT/PCBM device to ~11 mA/cm^2 for RR P3HT/PCBM device, as fabricated in our lab by Dr. Y. Zhang. The absorption spectrum of RR P3HT/PCBM is well structured with distinct vibronic bands at ~2.27 eV and ~2.06 eV that are also a characteristic of well ordered chains of P3HT and lamellar structure [46].The PL spectrum of RRa P3HT contains an additional band at ~1.3eV, due to charge transfer exciton, CTE [104]. The energy of this new transition is lower than singlet exciton for either PCBM or P3HT (as presented in Figure 85). CT states are the result of interfacial electronic interactions at the heterojunction of the donor and an acceptor.[105, 106] These states can be viewed as

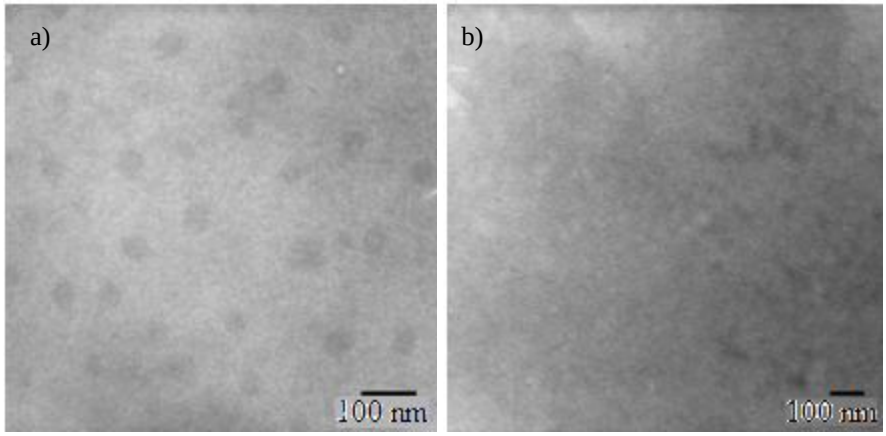

Figure 84 The TEM images of: a) RR P3HT/PCBM blend where we can see phase separation. The dark regions correspond to the PCBM aggregates. b) RRa P3HT/PCBM blend with no visible phase separation.

hybrid states caused by the wavefunction overlap between a donor and an acceptor molecule that are in close contact. Mazumdar et al. explains CTE as a quantum mechanical superposition of the intrachain exciton and the interchain Coulombically-bound polaron-pair, which exhibits picoseconds photoinduced absorption at energies characteristic of both the neutral exciton and charged polarons [107, 108].

The appearance of a CT state in the PL spectrum confirms that the mechanism of photoinduced charge transfer at the donor-acceptor interface is not a single step process [109]. The CT state has a significant role in the charge separation and recombination mechanism in organic solar cells. Since the CTE are loosely bound, the binding energy is lower than in Frenkel excitons, and in a simplified picture these states can be treated as a loosely bound polaron pair. The polaron pair can dissociate and therefore increase the photocurrent and PCE of organic solar cells[110]. However, in the case of RRa P3HT blend, the CTE leads to a long lived, red shifted PL emission [109, 111, 112].

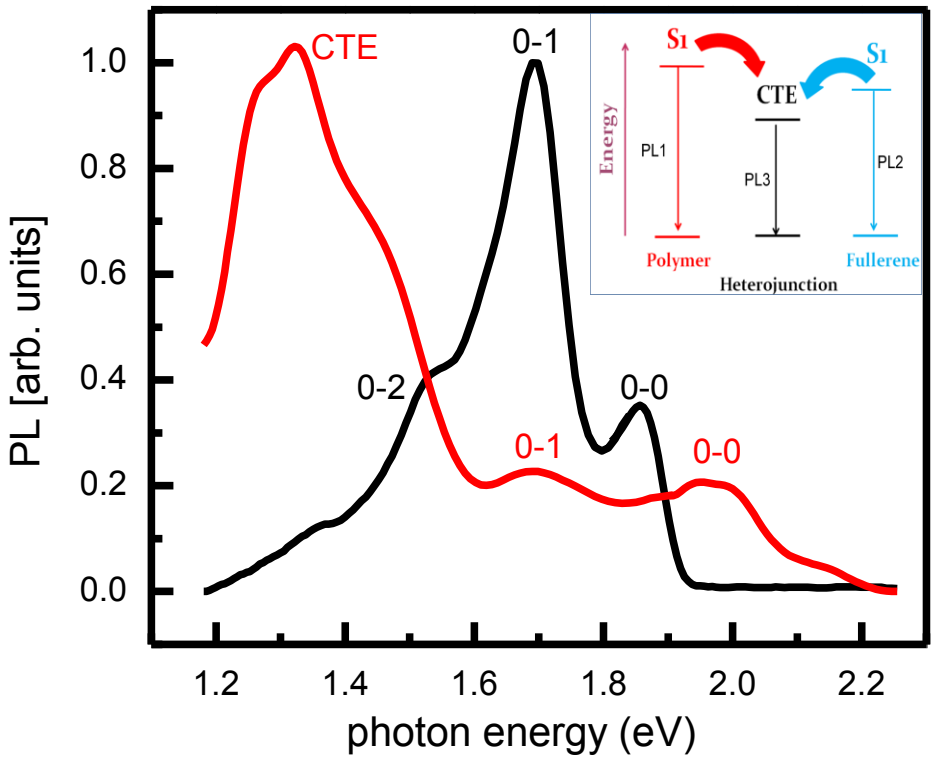

Figure 85 The PL spectra of RR P3HT:PCBM blend (black) and RRa P3HT:PCBM blend (red). The inset shows a schematic energy level diagram for electronic excitations in conjugated polymer/fullerene blends.

Benson-Smith et al. proposed that CT exciton is independent of the bandgap and morphology of polymers [106]. This might be the case in MDO-PPV/PCBM blend [104]. However, our studies of the RR P3HT and RRa P3HT blends contradict this suggestion.

We see distinct CT emission in RRa P3HT blend but not in RR-P3HT blend. The polymer backbone in RRa P3HT is less rigid with more degrees of freedom than in RR P3HT chains. This results in a formation of lamellas to a lesser degree [37], and affects the morphology of the blend. The TEM image of RRa P3HT blend shows no aggregation and phase separation.The RRa P3HT and PCBM molecules are close to each other. This results in a larger overlap of the wavefunctions than in RR P3HT blend. Consequently,

we conclude that rigidness of the polymer chain and therefore morphology of the blend does influence CT states, and that the CTE recombination has a significant impact on the reduction of PCE in an organic solar cell.

Figure 86 shows photoinduced absorption spectra of RR P3HT and RRa P3HT blends with PCBM. Both blends PA spectra are dominated by polaron bands. P1 and P2 PA bands are due to positive polarons on polymer chains. P1 photinduced absorption band in RR P3HT blend is red shifted with respect to the RRa P3HT inferring a higher order and aggregation in RR P3HT [46, 47]**.** P2 photoinduced absorption band in RRa P3HT blend is narrower, more localized than in RR P3HT. In both blends at ~ 1.2 eV we can see another photoinduced absorption band that corresponds to the negative polaron on PCBM molecules.

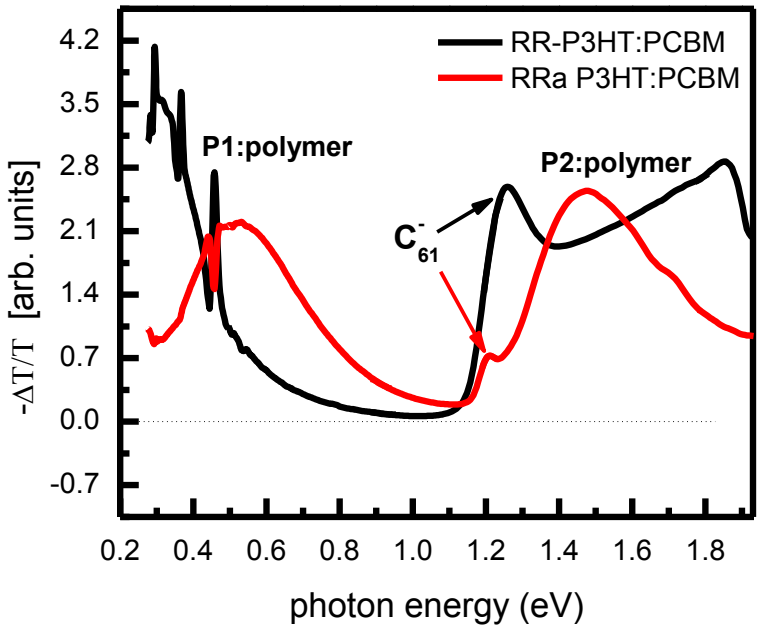

Figure 86 The photoinduced absorption spectra of RR P3HT:PCBM blend (black) and RRa P3HT:PCBM blend (red).P1 and P2 stand for polaron PA bands due to positive polarons on the polymer chains, and C^-_{61} stands for a negative polaron on the PCBM molecules.

5.2.3. Magnetic resonance studies

In order to explore the spin nature of the PA bands we performed magnetic resonance studies. Figure 87 shows the spin 1/2 PADMR resonances of RR P3HT/PCBM and RRa P3HT/PCBM blends. PADMR of RR P3HT/PCBM is asymmetric which points to two resonance contributions due to positive polarons on RR P3HT and negative polarons on PCBM that have different g-values. The g-values of RR P3HT and PCBM are relatively close, namely 2.002 [113] and 1.9995 [114], respectively; and since the frequency of the microwave in our PADMR apparatus is ~ 3 GHz we were unable to clearly resolve these two contributions. Using a Gaussian fit we were able to assign resonance contributions to polarons on RR P3HT and PCBM. Assuming that an integrated PADMR corresponds to the number of spin carriers, we can conclude that there are more spin carriers on PCBM molecules than on RR P3HT chains. To confirm this we present our LESR results later in the chapter.

Figure 87 (b) shows spin ½ PADMR resonance of RRa P3HT/PCBM film. The resonance is broader and the contributions of positive and negative polarons are more obvious, possibly due to a slightly different g-factor for RRa P3HT. The resonance contributions of positive polarons on RRa P3HT chains and negative polarons on PCBM molecules seem to be equal. However, below 970 Gauss and above 1020 Gauss we see shoulder-like features that might be due to the triplet exciton on the PCBM molecules as seen in the inset of Figure 88(a).

The triplet powder pattern is more dominant in PLDMR as presented in Figure 88(a). In Figure 88(b) we see that the PADMR of PCBM and the PLDMR of RRa P3HT/PCBM blend overlap. Consequently, they have equal values of the zero-field

splitting parameter D ≈ 40 Gauss. The PLDMR of the RRa P3HT/PCBM film is positive. This is caused by the microwave induced increase in radiative recombination, which may be due to triplet-triplet annihilation on PCBM molecules[115].

Furthermore, we explored the resonance at different photon energies, namely 0.47 eV the energy of polaron P1, and 1.47 eV which we suspect is due to polaron localized on the P3HT chain. From Figure 89 (a) and (c) we see that the resonance shape changes. The resonance at 1.47 eV is slightly broader (28 Gauss) with more obvious contributions of positive and negative polarons than the resonance at 0.47 eV (21 Gauss).

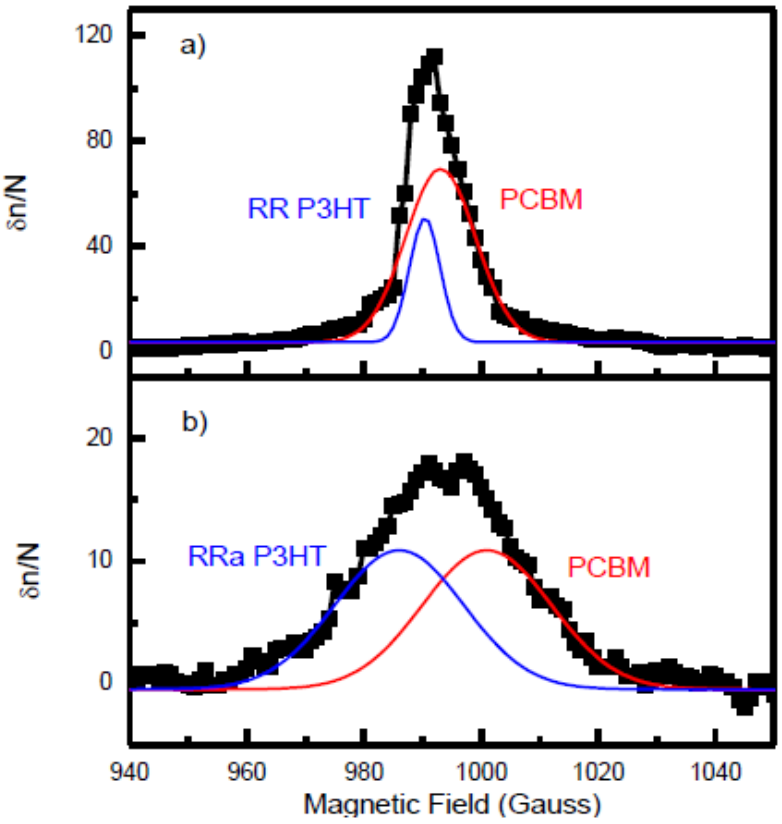

Figure 87 PADMR spectra of **a)** RR P3HT/PCBM blend the collected data are in black with the fit of resonance contributions due to RR P3HT (blue) and PCBM (red); and **b)** RRa P3HT/PCBM blend (black) with the fit of resonance contributions due to RRa P3HT (blue) and PCBM (red)

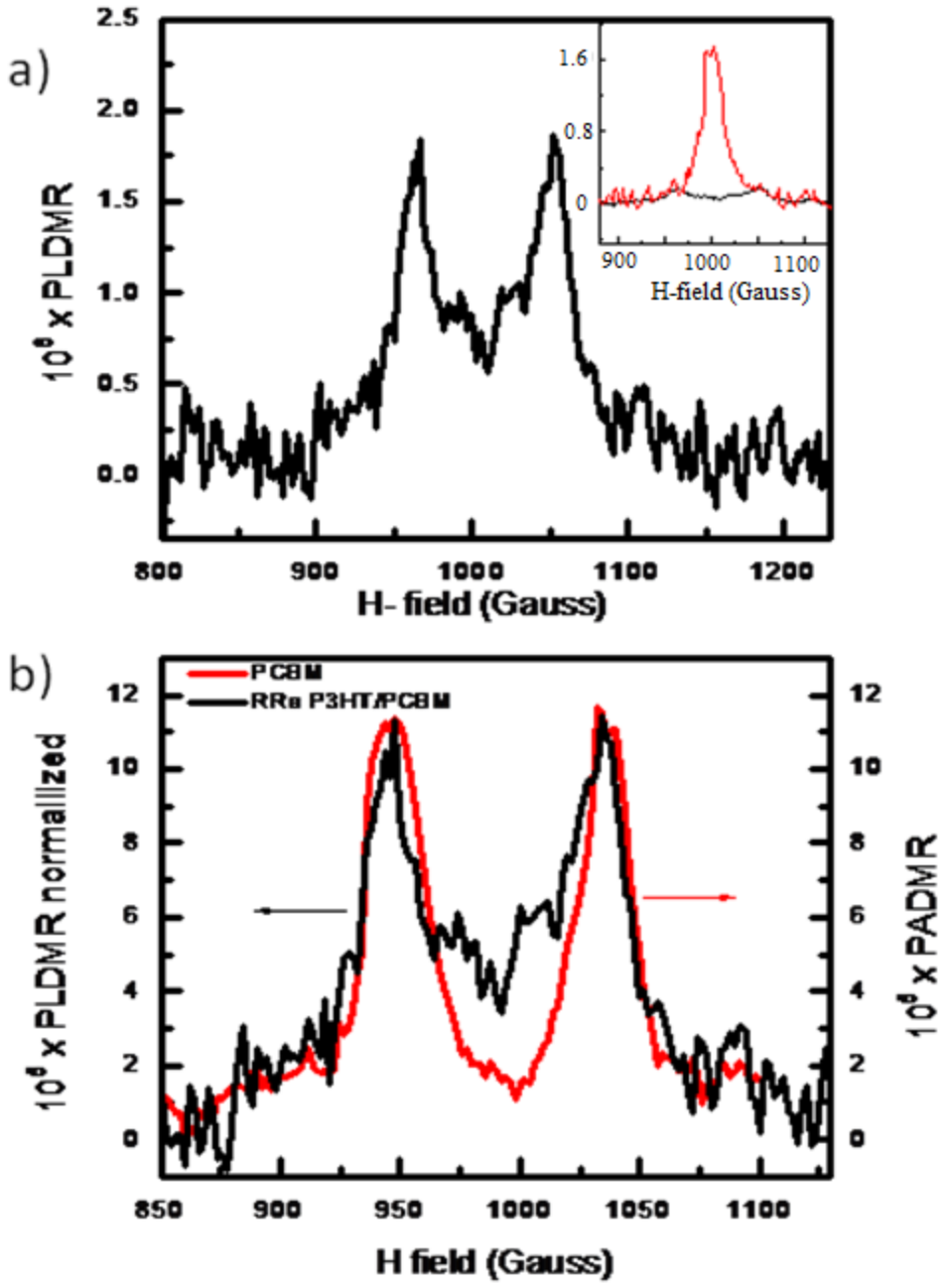

Figure 88 The PLDMR resonance a) RRa P3HT/PCBM film with characteristic triplet powder pattern; the inset shows PADMR of the same blend (red) with shoulders that correspond to PLDMR (black). b) PLDMR –triplet powder pattern of RRA P3HT blend (black) corresponds to triplet powder pattern of PCBM – PADMR (red)

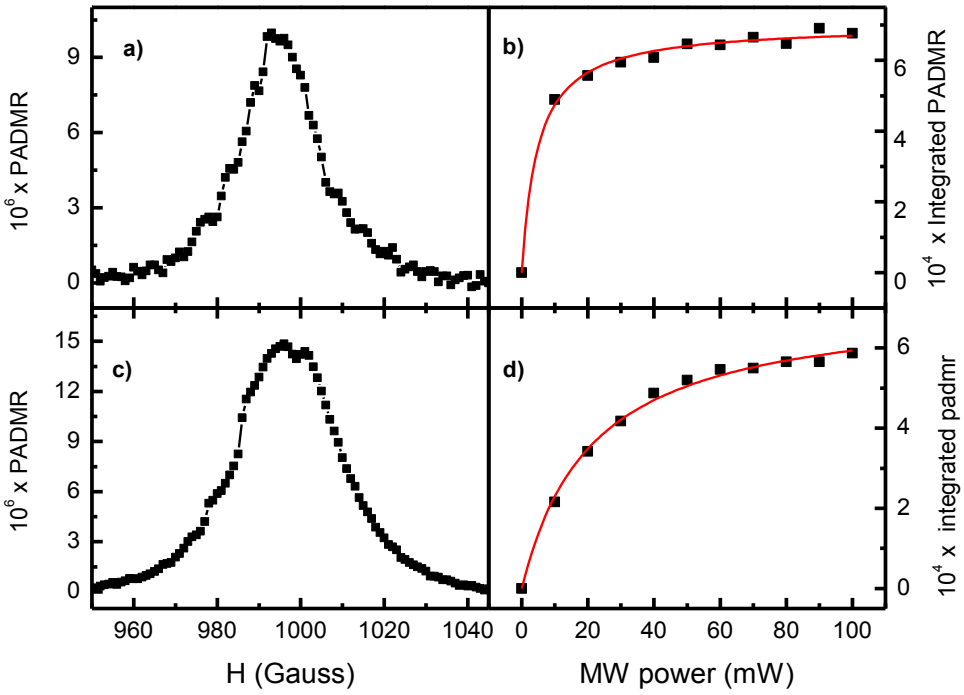

Figure 89 PADMR resonance and its saturation behavior: a) PADMR resonance of RRa P3HT/PCBM blend at the P1 photon energy of 0.44 eV; b) saturation behavior of integrated PADMR at 0.44 eV (black squares) fit according to the saturation equation (red line); c) resonance of RRa P3HT/PCBM blend at the P2 photon energy of 1.47 eV; b) saturation behavior of integrated PADMR at 1.47eV;

The saturation behavior of these two resonances is different; the resonance at 0.47 eV saturates faster than the resonance at 1.47 eV. Consequently, the spin relaxation times are different. Data presented in Figure 89 (b) and (d) are fit according to saturation equation:

$$\int PADMR \sim \frac{P_{MW}}{P_{MW}+P_S}, \tag{5.1}$$

where PADMR is integrated PADMR resonance, P_{MW} is microwave power and P_S is given by

$$P_S = \alpha\Gamma_{\text{eff}}; \tag{5.2}$$

α is an experimentally determined constant and Γ_{eff} is given by relation below

$$\Gamma_{eff} = \gamma + \frac{1}{2}\gamma_{SL}; \tag{5.3}$$

γ is average polaron-pair recombination rate and γ_{SL} is reciprocally proportional to spin relaxation time.

$$\gamma_{SL} = \frac{1}{T_{SL}}. \tag{5.4}$$

We can assume that he change in P_S reflects the change in T_{SL}. [116] From Figure 89 where integrated PADMR was fit according to equation 5.1 we found that ratio of PS for the resonance at 0.44 eV and the resonance at 1.47 eV is 0.23. This suggests that the spin relaxation time of the spin species at 0.44 eV is much longer than the spin relaxation time at 1.47 eV.

Similar measurements were done with RR P3HT/PCBM blend at photon energies: 0.4 eV (P1 due to polarons on the RR P3HT chains), 1.26 eV (due to negative polarons on PCBM molecules), and 1.7 eV (P2 due to polarons on RR P3HT chains) as presented in Figure 90. We notice that the resonance shape differs depending on the photon energy. The resonance at 0.4 eV is more symmetric than that at 1.26 eV and 1.7 eV. The saturation behavior differs as well. The resonance at 1.26 eV saturates the fastest. Using equation (5.1) we can estimate Ps for the polarons at 0.4 eV, 1.26 eV, and 1.7 eV to be

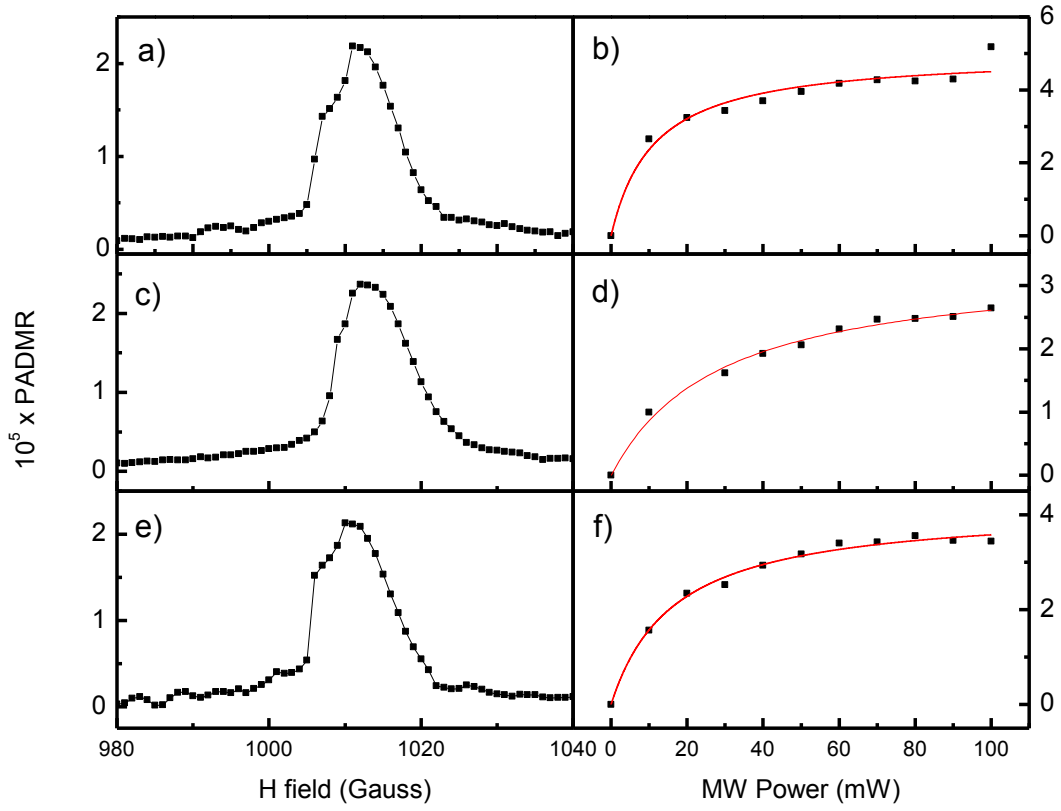

Figure 90 The PADMR resonance of RR P3HT/PCBM blend film: a) at 1.26 eV – the PA band due to negative polarons on PCBM molecules, c) at 0.4 eV – the PA band due to P1, and e) at 1.7 eV – the PA band due to P2; the saturation behavior of the integrated PADMR vs. microwave (MW) power: b) at 1.26 eV, d) at 0.4 eV, and f) at 1.7 eV.

29±3, 11±3, and 17±2. If we assume that the PA band at 1.26 eV is due to two different species, mobile and trapped polarons with mean lifetimes of ~5 ms and ~100 μs [117] then the values of P_S (equations 5.2 and 5.3) can be affected by their different recombination rates. According to the resonance shape we conclude that the resonance contributions of positive polarons on P3HT and negative polarons on PCBM change with photon energy. However, 3 GHz microwave does not allow us to resolve these

contributions clearly. Therefore further exploration using LESR with 9 GHz microwave was desirable.

As discussed in Chapter 4, LESR is a direct method for detecting and studying photo-generated polarons. [118] The ESR measurements were at first done at 10K, with a microwave power of 0.3mW and high Q value, above 3000. Figure 91 shows the actual measurements: ESR often referred to as "dark" signal and the measurement that was done while sample was illuminated by laser light (excitation wavelength of 488 nm) referred to as "light on".

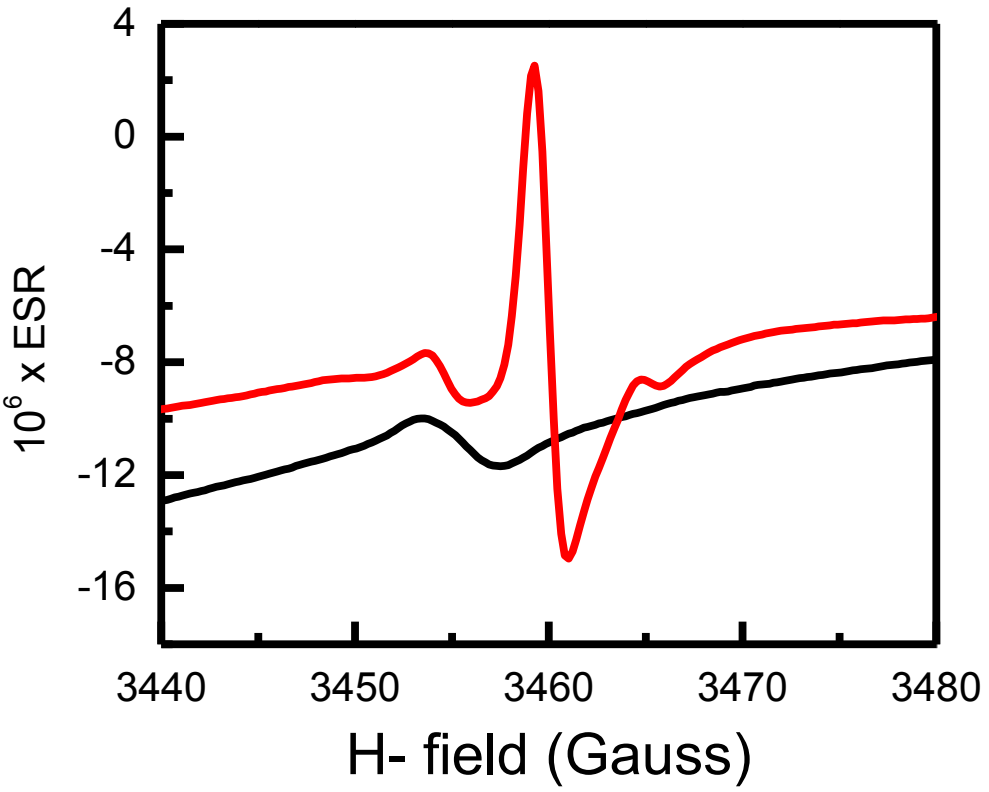

Figure 91 The RR P3HT/PCBM blend ESR spectra before exposing the sample to the laser light (black) and when illuminated with laser light (red line) at 10K.

It is worth noting that both pristine π-conjugated polymers and pristine PCBM are known not to have ESR signal, yet when blended ESR and LESR signals are enhanced. [119, 120] The ESR signal corresponds to trapped polarons. [119-121]In RR P3HT/PCBM blend the "light on" measurement is about 10 times larger than the ESR measurement, which allows us to neglect the thermal effects (signal fluctuation due to small changes in temperature of the sample due to the laser illumination).

The LESR or RR P3HT/PCBM blend is achieved by subtracting ESR from the "light on" measurement (Figure 92(a)). As discussed in Chapter 2, the result is the signal that can be fit with a derivative of a Gaussian or Lorentzian lines. However, here we have more than one contribution to the resonance that can be nicely resolved. The integrated LESR (Figure 92(b)) is reminiscent of the PADMR results except that the two resonance contributions are well resolved here. The contribution at the lower magnetic field is assigned to RR P3HT that has a higher g-factor, and the contribution at higher magnetic field is assigned to spin carriers on PCBM.

Assuming that the double integrated LESR is proportional to the number of spin carriers[120], we can conclude that PCBM has 2.5 times more spin carriers than RR P3HT. This conclusion contradicts the fact that the sample has to remain charge neutral and that LESR signal originates from a photo-induced charge transfer reaction that creates equal number of spins (electrons on the fullerene and holes on the polymer).[120] Possible explanations for this phenomenon are:

- The formation of both positive and negative polarons on PCBM aggregates, which is consistent with our study of fullerene derivatives in Chapter 4

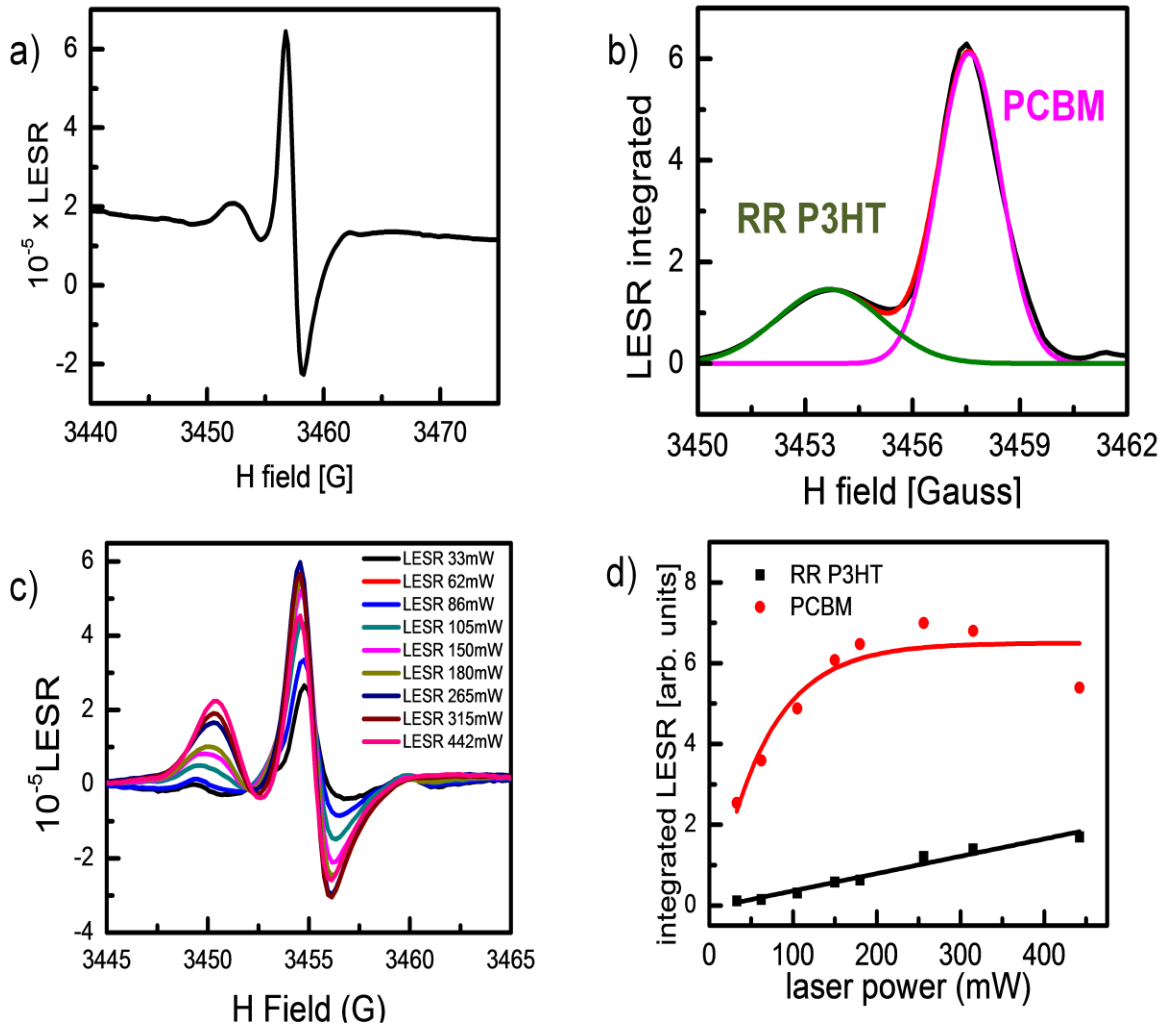

Figure 92 RR P3HT/PCBM blend **a)** LESR; **b)** integrated LESR fit with two Gaussians corresponding to contributions of RR P3HT and PCBM; **c)** LESR at different power of the laser (488 nm excitation wavelength); **d)** saturation behavior of integrated LESR of RR P3HT and PCBM as a function of laser power. Experiments were done at 10 K, ~9 GHz microwave frequency, at ~0.3 mW of microwave power.

- The formation of bipolarons on RR P3HT, two like-charged polarons that have opposite spins and therefore spin singlet.[122]
- The spin relaxation time of the spin ½ species on the PCBM and P3HT are not equal to one another.

We repeated the LESR measurements at a different laser power and observed a different saturation behavior of the resonances due to RR P3HT and PCBM (Figure 92(c) and (d)).[119, 123] As previously noticed in PADMR measurements the resonance due to spin carriers on PCBM saturates faster, consequently having longer spin-lattice relaxation times. In addition, the resonance corresponding to PCBM is narrower than the resonance line corresponding to RR P3HT. According to the process of motional narrowing, the narrow line is expected to be evidence of fast motion. Consequently, we can conclude that spins on PCBM molecules have higher mobility than spins on RR P3HT chains.[124] Also this result is in agreement with the third explanation of the asymmetry in the LESR signal, namely the spin polarization is more maintained in PCBM due to the longer spin relaxation time.

The LESR technique can be used to find the g-factor of each resonance contribution. First we calibrated the system with DPPH that has a known g-factor of 2.0036.[125] Next, we repeated the procedure to obtain the LESR of RR P3HT/PCBM blend but this time at 78 K, to avoid too long spin-lattice relaxation times that at 10 K leads to lower signal.[121] We also measure LESR under low laser power (2mW), again to avoid saturation that we can see in Figure 92(d). We integrated the LESR, obtaining a resonance that resembles PADMR and can be fit with Lorentzian lines. In order to find

more reliable g-values we converted the x-axis from magnetic field to g-factor, according to the following equation:

$$g = \frac{h}{\mu}\frac{\nu}{B_0} = 714.4775\ \frac{\nu}{B_0}. \quad (5.5)$$

where ν is frequency of microwave and B_0 is magnetic field and 714.4775 represents the ratio between the Plank constant, h and Bohr magneton, μ.

Looking at Figure 93 (b) the integrated LESR cannot be fit with only two Lorentzians, since there is a third contribution.

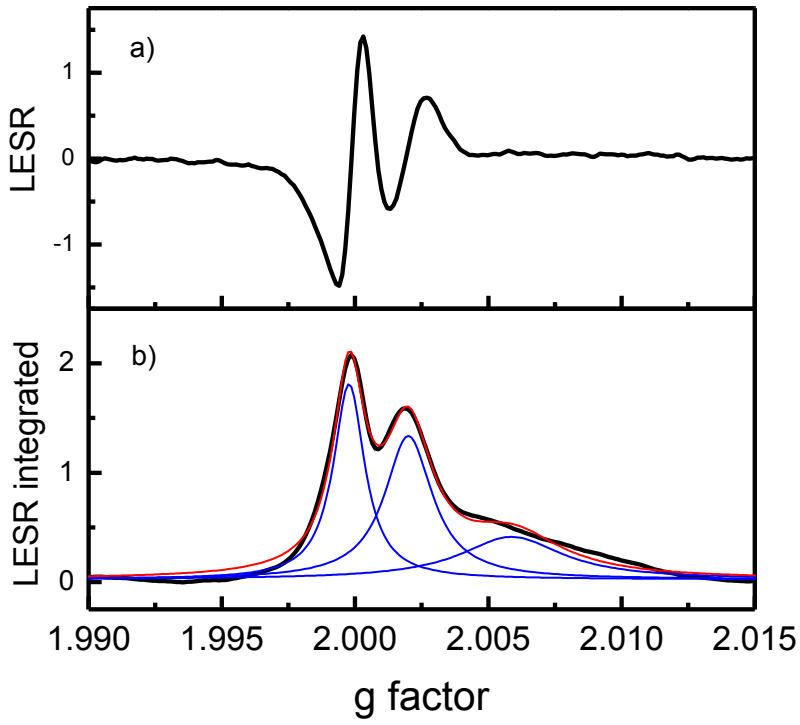

Figure 93 RR P3HT/PCBM blend **a)** LESR at 78 K, **b)** integrated LESR (black) with 3 Lorentzian lines fit, each Lorentzian line (blue) represents a resonance contribution with different g-factor; the red line represents the sum of all of three Lorentzians.

The first two contributions are due to polarons on RR P3HT and PCBM with g-factors of 1.9998 and 2.002, respectively. Since the fit of the third contribution is not exact, we can say that g-factor is ~ 2.0059, larger than the g-factor of a free electron. Likewise, Krichniyi et al. were not able to fit their LESR results of RR P3HT/PCBM blend with only two Lorentzian lines. According to their interpretation, the LESR spectrum consists of Lorenzian doublet of mobile polarons on polymer chain and fullerene molecule, as well as Gaussian contributions of localized positive polarons on the polymer and negative fullerene anions pinned by polymer matrix. [126] The deviation of a g factor from the value of free electron can be explained by uncompensated angular momentum that induces an additional magnetic field due to $\sigma \rightarrow \pi \rightarrow \sigma^*$ transition[126].

ESR and "light on" measurements of RRa P3HT/PCBM blend are of the same order of magnitude as shown in Figure 94. Consequently, we cannot treat the LESR as reliable in this case because the features of the spectrum can be due to the change of temperature due to laser illumination. We indeed observed that signal fluctuations occur with temperature change. [127] The sample is not immersed inside of liquid helium but placed in vacuum inside of a quartz tube. Therefore, its temperature is dependent on heat transfer through the quartz tube. Nevertheless we observed a clear signature of spin ½ on the polymer and fullerene molecules (Figure 94(b)).

5.2.4. Conclusion

The regioregularity of P3HT affects the morphology of the blend as it can be seen in TEM images. The blend of PCBM with RR P3HT is characteristic by phase separation, where the blend with RRa P3HT has homogenous morphology without phase separation.

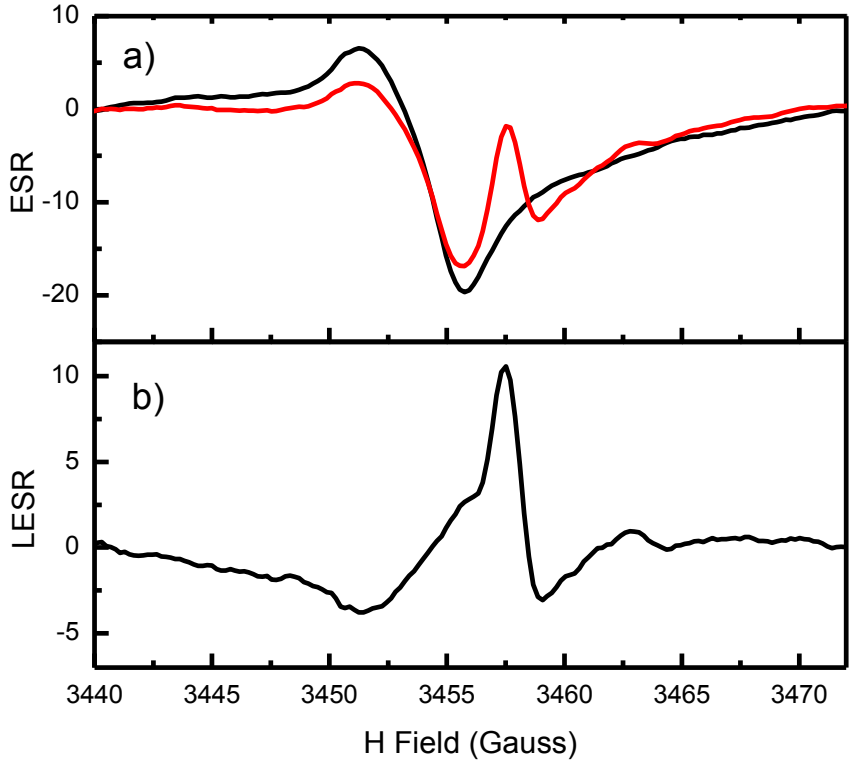

Figure 94 RRa P3HT/PCBM blend **a)** ESR (black) and "light on" (red) measurement; **b)** LESR at 10K

In the PL spectrum of RRa P3HT blend at low photon energy we can see the emission due to CTE recombination that hinders the performance of solar cells based on this blend.

Photoinduced absorption spectra of both blends are dominated by polaron PA bands. At 1.2 eV we see PA band due to negative polaron on PCBM. Hoewever, the P1 and P2, PA bands due to positive polaron on the polymer chain are more localized in RRa P3HT. PADMR and LESR confirmed this PA band assignment.

The PADMR of RRa P3HT blend shows the same spin contribution to the resonance for both RRa P3HT and PCBM. The resonance is broader than in the RR

P3HT blend inferring the lower mobility of polarons in this blend. The spin 1 triplet powder pattern (corresponding to PLDMR of PCBM isolated molecules) dominates PLDMR of this blend. This might be caused by triplet-triplet annihilation on PCBM . On the other hand, PADMR and LESR of RR P3HT/PCBM blend showed that PCBM contributes more spin carriers to the resonance than RR P3HT. This conflict with charge neutrality can be resolvedby considering the longer spin relaxation time of spin ½ on the PCBM molecules.

5.3. RR P3HT / bis-[60]PCBM blend

5.3.1. Introduction

Bis-PCBM, a bisaduct analogue of PCBM[128], was introduced in Chapter 4. The advantage of bis-PCBM is that its LUMO is 135 meV higher than that of PCBM.[81] Therefore when used as an acceptor material, then the open circuit voltage is enhanced and PCE increases from 3.8% to 4.5%. [79] In this section we present our optical and magnetic resonance study of RR P3HT/bis-PCBM blend with the weight ratio 1.2:1.

5.3.2. Optical studies

Similarly to the PL spectrum of RR P3HT/ PCBM, the PL spectrum of RR P3HT/bis-PCBM has distinct phonon side bands indicating formation of aggregates. However, the ratio between 0-0 and 0-1 phonon side bands in bis-PCBM blend is larger than in PCBM blend (Figure 95). This result points to different degrees of order and crystalization. [65, 129] Since the PL of the blend is almost entirely due to the polymer, the more distinct phonon side bands and lower ratio of 0-0 to 0-1 phonon side bands indicate higher aggregation of the polymer. It would be expected that due to different

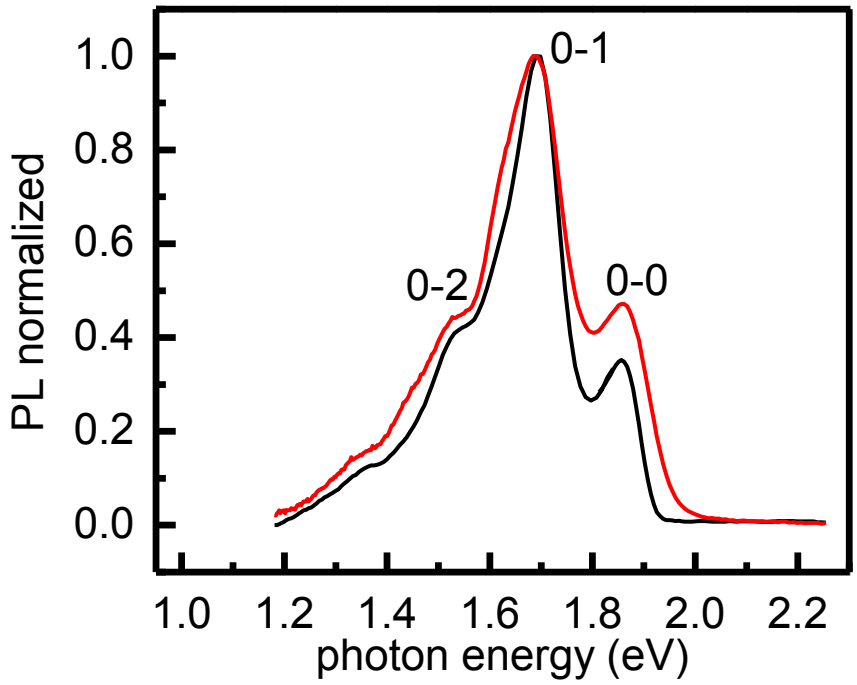

Figure 95 The PL spectra of RR P3HT/PCBM film (black) and RR P3HT/bis-PCBM (red) at 50K with excitation wavelength of 488 nm.

structure of the bis-PCBM molecule, namely two functional side groups, the packing of the polymer chains might not be disrupted to the same degree as in the blend with PCBM. And that might be true in the films before annealing. However, we studied annealed films, and according to Figure 96 (b) the crystallinity of P3HT recovers with annealing to the highest degree in the PCBM blend film.[62] Faist et al. presented a very nice work on multiple adduct fullerene blends with RR P3HT.[62] In their study they compared absorption of pristine RR P3HT to absorption of its blends with PCBM, bis-PCBM, and tris-PCBM as shown in Figure 96. There we see that for annealed film of bis-PCBM blend, absorption due to P3HT, in the visible region, is lower than in pure P3HT film or its blend with PCBM. Moreover, the absorption shoulder at ~610 nm, indicator of degree

of P3HT crystallinity [43, 62], decreases with addition of fullerene derivatives indicating disruption of P3HT chain packing by the fullerenes (Figure 96 (a)). It is suggested that this is the result of size exclusion effect, where the additional side chains attached to fullerene cage prevents bis-PCBM to closely approach P3HT chains and disrupt their stacking.[62]

However, with annealing the order of P3HT chains becomes restored. In annealed films (Figure 96 (b)), according to this feature the degree of crystallinity of P3HT is smaller in bis-PCBM blend than in PCBM blend which is in agreement with our PL results depicted in Figure 95.

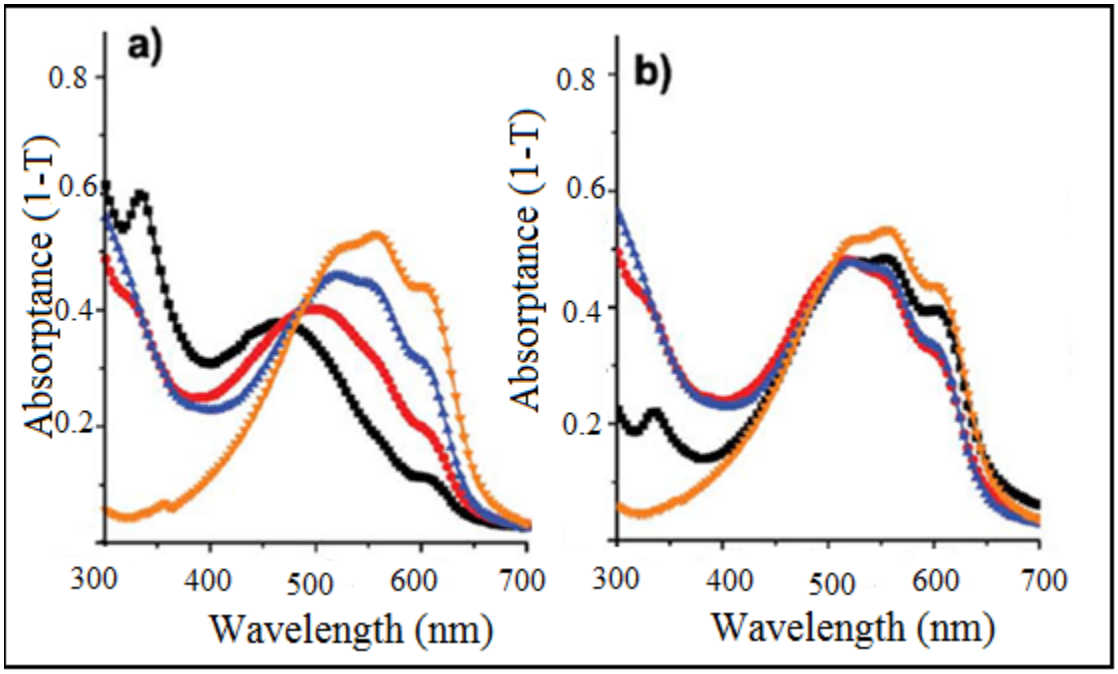

Figure 96 The absorbance spectra of pure RR P3HT (orange), RR P3HT/PCBM (black), RR P3HT/bis-PCBM (red), and RR P3HT/tris-PCBM (blue) films before **(a)** and after **(b)** annealed at room temperature.[62]

Figure 97 shows the PL spectra of RR P3HT/bis-PCBM blend before and after annealing (at 150º, for 30 min). The P spectrum decreases (~3.35 times) in intensity after the annealing process. The quenching of PL is the result of the improved exciton dissociation at the interface [62]. The ratio of 0-0 and 0-1 vibrational transitions decreases as well, indicating improved aggregation of P3HT. Moreover, the PL emission spectrum gets broader with annealing probably due to the emission from the aggregates [129].

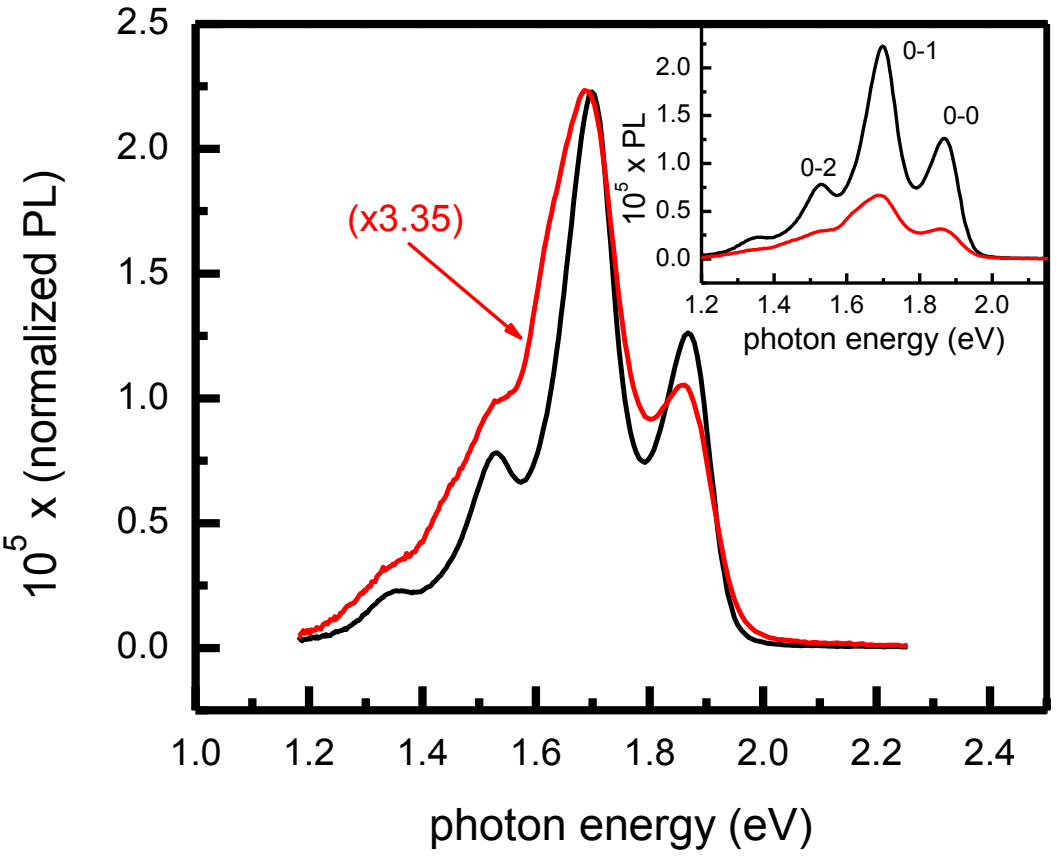

Figure 97 The PL spectra of RR P3HT/bis-PCBM film before (black) and after annealing (red) at 150ºC for 30 min. The inset shows the unaltered data. Both films were spin-coated under the same conditions at 700 rpm for 13 seconds.

The PA spectrum (Figure 98) is dominated by polaron excitation just as in RR P3HT/PCBM blend because of the quenching of the triplet PA by charge transfer. [59] P1 and P2 are PA bands are due to positive polarons on the polymer chain and the PA band at ~ 1.26 is due to polarons on bis-PCBM molecule.

We do not observe any PA shift induced by thermal annealing. However the intensity of P1 PA band decreased. This may be due to planarization of polymer chains caused by annealing. The annealing process causes P3HT to exclude the PCBM molecules and form ordered domains [130].

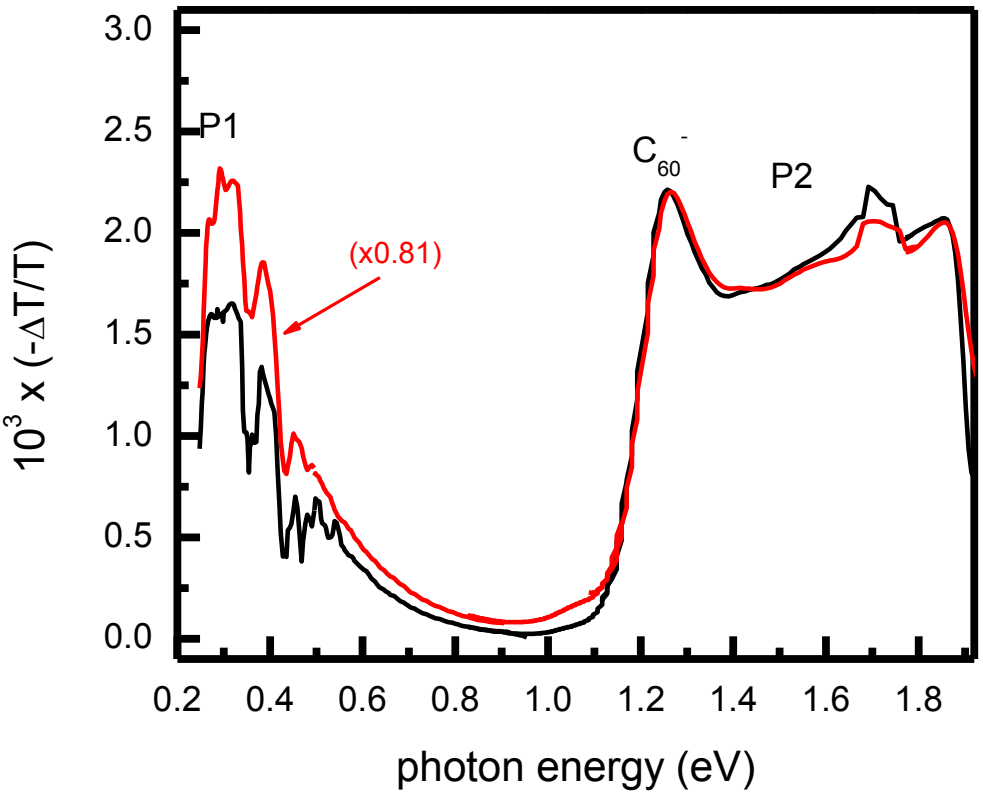

Figure 98 The PA spectra of RR P3HT/bis-PCBM films after (black) and before annealing (red). Measurement was done at 50K, with excitation wavelength of 488nm.

Figure 99 shows the PA spectra with below the gap excitation, namely 1.54 eV. Below the gap photoinduced absorption is decreased by an order of magnitude compared to the above the gap PA. Polaron excitations still dominate the spectrum.

However, the polarons photo-generated with below the gap excitation are more localized. According to the large out-of-phase component we can conclude that they have much longer mean lifetimes than the polarons formed with above the gap excitation. Possible explanation for the generation of polarons with below the gap excitation is the existence of charge transfer complexes (CTC) deep inside the gap [131].

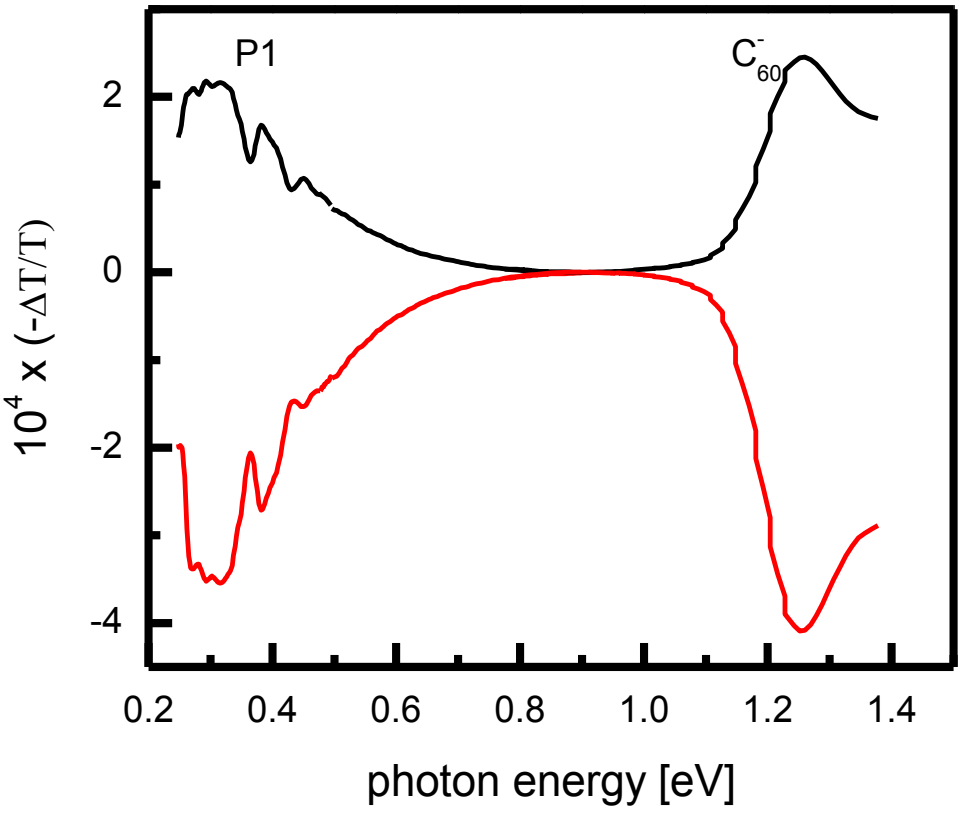

Figure 99 The PA spectra of RR P3HT/bis-PCBM film after annealing with excitation wavelength of 808 nm, below the gap at 30 K. The spectrum contains both in-phase (black) and quadrature (red) components.

5.3.3. Magnetic resonance studies

Figure 100 depicts PADMR of RR P3HT/bis-PCBM film. The ~20 Gauss narrow resonance at ~1000 Gauss is asymmetric and can only be fit with three Lorentzian lines. Consequently, the resonance at ~1000 Gauss represents the sum of three resonances due to mobile polarons on the polymer at ~998 Gauss and bis-PCBM at ~1004 Gauss, and trapped polarons on the polymer chain at ~978 Gauss.[119] According to the PADMR spectrum it seems that the resonance contribution due to the polarons on bis-PCBM is larger than the contribution of positive polarons on RR P3HT chains.

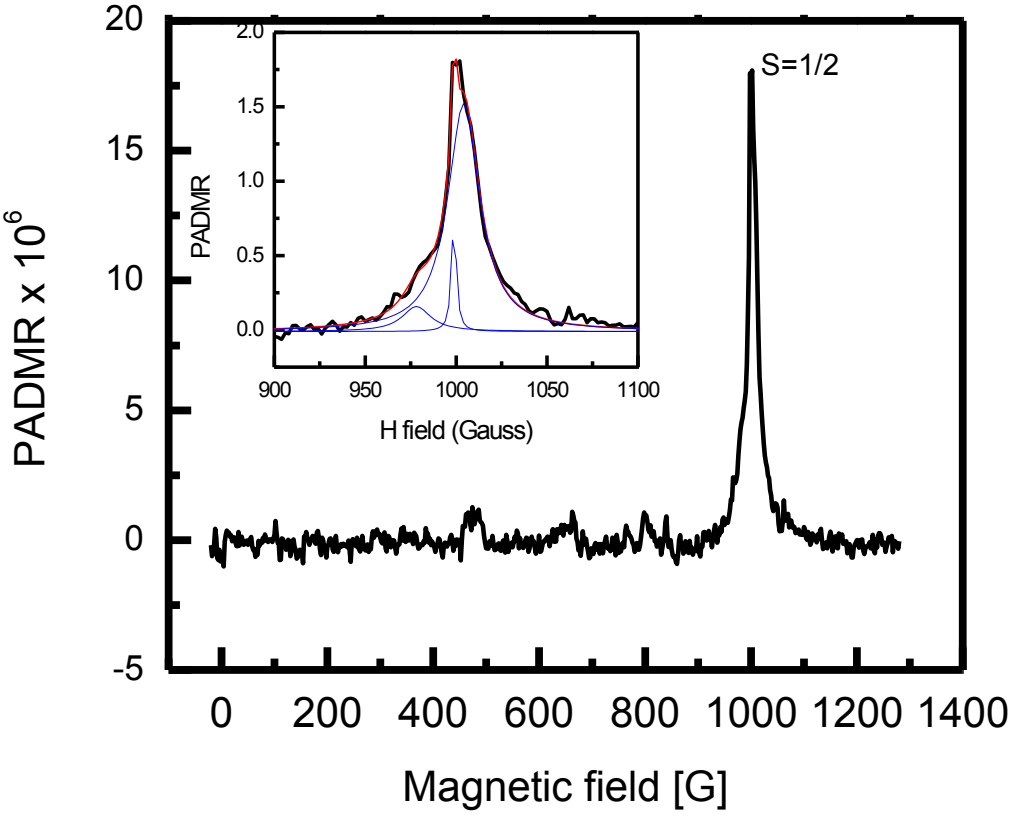

Figure 100 The PADMR of annealed RR P3HT/bisPCBM film with the narrow spin ½ resonance at ~1000 Gauss and possible spin 1 resonance at ~500 Gauss. The inset shows the fit(red) of the narrow resonance (black) at 1000 Gauss with three Lorentzian lines (blue).

Figure 101 shows the spin ½ resonance with both excitations below and above the gap. The resonance due to below the gap excitation is less asymmetric than the resonance due to above the gap excitation, and can be fit with two Lorentzian lines centered at 1003 Gauss and 998 Gauss(as shown in the inset of Figure 101). Consequently, the resonance at lower magnetic field, ~978 Gauss, (higher g-value) due to trapped polarons is diminished.

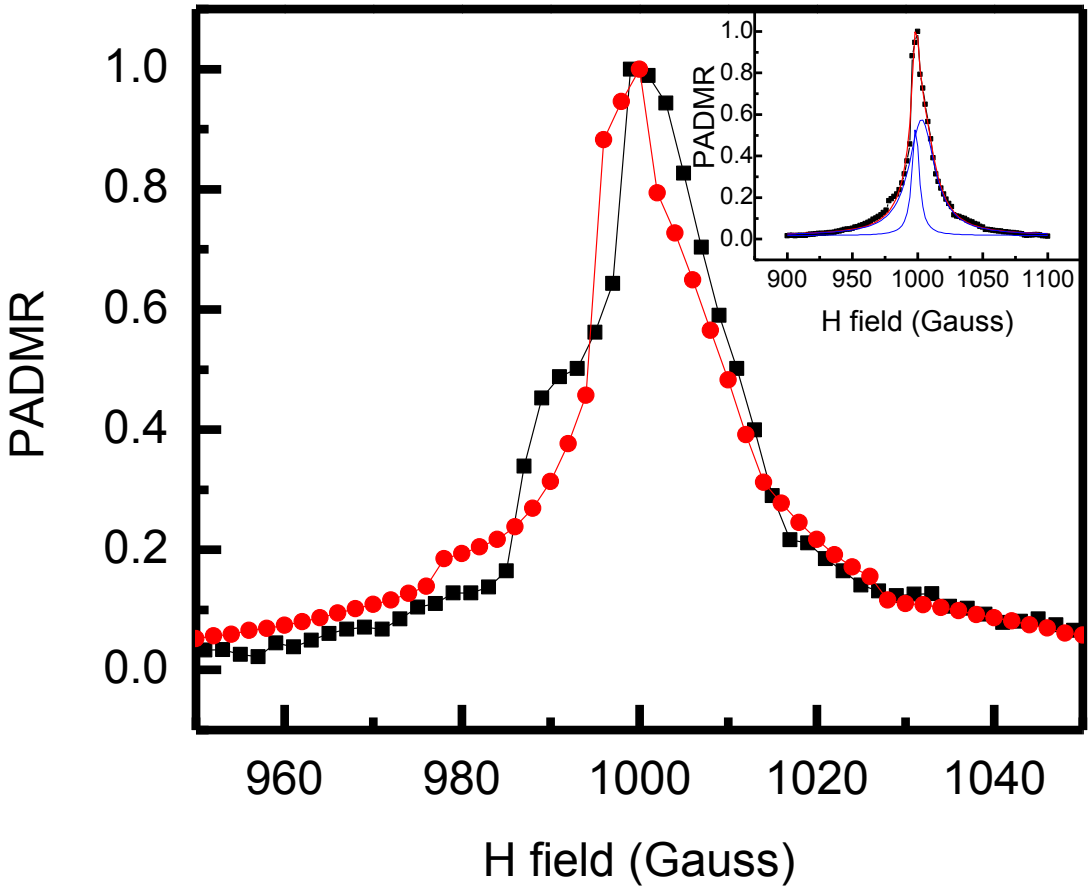

Figure 101 The PADMR of RR P3HT/bis-PCBM with above the gap excitation (black) and below-the-gap excitation (red). The inset shows PADMR with below-the-gap excitation fit with two Lorentzian lines (blue)

According to power dependence of integrated PADMR shown in Figure 102 below-the-gap excitation saturates faster and therefore has longer spin-lattice relaxation time [116]. From equation 5.1 and the fit of the data we find that Ps for above-the-gap excitation is 58±19 and for the below the gap Ps is 27±9. Nevertheless, the large standard deviation does not make these results reliable. Moreover, the polarons photo-generated with below the gap excitation are long lived [131] and according to equation 5.3 the polaron recombination rate also affects (decreases) the value of Ps.

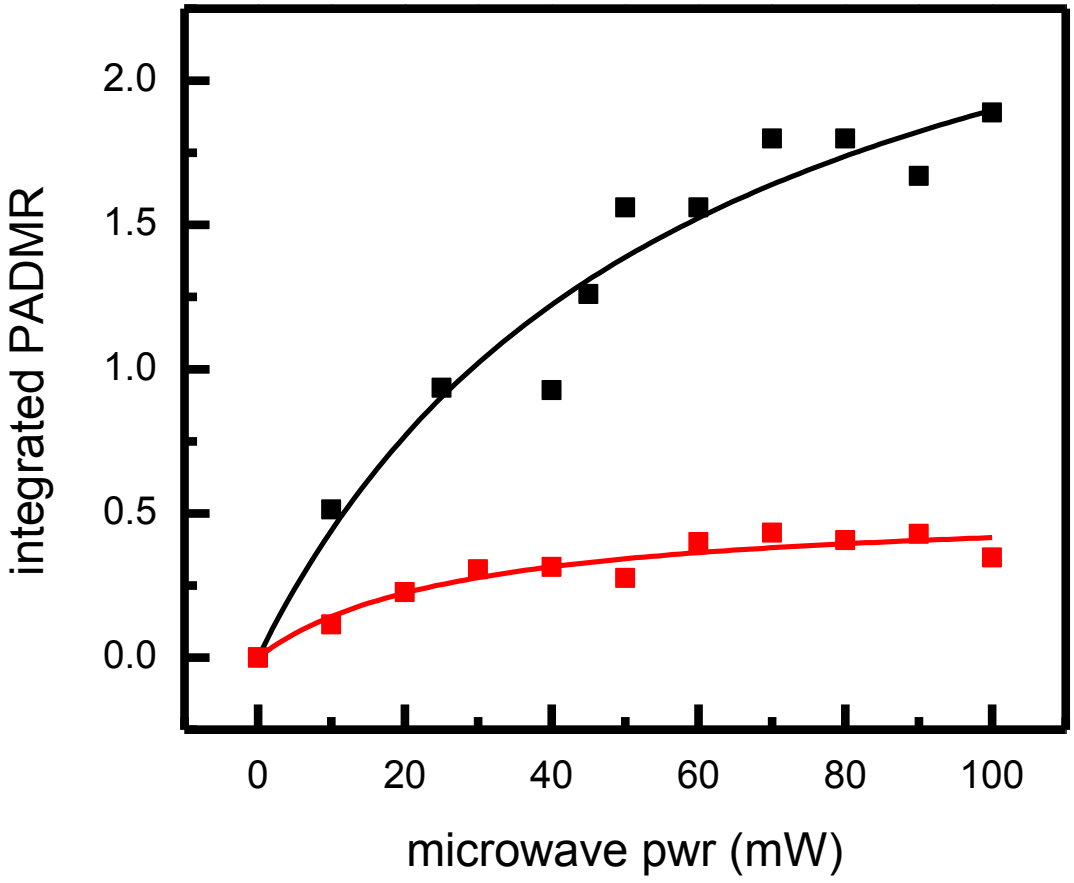

Figure 102 The integrated PADMR of RRa P3HT/bis-PCBM as a function of microwave power for above the gap excitation (black) and below the gap excitation (red). The data were fit according to equation 5.1 (solid lines).

Figure 103 shows the PLDMR of the blend. The signal to noise ratio is inferior to the pure polymer, because of the quenching of photoluminescence caused by addition of bis-PCBM. The resonance seems to be more symmetric than the PADMR resonance. Based on still significant PLDMR and frequency dependent PLDMR presented in Figure 104 we conclude that PLDMR is due to spin-dependent delayed photoluminescence arising from nongeminate recombination of polaron pairs.[132, 133]

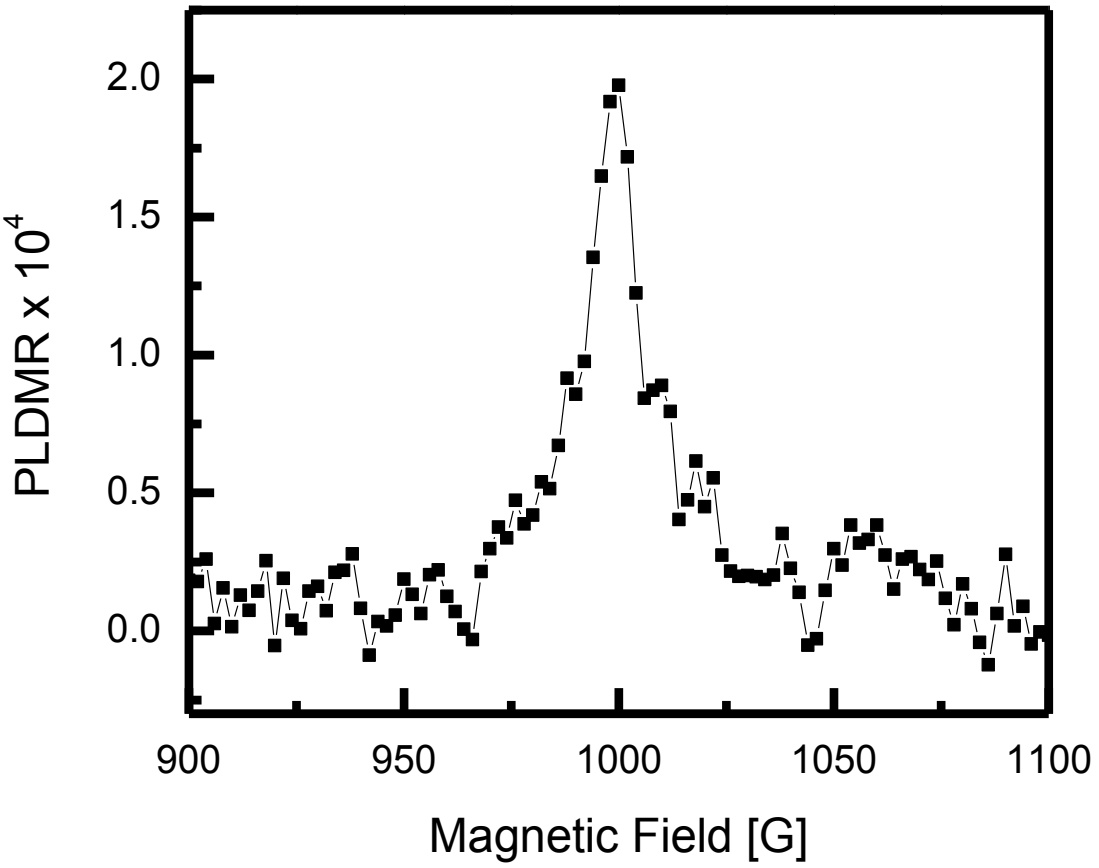

Figure 103 The PLDMR of RR P3HT/bis-PCBM with spin ½ resonance at ~1000 Gauss.

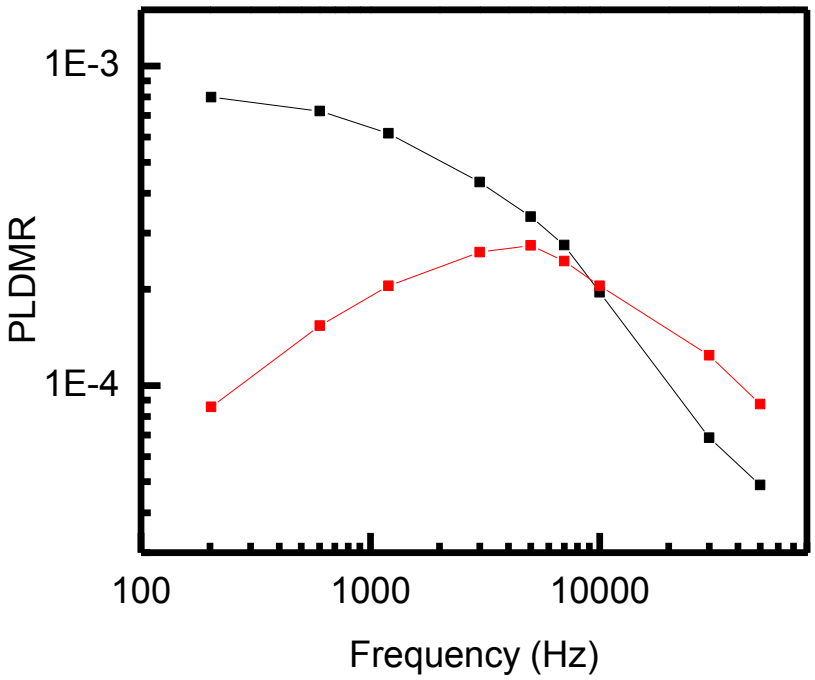

Figure 104 The PLDMR as a function of frequency of microwave modulation. Crossing between in phase (black) and quadrature (red) takes place at 10 kHz.

5.3.4. Conclusion

RR P3HT/bis-PCBM blend used as active material in OPVC yields higher power conversion efficiency. The PL spectrum with well resolved phonon side bands shows a high degree of chain packing in P3HT. Because of the two bulky side chains, bis-PCBM molecules are not capable of approaching P3HT and destroy the packing of P3HT chains. The PA spectrum is dominated by long lived polaron excitations indicating the charge separation. The below the gap photo-excitation shows that there are CT states deep in the gap. The annealing process recovers the crystallization of P3HT which is visible in quenching of PL emission and P1 PA band. The PADMR resonance can be fit by three Lorentzian lines due to resonances caused by mobile polarons on bis-PCBM and RR P3HT chains, and trapped polarons in polymer matrix. In contrast the PADMR resonance

with below the gap excitation can be fit by two Lorentzian lines showing diminished resonance due to trapped polarons. Based on our PLDMR studies we conclude that PLDMR resonance is due to spin-dependant delayed photoluminescence.

5.4. RR P3HT / ICBA blend

5.4.1. Introduction

Slight alterations to the structure of PCBM molecule**,** or adding additional functional groups such as in bis-PCBM can lead to a better performing OPVC.[134] In this section we study the blend of RR P3HT with Indene-C_{60} bis-adduct. When used as active material in OPVC it yields power conversion efficiencies up to 6.5%.[88] ICBA has a higher LUMO (by 0.17 eV), stronger visible absorption, and better solubility than PCBM .[89, 135] By using optical and magnetic resonance techniques we explored the consequences of a higher LUMO level and different more compact molecular structure of ICBA compared to that of PCBM and its multiadducts. Moreover, we explored the effects of thermal annealing that usually improves performance of a solar cell due to higher Jsc, coming from improved crystalinity of P3HT and increased hole mobility.[87]

5.4.2. Optical studies

Figure 105 compares the PL spectra of RR P3HT/ICBA blend before and after annealing. The PL spectrum after annealing is significantly red shifted (by ~50 meV) and the intensity ratio of 0-0 to 0-1 phonon side bands decreases. These results indicate the higher order and crystalinity of P3HT domains. [46, 47, 62] The PL of annealed sample is significantly quenched suggesting decreased radiative recombination[136]. The annealing induced PL quenching is consistent with our PL quantum efficiency results,

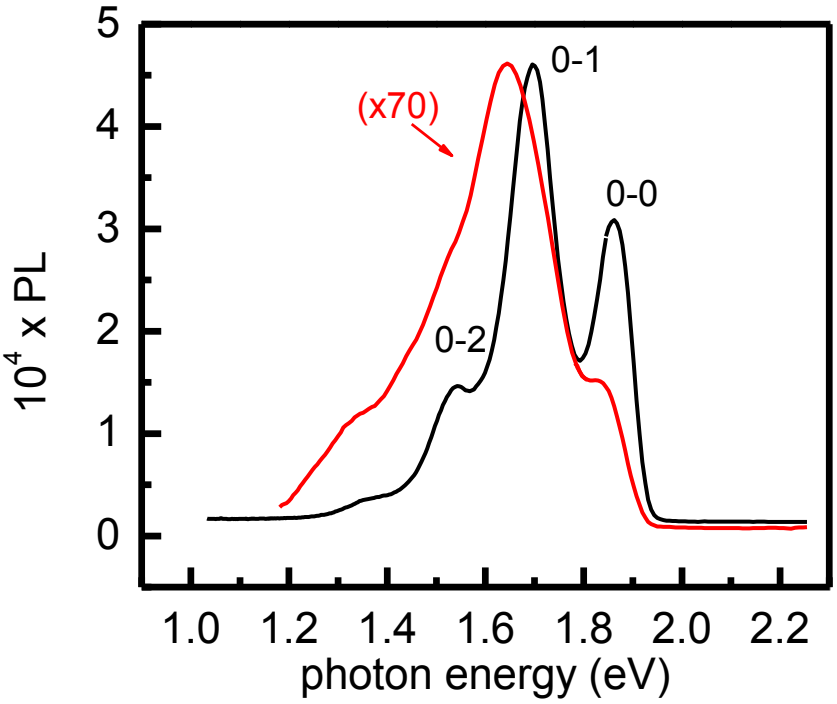

Figure 105 The PL spectra of RR P3HT/ICBA before (black) and after annealing (red) at 30 K and excitation wavelength of 488 nm.

where the PLQE decreases from ~1.2 % for the as cast sample to ~0.7 % for the annealed sample. On the other hand, the PL of the annealed film is broader and featureless compared to the film as cast. This can be attributed to the emission from the aggregates that form to a larger degree due to annealing. [129]

The PA spectrum (Figure 106) is dominated by polaron bands. P1 PA band is due to polarons on the polymer with a peak at ~ 0.1 eV, and is diminished with thermal annealing because of recrystallization of P3HT chains[130]. At ~1.25 eV we see a PA band due to polarons on ICBA. This band is slightly red shifted with annealing, indicating increased aggregation of ICBA. Delocalized P2 band due to polarons on the polymer increases in intensity with annealing process as well as photobleaching at ~2 eV.

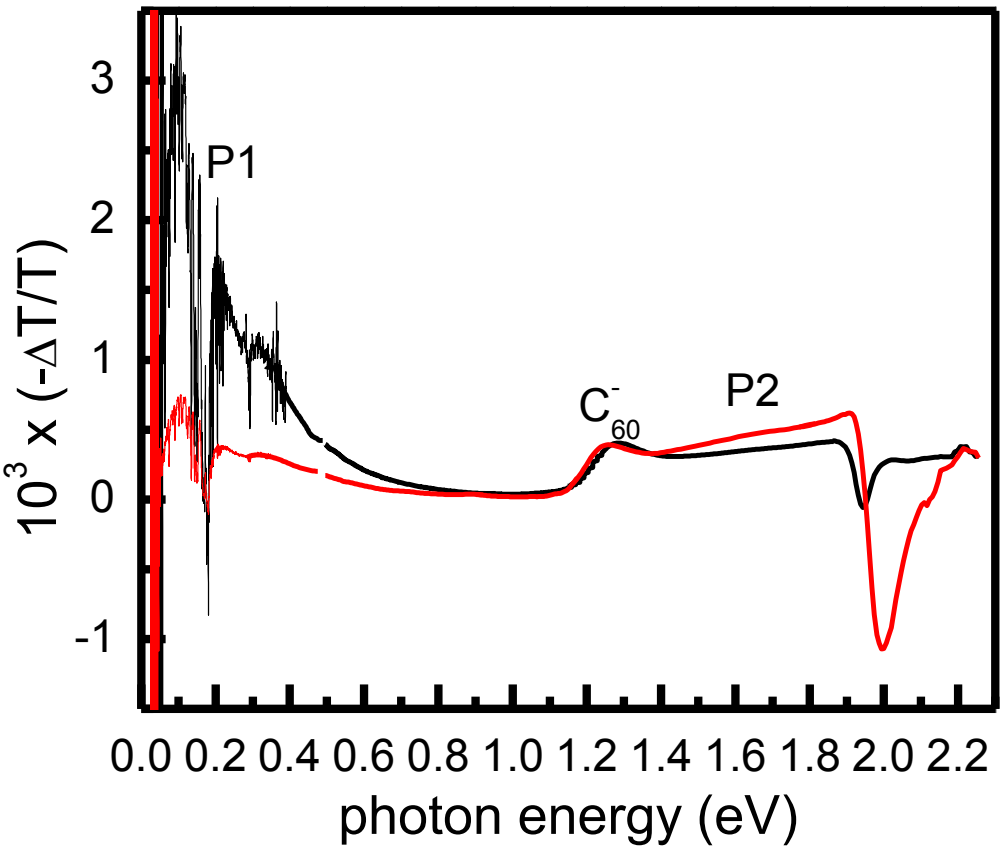

Figure 106 The PA spectra of RR P3HT/ICBA before (black) and after (red) annealing at 30 K and excitation wavelength of 488 nm.

In order to investigate the kinetics of PA bands in RR P3HT/ICBA blend we performed frequency dependent PA at four different photon energies (0.5 eV, 1,25 eV, 1.66 eV and 1.86 eV) and two laser powers, namely 100 mW and 400 mW. According to the results presented in Table 1, the mean lifetimes of polarons on the polymer and ICBA are dependent on excitation power and exhibit characteristics of bimolecular recombination. The recombination dynamics of photoexcitation at 1.86 eV seems to be somewhat different but still have a contribution of bimolecular recombination.

Table 1 Results of frequency dependant PA of RR P3HT/ICBA

Wavelength [nm]	Photon energy [eV]	Laser power [mW]	α Dispersive parameter	τ [s] the mean lifetime
667	1.86E+00	100	0.68	1.02E-03
667	1.86E+00	400	0.66	3.19E-04
747	1.66E+00	100	0.75	4.60E-04
747	1.66E+00	400	0.72	2.00E-04
992	1.25E+00	100	0.85	3.12E-04
992	1.25E+00	400	0.82	1.50E-04
2500	4.96E-01	100	0.75	3.32E-04
2500	4.96E-01	400	0.75	1.59E-04

5.4.3. Magnetic resonance studies

PADMR of RR P3HT/ICBA shows a spin ½ , ~20 Gauss narrow, asymmetric resonance at ~1000 Gauss (Figure 107). It is possible to fit the resonance with two Lorentzian lines. Consequently, we conclude that the resonance consists of at least two contributions, a ~14 Gauss narrow resonance centered at ~ 997 Gauss and a ~106 Gauss wide resonance centered at 994 Gauss. The area under the wide resonance is two times larger than the area under the narrow resonance indicating twice as many spin carriers. According to our previous studies we expect resonance contributions to be due to mobile polarons on the polymer chains and fullerene molecules and trapped polarons.

However, the 106 Gauss is too wide for a resonance caused by a spin ½ species.[59] It is likely that this resonance is caused by isotropic polaron pairs in triplet configuration resulting in a broad full field triplet (spin 1) powder pattern [137].

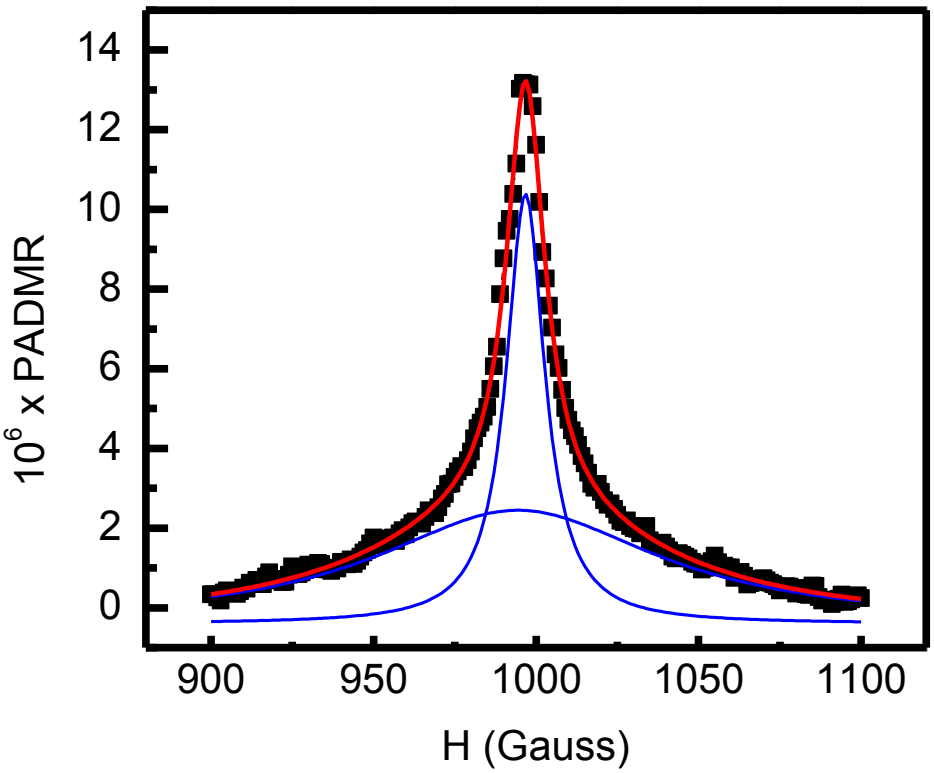

Figure 107 The PADMR of RR P3HT/ICBA at 1.6 eV (black full squares) fit with the sum (red) of two Lorentzian lines (blue). Measurement was done at 12 K, with 488 nm excitation wavelength, and 3 GHz microwave.

Further studies involving higher frequency microwave (9 GHz) can elucidate these resonance contributions. In Figure 108 δN/N (PADMR divided by PA) at different photon energy corresponding to PA bands is presented. We see that the intensity of δN/N changes with photon energy.The integrated PADMR as a function of microwave intensity at 1.6 eV and 1.25 eV is presented in Figure 109. The resonance due to polarons on ICBA saturates faster indicating longer spin-lattice relaxation times. The data were fit according to equation 5.1 and we get the following values of Ps, 9±3 for resonance at 1.6 eV and 21±3 for resonance at 1.25 eV.

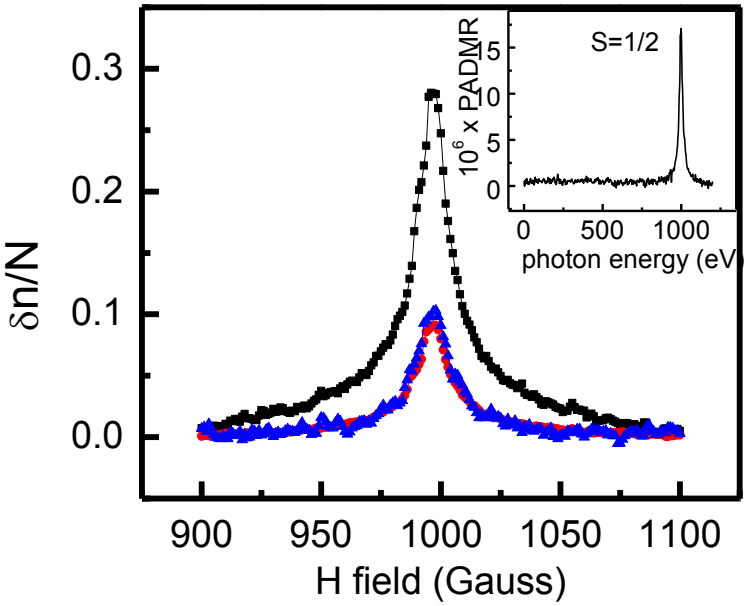

Figure 108 The PADMR of RR P3HT/ICBA blend normalized by PA at 1.6 eV - energy of P2 band (black), 1.25 eV –energy of the PA band due to polarons on ICBA (red), and 0.4 eV- energy of P1 PA band (blue). The inset shows PADMR scanned from 0 Gauss to 1200 Gauss with the narrow asymmetric resonance and no half field resonance due to spin 1.

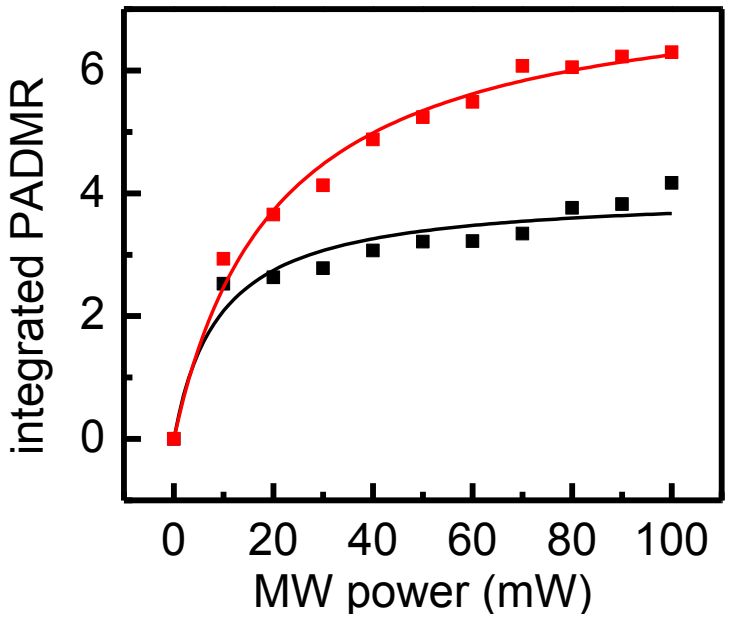

Figure 109 Integrated PADMR vs. microwave power at 1.6 eV-energy of P2 PA band (black) and at 1.25 eV-energy of PA band due to polarons on bis-PCBM (red).

The ESR measurements were taken at 78 K to avoid too long spin-lattice relaxation times. In Figure 110 three measurements are presented: ESR – before the sample was exposed to light, "light on" while sample was exposed to laser light, and "light off" taken immediately after the laser was turned off. The ESR and "light off" measurements are not identical, indicating that beside the prompt signal there is also the persistent contribution that originates from deep traps due to disorder.[119] The LESR shown in Figure 111 was obtained by subtracting ESR from "light on" consequently the signal is due to photogenerated species. The ESR signal of the blend is mostly due to ICBA as shown in Figure 112 .The intensity of "light on" signal is significantly larger than intensity of ESR.

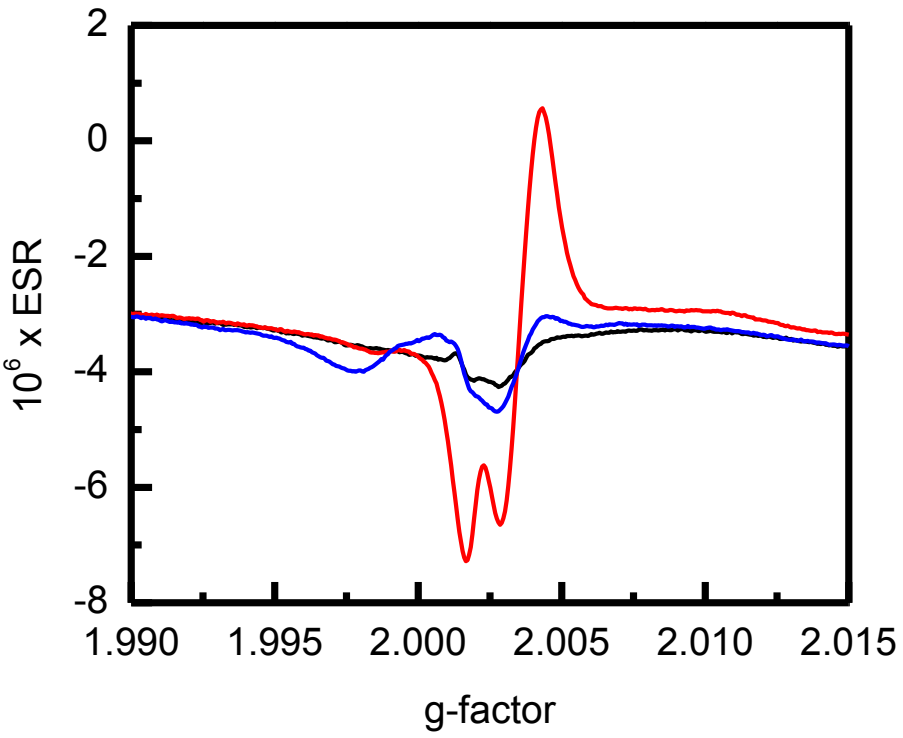

Figure 110 ESR (black), "light on" (red), and "light off" (blue) measurements of RR P3HT/ICBA annealed blend. The measurements were done at 78 K, with excitation wavelength of 488 nm and 100 mW power, and ~9 GHz microwave with 0.3 mW power.

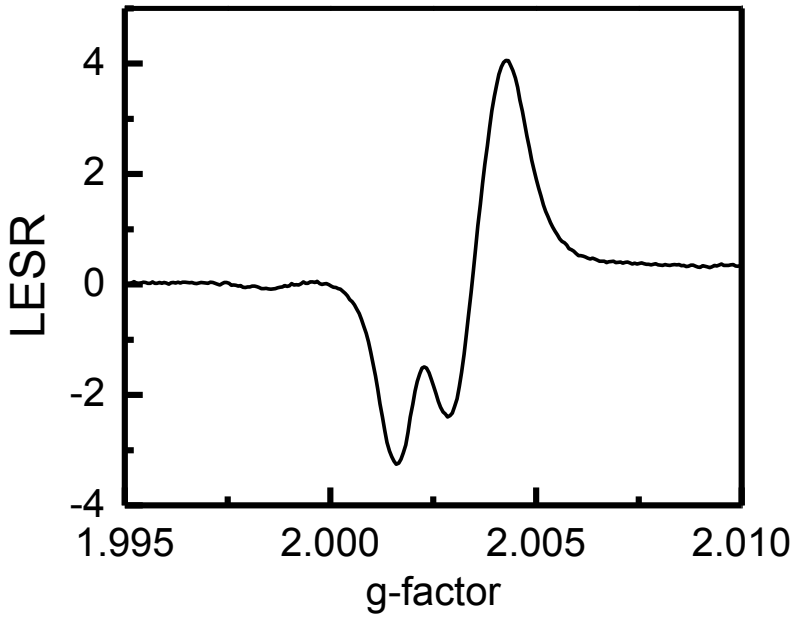

Figure 111 The LESR of RR P3HT/ICBA .

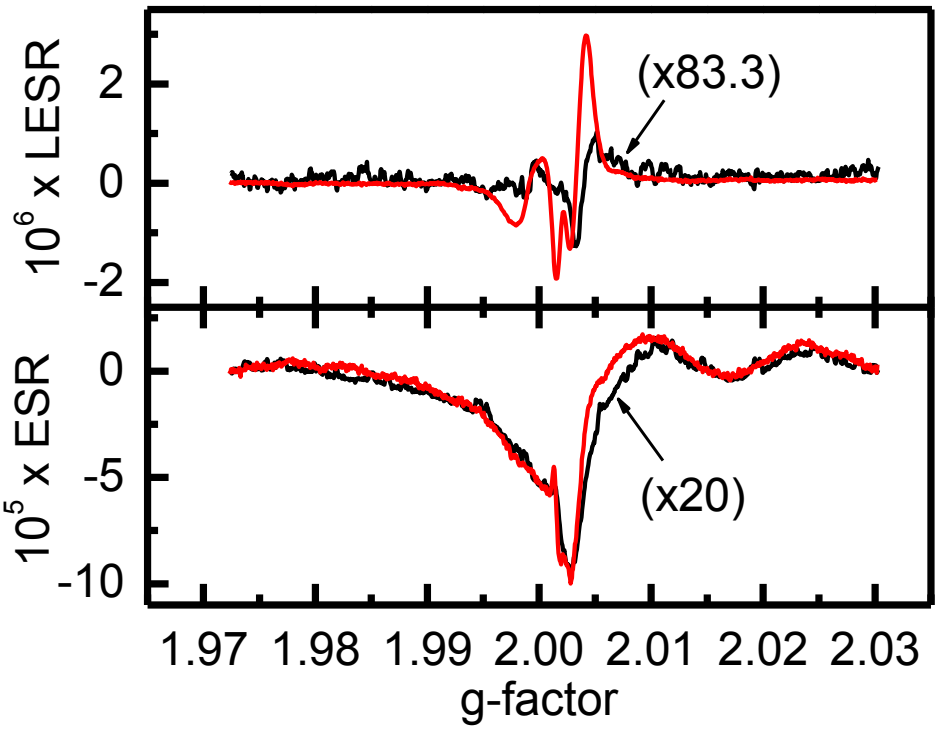

Figure 112 LESR and ESR of ICBA and its blend **a)** LESR of pure ICBA (black) multiplied by 83.3 and ICBA blend with RR P3HT (red); **b)** ESR of pure ICBA (black) multiplied by 20 and ESR of ICBA blend (red). Measurements were done at 78 K with laser power of 10mW.

Integrating LESR signal we get a spectrum that resembles the PADMR. Due to high frequency microwave we are able to resolve resonances due to mobile polarons on ICBA and P3HT, and trapped polarons.[120] The fit was done with three Lorenzian lines obtaining the following g-factors: 1.9988 due to mobile polarons on ICBA 2.0019 due to mobile polarons on RR P3HT, and 2.0033 due to trapped polarons. Figure 113 shows the fit of integrated LESR and the three resonance contributions. Again, if we assume that the area under integrated LESR line indicates the number of spin carriers [119], then the ICBA has ~4 times more mobile spin carriers than P3HT.

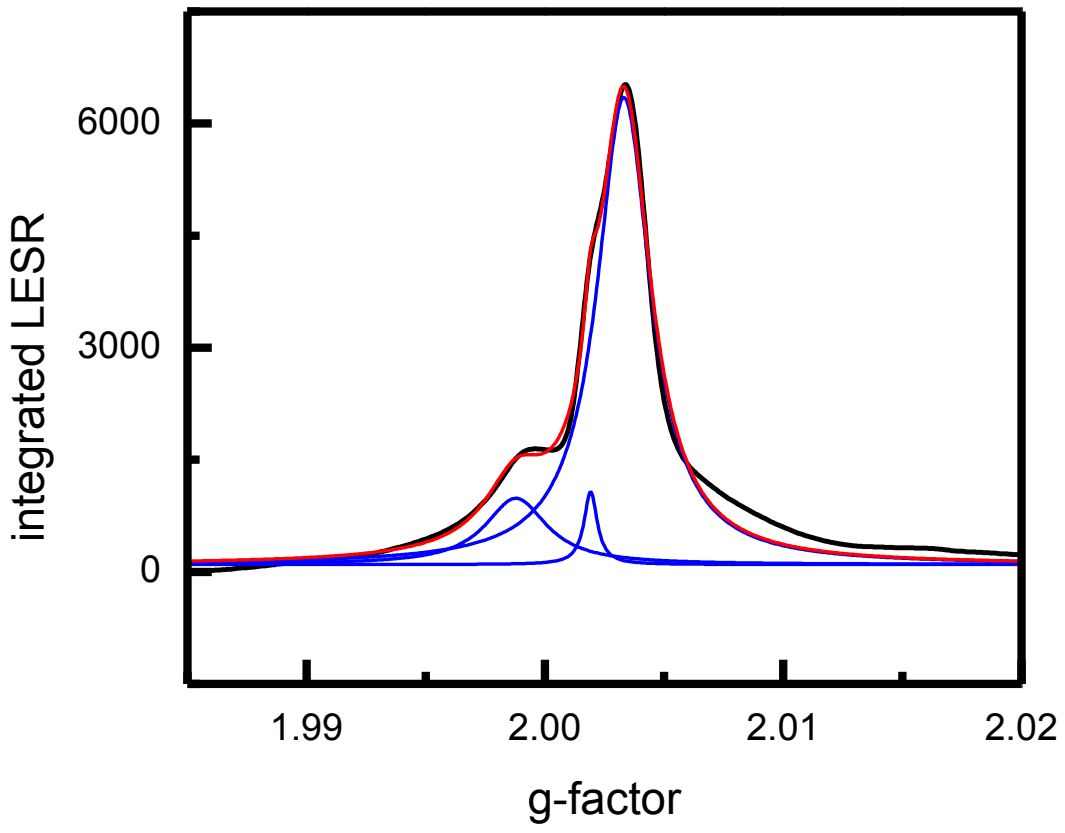

Figure 113 Integrated LESR (black) fitted with sum (red) of three Lorentzian lines (blue). The laser power was 50 mW.

Furthermore, we performed LESR measurements at different laser powers, namely 2 mW, 10 mW, 50 mW, and 100 mW. We see that the intensity of LESR signal due to polarons on the polymer chains increases with the laser power (Figure 114). However, the LESR signal due to the polarons on ICBA decreases with laser power, which can be seen in Figure 115, where we show the integrated LESR. Consequently, we conclude that polarons on P3HT and polarons in ICBA have different dynamics and saturation behavior.

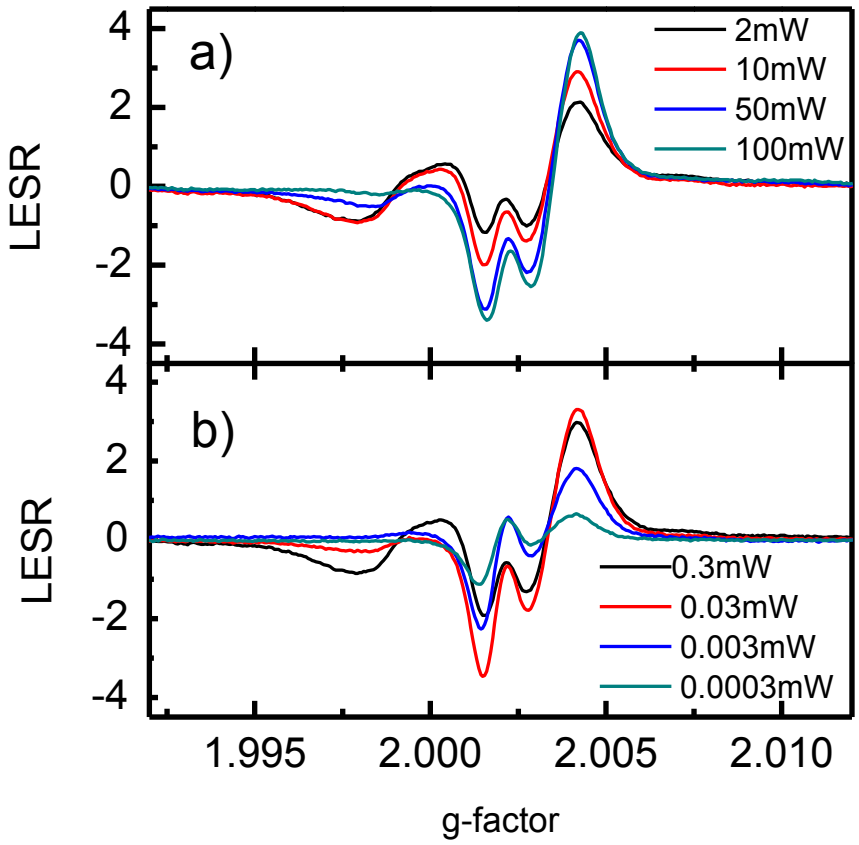

Figure 114 The LESR of RR P3HT/ICBA blend at 78 K **a)** at different laser power, **b)** at different microwave power.

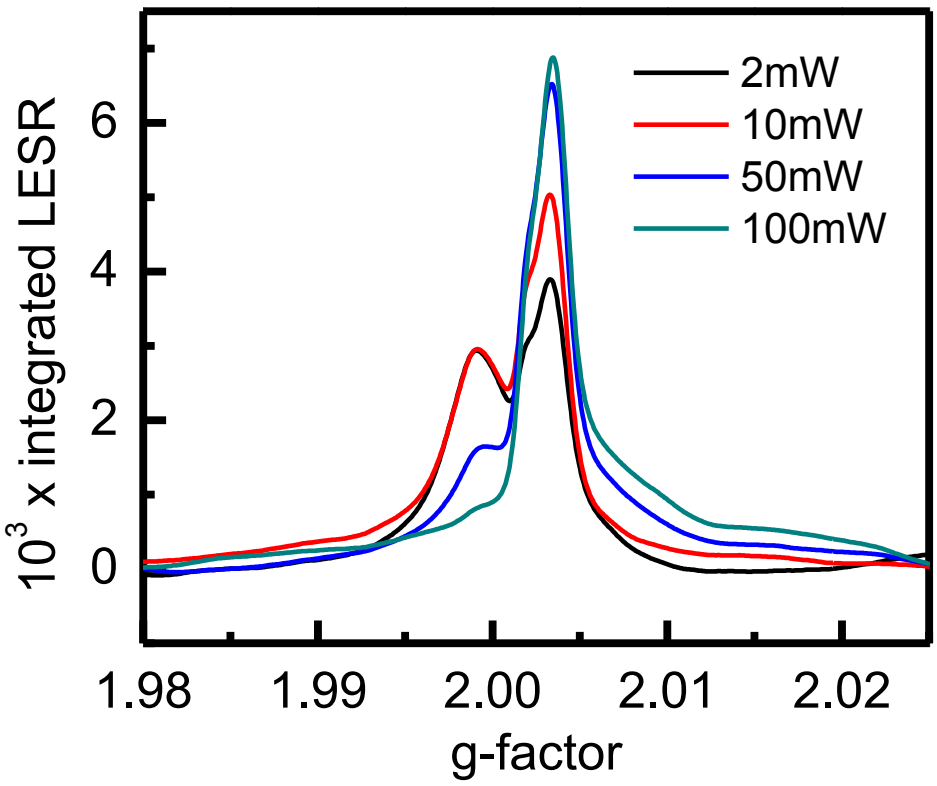

Figure 115 Inegrated LESR of RR P3HT/ICBA blend at 2 mW (black), 10 mW (red), 50 mW (blue), and 100 mW (turquoise) of laser power.

Also the saturation behavior of P3HT and ICBA polarons as a function of microwave power is very different. Consistent with our PADMR measurements the LESR signal due to polarons on P3HT saturates faster with microwave power than the LESR signal due to polarons on ICBA. This indicates that spin-lattice relaxation times for P3HT polarons are longer than for ICBA polarons.

5.4.4. Conclusion

According to our optical measurements when ICBA is mixed with P3HT due to its compact morphology it is capable to approach closely to P3HT chains and distort

packing. This is reflected in a high ration of 0-0 to 0-1 phonon side bands in PL spectra. The annealing process causes the ICBA molecules to be expelled from the polymer matrix and the P3HT is able to recrystallize. We can see that in PL spectrum by decreased ratio of 0-0 to 0-1 phonon side bands, decreased P1 PA band, increased delocalization of P2 PA band and photobleaching in photoinduced absorption spectrum. PADMR shows that the resonance is due to at least two polaronic contributions. However, with LESR we were able to resolve these contributions, find their g-factors, and assign them to mobile polarons on P3HT (g=2.0019) and ICBA (g=1.9988), and trapped polarons in P3HT matrix (g=2.0033). Frequency dependent PA measurement resulted in comparable mean lifetimes for mobile polarons at~0.5 eV, 1.25 eV, and 1.66 eV. However, the polarons at 1.86 eV have longer lifetime confirming the existence of trapped polarons that we see in LESR. Both PADMR and LESR results indicate that the number of mobile spin species on ICBA is larger than on P3HT.This can be either explained by existence of both positive and negative polarons in ICBA or by formation of spinless bipolarons on P3HT.

5.5. TAES-V/[C_{70}]PCBM

5.5.1. Introduction

In the previous sections of this chapter we focused on blends with acceptor materials with different LUMO levels and molecular structure. Here we will discuss the new donor material, TAES –V, supplied by Plextronics, Inc blended with $PC_{70}BM$. It is important to understand the photophysics of this blend, since it yields OPVC with power conversion efficiencies of ~7%.

5.5.2. Optical studies

As discussed in Chapter 3, TAES-V is a novel low band gap copolymer with absorption peak at ~2.1 eV. For this reason, to improve the absorption of the blend, instead of $PC_{60}BM$, $PC_{70}BM$ is used as an acceptor because of its enhanced absorption in the visible region as shown in Figure 116. The low absorption of $PC_{60}BM$ can be attributed to the high symmetry of C_{60} making the lowest energy transitions formally dipole forbidden. When the C_{60} moiety in PCBM is replaced with less symmetrical C_{70}, these transitions become allowed and absorption of the fullerene derivative increases.[76, 138]

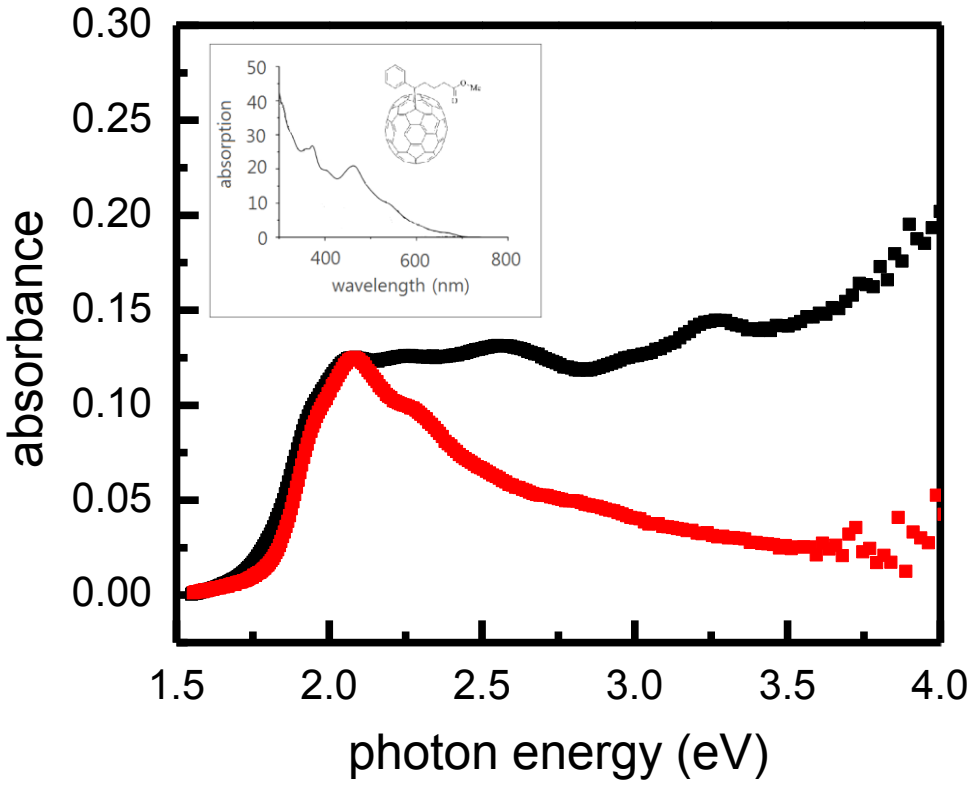

Figure 116 Ground state absorption spectrum of TAES-V/$PC_{70}BM$ (black) and pure TAES-V (red) films at ambient pressure and room temperature. The inset shows the absorption of pure $PC_{70}BM$ and its molecular structure.[76]

The PL spectra of both pure TAES-V polymer and TAES-V/PC70BM blend films are shown in Figure 117. Based on our results, we can conclude that the PL emission is entirely due to the polymer. The PL emission significantly decreases when TAES-V is blended with PC70BM (the inset of Figure 117) due to charge separation at the interface.[139] This is consistent with PL quantum efficiency that decreases from 17 % in pure polymer to 6 % in the blend. Moreover, the ratio of the intensity of 0-0 to 0-1 phonon side bands decreases in the blend indicating the formation of the aggregates.[46, 47] In addition, the PL spectrum of the blend is featureless compared to the pure polymer that might be caused by emission from the aggregates.[129]

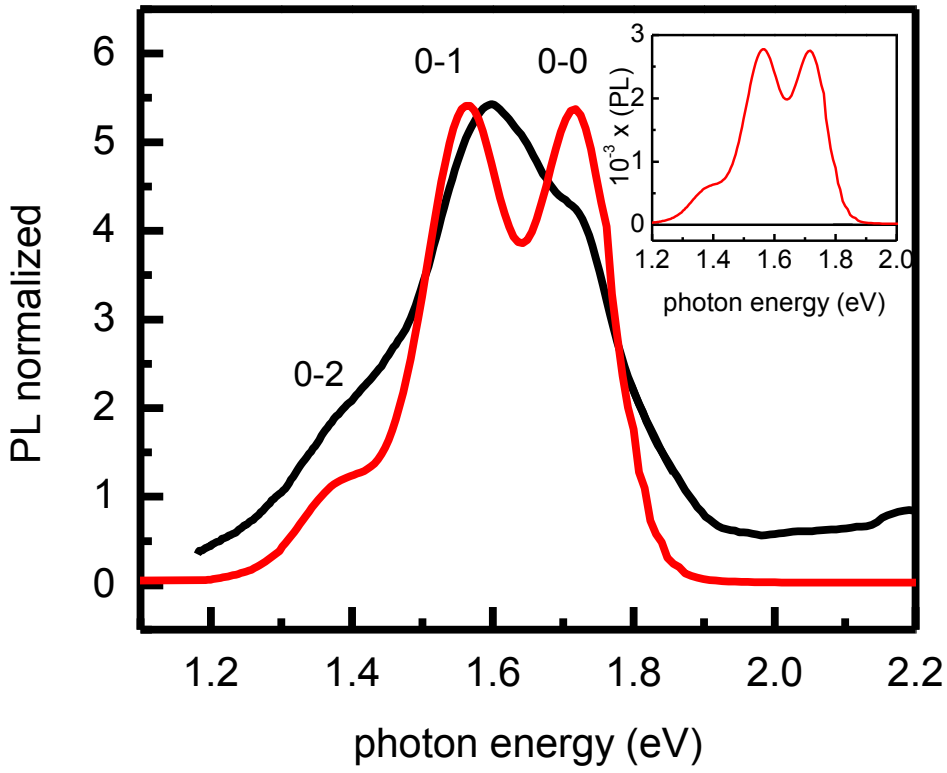

Figure 117 The normalized PL spectra of TAES-V/PC70BM blend (black) and pure TAES-V polymer (red) films. The inset shows the actual PL spectra without

normalization, where the PL of the blend is significantly diminished. The measurements were done at 50 K, the laser power of 100 mW and wavelength 514 nm.

The photoindeced absorption spectra of the pure TAES-V polymer and its blend with $PC_{70}BM$ are presented in Figure 118. With addition of $PC_{70}BM$ we break the packing of TAES-V chains and introduce disorder and therefore another PA band due to polaron in the polymer, P1 appears at a low energy.[130, 140]

In the pure polymer the PA spectrum is dominated either by triplet exciton or an intrachain CT exciton as discussed in Chapter 3. However, based on ps transient PA done in our group, we know that this band is excited instantaneously and therefore cannot be a triplet exciton. In the blend we see slight red shift of this band to 1.02 eV and an additional shoulder at ~ 1.2 eV that might be due to polarons on $PC_{70}BM$.

Well structured photobleaching (PB) appears at ~1.9 eV and its phonon replica at ~2.03 eV. Compared to the PA spectrum of the pure polymer the band at 1.9 eV does not seem to shift whereas the band at 2.03 eV slightly red shifts. This implies that these two bands are not of the same origin.

Figure 119 shows the electroabsorption spectrum of the blend that is proportional to the derivative of absorption. At ~ 1.93 eV we see zero crossing due to Stark shift of the lowest exciton state, 1Bu. There are also two well resolved phonon side bands related to 1Bu at ~1.94 eV and 2.09 eV. We also see an induced absorption feature assigned as mAg at ~2.44 eV. [141] According to this spectrum we do not see the signature of interchain CTC found at the photon energies below the gap.[142] However, in agreement with previously shown PB spectrum there is the intrachain CTE at ~ 1.9 eV. The separation of the EA contribution of excitons and continuum band was used to find the exciton binding energy, ~0.5 eV.[141-143]

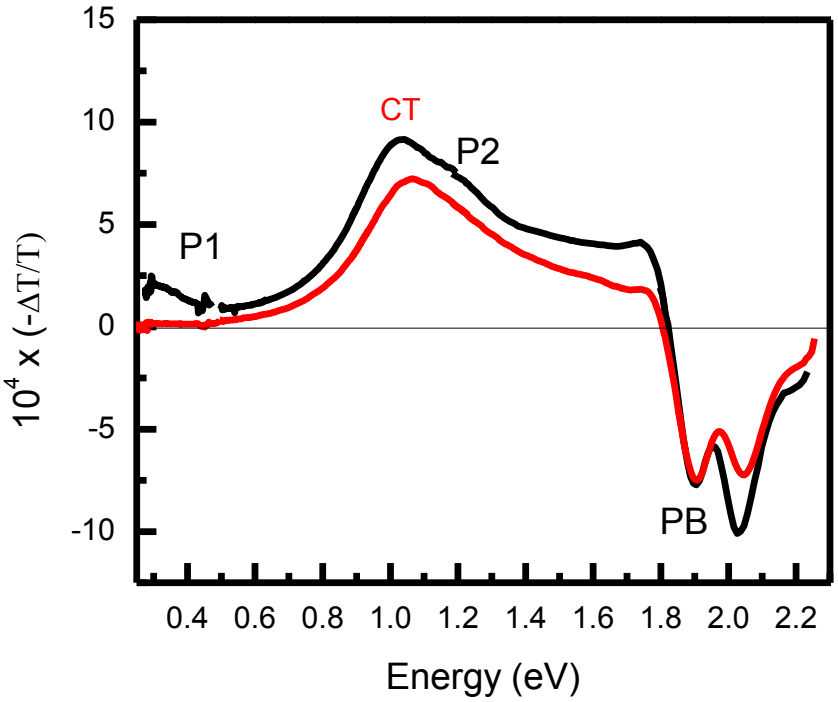

Figure 118 The photoinduced absorption spectra of TAES-V/$PC_{70}BM$ blend (black) and pure TAES-V film (red) with assigned PA bands. The measurements were done at ~50 K, with 100 mW of laser power and 514 nm wavelength.

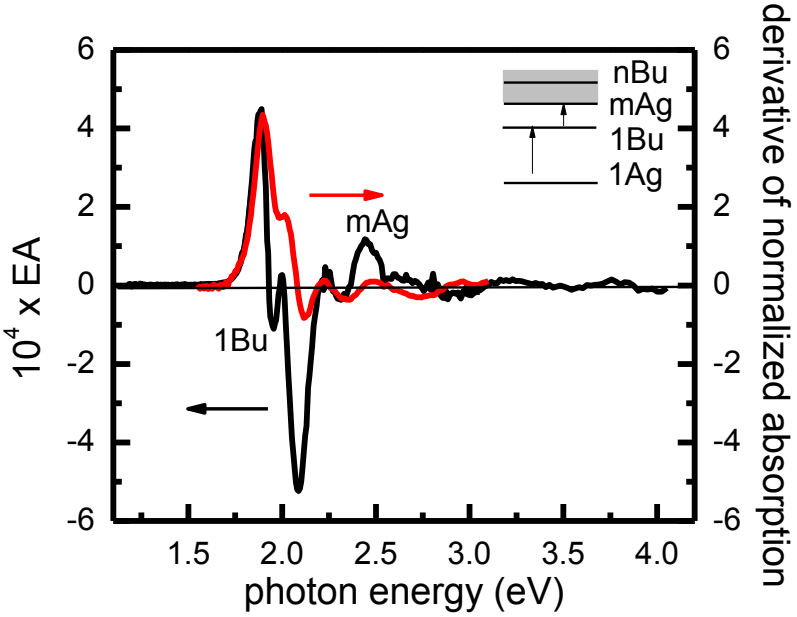

Figure 119 The electroabsorption spectrum (black) and derivative of absorption (red) of TAES-V/$PC_{70}BM$ film with energy level diagram. The measurement was done at ~50 K.

5.5.3. Magnetic resonance studies

To understand the nature of the photoexcitations dominant in the PA spectra we performed PADMR and PLDMR measurements.

Figure 120 shows the PADMR resonance of the TAES-V blend at 1.2 eV photon energy. The full H-PADMR spectrum consist of a narrow spin ½ resonance ~1000 Gauss and a half field spin 1 additional resonance at ~400 Gauss. The spin ½ resonance is somewhat asymmetric indicating that it might consist of contributions of both $PC_{70}BM$ and TAES-V polarons. Consequently, the PA band at 1.2 eV is due to polarons from the fullerene and the polymer. On the other hand, PADMR that was done at 1.07 eV (Figure 121) shows significantly weaker spin resonance at ~1000 Gauss and much stronger HF spin 1 resonance. This confirms that the PA band at 1.07 eV might be due to intrachain CT exciton. In contrast with our previous experience with blends, the PLDMR (Figure 122) of this blend is much stronger than the PADMR and has much better signal-to-noise ratio. We see very strong spin ½ resonance at ~1000 Gauss and distinct HF spin 1 resonance at ~400 Gauss.

The λ-PADMR spectrum is presented in Figure 123. The photoinduced absorption measurement from 0.8 eV to 2.3 eV was first done at 0 Gauss magnetic field and then at 1000 Gauss resonance condition. The magnetic field does not cause much change in PB energy range. However, at 1000 Gauss the PA band at 1.07 eV gets diminished. This observation is in agreement with our H-PADMR measurement at 1.07 eV. The 1.2 eV PA band persists under the resonant condition, which is again consistent with our H-PADMR

measurement at 1.2 eV. Moreover, an additional PA band at 1.6 eV appears under the resonant condition.

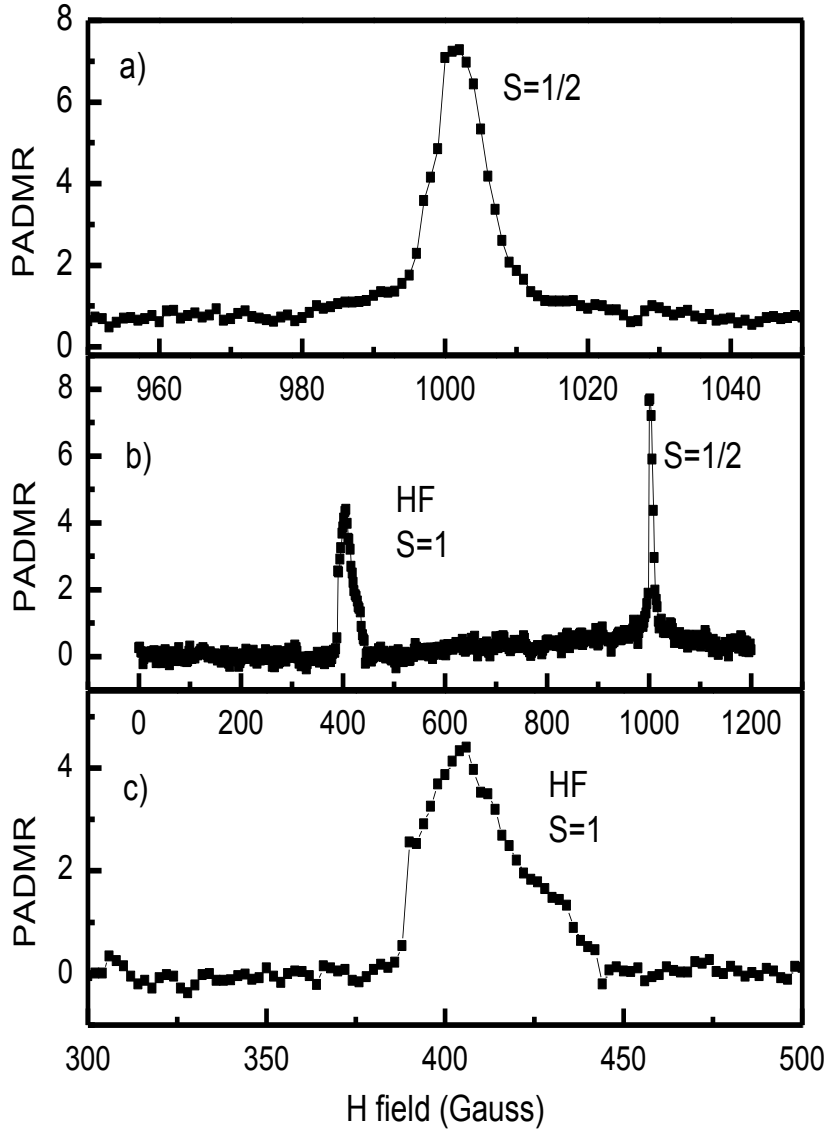

Figure 120 The PADMR of TAES-V/PC70BM blend at 1.2 eV: **a)** the somewhat asymmetric resonance due to doublet (spin ½) at ~1001 Gauss, **b)** the PADMR scanned from 0 to 1200 Gauss with resonances due to spin 1 and spin 1/2 , **c)** HF S=1 resonance at ~404 Gauss. The measurement was done at 10K, with 500 mW laser power and 514 nm wavelength.

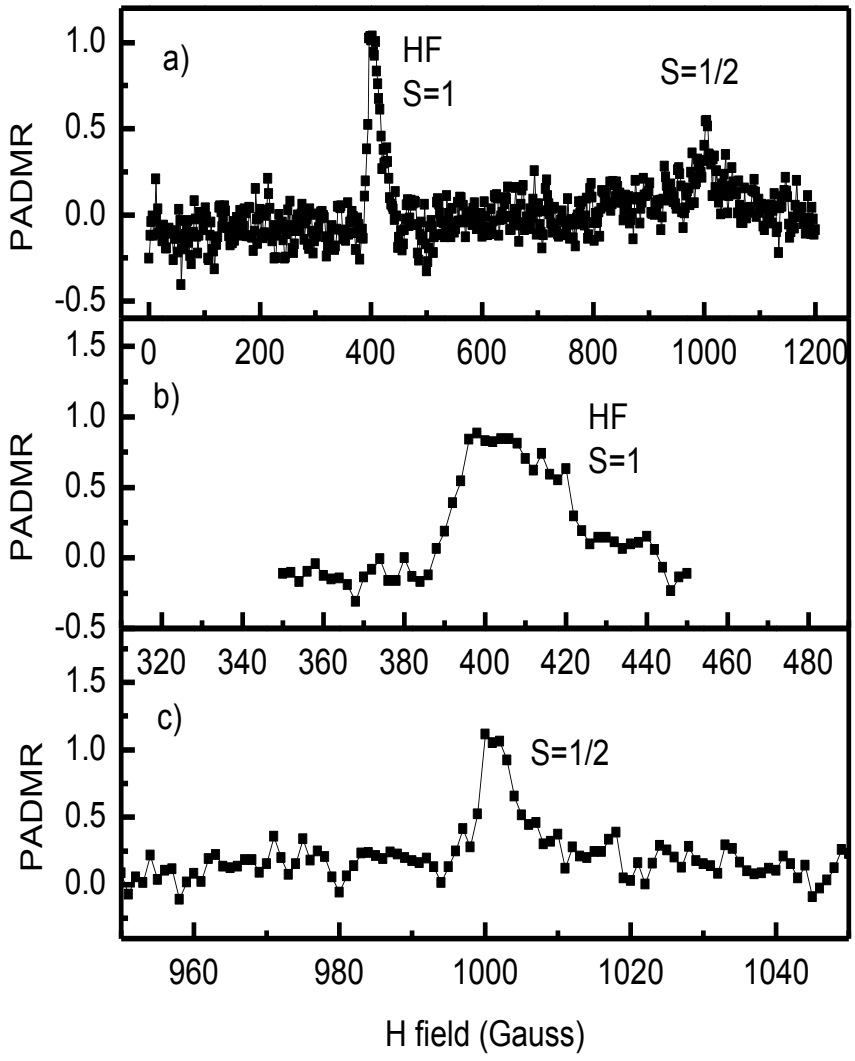

Figure 121 The PADMR of TAES-V/PC70BM blend at 1.07 eV: **a)** the PADMR scanned from 0 to 1200 Gauss with resonances due to spin 1 and spin 1/2 , **b)** HF S=1 resonance at ~400 Gauss **c)** the weak resonance due to doublet (spin ½) at ~1000 Gauss. The measurement was done at 10K, with 500 mW laser power and 514 nm wavelength.

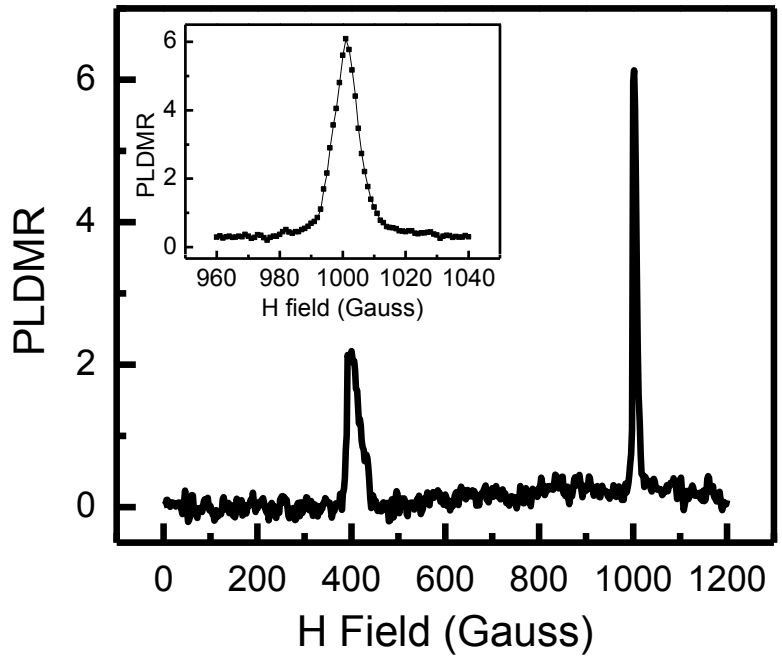

Figure 122 The PLDMR of TAES-V/PC70BM blend with resonances at ~1000 Gauss due to spin ½ and HF spin 1 resonance at ~400 Gauss. The inset shows the spin ½ resonance averaged over several measurements.

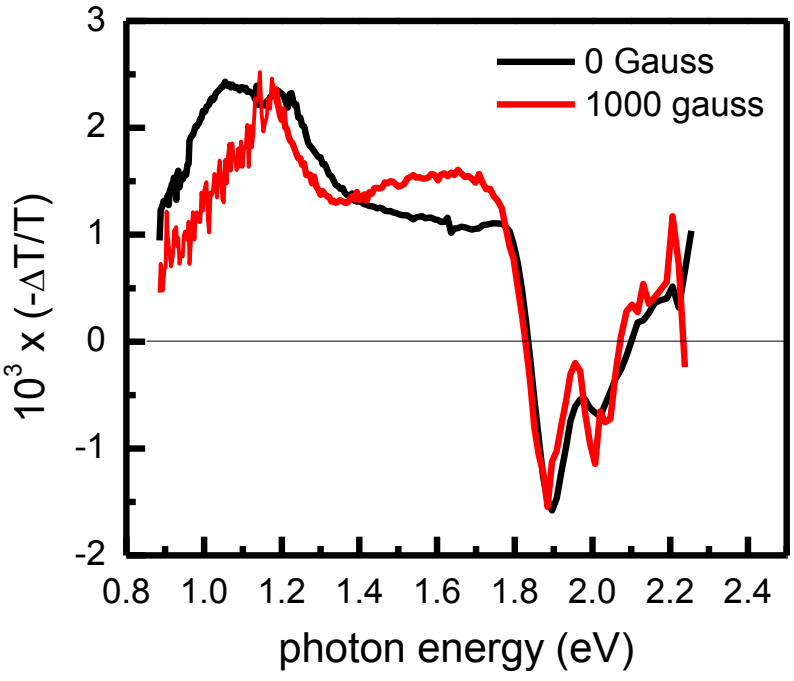

Figure 123 The PA spectra of TAES-V/PC70BM blend at 0 Gauss and 1000 Gauss.

When the PADMR resonance saturation behavior of TAES-V/PC70 blend is compared to RR P3HT/PCBM blend we conclude that TEAS-V blend does not saturate much faster with the microwave power. Using equation 5.1 we can fit the data in Figure 124 and extract P_S for both blends, 24 ± 6 for RR P3HT blend and 18 ± 2 for TAES-V blend. We can see that the standard deviation is too large to draw the conclusion that TAES-V has larger spin-lattice relaxation time than the RR P3HT blend.

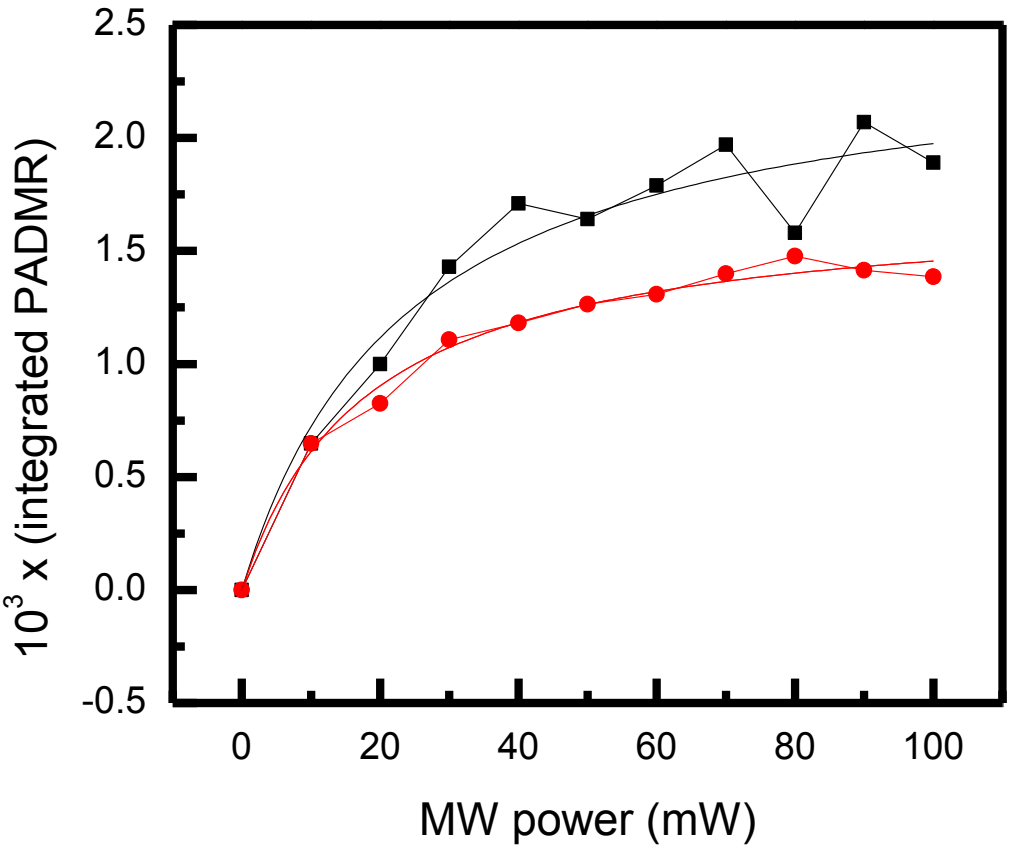

Figure 124 The integrated PADMR spin ½ resonance as a function of microwave power for RR P3HT/PCBM (black) and TAES-V/PC70BM (red).

In the past we were been able to resolve the resonance contributions by using an LESR apparatus with a higher microwave frequency (~9GHz). Figure 125(a) shows the LESR of TAES-V blend. It is worth noting that in this blend the "light on" signal is not much larger (just by factor of 2 or 3) than ESR signal as shown in Figure 125(b). There is a slight difference between the ESR and "light off" signals indicating existence of trapped charges. When LESR of the pure polymer is compared to the LESR of the blend (Figure 126), we can see that addition of PC70BM causes an increase of the intensity of the signal. We also can see an addition to the resonance at the lower g-values due to $PC_{70}BM$ polarons. When integrated the LESR signal can be fit it with four Lorentzian lines, instead of three in the pure polymer (Figure 127). We obtained the following g-factors: 1.9898 ± 0.0002, 2.00081±0.00006, 2.00231±0.00001, and 2.0059±000003. The last three g-factors are close to the g-factors that we obtained for the pure TAES-V polymer, namely 2.00078 ± 0.00008, 2.00214±0.00002, and 2.00537±0.00004 in Chapter 3. Therefore these g-factors can be assigned to resonances due to donor and acceptor moieties, as well as trapped polarons. [119] The negative resonance may be due to trapped polarons. The standard deviation of g-factors is meaningless because the ESR apparatus is limited in measuring g-factor beyond the fourth decimal digit.

It is also worth noting, that according to Figure 127 the contribution of polarons on $PC_{70}BM$ is smaller than the contribution of polarons on the polymer which is consistent with existence of both donor and acceptor blocks in this copolymer.

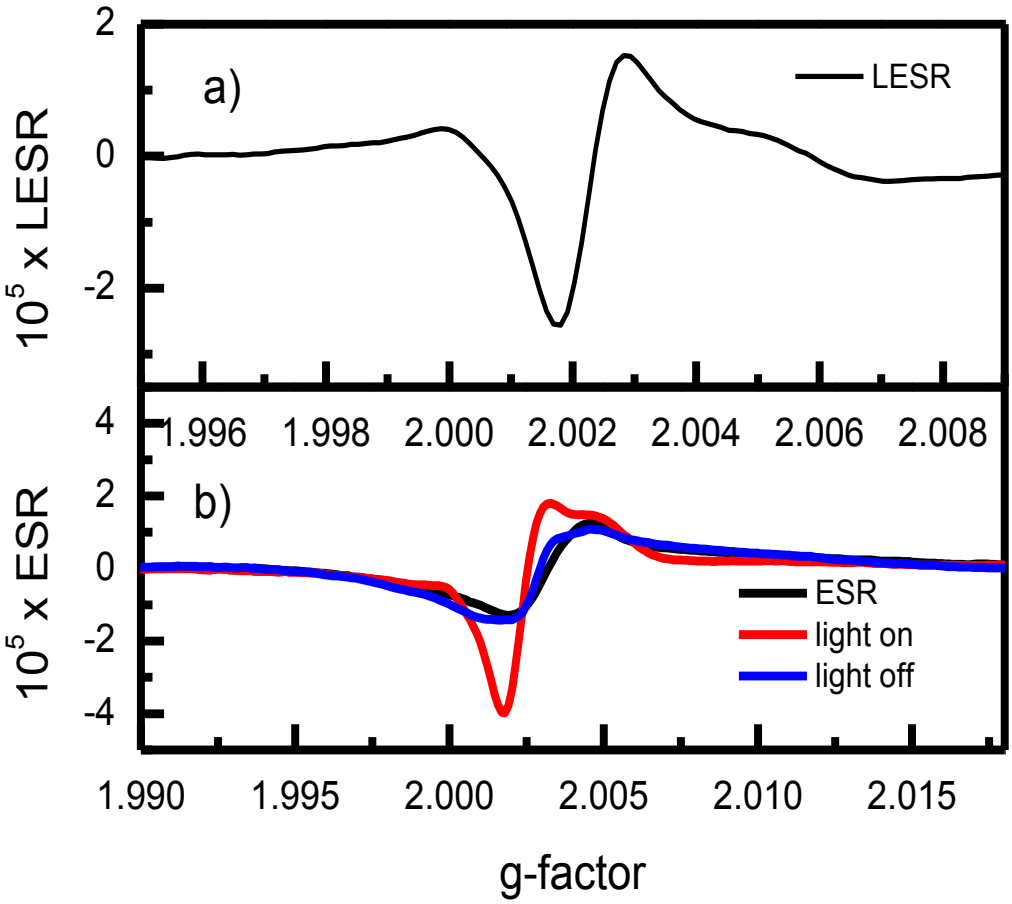

Figure 125 TAES-V/$PC_{70}BM$ blend **a)** the LESR, **b)** ESR (black), "light on" (red), and "light off" (blue). The measurement was done at 78 K.

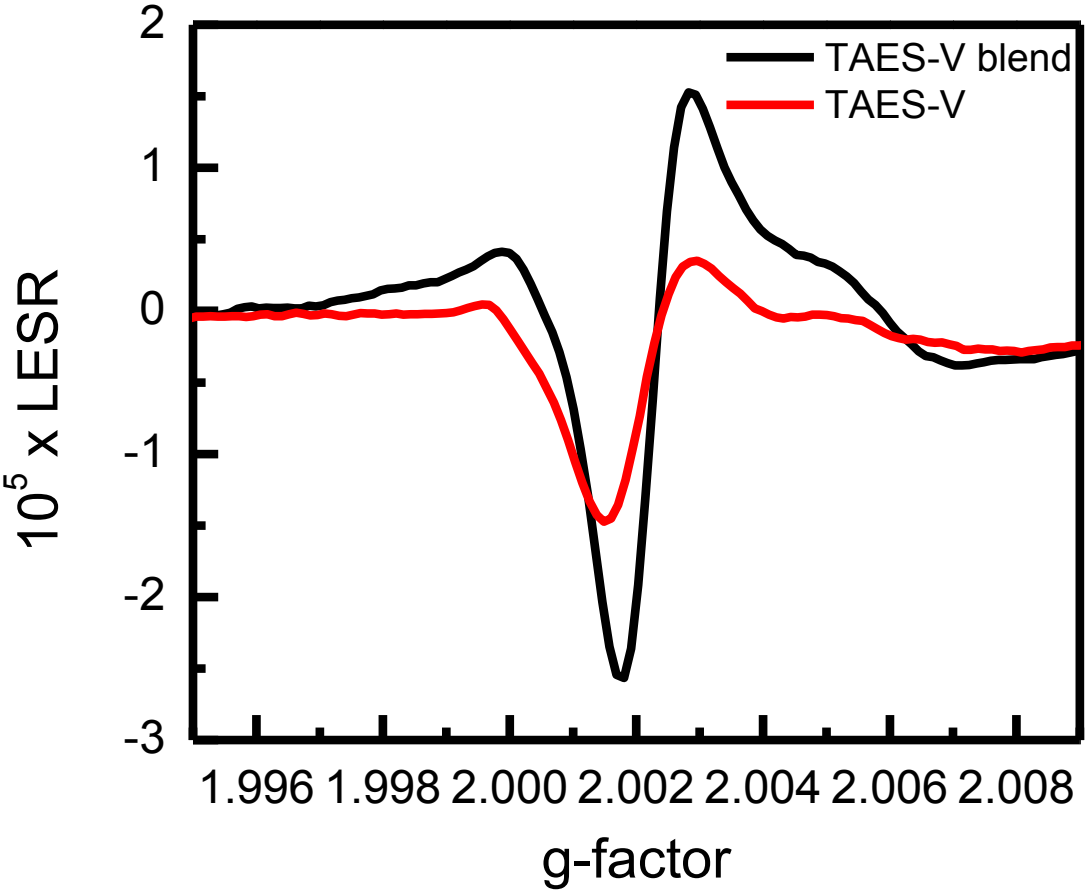

Figure 126 The LESR of TAES-V/PC70BM blend (black) and pure TAES-V polymer (red). The measurement was done at 78K.

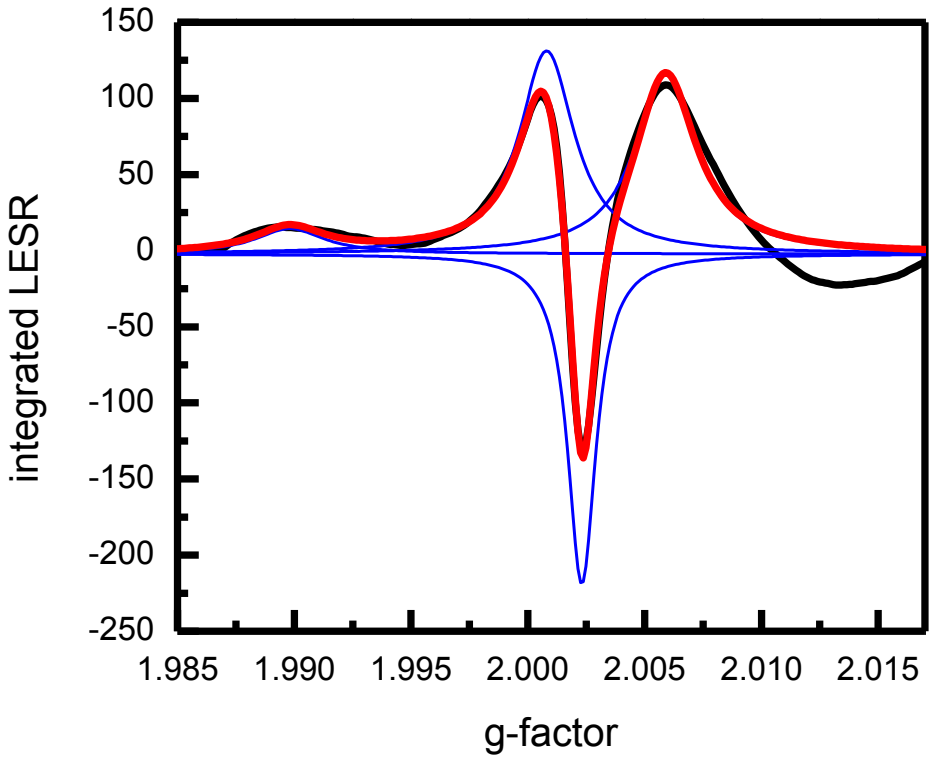

Figure 127 The integrated LESR of TAES-V/$PC_{70}BM$ blend fit with four Lorentzian lines. The four resonance contributions have the following g-factors: 1.990, 2.0008, 2.002, and 2.006.

5.5.4. Conclusion

TAES-V low band gap copolymer when blended with PC70BM yields organic solar cells with higher power conversion efficiency than any other blend studied here. The pure TAES-V consists of both donor and acceptor moieties that cause the rise of intrachain CT exciton examined in Chapter 3. Based on photoinduced absorption, electroabsorption and PADMR studies the intrachain CT exciton still persist in the blends and we do not see a signature of interchain charge exciton. The charge separation at the interface of the polymer and the fullerene still occurs based on decreased PL and PLQE when PC70BM is introduced in the polymer matrix. Based on our H-PADMR and λ-

PADMR studies the PA band at 1.2 eV is caused by polarons on both polymer and fullerene. However, we have an additional band showing up at ~1.6 eV at resonance condition that might be due to polaron pairs. LESR of the blend is mostly due to the pure polymer with a small addition of negative $PC_{70}BM$ polarons. In contrast to RR P3HT/PCBM blend in this case the most charges are located on the polymer.

5.6. General conclusion

Since optimizing of RR P3HT/PCBM blend seems to reach its limit, there are two main approaches in improving PCE of OPVC, namely modifying a donor or acceptor material. In this chapter we studied four different blends RR P3HT/PCBM, RR P3HT/bis-PCBM, RR P3HT/ICBA, and TAES-V/$PC_{70}BM$. Our project encompassed both approaches to the improvement of power conversion efficiency of an organic solar cell, namely raising the LUMO level of the acceptor and lowering the LUMO level of the donor.

First we replaced PCBM with bis-PCBM and ICBA. Both acceptors yield better power conversion efficiencies than PCBM blend. This is mainly due to the higher LUMO level and improved V_{oc}. The morphology of the blend also plays a significant role. Bis-PCBM is bulkier with its two side-chains than the PCBM molecule and it is not capable of destructing the packing of the P3HT chains as much as PCBM. ICBA is compact and it is able to approach the P3HT chains much closer. However, the thermal annealing process helps to expel the fullerene molecules out of P3HT chains and restore the crystallites. Based on magnetic resonance studies we see in all of three blends with P3HT more polarons on the fullerene molecules than on P3HT chains. This could be due

either to formation of spinless bipolarons on the polymer or the existence of both positive and negative polarons on the fullerene aggregates.

The second approach to improve the PCE is to modify the donor polymer. Here we studied a blend of a low-band gap copolymer TAES-V, which has both donor and acceptor moieties on its chains. Based on photoinduced absorption, electroabsorption, and PADMR experiments we see that intrachain CTE persists in the blends. We were not able to see the signature of interchain CTE in the electroabsorption spectrum. We conclude that the dominant PA band at 1.07 eV might be due to intrachain CT complex in triplet configuration and the PA band at 1.2 eV to polarons on both the polymer and the fullerene. The LESR studies indicated that there are more charges on the polymer than on the fullerene in contrast to the other three blends.

In conclusion it seems that modification of a donor material is so far a more successful approach to the improvement of the power conversion efficiency of organic solar cells.

CHAPTER 6

ISOTOPE EFFECT IN SPIN RESPONSE OF II-CONJUGATED POLYMER FILMS

6.1. Introduction

Hyperfine interaction (HFI) has an important role in organic magneto-electronic devices[144] and spin response processes such as ODMR in organic semiconductor films.[145] In this study we replaced all strongly coupled hydrogen atoms (^{1}H with nuclear spin $I=^{1}/_{2}$) in the organic π-conjugated polymer poly(dioctyloxy) phenylenvinylene (DOO-PPV, called H-polymer in this study with deuterium atoms (^{2}H with nuclear spin I=1, called D-polymer) as shown in Figure 128. This way we can alter HFI, mainly HFI constant a, that determines spin-relaxation time, T_{SL} of spin carriers. For devices such as organic spin-valves (OSV) this means that injected carriers will have different spin diffusion length changing its performance. Here we will concentrate on studying spin influence on hydrogen isotope exchange on the magnetic response in ODMR of thin films, where spin-dependant recombination of photogenerated spin ½ polaron pairs is enhanced under magnetic resonance conditions.

Published in Nature Materials 9, 345-352 (2010) by Tho D. Nguyen, Golda Hukic-Markosian, Fujian Wang, Leonard Wojcik, Xiao-Guang Li, Eitan Ehrenfreund and Z. Valy Vardeny

Figure 128 D- and H- polymer structures and their basic optical properties. a, The photoluminescence spectra of the D- and H- polymers, which show a two-phonon replica. The inset shows the resonant Raman spectra of the two polymers, where the vertical lines emphasize the D-polymer frequency redshift the C-C (~1300cm^{-1}) and C=C (~1500cm^{-1}) stretching vibrations, respectively. **b, c,** The basic repeat unit of the synthesized D- and H-DOO-PPV polymers. H- and D- stand for protonated (^{1}H) and deuterated (^{2}H), respectively, and R^1 is an end-capped molecule used to terminate the polymerization process.

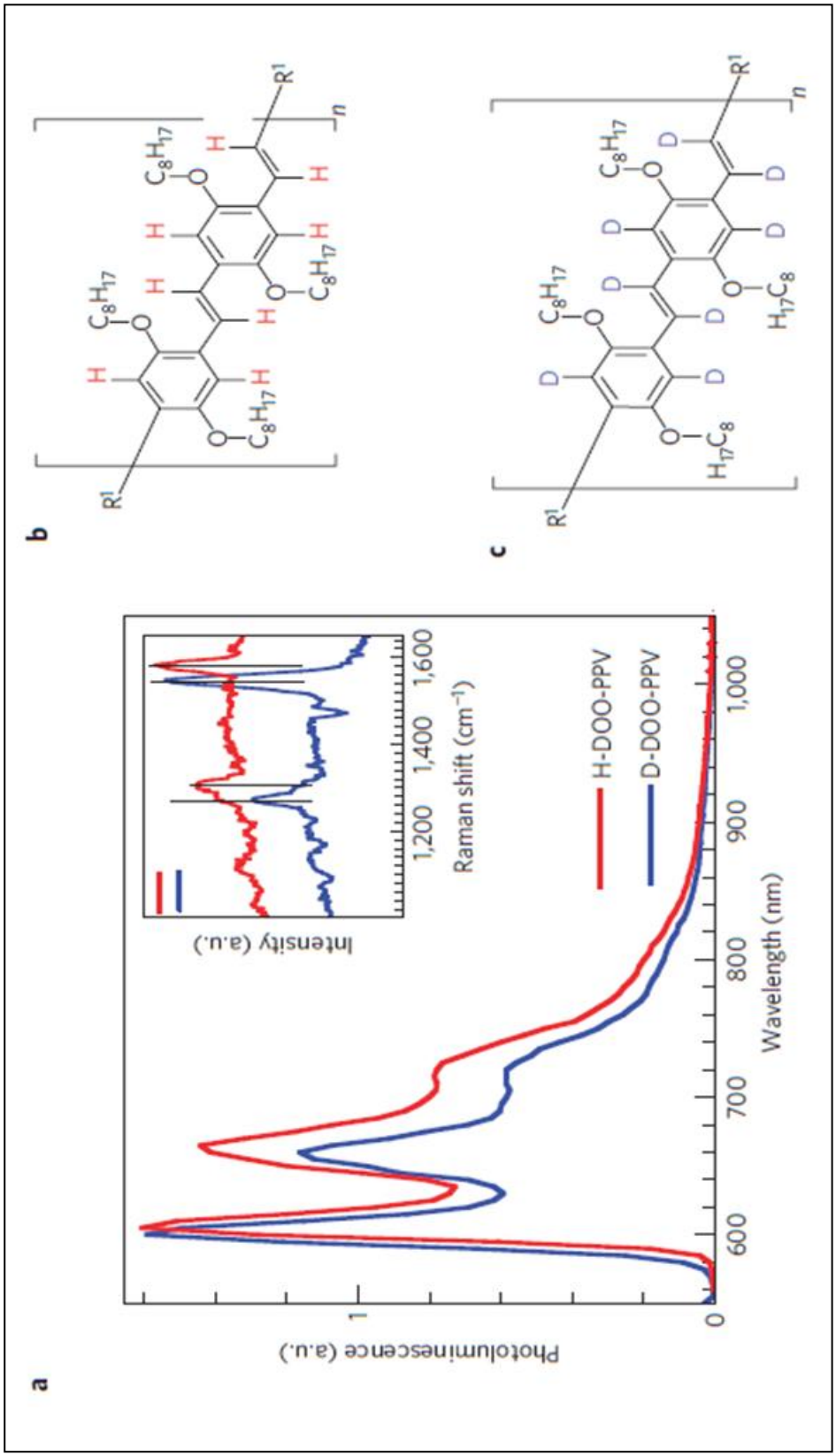
a
Photoluminescence (a.u.)
1
0
600
700
800
900
1,000
Wavelength (nm)
H-DOO-PPV
D-DOO-PPV
Intensity (a.u.)
1,200
1,400
1,600
Raman shift (cm⁻¹)
b
c

6.2. Polaron spin ½ resonance line broadening due to hyperfine splitting and inhomogeneity

The spin ½ density of the polaron excitation in π-conjugated polymer chains is usually spread over several repeat units, which may consist of about N=10 CH building blocks.[146] Consequently the polaron spin1/2 ODMR (and ESR) line shape at resonance conditions is susceptible to interactions with N protons in the immediate vicinity of the backbone intrachain carbon atoms. Having nuclear spin ½, each coupled proton splits the two electron-polaron spin levels (ms=±1/2) into two electron-polaron/proton levels via hyperfine interaction (HFI); and these lines are further split by the other N-1 coupled protons[147]. Therefore, the energy levels of the ensemble system containing one electron-polaron and N protons depend on the HFI constant a and field B, which is given by Hamiltonian:

$$\mathcal{H} = \mathcal{H}_{HF} + \mathcal{H}_{Z} \tag{6.1}$$

In equation (6.1) $\mathcal{H}_Z = g\mu_B B S_Z$ is the electronic Zeeman component (we ignore nuclear Zeeman interaction), and $\mathcal{H}_{HF} = (\sum_n a_n \boldsymbol{S} \cdot \boldsymbol{I_n})$ is isotropic HFI term. Here a_n, $\mathbf{I_n}$ (I_n=½) are the HFI constant and nuclear spin operator of the n-th nucleus (n=1,…,N), and **S** (S=$^1/_2$) is electron–polaron spin operator. Solving Hamiltonian equation (6.1) in the high field limit ($\mu_B B >> a$) we obtain that each of the $m_s=\pm^1/_2$ electron-polaron energy level splits into 2^N levels for (I=$^1/_2$). As a result there are 2^N $m_s=^1/_2$ to $m_s=-^1/_2$ allowed optical transitions in the GHz range (hereafter, 'satellite lines') that leave the nuclear spins unchanged. In general, the satellite lines do not have equal spacing since a_n in equation (6.1) are not equal to each other in the most general sense. The satellite lines

form a distribution in B of which width, Δ_{HF}, can be conveniently calculated from the square root of the second moment[147]:

$$\Delta_{HF} = 2[\sum_n (B_n - B_0)^2 / 2^N]^{1/2}, \quad (6.2)$$

where B_0 is the resonance field in the absence of HFI, and B_n are the resonance fields for the satellite lines. For a uniform spin distribution we take a_n=a/N; and consequently there are N+1 nondegenerate electron/proton energy levels, which when using equation (6.2) give Δ_{HF}~a/√N. Under this condition we find for the polaron excitation in DOO-PPV polymer chans with N=10, Δ_{HF}~0.3a.

In amorphous solids such as π-conjugated polymer films, the spin ½ resonance line is inhomogeneously broadened. In this case the HF split resonance is composed of 2^N (or N+1 for a_n constant and I=$^1/_2$) bands centered at B_n, each having a line shape, L(B-B_n) with full width at half maximum (FWHM), Δ_L that is determined by the inhomogeneity in the sample. When the inhomogeneous broadening Δ_L is large enough such that the HFI split resonance appears as a single, nonsplit continuous band (i.e., $\Delta_L > \Delta_{HF}$). Then the composite resonance FWHM is approximately given by the sum $\Delta_{HF}+\Delta_L$.

6.3. ODMR

For the ODMR investigations, we used and S-band resonance system at ~3GHz and 10K where the microwave power, P_{MW}, was modulated at ~200Hz. The photoluminescence intensity increases as a result of enhancement of photogenerated polaron-pair recombination in the polymer film on microwave absorption at resonance; therefore, the ODMR signal appears at B~100mT, which corresponds to spin-1/2 species

with g≈2. Figure 129(a) and b show the spin-$^1/_2$ ODMR polaron pairs in H- and D-polymer films, respectively. Importantly, the resonance in the D-polymer is narrower than that in H-polymer; at small P_{MW} the resonance full-width at half maximum is $\delta B_D \approx 0.7$mT in D-polymer compared to $\delta B_H \approx 1.2$mT in the H-polymer (Figirue 129(c)). As a(D)=a(H)/6.5[147], we expect to obtain a much narrower δB_D; however, δB is also determined by the wavefunction extent of the polaron on the polymer chain, which determines its spin-density spread on the number of hydrogen nuclei, N, of the polymer chain[148] . Thus, a and N together determine and 'intrinsic' HFI linewidth, δBHF, which for spin-1/2 nuclei is approximately given by $\delta B_{HF}=a/\sqrt{N}$. In addition, the inhomogeneous broadening causes an 'extrinsic' linewidth, δB_{inh}. When $\delta B_{inh} < \delta B_{HF}$, the resonance linewidth δB, can be approximately written as:

$$\delta B \approx \delta B_{HF} + \delta B_{inh} + \delta B_0, \tag{6.3}$$

where δB_0 ($<\delta B_{HF}$) is the homogeneous linewidth ($\sim 1/T_2$, the dephasing rate). The spin density distribution among N C-H units decreases the effective HFI, a_{eff}, of each nucleus; a uniform polaron spin distribution leads to $a_{eff}=a/N$[148]. For the H-polymer, HFI with one spin-1/2 nucleus splits the resonant lines into two separate lines, with ΔB=a [149]. With electronic spin distribution on N nuclei, the two lines are further split into (N+1) satellite lines with unequal intensity that are separated from each other by $\Delta B_{eff}=a_{eff}$, and can be readily calculated (equation (6.2)). The solid line in Figure 129 (a) for the H-polymer is a model calculation for the spin-1/2 resonance assuming N=10, where a(H)=3.5mT and $\delta B_{inh}+\delta B_0=0.65$mT (equation (6.3)); it is in excellent agreement with

Figure 129 Isotope dependence of the spin-1/2 ODMR response in DOO-PPV polymers. a, b, The normalized spin-1/2 ODMR response in the H- and D-polymers; the lines through the data points are based on a model fit taking into account the HFI splitting and the polaron spin density spread on the polymer chain, as well as inhomogeneous and natural line-broadening contributions to the resonance with (equation 6.3) . c, The microwave power (P_{MW}) dependence on the integrated ODMR signal intensity for the two polymers; the lines through the data points are model fit using saturation equation. d, The microwave power dependence of the ODMR linewidth for the two polymers; the lines through the data points are model fits based on equation (6.5)

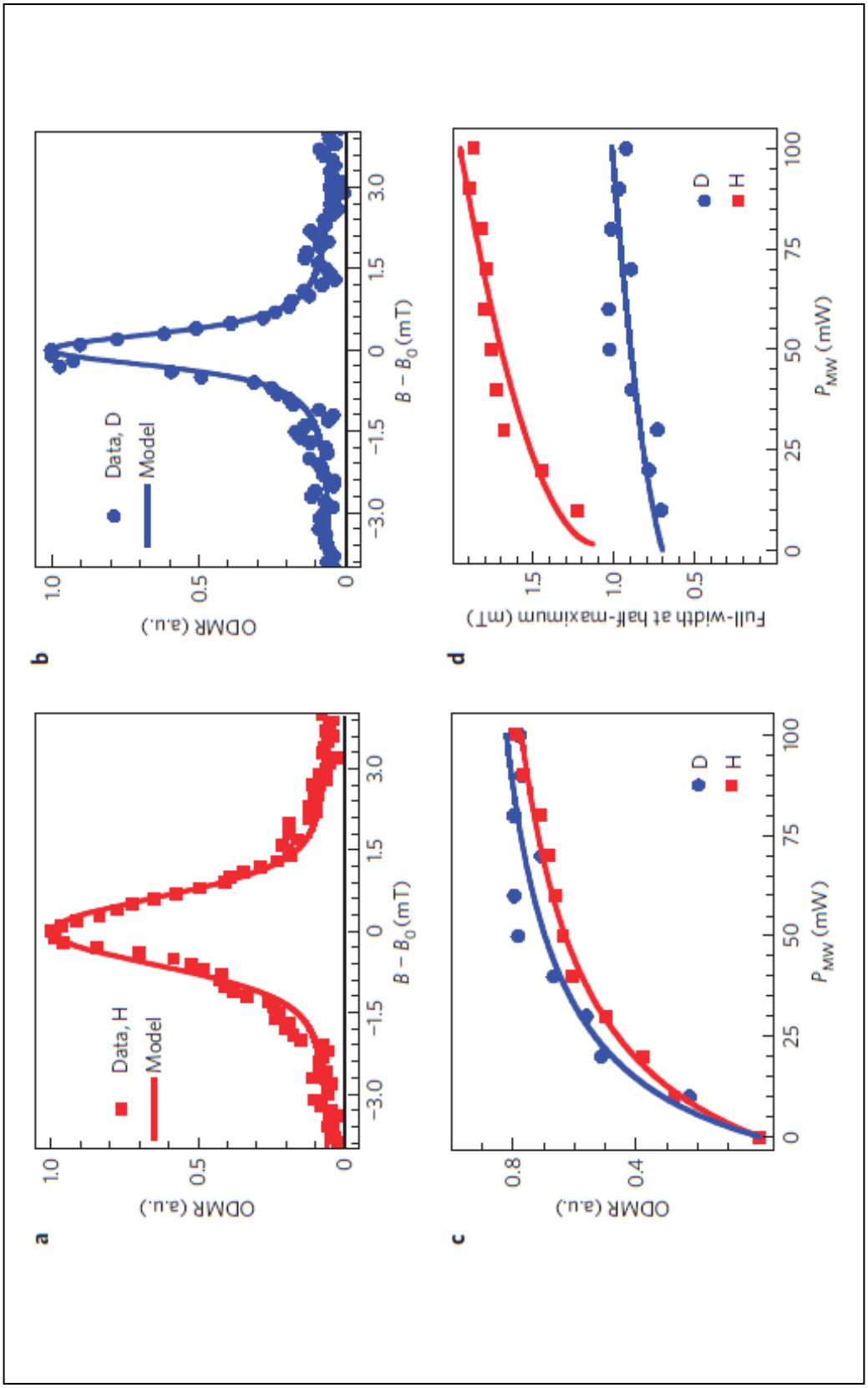
a
b
c
d
ODMR (a.u.)
1.0
0.5
0
Data, H
Model
−3.0
−1.5
0
1.5
3.0
B − B0 (mT)
Data, D
Model
0.8
0.4
D
H
0
25
50
75
100
PMW (mW)
Full-width at half-maximum (mT)
1.5
1.0
0.5

the data. For the D-polymer with a spin-1 nucleus, each resonant line is split into three separate lines, which are further split (2N+1) satellite lines for N C-H units. The solid line in Figure 129 (b) for the D-polymer was similarly calculated using N=10 and $\delta B_{inh}+\delta B_0=0.65$mT but with a(D)=a(H)/6.5=0.54mT. The excellent agreement with the data using the known a(D)/a(H) ratio indicates that the model calculation captures the main effect of the hydrogen isotope exchange on the g≈2 ODMR line in the polymer. Figure 129(c) shows the dependence of the g≈2 ODMR line intensity, δPL, on P_{MW} for both H- and D- polymers. The ODMR intensity shows a saturation behavior [150], namely $\delta PL \sim P_{MW}/(P_{MW}+P_S)$, where $P_S=\alpha\Gamma_{eff}$, α is an experimentally determined constant and Γ_{eff} is given by relation [151]:

$$\Gamma_{eff} = \gamma + \frac{1}{2}\gamma_{SL}, \tag{6.4}$$

where γ is the average polaron-pair recombination rate and $\gamma_{SL}=T_{SL}^{-1}$. As the polaron-pair recombination process at B~0.1T is not expected to depend on isotope exchange, the variation in P_S on deuteration reflects changes in γ_{SL} (see equation (6.4)). Figure 129(c) shows that P_S is smaller for the D-polymer; in fact from the data fit we obtain the ratio: $P_S(H)/P_S(D)=1.4$, and using equation (6.4) we conclude that γ_{SL} is smaller in D-polymer because of the weaker HFI. In the following, we more precisely determine ration, η, of the γ_{SL} rates for the polarons in the two isotope polymers, using a complimentary ODMR method.

Figure 129(d) shows that ODMR linewidth, δB, nonlinearly increases with PMW in both polymers, and the increase is steeper for the H-polymer. The increase in δB may

be related to the magnetic field strength, B_1, of the microwave electromagnetic radiation, which influences the homogeneous linewidth δB_0 through the relation [152]:

$$\delta B_0(P_{MW}) = \delta B_0(0)\left[1 + \frac{\beta}{\gamma_{SL}} P_{MW}\right]^{1/2}. \quad (6.5)$$

where $\beta = (T_2\, \delta B_0(0)\, \alpha)^{-1}$ and $P_{MW} = \alpha(B_1)^2$. As $\delta B_0(0)$ and β are independent of the hydrogen isotope, form the excellent fit to the data in Figure 129 (d) using equation (6.5) we determine the ratio η to be $\eta \equiv \gamma_{SL}(H)/\gamma_{SL}(D) \approx 4$. This indicates that spin relaxation time of the polarons in D-polymer is substantially longer than in the H-polymer, and this should increase the spin-diffusion length of spin-polarized carriers in OSV device based on this polymer.

6.4. Conclusion

ODMR study of two polymer isotopes shows that resonance in D-polymer is narrower than the resonance in H-polymer indicating weaker HFI in D-polymer. Further studies of ODMR dependence on power of microwave we find out that spin relaxation rate in H-polymer is four times greater than in D-polymer, resulting in longer spin lattice relaxation time and longer spin diffusion length in D-polymer; which makes D-polymer better suited for higher performing OSV devices.

CHAPTER 7

CONCLUSION

In this work we studied films of several electron donors, acceptors, and their blends that are used in photovoltaic applications, by means of optical (PA, PL, EA) and magnetic resonance (PLDMR, PADMR, and LESR) probes. We used continuous wave spectroscopy, which allows us to study mainly long- lived photoexcitations such as triplet excitons, polarons, and polaron pairs.

We studied: RR P3HT and RRa P3HT - common donor materials; TAES-V copolymer with a low band-gap; PCBM, bis PCBM and ICBA fullerene derivatives with different LUMO levels that are used as electron acceptors.

In the past 10 years the RR P3HT regioregularity continuously improved, yielding higher power conversion efficiencies when used as active material in solar cell applications. PLQE of the newest RR P3HT has increased almost 10 times, which can be attributed to fewer defects. The PA spectrum of high molecular weight (superior regioregularity) RR P3HT does not show a PA band at low photon energy, previously assigned to PA band (P1) of separated polarons. The PADMR shows that the dominant PA band in this polymer is due more to delocalized than localized triplet excitons, as in RRa P3HT.

Ultrafast photomodulation shows that with decreased MW a new band at 0.55 eV appears in the PA spectrum that does not share the same dynamics as the band at 0.95 eV that belongs to excitons. We thus conclude that this PA band is either due to trapped excitons in defects, or to excitons in the polymer aggregates. We also studied TAES-V, a novel low band gap (~1.7 eV) polymer composed of three copolymers of the structure D-A-D. When used in OPVC it provides a 7% power conversion efficiency that can be partially due to its red shifted absorption. PL of this polymer is very well structured indicating long conjugated chains and high regioregularity. The 0-0 vibronic transition is very strong, almost equal to the 0-1 transition that is typical of single molecules, suggesting low aggregation of the undoped pure polymer. PLQE is very high, 17%, that can be attributed to intrachain exciton recombination. Photoinduced absorption shows only one PA peak at ~1.06 eV that is due to triplets. PLDMR clearly shows spin-1 triplet powder pattern with both full field and half field resonances. It also shows another sharp asymmetric resonance due to spin-1/2 that we do not see in PA. Therefore the PLDMR can be the result of both triplet and polaron pair resonances, where shoulders of polaron-pair might be buried in triplet powder pattern, giving us very large D and E zero field splitting parameters. Different saturation behavior of PLDMR with increased microwave power of half field resonance as opposed to the resonance at 1011 G confirms that they are due to different photogenerated species. The narrow spin-1/2 resonance consists of two positive and one negative contribution. With the LESR we are able to clearly resolve these contributions and confirm the negative resonance. The negative resonance may be due to nonradiative trapping of polarons by radical ions on the acceptor copolymer, which can be the cause of a large ESR signal.

The results of optical and magnetic resonance studies of three fullerene derivatives - PCBM, bis-PCBM and ICBA- were also presented. Depending on their absorption and LUMO energy level they produce OPVCs with largely different PCE. The absorption and the LUMO of a fullerene derivative can be changed by altering its molecular structure, namely the addition of functional side groups to the PCBM cage. The addition of only one functional group can raise the LUMO level by ~110 meV. However, this affects the film morphology. The addition of more than two functional groups hinders the aggregation in films, and consequently also the charge transport. The easier approach is to synthesize a new fullerene derivative with shorter side chains that would not disrupt the packing of molecules and the aggregation such as ICBA. ICBA is a fullerene derivative where two indene side groups are added to the C_{60} cage. Its superiority over PCBM is reflected in better solubility, broader absorption in the visible region, a higher LUMO energy level, the capability in closer molecule packing and more distinct phase separation.

In the study of polymer/fullerene blends we mixed RR P3HT with bis-PCBM and ICBA. Both acceptors yield better power conversion efficiencies than that in PCBM blend. This is mainly due to the higher LUMO level and improved V_{oc}. The morphology of the blend also plays a significant role. Bis-PCBM is bulkier with its two side-chains than the PCBM molecule and it is not capable of destructing the packing of the P3HT chains as much as PCBM. ICBA is compact and it is able to approach the P3HT chains much closer. However, the thermal annealing process helps to expel the fullerene molecules out of P3HT chains and restore the crystallites. Based on magnetic resonance studies we see in all of three blends with P3HT more spin ½ polarons on the fullerene

molecules than on the P3HT chains. This could be due either to formation of spinless bipolarons on the polymer, or the existence of both positive and negative polarons on the fullerene aggregates. Another possibility is that T1 in the fullerene is longer than that in the polymer and thus the LESR signal, which is related to the number of polarized spin ½, is larger in the fullerene matrix.

We also studied a blend of a low-band gap copolymer TAES-V, which has both donor and acceptor moieties on its chains. Based on photoinduced absorption, electroabsorption, and PADMR experiments we conclude that intrachain CTE persists in the blends. We were not able to see the signature of interchain CTE in the electro-absorption spectrum. We conclude that the dominant PA band at 1.07 eV might be due to intrachain CT complex in triplet configuration and the PA band at 1.2 eV to polarons on both the polymer and the fullerene. The LESR studies indicated that there are more charges on the polymer than on the fullerene in contrast to the other three blends. These results are consistent with the existence of both donor and acceptor moieties on this copolymer.

In conclusion, based on our study of P3HT it seems that using a donor with better order and organization of polymer chains we broaden the absorption into IR, promote the charge separation at the donor/acceptor boundary and increase the charge mobility; and therefore increase power conversion efficiency of a solar cell. In addition the modification of a HOMO of a donor material is a far more successful approach to the improvement of the power conversion efficiency of organic solar cells.

Polymers can preserve the spin information over extremely long times, and therefore they can be used to carry information by means of the electron spin. The spin

relaxation is affected by spin-orbit coupling and hyperfine interaction. The nuclear spins in organics mostly originate from isotopes such as ^{1}H (I=1/2), ^{13}C (I=1/2), or ^{14}N (I=1). Consequently, the hyperfine interaction as well as spin relaxation time can be altered when an organic material is enriched with these isotopes. We studied DOO-PPV (H-polymer) and DOO-PPV enriched with deuterium (D-polymer). ODMR study of these two polymer isotopes shows that the resonance in D-polymer is narrower than the resonance in H-polymer indicating weaker HFI in the former. From further studies of ODMR dependence on microwave power we discovered that the spin relaxation rate in H-polymer is four times larger than in D-polymer, resulting in longer spin lattice relaxation time and longer spin diffusion length in D-polymer; which makes D-polymer better suited for higher performing OSV devices.

APPENDIX

GLOSSARY OF ABBREVIATIONS

Abbreviation	Full name
bis-PCBM	bis-adduct of phenyl C61-butyric acid methyl ester
C60	fullerene, a spherical molecule consisting of 60 carbon atoms
CTE	charge transfer exciton
CW	continuous wave
DIA	doping induced absorption
DOO-PPV	poly(2,5-dioctyloxy-p-phenylenevinylene)
DPPH	2,2-diphenyl-1-picrylhydrazyl
EA	electro absorption
ESR	electron spin resonance
eV	electron Volt
FF	Fill Factor
g	Lande g-factor
HFI	hiperfine interaction
HOMO	highest ocupied molecular orbital
ICBA	indene-C60 bis-adduct
IV	curent voltage characteristics
Jsc	short circuiet current density
kDa	kilo Dalton - unit of molecular weight equal to atomic weight of H-atom
LESR	light induced electron spin resonance
LUMO	lowest unocupied molecular orbital
MW	microwave
OD	optical density
ODMR	optically detected magnetic resonance
OLED	organic light emiting diode
OPVC	organic photovoltaic cell
OSV	organic spin valve

P	polaron
P3HT	poly(3-hexylthiophene)
PA	photoinduced absorption
PADMR	photoinduced absorption detected magnetic resonance
PCBM	phenyl C61-butyric acid methyl ester
PCE	power conversion efficiency
Abbreviation	**Full name**
PCP	π-conjugated polymers
PL	photoluminescence
PLDMR	photoluminescence detected magnetic resonance
PLQE	photoluminescence quantum efficiency
PP	polaron pair
RR	regioregular
RRa	regio-random
S	singlet
T	triplet
TEM	tunneling electron microscopy
Voc	open circuit voltage
WOLED	white organic light emiting diode
XRD	x-ray diffraction

`

REFERENCES

[1] G. Inzelt, in Conducting Polymers, Springer Berlin Heidelberg, 2008, p. 265.

[2] C. J. Brabec, N. S. Sariciftci, and J. C. Hummelen, Advanced Functional Materials 11 (2001) 15.

[3] C. J. Brabec, S. Gowrisanker, J. J. M. Halls, D. Laird, S. Jia, and S. P. Williams, Advanced Materials 22 (2010) 3839.

[4] S. Günes, H. Neugebauer, and N. S. Sariciftci, Chemical Reviews 107 (2007) 1324.

[5] H. Spanggaard and F. C. Krebs, Solar Energy Materials and Solar Cells 83 (2004) 125.

[6] N. S. S. Harald Hoppe, Journal of Materials Research Society 19 (2004).

[7] Yam, WOLEDs and Organic Photovoltaics : Recent Advances and Applications, Green Energy and Technology, 2010.

[8] Z. Bao, Organic Field-Effect Transistors, CRC Press, Boca Raton, 2007.

[9] S. Sanvito, Nature Materials 6 (2007) 803.

[10] A. J. Heeger, S. Kivelson, J. R. Schrieffer, and W. P. Su, Reviews of Modern Physics 60 (1988) 781.

[11] R. E. Peierls, ed., Quantum Theory of Solids, The Clarendon Press, Oxford, 1955.

[12] W. P. Su, J. R. Schrieffer, and A. J. Heeger, Physical Review B 22 (1980) 2099.

[13] S. Mazumdar and S. N. Dixit, Physical Review Letters 51 (1983) 292.

[14] D. K. Campbell and A. R. Bishop, Nuclear Physics B 200 (1982) 297.

[15] H. A. Mizes and E. M. Conwell, Physical Review B 50 (1994) 11243.

[16] J. L. Bredas and G. B. Street, Accounts of Chemical Research 18 (1985) 309.

[17] A. L. Fahrenbruch and R. H. Bube, ed., Fundamentals of Solar Cells. Photovoltaic Solar Energy Conversion, Academic Press: New York, 1983.

[18] B. A. Gregg, The Journal of Physical Chemistry B 107 (2003) 4688.

[19] A. J. Moulé and K. Meerholz, Advanced Materials 20 (2008) 240.

[20] Y. Gao and J. K. Grey, Journal of the American Chemical Society 131 (2009) 9654.

[21] L.-M. Program, 2007.

[22] J. Kido, K. Hongawa, K. Okuyama, and K. Nagai, Applied Physics Letters 64 (1994) 815.

[23] M. C. Gather, A. Köhnen, and K. Meerholz, Advanced Materials 23 (2011) 233.

[24] M. A. Baldo, D. F. O'Brien, Y. You, A. Shoustikov, S. Sibley, M. E. Thompson, and S. R. Forrest, Nature 395 (1998) 151.

[25] J. Orenstein, Z. Vardeny, G. L. Baker, G. Eagle, and S. Etemad, Physical Review B 30 (1984) 786.

[26] Z. Vardeny, E. Ehrenfreund, O. Brafman, M. Nowak, H. Schaffer, A. J. Heeger, and F. Wudl, Physical Review Letters 56 (1986) 671.

[27] M. Wohlgenannt, W. Graupner, G. Leising, and Z. V. Vardeny, Physical Review B 60 (1999) 5321.

[28] O. Epshtein, Y. Eichen, E. Ehrenfreund, M. Wohlgenannt, and Z. V. Vardeny, Physical Review Letters 90 (2003) 046804.

[29] K. S. Cole and R. H. Cole, The Journal of Chemical Physics 9 (1941) 341.

[30] J. Charles P. Poole, ed., Electron Spin Resonance: A Comprehensive Treatise on Experimental Techniques, Interscience Publishers, a division of John Wiley & Sons, 1967.

[31] L. D. S. Yadav, ed., Organic Spectroscopy, Kluwer Academic Publishers, Dordrecht, Netherlands, 2005.

[32] P. H. Rieger, ed., Electron Spin Resonance: Analysis and Interpretation, The Royal Society of Chemistry, Cambridge, 2007.

[33] C. P. Slichter, ed., Principles of Magnetic Resonance, Springer, Heidelberg, 1996.

[34] G.W. Ewing, Analytical Instrumentation Handbook, Marcel Dekker, Inc., New York,1997.

[35] R. D. McCullough, Advanced Materials 10 (1998) 93.

[36] R. S. Lowe, R.D. McCullough, Method of Forming Poly-(3-Substituted) Thiophenes, United States Patent and Trademark Office, Carnegie Melon University, Pittsburgh, 2000.

[37] Y. Kim, S. Cook, S. M. Tuladhar, S. A. Choulis, J. Nelson, J. R. Durrant, D. D. C. Bradley, M. Giles, I. McCulloch, C.-S. Ha, and M. Ree, Nature Materials 5 (2006) 197.

[38] J. Y. Kim, K. Lee, N. E. Coates, D. Moses, T.-Q. Nguyen, M. Dante, and A. J. Heeger, Science 317 (2007) 222.

[39] M. Trznadel, A. Pron, M. Zagorska, R. Chrzaszcz, and J. Pielichowski, Macromolecules 31 (1998) 5051.

[40] R. J. Kline, M. D. McGehee, E. N. Kadnikova, J. Liu, and J. M. J. Fréchet, Advanced Materials 15 (2003) 1519.

[41] R. J. Kline, M. D. McGehee, E. N. Kadnikova, J. Liu, J. M. J. Fréchet, and M. F. Toney, Macromolecules 38 (2005) 3312.

[42] C. Goh, R. J. Kline, M. D. McGehee, E. N. Kadnikova, and J. M. J. Frechet, Applied Physics Letters 86 (2005) 122110.

[43] A. Zen, J. Pflaum, S. Hirschmann, W. Zhuang, F. Jaiser, U. Asawapirom, J. P. Rabe, U. Scherf, and D. Neher, Advanced Functional Materials 14 (2004) 757.

[44] O. J. Korovyanko, R. Oesterbacka, X. M. Jiang, Z. V. Vardeny, and R. A. J. Janssen, Physical Review B 64 (2001) 235122.

[45] H. Sirringhaus, P. J. Brown, R. H. Friend, M. M. Nielsen, K. Bechgaard, B. M. W. Langeveld-Voss, A. J. H. Spiering, R. A. J. Janssen, E. W. Meijer, P. Herwig, and D. M. de Leeuw, Nature 401 (1999) 685.

[46] J. Clark, C. Silva, R. H. Friend, and F. C. Spano, Physical Review Letters 98 (2007) 206406.

[47] F. C. Spano, J. Clark, C. Silva, and R. H. Friend, The Journal of Chemical Physics 130 (2009) 074904.

[48] X. M. Jiang, R. Österbacka, O. Korovyanko, C. P. An, B. Horovitz, R. A. J. Janssen, and Z. V. Vardeny, Advanced Functional Materials 12 (2002) 587.

[49] C. X. Sheng, M. Tong, S. Singh, and Z. V. Vardeny, Physical Review B 75 (2007) 085206.

[50] R. Österbacka, C. P. An, X. M. Jiang, and Z. V. Vardeny, Science 287 (2000) 839.

[51] L. S. Swanson, J. Shinar, and K. Yoshino, Physical Review Letters 65 (1990) 1140.

[52] L. Huo, J. Hou, S. Zhang, H.-Y. Chen, and Y. Yang, Angewandte Chemie International Edition 49 (2010) 1500.

[53] D. Mühlbacher, M. Scharber, M. Morana, Z. Zhu, D. Waller, R. Gaudiana, and C. Brabec, Advanced Materials 18 (2006) 2884.

[54] J. Peet, J. Y. Kim, N. E. Coates, W. L. Ma, D. Moses, A. J. Heeger, and G. C. Bazan, Nature Materials 6 (2007) 497.

[55] J. Hou, H.-Y. Chen, S. Zhang, G. Li, and Y. Yang, Journal of the American Chemical Society 130 (2008) 16144.

[56] J. Hou, H.-Y. Chen, S. Zhang, R. I. Chen, Y. Yang, Y. Wu, and G. Li, Journal of the American Chemical Society 131 (2009) 15586.

[57] G. Dennler, M. C. Scharber, and C. J. Brabec, Advanced Materials 21 (2009) 1323.

[58] P. K. H. Ho, J.-S. Kim, N. Tessler, and R. H. Friend, The Journal of Chemical Physics 115 (2001) 2709.

[59] P. A. Lane, X. Wei, and Z. V. Vardeny, Physical Review B 56 (1997) 4626.

[60] H. P. Gislason and G. D. Watkins, Physical Review B 33 (1986) 2957.

[61] N. S. Sariciftci, L. Smilowitz, A. J. Heeger, and F. Wudl, Synthetic Metals 59 (1993) 333.

[62] M. A. Faist, P. E. Keivanidis, S. Foster, P. H. Wöbkenberg, T. D. Anthopoulos, D. D. C. Bradley, J. R. Durrant, and J. Nelson, Journal of Polymer Science Part B: Polymer Physics 49 (2011) 45.

[63] C. J. Brabec, M. Heeney, I. McCulloch, and J. Nelson, Chemical Society Reviews 40 (2011) 1185.

[64] Q. L. Song, C. M. Li, M. B. Chan-Park, M. Lu, H. Yang, and X. Y. Hou, Physical Review Letters 98 (2007) 176403.

[65] S. Cook, H. Ohkita, Y. Kim, J. J. Benson-Smith, D. D. C. Bradley, and J. R. Durrant, Chemical Physics Letters 445 (2007) 276.

[66] N. C. Nicolaidis, B. S. Routley, J. L. Holdsworth, W. J. Belcher, X. Zhou, and P. C. Dastoor, The Journal of Physical Chemistry C 115 (2011) 7801.

[67] Q. L. Song, C. Gong, H. B. Yang, and C. M. Li, Solar Energy Materials and Solar Cells 94 (2010) 2422.

[68] X. Wei and Z. V. Vardeny, Physical Review B 52 (1995) R2317.

[69] P. A. Lane, L. S. Swanson, Q. X. Ni, J. Shinar, J. P. Engel, T. J. Barton, and L. Jones, Physical Review Letters 68 (1992) 887.

[70] H.-Y. Chen, J. Hou, S. Zhang, Y. Liang, G. Yang, Y. Yang, L. Yu, Y. Wu, and G. Li, Nature Photonics 3 (2009) 649.

[71] M. Morana, M. Wegscheider, A. Bonanni, N. Kopidakis, S. Shaheen, M. Scharber, Z. Zhu, D. Waller, R. Gaudiana, and C. Brabec, Advanced Functional Materials 18 (2008) 1757.

[72] N. Blouin, A. Michaud, and M. Leclerc, Advanced Materials 19 (2007) 2295.

[73] H. S. K. Yong Zhang, Yip Hin-Lap, Ying Sun, Acton Orb, Jen Alex K.-Y., Chemistry of Materials 22 (2010) 2696.

[74] Y. Zou, A. Najari, P. Berrouard, S. Beaupré, B. Réda Aïch, Y. Tao, and M. Leclerc, Journal of the American Chemical Society 132 (2010) 5330.

[75] L. Zheng, Q. Zhou, X. Deng, M. Yuan, G. Yu, and Y. Cao, The Journal of Physical Chemistry B 108 (2004) 11921.

[76] M. M. Wienk, J. M. Kroon, W. J. H. Verhees, J. Knol, J. C. Hummelen, P. A. van Hal, and R. A. J. Janssen, Angewandte Chemie International Edition 42 (2003) 3371.

[77] L. M. Popescu, P. Hof, A. B. Sieval, H. T. Jonkman, and J. C. Hummelen, Applied Physics Letters 89 (2006) 213507.

[78] F. B. Kooistra, J. Knol, F. Kastenberg, L. M. Popescu, W. J. H. Verhees, J. M. Kroon, and J. C. Hummelen, Organic Letters 9 (2007) 551.

[79] M. Lenes, G. J. A. H. Wetzelaer, F. B. Kooistra, S. C. Veenstra, J. C. Hummelen, and P. W. M. Blom, Advanced Materials 20 (2008) 2116.

[80] D. Kronholm, J. C. K. Hummelen, Spie Newsroom, DOI:10.1117/2.120810.1232 (2008).

[81] J. M. Frost, M. A. Faist, and J. Nelson, Advanced Materials 22 (2010) 4881.

[82] G. Yu, J. Gao, J. C. Hummelen, F. Wudl, and A. J. Heeger, Science 270 (1995) 1789.

[83] G. Li, V. Shrotriya, J. Huang, Y. Yao, T. Moriarty, K. Emery, and Y. Yang, Nature Materials 4 (2005) 864.

[84] W. Ma, C. Yang, X. Gong, K. Lee, and A. J. Heeger, Advanced Functional Materials 15 (2005) 1617.

[85] C. J. Brabec, A. Cravino, D. Meissner, N. S. Sariciftci, T. Fromherz, M. T. Rispens, L. Sanchez, and J. C. Hummelen, Advanced Functional Materials 11 (2001) 374.

[86] J. Li, N. Sun, Z.-X. Guo, C. Li, Y. Li, L. Dai, D. Zhu, D. Sun, Y. Cao, and L. Fan, The Journal of Physical Chemistry B 106 (2002) 11509.

[87] J. A. Mikroyannidis, A. N. Kabanakis, S. S. Sharma, and G. D. Sharma, Advanced Functional Materials 21 (2011) 746.

[88] G. Zhao, Y. He, and Y. Li, Advanced Materials 22 (2010) 4355.

[89] Y. He, H.-Y. Chen, J. Hou, and Y. Li, Journal of the American Chemical Society 132 (2010) 1377.

[90] D. W. S. Laird, R.; Richter, H.; Vejins, V.; Scott, L.; Lada, T.A, Vol. WO/2008/018931, 2008.

[91] D. Weng, H. K. Lee, K. Levon, J. Mao, W. A. Scrivens, E. B. Stephens, and J. M. Tour, European Polymer Journal 35 (1999) 867.

[92] N. Yevlampieva, T. Dmitrieva, E. Melenevskaya, I. Zaitseva, and E. Ryumtsev, Polymer Science Series A 49 (2007) 284.

[93] G. A. Polotskaya, S. V. Gladchenko, and V. N. Zgonnik, Journal of Applied Polymer Science 85 (2002) 2946.

[94] O. Parisel, G. Berthier, and E. Migirdicyan, Canadian Journal of Chemistry 73 (1995) 1869.

[95] R. K. M. Bouwer and J. C. Hummelen, Chemistry – A European Journal 16 (2010) 11250.

[96] J. J. M. Halls, J. Cornil, D. A. dos Santos, R. Silbey, D. H. Hwang, A. B. Holmes, Br, eacute, J. L. das, and R. H. Friend, Physical Review B 60 (1999) 5721.

[97] M. D. Irwin, D. B. Buchholz, A. W. Hains, R. P. H. Chang, and T. J. Marks, Proceedings of the National Academy of Sciences 105 (2008) 2783.

[98] S. Morita, Solid State Communications 82 (1992) 249.

[99] P. Schilinsky, C. Waldauf, and C. J. Brabec, Applied Physics Letters 81 (2002) 3885.

[100] M. Reyes-Reyes, K. Kim, and D. L. Carroll, Applied Physics Letters 87 (2005) 083506.

[101] T. J. Savenije, J. E. Kroeze, X. Yang, and J. Loos, Advanced Functional Materials 15 (2005) 1260.

[102] A. Pivrikas, G. Juscaronka, A. J. Mozer, M. Scharber, K. Arlauskas, N. S. Sariciftci, H. Stubb, and R. Osterbacka, Physical Review Letters 94 (2005) 176806.

[103] G. Juska, K. GeneviCius, N. Nekrasas, G. Sliauzys, and R. Osterbacka, Applied Physics Letters 95 (2009) 013303.

[104] M. Hallermann, I. Kriegel, E. Da Como, J. M. Berger, E. von Hauff, and J. Feldmann, Advanced Functional Materials 19 (2009) 3662.

[105] H. Alves, A. S. Molinari, H. Xie, and A. F. Morpurgo, Nature Materials 7 (2008) 574.

[106] J. J. Benson-Smith, L. Goris, K. Vandewal, K. Haenen, J. V. Manca, D. Vanderzande, D. D. C. Bradley, and J. Nelson, Advanced Functional Materials 17 (2007) 451.

[107] Z. Wang, S. Mazumdar, and A. Shukla, Physical Review B 78 (2008) 235109.

[108] K. Aryanpour, D. Psiachos, and S. Mazumdar, Physical Review B 81 (2010) 085407.

[109] A. C. Morteani, A. S. Dhoot, J. S. Kim, C. Silva, N. C. Greenham, C. Murphy, E. Moons, S. Ciná, J. H. Burroughes, and R. H. Friend, Advanced Materials 15 (2003) 1708.

[110] M. A. Loi, S. Toffanin, M. Muccini, M. Forster, U. Scherf, and M. Scharber, Advanced Functional Materials 17 (2007) 2111.

[111] A. C. Morteani, R. H. Friend, and C. Silva, Chemical Physics Letters 391 (2004) 81.

[112] A. C. Morteani, R. H. Friend, and C. Silva, The Journal of Chemical Physics 122 (2005) 244906.

[113] D. Motaung, G. Malgas, and C. Arendse, Journal of Materials Science 45 (2010) 3276.

[114] N. S. S. Sam-Shajing Sun, ed., Organic Photovoltaics: Mechanism, Materials, and Devices, CRC Press, Boca Raton, 2005.

[115] V. Dyakonov, G. Osler, M. Schwoerer, and E. L. Frankevich, Physical Review B 56 (1997) 3852.

[116] T. D. Nguyen, G. Hukic-Markosian, F. Wang, L. Wojcik, X.-G. Li, E. Ehrenfreund, and Z. V. Vardeny, Nature Materials 9 (2010) 345.

[117] T. Kobayashi, K. Kinoshita, T. Nagase, and H. Naito, Physical Review B 83 (2011) 035305.

[118] K. Marumoto, Y. Muramatsu, N. Takeuchi, and S. Kuroda, Synthetic Metals 135-136 (2003) 433.

[119] V. I. Krinichnyi and E. I. Yudanova, Journal of Renewable and Sustainable Energy 1 (2009) 043110.

[120] V. Dyakonov, G. Zoriniants, M. Scharber, C. J. Brabec, R. A. J. Janssen, J. C. Hummelen, and N. S. Sariciftci, Physical Review B 59 (1999) 8019.

[121] K. Marumoto, M. Kato, H. Kondo, S. Kuroda, N. C. Greenham, R. H. Friend, Y. Shimoi, and S. Abe, Physical Review B 79 (2009) 245204.

[122] J. Behrends, A. Schnegg, K. Lips, E. A. Thomsen, A. K. Pandey, I. D. W. Samuel, and D. J. Keeble, Physical Review Letters 105 (2010) 176601.

[123] G. Zoriniants, V. Dyakonov, M. Scharber, C. J. Brabec, R. A. J. Janssen, J. C. Hummelen, and N. S. Sariciftci, Synthetic Metals 102 (1999) 1241.

[124] Houz, Eacute, and M. Nechtschein, Physical Review B 53 (1996) 14309.

[125] J. Krzystek, A. Sienkiewicz, L. Pardi, and L. C. Brunel, Journal of Magnetic Resonance 125 (1997) 207.

[126] V. I. Krinichnyi, E. I. Yudanova, and N. G. Spitsina, The Journal of Physical Chemistry C 114 (2010) 16756.

[127] A. Kawamori, J. Yamauchi, H. Ohta, ESR in the Twenty-First Century, ScienceDirect, Elsevier, Amsterdam; Boston, 2001.

[128] F. Diederich and R. Kessinger, Accounts of Chemical Research 32 (1999) 537.

[129] M. Theander, A. Yartsev, D. Zigmantas, Sundstr, ouml, V. m, W. Mammo, M. R. Andersson, O. Ingan, Physical Review B 61 (2000) 12957.

[130] R. A. Marsh, J. M. Hodgkiss, S. Albert-Seifried, and R. H. Friend, Nano Letters 10 (2010) 923.

[131] T. Drori, C. X. Sheng, A. Ndobe, S. Singh, J. Holt, and Z. V. Vardeny, Physical Review Letters 101 (2008) 037401.

[132] M. Wohlgenannt, C. Yang, and Z. V. Vardeny, Physical Review B 66 (2002) 241201.

[133] B. Schweitzer, V. I. Arkhipov, and H. Bässler, Chemical Physics Letters 304 (1999) 365.

[134] G. Zhao, Y. He, Z. Xu, J. Hou, M. Zhang, J. Min, H.-Y. Chen, M. Ye, Z. Hong, Y. Yang, and Y. Li, Advanced Functional Materials 20 (2010) 1480.

[135] Y.-J. Cheng, C.-H. Hsieh, Y. He, C.-S. Hsu, and Y. Li, Journal of the American Chemical Society 132 (2010) 17381.

[136] J. J. Dittmer, R. Lazzaroni, P. Leclère, P. Moretti, M. Granström, K. Petritsch, E. A. Marseglia, R. H. Friend, J. L. Brédas, H. Rost, and A. B. Holmes, Solar Energy Materials and Solar Cells 61 (2000) 53.

[137] E. L. Frankevich, A. A. Lymarev, I. Sokolik, F. E. Karasz, S. Blumstengel, R. H. Baughman, and H. H. Hoerhold, Physical Review B 46 (1992) 9320.

[138] J. W. Arbogast and C. S. Foote, Journal of the American Chemical Society 113 (1991) 8886.

[139] M. Drees, K. Premaratne, W. Graupner, J. R. Heflin, R. M. Davis, D. Marciu, and M. Miller, Applied Physics Letters 81 (2002) 4607.

[140] J. Poplawski, E. Ehrenfreund, J. Cornil, J. L. Bredas, R. Pugh, M. Ibrahim, and A. J. Frank, Synthetic Metals 69 (1995) 401.

[141] M. Tong, C. X. Sheng, and Z. V. Vardeny, Physical Review B 75 (2007) 125207.

[142] J. Holt, S. Singh, T. Drori, Y. Zhang, and Z. V. Vardeny, Physical Review B 79 (2009) 195210.

[143] L. Sebastian and G. Weiser, Physical Review Letters 46 (1981) 1156.

[144] F. Pulizzi, Nature Materials 8 (2009) 691.

[145] D. R. McCamey, H. A. Seipel, S. Y. Paik, M. J. Walter, N. J. Borys, J. M. Lupton, and C. Boehme, Nature Materials7 (2008) 723.

[146] K. Fesser, A. R. Bishop, and D. K. Campbell, Physical Review B 27 (1983) 4804.

[147] A. Carrington and A. D. McLachlan, Introduction to Magnetic Resonance with Applications to Chemistry and Chemical Physics, Harper & Row, New York, 1967.

[148] B. R. Weinberger, E. Ehrenfreund, A. Pron, A. J. Heeger, and A. G. MacDiarmid, The Journal of Chemical Physics 72 (1980) 4749.

[149] A. J. Drew, J. Hoppler, L. Schulz, F. L. Pratt, P. Desai, P. Shakya, T. Kreouzis, W. P. Gillin, A. Suter, N. A. Morley, V. K. Malik, A. Dubroka, K. W. Kim, H. Bouyanfif, F. Bourqui, C. Bernhard, R. Scheuermann, G. J. Nieuwenhuys, T. Prokscha, and E. Morenzoni, Nature Materials 8 (2009) 109.

[150] C. G. Yang, E. Ehrenfreund, and Z. V. Vardeny, Physical Review Letters 99 (2007) 157401.

[151] C. G. Yang, E. Ehrenfreund, F. Wang, T. Drori, and Z. V. Vardeny, Physical Review B 78 (2008) 205312.

[152] A. Abragam and H. Y. Carr, Physics Today 14 (1961) 56.